STRUCTURAL FRAMEWORK OF THE TAVŞAN GOLD DEPOSIT IN TAVŞANLI DISTRICT / KÜTAHYA PROVINCE / TÜRKİYE

A THESIS SUBMITTED TO
THE GRADUATE SCHOOL OF NATURAL AND APPLIED SCIENCES
OF
MIDDLE EAST TECHNICAL UNIVERSITY

BY

FURKAN OĞUZ

IN PARTIAL FULFILLMENT OF THE REQUIREMENTS
FOR
THE DEGREE OF MASTER OF SCIENCE
IN
GEOLOGICAL ENGINEERING

DECEMBER 2024

Approval of the thesis:

STRUCTURAL FRAMEWORK OF THE TAVŞAN GOLD DEPOSIT IN TAVŞANLI DISTRICT / KÜTAHYA PROVINCE / TÜRKİYE

submitted by **FURKAN OĞUZ** in partial fulfilment of the requirements for the degree of **Master of Science** i**n Geological Engineering, Middle East Technical University** by,

Prof. Dr. Naci Emre Altun
Dean, **Graduate School of Natural and Applied Sciences** _____

Prof. Dr. Erdin Bozkurt
Head of the Department, **Geological Engineering** _____

Prof. Dr. Erdin Bozkurt
Supervisor, **Geological Engineering, METU** _____

Examining Committee Members:

Prof. Dr. Nuretdin Kaymakçı
Geological Engineering, METU _____

Prof. Dr. Erdin Bozkurt
Geological Engineering, METU _____

Assist. Prof. Dr. Ali İmer
Geological Engineering, METU _____

Prof. Dr. Erman Özsayın
Geological Engineering, Hacettepe University _____

Assoc. Prof. Dr. H. Evren Çubukçu
Geological Engineering, Hacettepe University _____

Date: 05.12.2024

I hereby declare that all information in this document has been obtained and presented in accordance with academic rules and ethical conduct. I also declare that, as required by these rules and conduct, I have fully cited and referenced all material and results that are not original to this work.

Name, Last name : Furkan, Oğuz

Signature :

ABSTRACT

STRUCTURAL FRAMEWORK OF THE TAVŞAN GOLD DEPOSIT IN TAVŞANLI DISTRICT / KÜTAHYA PROVINCE / TÜRKİYE

Oğuz, Furkan
Master of Science, Geological Engineering
Supervisor : Prof. Dr. Erdin Bozkurt

December 2024, 193 pages

The Tavşan Gold Deposit, situated along the boundary between the Tavşanlı and Afyon Zones in northwestern Anatolia, is hosted by diverse geological history involving ophiolitic complexes, accretionary wedges, and continental-margin sedimentary sequences. Detailed geological and structural mapping, combined with diamond drilling, petrographic and geochemical analyses, reflected light microscopy observations, cross-sections, kinematic signatures, stress analysis and 3D geological model, have identified multiple episodes of mineralization, each closely associated with and spatially confined to zones of deformation, primary and subsequent low-angle faults and later-stage strike-slip faults. Episodic reactivation of these faults, suggests a dynamic tectonic environment where compressional and extensional forces alternated, provided repeated conduits for hydrothermal fluids, which precipitated silica-rich, sulphide associated gold-bearing jasperoid bodies at key lithological contacts between carbonate and ophiolitic units with hydrothermal silicification and de-carbonatization. The study also reveals structural development of the study area including zones of cataclastic flow breccias, fault-related shearing and fractures that provided favourable pathways, as well as zones of mineralization and subsequent ore deposition. Spatial zoning in metallic associations and variations

in ore-forming fluids suggest that presence of antimony mineralization and high arsenic geochemical anomalies further supports the nature of the deposit. The results contribute not only to the broader understanding of the tectonic evolution of the Tavşanlı Zone but also contributes valuable insights for future mining exploration strategies in similar structurally complex mineral deposit terranes. This work highlights the significance of episodic deformation in the formation of economically viable gold deposits.

Keywords: Mineral deposit, structural geology, gold, Tavşanlı Zone, Western Anatolia

ÖZ

TAVŞAN ALTIN YATAĞINDA YAPISAL KONTROLLER TAVŞANLI İLÇESİ / KÜTAHYA İLİ / TÜRKİYE

Oğuz, Furkan
Yüksek Lisans, Jeoloji Mühendisliği
Tez Yöneticisi: Prof. Dr. Erdin Bozkurt

Aralık 2024, 193 sayfa

Tavşan Altın Yatağı, kuzeybatı Anadolu'da Tavşanlı ve Afyon Zonları arasındaki sınırda yer almakta olup, ofiyolitik kompleksler, yığışım prizması ve kıta kenarı tortul dizilimleri içeren karmaşık bir jeolojik geçmişe sahiptir. Detaylı jeolojik ve yapısal haritalama, sondaj çalışmaları verileri, petrografik analizler, jeo-kimyasal incelemeler, yansıyan ışık mikroskobu, kesitler, kinematik işaretler, gerilim analizleri ve 3D jeolojik modellemeler kullanılarak mineralizasyonun birden fazla evresi belirlenmiştir. Bu evrelerin her biri, deformasyon zonlarıyla, birincil ve ardışık düşük açılı faylar ile daha sonra gelişen doğrultu atımlı faylar ile yakından ilişkilidir ve bu yapılarla sınırlıdır. Bu fayların epizodik yeniden etkinleşmesi, sıkışmalı ve genişlemeli kuvvetlerin dönüşümlü olarak etkili olduğu dinamik bir tektonik ortamı işaret etmektedir. Bu durum, karbonat ve ofiyolitik birimler arasındaki önemli litolojik kontaklarda hidrotermal silisleşme ve karbonat başkalaşımı ile birlikte silis bakımından zengin, sülfürle ilişkili altın taşıyan jasperoid oluşumlarının çökelmesini sağlayan tekrarlı hidrotermal akışkan yolları sağlamıştır. Çalışma ayrıca fay zonları boyunca gelişen ezilme breşleri ve fayla ilişkili makaslama ve kırık zonları gibi akışkan akışı için elverişli yollar oluşturduğunu ve mineralizasyonun yoğunlaştığı yerel cevher birikimlerine zemin

hazırladığını göstermektedir. Metalik birlikteliklerdeki mekânsal zonlanma ve cevher oluşturan sıvılardaki değişimler, antimon mineralizasyonu ve yüksek arsenik jeo-kimyasal anomalilerinin varlığı, yatağın karakterini daha da desteklemektedir. Elde edilen sonuçlar, yalnızca Tavşanlı Zonu'nun tektonik evrimini anlamaya katkı sağlamakla kalmayıp, benzer yapısal olarak karmaşık mineral yataklarının keşfi için değerli içgörüler de sunmaktadır. Bu çalışma, ekonomik açıdan önemli altın yataklarının oluşumunda epizodik deformasyonun önemini vurgulamaktadır.

Anahtar Kelimeler: Maden yatakları, yapısal jeoloji, altın, Tavşanlı Zonu, Batı Anadolu

To my lovely wife & family

ACKNOWLEDGMENTS

I would like to express my deepest gratitude to Prof. Dr. Erdin Bozkurt, my supervisor, for his invaluable guidance, mentorship, and the countless opportunities he has provided me. His thoughtful and constructive criticism taught me to approach problems from diverse perspectives and the significance of making impartial observations. I am truly thankful to Prof. Dr. Erdin Bozkurt for generously sharing his wisdom and experience throughout this journey. His expertise proved indispensable in navigating the complexities of geological features, and I am forever indebted to him.

I am immensely grateful to Ariana Resources plc, particularly Dr. Kerim Şener, for their support in making this study possible.

I would like to express my heartfelt thanks to Berkin Uğurlu, Burak Mert, Önder Öztürk and İsmail Aksoy for their invaluable assistance during my field studies in Tavşanlı and subsequent research.

I would like to acknowledge and appreciate the assistance of Zack van Coller and Ruth Woodcock for helping with Leapfrog Geo, which enabled me to carry out 3-D geological model studies.

I extend my sincere appreciation to Prof. Dr. Kaan Sayıt and Assist. Prof. Dr. Ali İmer for laying the foundation of my mineral recognition skills and enabling me to understand thorough thin section studies.

I am grateful to my colleagues and friends, Akın Çil and Hakan Bora Okay for his constructive feedback and helpful discussions, which enriched my work.

I would like to express my profound appreciation to my beloved wife, Sinem Oğuz, and my parents, Halil and Fatma Oğuz, as well as my brothers Fatih and Harun Oğuz, for their unwavering support, encouragement, and patience throughout my studies.

In conclusion, I am deeply thankful to everyone who has contributed to my academic journey, directly or indirectly. Your support has been invaluable, and I am truly grateful for the impact you have had on my personal and professional growth.

TABLE OF CONTENTS

ABSTRACT v

ÖZ vii

ACKNOWLEDGMENTS x

TABLE OF CONTENTS xi

LIST OF TABLES xiv

LIST OF FIGURES xv

CHAPTERS

1 INTRODUCTION 1

1.1 Description and Location 1

1.2 Mining and Exploration History of the Study Area 3

1.3 Purpose and Scope 4

1.4 Methodology 5

1.5 Previous Studies 10

1.6 Regional Geology 14

2 GEOLOGY OF TAVŞAN GOLD DEPOSIT 23

2.1 Kırkbudak Formation 28

2.2 Budağan Formation 30

2.3 İmranlar Formation 32

2.4 Dağardı Ophiolitic Mélange 33

2.4.1 Radiolarian Chert 34

2.4.2 Peridotites 36

2.4.3 Limestone Blocks 37

2.4.4 Basalt 39
2.4.5 Turbidites 41
2.4.6 Volcaniclastics 43
2.4.7 Dikes 44
2.5 Taşbaşı Formation 46
2.6 Tavşan Gold Deposit 46
2.6.1 Reflected Light Ore Microscopy 51
2.6.2 Surface Geochemistry of Tavşanlı Gold Deposit 55
3 STRUCTURAL GEOLOGY 65
3.1 Bedding Planes 66
3.2 Foliation 70
3.3 Faults 74
3.3.1 Low-Angle Faults 74
3.3.2 High-Angle Faults 83
3.3.3 High to Moderate Angle Faults in Ophiolitic Mélange 87
3.3.4 Faulting and Mineralization: Core Sample Review 97
4 DISCUSSION 109
4.1 Structural Controls on Mineralization 109
4.1.1 Timing of Structures and Its Relationship with Mineralization 114
4.2 3-D Geological Model of Tavşan Gold Deposit 119
4.2.1 Deposit Scale Geological Model 119
4.2.2 Pit Scale Geological Model 127
4.3 Mineralization Style of the Tavşan Deposit 139
5 CONCLUSIONS 145

REFERENCES 149

APPENDICES 167

A. Summary Table of Followed Methodology 167

B. Fault Measurement..... 168

C. Foliation Measurement 170

D. Bedding Plane Measurement 174

E. Geological Maps 175

F. Rock Assays..... 179

LIST OF TABLES

TABLES

Table 2.1. Correlation matrix of selected elements. 56
Table 2.2. Correlation matrix of the multi-element rock samples. 60
Table 3.1. Number of measures and dominant orientation of structures. 65
Table 3.2. Au ppm laboratory assay values for sampling intervals and intercepts. 106
Table 3.3. Table showing the Au (ppm) and As (ppm) assay values for intervals of above drill hole. 107

LIST OF FIGURES

FIGURES

Figure 1.1. Geological map showing the location of the study area (from Okay, 2001). Tavşanlı gold deposit lies on the boundary between Tavşanlı and Afyon zones. Inset map indicates the location of the geological map. 1
Figure 1.2. Geological map of the Tavşanlı gold deposit and nearby area (redrawn from 25k geological map of MTA). Black rectangle shows the location of the deposit. 2
Figure 1.3. Summary of March 2024 Tavşan Resources as classified and reported in accordance with JORC 2012. Reporting is based on a 1.5 g/t Au cut-off grade for high-grade domains and a 0.5 g/t Au cut-off grade for all other domains (from www.arianaresourcesplc.com). 4
Figure 1.4. Steps followed during the thesis studies over the timeline..... 6
Figure 1.5. Geographic subdivision of Türkiye (Ketin, 1966). 15
Figure 1.6. Simplified tectonic map of Türkiye showing major neotectonic structures and provinces (from Bozkurt, 2001). 16
Figure 1.7. Tectonic map of north-eastern Mediterranean region showing the major sutures and continental blocks. Sutures are shown by heavy lines with the polarity of former subduction zones indicated by filled triangles. Izmir-Ankara Suture (IAES), Northern (NAFZ) and Eastern Anatolian Fault Zone (EAFZ), and Bitlis Suture (BS). (from Okay, 2008). Study area is highlighted with red rectangle. 17
Figure 1.8. The main tectonic units of the Anatolides in western Anatolia are from north to south; the Tavşanlı Zone, the Afyon Zone and the Menderes Massif. Taurides are Lycian Nappes, Beydağları and Geyik Autochthone (redrawn from Pourteau et al., 2015). Black rectangle includes location of the study area..... 18
Figure 1.9. Tectonostratigraphic units of Tavşanlı Zone (from Okay et. al. 2013). 19
Figure 1.10. Time scale showing the age of sedimentation, timing of magmatism and metamorphism in the various tectonic units of Western Anatolia (from Plunder et. al., 2016). 21

Figure 2.1. Columnar section of Tavşan gold deposit (redrawn from Explanatory Booklet of the MTA 1:100 000 Scale Geological Map of Türkiye I21 Sheet and Ersoy et al., 2014). 24
Figure 2.2. Geological map of the Tavşan gold deposit created in thesis studies. .. 25
Figure 2.3.NW–SE cross Section along A-A'. The section line is shown on Figure 2.2. 26
Figure 2.4. NE–SW cross Section along B-B'. The section line is shown on Figure 2.2. 26
Figure 2.5. Outcrop map of the study area. 27
Figure 2.6. Field view of the low-grade schists from the Kırkbudak formation. Note well-developed schistosity. Hammer is 38 cm long. 29
Figure 2.7. Close-up view from a schist hand specimen belonging to Kırkbudak formation. 29
Figure 2.8. Views from the thick-bedded to massive micritic limestones of the Budağan formation. (B) and (C) are hand specimen and core samples, respectively. 31
Figure 2.9. (A) A view of the Budağan formation, a dirty limestone outcrop; this horizon is characterized by calcite veinlets. (B) Core sample shows sand size bedded sediments in limestone (see section bounded by orange lines). Limestone is also brecciated (encircled by green line) and is cut by a calcite veinlet (encircled by blue line). 31
Figure 2.10. Field view from sandstones of the İmranlar formation. Hand specimens of sandstone and mudstone. 33
Figure 2.11. Field view from radiolarian chert in the central part of the study area. 34
Figure 2.12. View from radiolarian chert hand specimen (A) and core samples (B). (C) Phacoidal domains of chert within mudstone. Note that the radiolarians are readily recognizable at the uppermost part of the photo (PPL view). 35
Figure 2.13. Field views from sheared peridotites in the northern side of study area. (A) Harzburgite and (B) serpentinized dunite. 36

Figure 2.14. Hand specimens of harzburgite (A) and dunite (B). (C) Polished thin section of serpentinized harzburgite under the microscope with XPL view. The rock is mainly composed of olivine, clinopyroxene, and orthopyroxene but primary phases are hardly recognizable (see encircled areas) since intense alteration destroyed most of them: olivine is totally altered to serpentine, orthopyroxene is also entirely altered and appears as bastite pseudomorphs while clinopyroxene appears as colourless, subhedral/anhedral grains with high birefringence. The sample is intensely carbonatized. (D) A view from core sample of a serpentinized harzburgite. 37
Figure 2.15. Field views from dolomitic limestone block of the Dağardı ophiolitic mélange in the northern (A) and southern (B) parts of the study area. 38
Figure 2.16. Views of hand specimens (A) and core samples (B) of recrystallized dolomitic limestone blocks in Dağardı ophiolitic mélange. 39
Figure 2.17. Field view from weathered submarine basalt outcrop in Dağardı ophiolitic mélange, pillow lavas brownish in colour. 40
Figure 2.18. Views of hand specimens (A), core samples (B) of basalts and (C) volcaniclastics (C). Note porphyritic basalt clast with brownish-coloured Ti-rich augite and olivine phenocrysts in "C". There olivine crystal is entirely altered to saponite (PPL view). 41
Figure 2.19. Field view from a turbidite outcrop in Dağardı ophiolitic mélange. .. 42
Figure 2.20. A view from (A) a turbidite hand specimen and (B) polished thin section under microscope with XPL view. Small, flaky grains are micas that have grown in response to low-grade metamorphism. Note that they are preferably aligned, defining foliation in the sample. 42
Figure 2.21. Field view of volcaniclastic outcrop in the northern part of the study area. 44
Figure 2.22. Views from (A) hand specimen of volcaniclastic unit with chert, mafic and ultramafic clasts; (B) basalt fragments and clinopyroxene aggregates, which are cut by thin veins of calcite and quartz (PPL view). 44

Figure 2.23. Field view form the hornblendite dike (marked with red line) intruding the ultramafics of the Dağardı ophiolitic mélange. 45
Figure 2.24. Views from hornblendite hand specimen (A) and thin section (B). PPL view shows hornblende crystals (green grains). Note that they are replaced by Ti-bearing phases (linear features) and opaques. 46
Figure 2.25. Map showing distribution of the jasperoid mineralization and outlines of Tavşan gold deposit. 47
Figure 2.26. Views of low-angle fault zone consisting of main jasperoid mineralization. Yellow iron-oxide rich clay fills cavities in the limestone, low-grade metamorphosed and sheared Dağardı ophiolitic mélange. 48
Figure 2.27. Views of fine-grained to sugary silicification, jasperoid blocks with solution cavities. 48
Figure 2.28. Field views of karstic cavity with breccias and silicification in the open pit. 49
Figure 2.29. View form core samples showing karstic cavities filled with brecciated limestone and clay-bearing sediments as a matrix. The fault zone is evident at depths between 19.80 m and 23.00 m, with fault gouge. 49
Figure 2.30. Detailed views of core samples, showing mineralization zone, as well as brecciation within ophiolitic units, jasperoid, and limestones. The fault zone is evident at depths between 41.00 m and 44.50 m, with a high concentration of gold (Au) mineralization, particularly 7.75 ppm and 2.57 ppm. The jasperoid breccia and carbonate breccia zones, visible between 44.00 m and 47.00 m, further exhibit varying levels of Au, with concentrations ranging from 0.45 ppm to 1.10 ppm. These observations suggest a complex structural framework and brecciation pattern, which are crucial for understanding the mineralization. 50
Figure 2.31. Views from stibnite minerals (metallic dark grey) with a needle-like texture developed within jasperoid. Some stibnite crystals are oxidized, turning beige while retaining the needle-like structure. 51
Figure 2.32. Hand sample of intensely silicified, sulphide minerals bearing high-grade mineralized zone and polished mouth in the section. 52

Figure 2.33. Reflected light microscopy images illustrating mineralogical features of the section: (A) Disseminated pyrite distribution, (B-C) Pyrite within large epidote grains, (D) Chalcopyrite disease with chalcopyrite replaced by sphalerite, (E) Needle-like rutile grains, (F-G) Chalcopyrite with covellite rims, and (G) Pyrite enclosed by chalcopyrite and chalcopyrite enclosed by covellite..... 53
Figure 2.34. Reflected light microscopy images show pyrite, chalcopyrite, and the presence of potential Au element in the rim of chalcopyrite within covellite (F), covellite is also found as inclusions within chalcopyrite. 55
Figure 2.35. Distribution of Fe anomalies in the study area. Note that Fe anomaly along the low-angle fault contact of the Dağardı ophiolitic mélange. 57
Figure 2.36. Distribution of Cr anomalies in the study area. Note that Cr anomaly along the low-angle fault contact of the Dağardı ophiolitic mélange. 58
Figure 2.37. Distribution of Ni anomalies in the study area. Note that Ni anomaly along the low-angle fault contact of the Dağardı ophiolitic mélange. 58
Figure 2.38. Map showing distribution of arsenic (As) anomalies from the pXRF soil samples. Anomaly boundaries indicate the jasperoid mineralization in the study area. 59
Figure 2.39. Spatial distribution of Au anomalies. Note that anomalies are concentrated within the jasperoid unit. 60
Figure 2.40. As anomaly distribution, aligned with the jasperoid unit, showing no significant presence in the ophiolitic mélange. 61
Figure 2.41. Sb anomalies, observed near the main jasperoid zone. 61
Figure 2.42. Elemental vectors illustrating the distribution of dominant geochemical clusters within the study area. 62
Figure 2.43. Map showing the lithological classification based on the geochemical clusters within jasperoid zone. Note how ophiolite units are distinctly separated. 63
Figure 2.44. Anomaly map showing the distribution of arsenic (As) across five potential faults. The first three faults, oriented N-S, display arsenic (As) anomaly discontinuities, while the fourth fault represents a wider anomaly zone. The fifth fault, oriented E-W, separate s areas with higher arsenic (As) anomalies. 64

Figure 3.1. Clustered areas of interest on geological map (Appendix E).....66
Figure 3.2. Geological map showing bedding plane orientations in limestones of the Budağan formation. 67
Figure 3.3. Field view from thick bedding in the limestone outcrops of the Budağan formation. 67
Figure 3.4. Field views from gently-dipping bedding planes in the limestones of the Budağan formation. 68
Figure 3.5. Field views from gently-dipping bedding planes in the micritic limestones of the Budağan formation. 68
Figure 3.6. (A) Stereonet of the bedding planes, plotted as great circles, poles to planes and great circles on an equal area and contour graph of the associated poles to the planes. The diagrams illustrate single dominant bedding orientation in the Tavşan gold deposit area. (B, C) Rose diagrams showing the geometry (strike and dip direction, respectively) of bedding planes. 69
Figure 3.7. Geological map showing the location and orientation of foliation measurements. 70
Figure 3.8. General appearance of foliation in the sheared peridotites of the Dağardı ophiolitic mélange observed in the open pit mine. Note sigma-type augen structure and C-S fabrics, indicating a top-to-the left (northeast) sense of shearing. The lower right diagram shows C-S fabrics of the foliation in the hanging-wall of a strike -slip fault. 71
Figure 3.9. (A) field view of foliation in the sheared peridotites. (B) Field view showing carbonate veins indicating a top-to-the left (northeast) sense of shearing. 72
Figure 3.10. (A) Stereonet of the foliation planes, plotted as great circles, poles to planes and great circles on an equal area and contour graph of the associated poles to the planes. The diagrams illustrate single dominant foliation orientation in the Tavşan gold deposit area. Rose diagrams showing strike (B) and dip direction (C) of foliation planes. 73

Figure 3.11. Geological map showing the location and orientation of faults in the Tavşan gold deposit. 75
Figure 3.12. Field views from the low-angle fault zone. (B) shows the deformation zone and jasperoid mineralization associated with faulting. Note that the jasperoid forms resistant exposures while the fault zone is characterized by an anastomosing pattern. 75
Figure 3.13. Close-up view from the low-angle fault zone between the Dağardı ophiolitic mélange in the upper plate and limestones of the Budağan formation. Note resistant jasperoid mineralization within the deformation zone of the low-angle fault. 76
Figure 3.14. Slope cut from the open pit mine that shows the contact between mineralization and low-angle fault zone. Jasperoid zone is marked by limonitic clay; the zone also contains fragments derived from limestone, jasperoid and Dağardı ophiolitic mélange. The orientation of the fault is 061˚N / 23˚NW..... 77
Figure 3.15. Field views showing close association of faulting and jasperoid mineralization within the ophiolitic melange. Black line represents fault surface. 77
Figure 3.16. Field view and idealized sketch illustrating undulated geometry of the low-angle fault. Yellow half arrows thrust motion to SE, black arrows, the normal motion to the NW..... 78
Figure 3.17. Views from a fault in the open pit mine. Note that the fault zone in close-up view (B) is marking sheared rocks and fault clay. 78
Figure 3.18. Field views showing close association of faulting, jasperoid mineralization and the Budağan Formation. Red dashed line jasperoid, blue one limestone unit. 79
Figure 3.19. A view from the low-angle fault zone, which is interpreted to form a pathway for ore-bearing fluids. Note oxidized clay-bearing jasperoid blocks within the fault zone. 79
Figure 3.20. Geological map showing the location and orientation of low-angle fault measurements in the open pit mine. 80

Figure 3.21. (A) Stereonet of the main low-angle fault planes, plotted as great circles, poles to planes and great circles on an equal area and contour graph of the associated poles to the planes. The diagrams illustrate single dominant fault orientation in the Tavşan gold deposit area. Rose diagrams showing strike (B) and dip direction (C) of low-angle fault planes.....82
Figure 3.22. (A) Stereonet of the low-angle fault planes in the open pit mine, plotted as great circles, poles to planes and great circles on an equal area and contour graph of the associated poles to the planes. The diagrams illustrate single dominant fault orientation. Rose diagrams showing strike (B) and dip direction (C) of low-angle fault planes.....83
Figure 3.23. Outcrop image of high angle fault (F2) measurements. A) shows the fault surface including D and E. B) shows the chatter marks and slicken line where the measurement is taken. C) fault surface with the measurement with rake. D) closest point measurement on F2. E) fault measurement with 48˚ rake.....84
Figure 3.24. A close-up view from a NW–SE high-angle fault plane with an attitude of 318˚N/72˚E, with a rake of 65˚N. The fault is an oblique-slip normal fault with sinistral component.....85
Figure 3.25 (A) Stereonet of the high-angle fault planes cutting and displacing the low-angle main fault. The planes are plotted as great circles, poles to planes and great circles on an equal area and contour graph of the associated poles to the planes. The diagrams illustrate single dominant fault orientation. Rose diagrams showing strike (B) and dip direction (C) of high-angle fault planes. 86
Figure 3.26. Geological map showing the location and orientation of the Örencik fault.....88
Figure 3.27. Fault measurement location and close view of fault surface in ophiolitic mélange. A) The point where the fault was measured. B) The closest point of fault measurement showing the slicken line and chatter marks with an orientation of 244˚N / 66˚W, 28˚S. 88
Figure 3.28. High angle fault measurement in ophiolitic mélange of As zone. A) Fault surface with chatter mark and slicken line, with an orientation of 070˚N / 50˚S,

27˚S. B) Another close image of fault surface showing different orientation of 310˚N / 70˚E, 70˚N. 89
Figure 3.29. (A) Stereonet of the moderate-angle Örencik fault plane, plotted as great circles, poles to planes and great circles on an equal area and contour graph of the associated poles to the planes. The diagrams illustrate single dominant fault orientation. Rose diagrams showing strike (B) and dip direction (C) of moderate-angle fault planes. 90
Figure 3.30. Geological map showing the location and orientation of mapped faults within the Dağardı ophiolitic mélange. 91
Figure 3.31. Views from high-angle fault observed within the Dağardı ophiolitic mélange. Note that the faults have dominant normal component. 92
Figure 3.32. Field view from conjugate faults with normal component and a graben structure forming in-between. 92
Figure 3.33. Field view from conjugate faults with normal component within the Dağardı ophiolitic mélange. Note that the fault planes are ornamented by striations with large rake angles, attesting a dominant normal faulting. The horst-and-graben structure is evident. 93
Figure 3.34. (A) A field view from pair of listric faults with normal component. Note the sigma-type structures confirm normal component of motion. (B) A view from a shear zone within serpentinized ultramafics of the Dağardı ophiolitic mélange. The C-S fabrics, sigma-type clasts and drag fold confirm normal component of the motion. 93
Figure 3.35. (A) Stereonet of the high-angle faults mapped within the Dağardı ophiolitic mélange, plotted as great circles, poles to planes and great circles on an equal area and contour graph of the associated poles to the planes. The diagrams illustrate single dominant fault orientation. Rose diagrams showing strike (B) and dip direction (C) of high-angle fault planes. 94
Figure 3.36. Geological map showing the location and orientation high-angle faults mapped within the limestones of the Budağan formation. 95

Figure 3.37. Field views from the high-angle faults mapped within the limestones of the Budağan formation. (A) General view of the outcrop while (B –D) are close-up views. 96
Figure 3.38. General (A) and close-up (B) views form a striated fault plane in the limestones of the Budağan formation. 96
Figure 3.39. (A) Stereonet of the high-angle faults mapped within the limestones of the Budağan formation, plotted as great circles, poles to planes and great circles on an equal area and contour graph of the associated poles to the planes. The diagrams illustrate single dominant fault orientation. Rose diagrams showing strike (B) and dip direction (C) of high-angle fault planes. 97
Figure 3.40. Core samples showing lithologies and their relations with mineralization and faults. Au (ppm) values are highlighted with yellow arrows for sampling intervals. 99
Figure 3.41. Potential high-angle faulting related jasperoid mineralization with 3.10 ppm Au. The beta angle of jasperoid contact is shown with yellow colour. 100
Figure 3.42. Core samples that show the polymictic hydrothermal breccia. 100
Figure 3.43. Core samples showing a void filled by reddish clay and collapse breccia. 101
Figure 3.44. Core samples show the cross-cutting relationship between jasperoid mineralization and quartz-carbonate veins. The area indicated with yellow dash line consist of intense quartz carbonate veins and stibnite. The assay value of this zone is given above table, which includes high antimony values. 102
Figure 3.45. Close-up view from a brecciated jasperoid enclosed by quartz veining. 103
Figure 3.46. Field view from the main zone in the Budağan massive micritic limestone with cavity. The close views of (A) limestone bedding showing the cavity and brecciated limestone, (B) the cavity and (C) brecciated limestone. The breccia contains jasperoid fragments and quartz carbonate filling. 103

Figure 3.47. Core-samples showing very high antimony (Sb) rich lens shaped zone (represented with yellow dash line) in massive micritic limestone in Budağan formation. 104
Figure 3.48. Core samples showing brecciated fault gauge belongs to post mineralization fault between massive jasperoid mineralization. In 17.80 meters of cores, Au (ppm) equivalent value is 3.34 ppm. 105
Figure 3.49. Core samples are indicating the fault zone which consist of jasperoid breccias. The contact of massive jasperoid is measured and beta angle is found as 44˚. 106
Figure 3.50. Yellow line represents brecciated jasperoid fragments in fault gauge. Red line indicates massive jasperoid while orange line belongs to the jasperoid carbonate breccia unit with quartz carbonate veinlets. 107
Figure 4.1. Google Earth image showing low-angle fault contact between the Dağardı ophiolitic mélange above and massive to thick-bedded micritic limestones of the Budağan formation below. The fault crosses the entire study area and forms the most prominent structure..... 110
Figure 4.2. Field view illustrating association of Dağardı ophiolitic mélange, jasperoid and limestone within the damage zone of the low-angle fault. Green dashed line indicates the contact of the Dağardı ophiolitic melange and jasperoid, which is the thrust that indicated with black line. Blue dashed line represents the boundary between jasperoid and limestone. Pink dashed line shows limonitic clay related with shearing; orange dashed lines mark boundary of late-stage quartz-carbonate veins cross-cutting the adjacent units. 113
Figure 4.3. A view from low-angle fault zone with C-S fabrics and sigma-type clasts, all indicating a top-to-the-NW motion. At present configuration, the fabrics are interpreted to suggest a normal motion along the low-angle fault. Similar information about the sense of motion along the fault is interpreted to suggest that the original thrust fault is later reactivated as a detachment fault. 113
Figure 4.4. Geological map showing off set of mineralized jasperoid along strike-slip (transfer) faults. 114

Figure 4.5. Field view and sketch illustrating the N00ºE to N20ºE-trending fault, displacing the jasperoid mineralization. 116
Figure 4.6. Core-samples showing antimony (Sb) rich lens shaped zone and quartz carbonate epithermal veins (represented with red dash line) in Budağan formation. 118
Figure 4.7. Topography of the study area and draped surface geological map in oblique view. 119
Figure 4.8. Structural measurements are combined to the geological map. Fault measurements are seen as a disk shape, which all oriented according to the strike and dip direction. 120
Figure 4.9. Showing the collar and traces of the drillholes location of the study area on the geological map and topography. 120
Figure 4.10. Showing the lithologically classified and color-coded state of the drillholes. 121
Figure 4.11. Classified zones in the drillhole based on Au ppm values in drillholes on geological map. In the legend, red colour shows the high values of Au, while the blue colour is the low values. 121
Figure 4.12. Correlation and comparison lithology distribution as indicated by core logging and surface geological mapping in the Tavşan gold deposit. 122
Figure 4.13. Correlation of logging data with surface geological mapping of Main Zone. 122
Figure 4.14. Chert unit of geological map and logged chert unit are correlated in West Zone. 123
Figure 4.15. Solid model within the context of a field-derived geological framework. 123
Figure 4.16. Comparison of 3-D lithological model with surface geological map. 124
Figure 4.17. Grade model built with Au 0.5 ppm cut-off containing the drillhole assay Au values. Yellow panel represent the grade model of Au. 125

Figure 4.18. Jasperoid lithological model and Au grade model combination. Pink panel represents the jasperoid model building from lithologies of drillhole data while the yellow panel is the grade model of Au. Low-angle fault (black line) and strike-slip fault (red line) effect the jasperoid mineralization. 125
Figure 4.19. Displacement along the strike-slip (transfer) faults has shifted sections of the jasperoid zones..... 126
Figure 4.20. (A) Final geological model of Tavşan gold deposit. Black line with bold half arrows represents the low-angle fault whereas the black line with double half arrows the strike-slip faults. Black and white arrows are representative of sense of motion for thrust and detachment faulting, respectively. (B) Combined Au grade and jasperoid mineralization model and the strike-slip faulting. (C) Relationship between strike-slip fault and the low-angle fault. 127
Figure 4.21. Tavşan open-pit geological map showing the alteration and lithology related features. 128
Figure 4.22. High-resolution topography and drone imagery of the open pit area. Geological map is draped on the topography. 129
Figure 4.23. Diamond drill holes within the lithologically classified and color-codes and open-pit slope geology. 130
Figure 4.24. Diamond drill hole assay in accordance with Au ppm values within the 0.5 ppm cut-off..... 130
Figure 4.25. Fault orientation measurements from pit slopes plotted on open pit geological map. Fault measurements are seen as a disk shape, which all are oriented according to the dip and dip direction..... 131
Figure 4.26. Foliation orientation measurements from pit slopes plotted on the open pit geological map. Foliation measurements are seen as a cone shape, which all are oriented according to the dip and dip direction..... 132
Figure 4.27. 3-D geological model of the Tavşan open-pit. 133
Figure 4.28. East–West cross section of 3-D geological model of open pit. 133
Figure 4.29. NW–SE-oriented 3-D cross-section comparing the geological model and surface geological map. Two separate legends and colour codes are used to

differentiate between the lithologies in the geological map and those in the 3-D model. 134
Figure 4.30. ENE–WSW-oriented 3-D cross-section showing the lateral extent of mineralization and the distribution of lithological units. 134
Figure 4.31. The gold grade model, depicted with a colour-coded scale, illustrates the spatial distribution of gold grades throughout the deposit. Red zones represent high-grade areas where Au values exceed 1.5 ppm, while blue zones indicate areas with gold below 0.25 ppm. The intermediate grades are represented by green (0.25 to 0.5 ppm) and orange (0.5 to 1.5 ppm) colours. The gradual colour transition from red to blue provides a visual representation of how gold mineralization decreases across the deposit. 135
Figure 4.32. The high-grade mineralization zones within the deposit, showing areas where assay values exceed 1.5 ppm Au. The figure focuses on these high-grade zones, indicated in red, alongside assay data from the diamond drill holes. 136
Figure 4.33. NE–SW-oriented cross-section of the grade model, showing the correlation between the shallow-dipping ore zones and the geological map of the open-pit area. 137
Figure 4.34. NW–SE-oriented cross-section of the grade model, depicting the same correlation between shallow-dipping ore zones and the geological map. 137
Figure 4.35. The spatial distribution of gold (Au) and antimony (Sb) in the grade model. 138

CHAPTER 1

INTRODUCTION

1.1 Description and Location

This thesis focuses on the Tavşan gold deposit, located in Tavşanlı Zone of Anatolia where the zone is composed mainly of Cretaceous high-pressure (HP) lithologies (blueschists), ophiolites, accretionary complex and intruding Eocene granodiorites (Figure 1.1). The southern part of the study area belongs to Afyon Zone, representing mica-shist, marble and Oligo-Miocene granodiorite. The Tavşanlı gold deposit is located ~6 km south of Balıköy, which is a historic mining town (Figure 1.2).

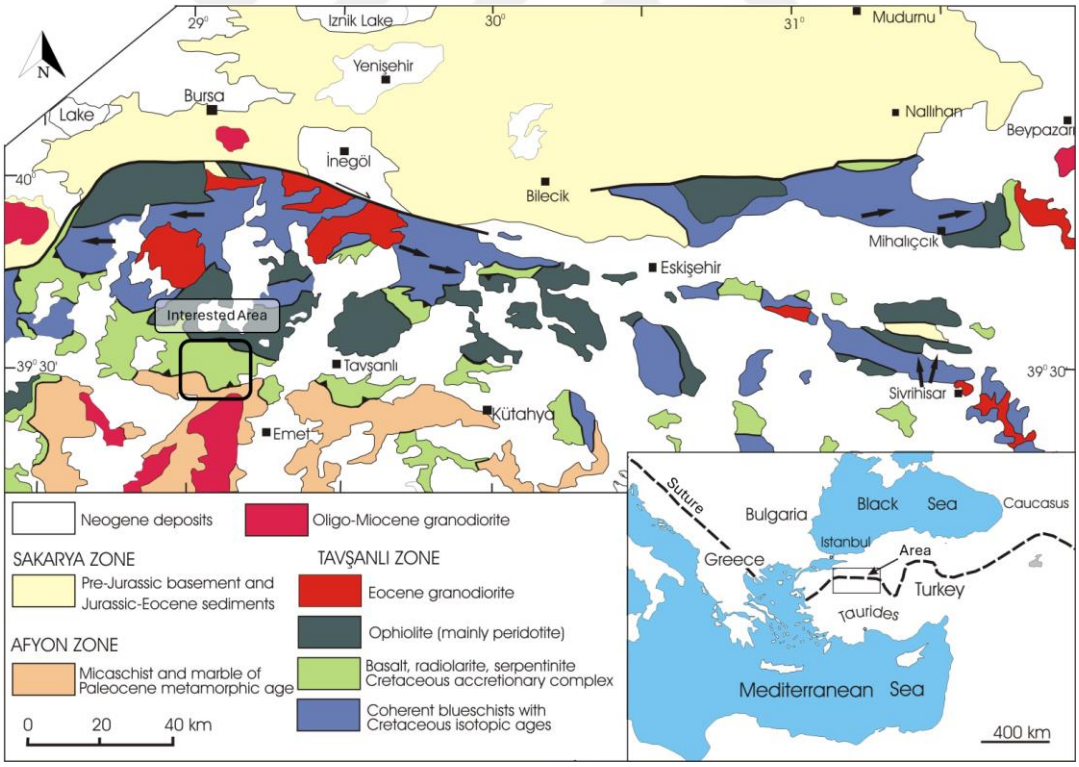

Figure 1.1. Geological map showing the location of the study area (from Okay, 2001). Tavşanlı gold deposit lies on the boundary between Tavşanlı and Afyon zones. Inset map indicates the location of the geological map.

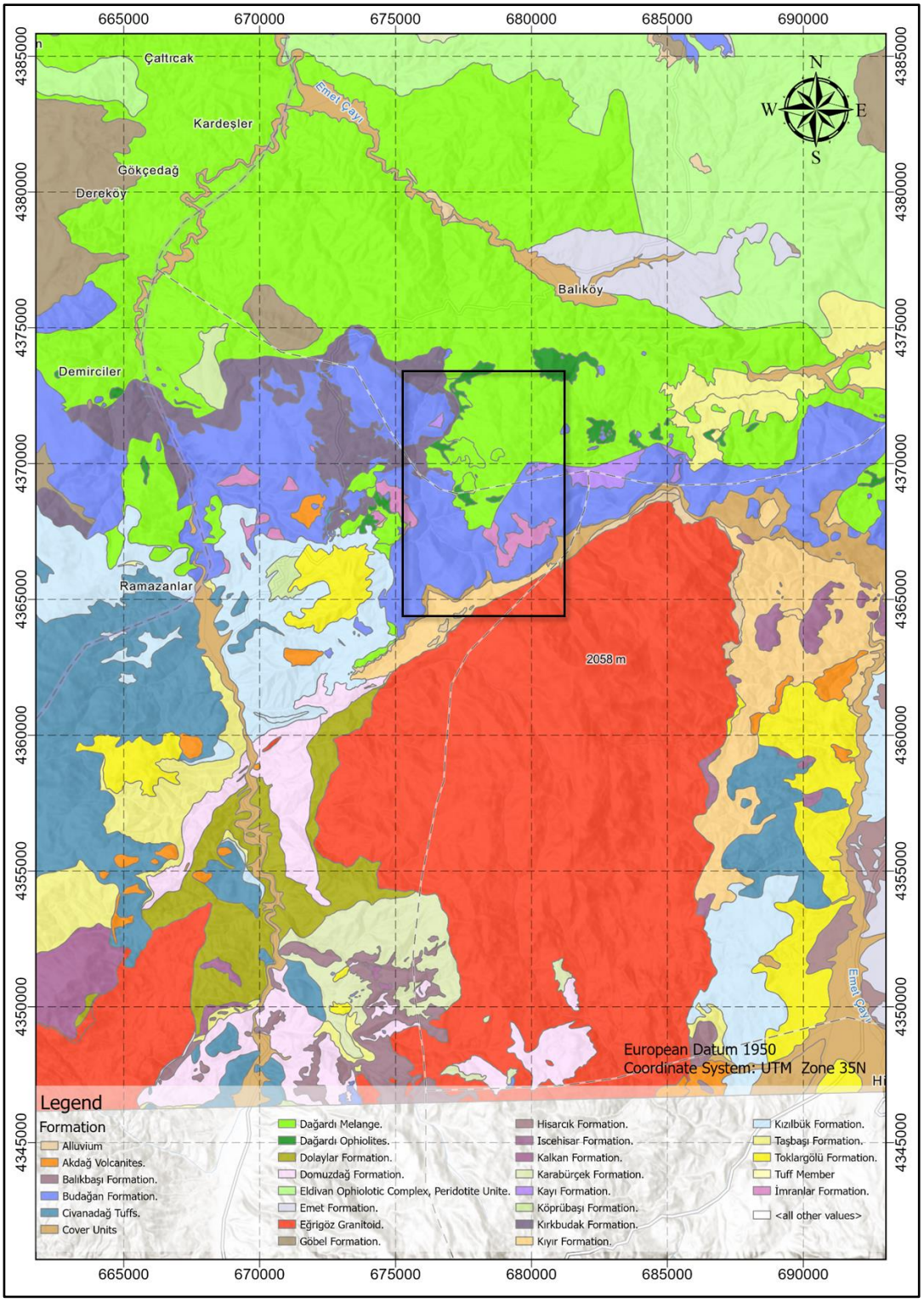

Figure 1.2. Geological map of the Tavşanlı gold deposit and nearby area (redrawn from 25k geological map of MTA). Black rectangle shows the location of the deposit.

1.2 Mining and Exploration History of the Study Area

Old mining activity at Kütahya and surroundings has an important and distinct place in the mining history of Türkiye. Mining activities in Kütahya region have started thousands of years ago and continued through the Ottoman period. Investigations in the neighbourhood of Tavşanlı have revealed old metallurgical remnants and findings of old underground mining. At Balıköy, there are remnants of crushing and transporting facilities that belong to the French and German old mining companies; the companies have used train railways to transport materials from the mine site.

Initial discovery of the Tavşan gold deposit was made by an Australian company, in the mid-1980s through diamond drilling in the southern part of Balıköy; there were subsequent exploration phases as well. In 1995, the General Directorate of Mineral Research and Exploration of Türkiye (MTA) conducted limited rock and soil sampling. In 1996, Teck-Cominco acquired the property and initiated geological mapping, reconnaissance exploration, and an extensive exploration program in 1997. Odyssey Resources later acquired the project in 2003, conducted additional drilling programs, trenching, and surface sampling. A total of 5,900 meters of drilling and 7,400 meters of trenching across the area revealed jasperoid-hosted, disseminated gold mineralization extending in northeast-southwest direction. Ariana Resources purchased the prospect from Odyssey in 2008, conducted check assaying to validate historical data and ensure confidence in quality assurance/quality control (QA/QC) procedures. The close agreement between historic and re-assay data supported the potential for a JORC compliant resource estimate.

The mineral resource classification follows the 2012 JORC code, with 13% of the resource classified as Measured and 58% as Indicated. The average grades for the resource are 1.5 ppm gold (Au) and 4.5 ppm silver (Ag). The total resource estimate is 311,000 ounces of gold and 1,104,400 ounces of silver (Figure 1.3).

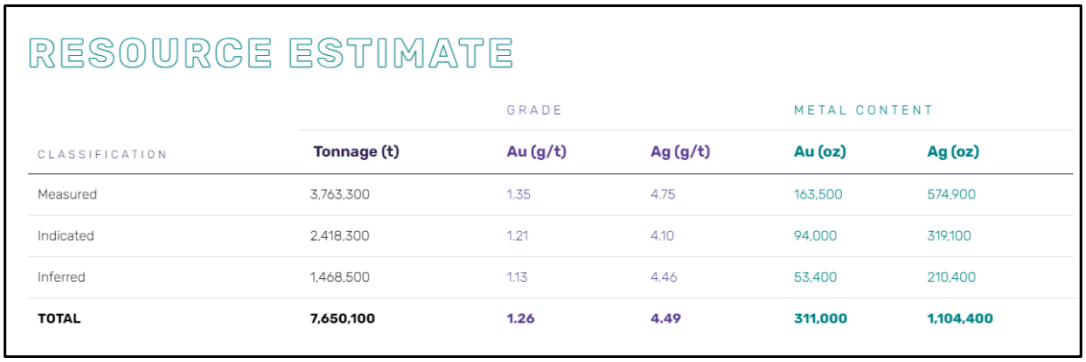

RESOURCE ESTIMATE

CLASSIFICATION	Tonnage (t)	GRADE Au (g/t)	GRADE Ag (g/t)	METAL CONTENT Au (oz)	METAL CONTENT Ag (oz)
Measured	3,763,300	1.35	4.75	163,500	574,900
Indicated	2,418,300	1.21	4.10	94,000	319,100
Inferred	1,468,500	1.13	4.46	53,400	210,400
TOTAL	**7,650,100**	**1.26**	**4.49**	**311,000**	**1,104,400**

Figure 1.3. Summary of March 2024 Tavşan Resources as classified and reported in accordance with JORC 2012. Reporting is based on a 1.5 g/t Au cut-off grade for high-grade domains and a 0.5 g/t Au cut-off grade for all other domains (from www.arianaresourcesplc.com).

Recently, Zenit Madencilik has taken over operations, conducting diamond drilling (15.000 meters of DDH), and constructing mine facilities across the project area.

1.3 Purpose and Scope

The purpose of the thesis is to explore control mechanism(s) on the mineralization in Tavşan gold deposit based on field studies and compilations from previous studies. Literature about the geology and regional tectonic events are also considered.

To explain more, this thesis primarily aims to provide evidence about (i) the characteristics and mechanism of deposit formation, (ii) how the deposit kinematically evolved, (iii) pathways of ore-bearing fluids and (iv) feeder mechanism(s). It is also suggested that understanding of this deposit may improve the way of exploring and targeting strategies for undiscovered deposits within the Tavşanlı Zone or elsewhere in Anatolia.

Specific research questions addressed in this thesis include;

1) Identifying regional and deposit-scale geological structures that may be responsible for hydrothermal system(s) and mineralization;
2) Determining the structural characteristics of the mineralization and geometry of the ore body;

3) Specifying spatial and temporal relationships between mineralization and structural elements within the Tavşan gold deposit;
4) Discussing role of faults in localizing and transferring the fertile hydrothermal fluids;
5) Establishing relationships of geological structures and geochemical signatures;
6) Assigning the type of gold mineralization at Tavşan gold deposit;
7) Constraining relative timing of ore-hosting systems and deformational (structural) phases and explore more about their role in better understanding of metallogenic framework of Tavşanlı Zone;
8) Defining kinematic evolution of the deposit

1.4 Methodology

The workflow of this study is organized into several sequential steps. First, a thorough literature review was conducted to gather and cross-reference previous studies, ensuring the accuracy of existing data and identifying potential gaps in knowledge. This was followed by fieldwork, which included geological mapping, the collection of structural data, and sampling for petrographic and geochemical analyses. Diamond drill holes were re-logged to verify the relationships among lithological units, mineralization, alteration, and structural features. After completing fieldwork and re-logging, the entire dataset was interpreted to extract meaningful insights and conclusions. Additionally, a 3-D model is prepared in order to provide a visual representation of the Tavşanlı gold deposit. The model is useful for better understanding and analysis of the ore-forming processes (Figure 1.4). Through these systematic steps, it was aimed to generate comprehensive insights and valuable contributions to the understanding of the study area.

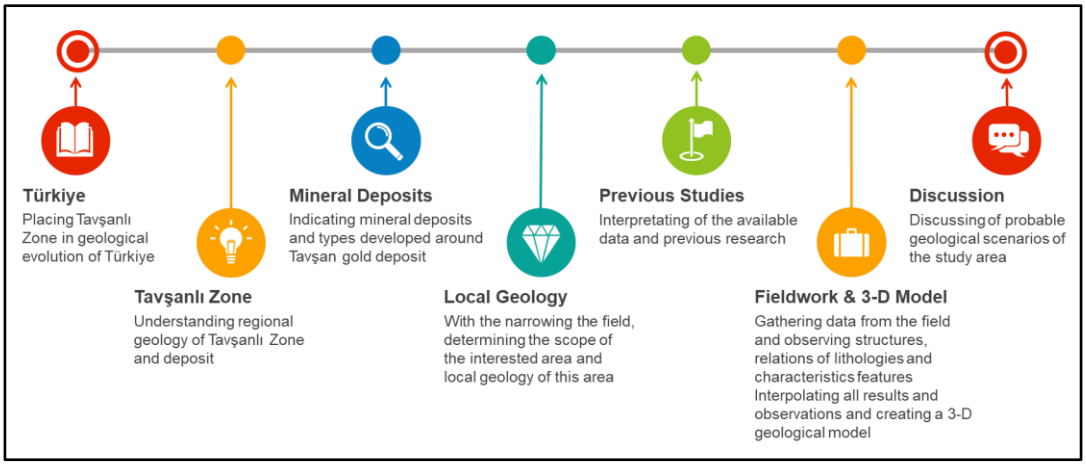

Figure 1.4. Steps followed during the thesis studies over the timeline.

Steps and methods are listed as below:

- All available digital data were compiled and assessed. All derivable tracks were located, an accurate track map prepared, and the track data were used to confirm the location of the Worldview Image. This way accuracy of existing data was checked, altered or re- compiled.
- Field observations were made initially along main and paved road cuts in order to have an overview of lithological units and their contact relationships. Then, with the detailed observations, lithological units are defined, and outcrop mapping has been carried out. Eventually, geologic mapping (at 1:500 to 1:5000 scale) has been conducted throughout the deposit area.
- Representative hand specimens from the main lithology types have been collected for petrographic analysis. Thin sections were prepared and analysed to identify petrological features of representative units in the study area. The thin sections were prepared in *"Ankara University"* and analysed by Prof.Dr. Kaan Sayıt at the *"Middle East Technical University, Department of Geological Engineering"*. Additionally, magnetic susceptibility (MagSus) and specific gravity of each rock type has been measured.
- More unaltered and altered rock samples have been collected for ore mineralogy and geochemical analysis. Portable X-ray fluorescence (pXRF) was used for major and trace element contents. Potential mineralized samples

are examined under the ore microscopy and analysed with fire assay (FA) and/or inductively coupled mass spectrometry (ICP-MS) methods at Zenit Laboratory.

- Portable X-Ray Fluorescence (pXRF)

Portable X-ray fluorescence (pXRF) spectrometry is a rapid, non-destructive method for determining the elemental composition of geological materials. Requiring minimal sample preparation, it is particularly suited for bulk analysis, such as screening trace and major elements in soils, rocks, and sediments. The methodology begins with sample preparation, where 250 g of soil or pulverized rock samples are transferred from field-collected calico bags to labelled plastic bags using the quartering method to ensure homogeneity. Before analysis, the pXRF instrument is calibrated using a certified steel plate, and its accuracy is verified by comparing readings to known elemental concentrations. Quality assurance is maintained by including certified reference materials (CRMs) and blank samples for every 20 analyses to monitor instrument consistency. The analysis itself involves three 30-second intervals, with beam-1 targeting trace elements, beam-2 for major elements, and beam-3 for controls, resulting in a total analysis time of 90 seconds per sample. To ensure data quality, Oreas CRMs with known element concentrations are used to validate results, with multiple CRMs selected to reflect the project's focus and element detection ranges. Blank samples, such as Oreas blanks containing 99% SiO_2 , are analysed to confirm the absence of contamination or background interference, ensuring reliability in the pXRF results.

- Geochemical Laboratory Analysis

In accredited geochemical laboratories, such as Zenit Madencilik Laboratory or ALS, the analysis of samples typically follows a rigorous and systematic workflow to ensure accurate and reproducible results. The process begins with the preparation of received samples, where they are first crushed to reduce particle size and subsequently pulverized to a fine, consistent powder. To verify particle size distribution, the pulverized material is screened using sieves to ensure it meets the

required specifications, commonly 85% passing 75 microns (15-30 grams of sample). Following sample preparation, acid digestion methods are employed to assess the acid solubility of target elements. Depending on the required analysis, either a two-acid (HCl-HNO_3) or four-acid (HCl-HNO_3 -HF-$HClO_4$) digestion method is applied, with the latter being more robust and capable of dissolving most silicate minerals. For gold and silver determination, the fire assay method is utilized, a well-established technique that involves fusion, cupellation, and final analysis via atomic absorption spectroscopy (AAS). Multi-element analysis for a broad suite of trace and major elements is commonly performed using inductively coupled plasma-mass spectrometry (ICP-MS) techniques, which provide high sensitivity and precision. This comprehensive workflow ensures the accurate quantification of elemental concentrations, meeting the quality control and assurance standards of internationally recognized laboratories.

For the conventional laboratory analysis method, blank samples are used to detect the cross-contamination and lab performance at detection limits. Crystaline dacite is chosen for blank material from a local quarry. During the quality assurance / quality control (QA/QC) procedures, single anomalies below the 2-3x detection limit (DL) is accepted, whereas the systematic bias above DL is unaccepted.

Certified reference materials (CRMs) are used during the laboratory analysis to monitor lab assay accuracy and precision. Taking into consideration of metal interest (Au, Ag, etc.) and grades (low, anomalous and economic ore), suitable CRMs is selected from the certified 50g pre-packaged CRMs from Ore Research & Exploration, Australia. During the QA/QC procedures, within ±2 standard deviations (SD) are acceptable. Consecutive failures indicate bias and isolated cases are acceptable between ±2 and ±3 SD. The values that are out of the ±3 SD are always rejected.

Field duplicates are another check samples that are used for identifying variability in sampling and geological heterogeneity. For the comparison and checking the

accuracy of the results, scatter plot (X vs Y plot, precision graphs) are used. Acceptable interval is below the 10 – 20 % for difference to assess reproducibility.

QA/QC samples (Blank, Standard, Duplicate) are inserted every 5th sample at a 19% insertion rate. Check Assays are conducted periodically (10% of samples) at an independent umpire lab to verify the primary lab's accuracy.

- IoGAS

Multi-element geochemical analysis is done by IoGAS software, with the help of Sinem Oğuz who is the geoscientist at Ariana Resources plc. Principal component analysis are applied on the same dataset to understand the vectoral behaviour of each element. Cluster analysis is another method applied on dataset after principal component analysis. The aim is to group the dataset according to the geochemical features of each sample.

- Potential gold-bearing samples and spots are selected. These samples are examined through reflected light microscopy, was applied to hand and core samples taken from high-grade mineralized zones of the Tavşan gold deposit, based on assay results. The study specifically targeted zones exhibiting intense silicification, sulphide mineralization, and jasperoid formation, which are possibly associated with gold mineralization in this region and allowed detailed examination of individual mineral phases.
- Structural data was collected from fault planes, foliations, lineation, veins, and dykes. Lithological contact and primary bedding orientations were also recorded.
- NE–SW-oriented mineralized zone is studied in detail in order to assess its possible relationship with the similarly trending fault.
- Cross-section(s) and a columnar section were prepared, based on field observations.
- Additionally, bench mapping in open pit was also conducted at 1:100 scale. Detailed mapping was very useful to define key lithological and structural

features. All data was recorded by using DGPS for precise spatial accuracy within centimetre (cm) scale error.

- Core samples totalling 18,900 meters from 381 previous exploration diamond drill holes of the Tavşan gold deposit were re-logged.
- Finally, all data was incorporated, interpretated and modelled in 3-D by using Leapfrog Geo.

The diagram showing workflow followed in thesis studies as a summary table in Appendix A.

1.5 Previous Studies

The Tavşan gold deposit in western Anatolia has been widely studied for its structural framework and mineralization. Research highlights the influence of lithological units, fault systems, and hydrothermal processes in forming gold-bearing jasperoid and silicified rocks. Previous researchers have highlighted the significance of silicification, brecciation, and fault-related fluid flow in localizing gold mineralization, particularly along carbonate-ophiolite boundaries. This section synthesizes the findings of notable studies to provide a comprehensive understanding of the geological and structural framework of the mineralization at Tavşan gold deposit.

Larson and Erler (1993) investigated the epithermal litho-geochemical signatures of precious metal mineralization at two prospects in western Turkey, Kursunlu and Örençik (Tavşan Gold Deposit), despite their distinct geological settings. They demonstrated that litho-geochemistry effectively delineates epithermal-style mineralization at both sites, highlighting a characteristic suite of trace elements, including Au, Ag, As, Sb, and Zn. At Kursunlu, mineralization is associated with silicified breccias along normal and detachment faults, whereas mineralization at Örencik occurs within jasperoid developed along a low-angle thrust fault that cuts through a mélange of serpentinites, greywackes, and limestones of Jurassic-

Cretaceous age. Drilling revealed that individual jasperoid outcrops are typically 100 m long and less than 20 m thick, with elevated gold and silver values found in silicified rocks, diminishing sharply in unaltered units. The study highlighted the importance of silicification along thrust faults in controlling mineralization and suggested that other mélange-hosted antimony-bearing occurrences in the region may hold similar exploration potential.

Jeffrey W. Hedenquist (2004) describes the Tavşan Gold Deposit features the presence of the Eğrigöz granite located to the south of the Kütahya fault, a regional-scale normal fault in western Anatolia. In this area, an ophiolitic sequence is emplaced above a platform carbonate unit, with the latter being silicified and mineralized by stibnite along northeast-southwest and east-southeast-west-northwest trending structures, as well as within hydrothermal breccias. The platform carbonate unit contains mostly micritic limestones with laminated silty interbeds; stromatolites are observed. Both the carbonate and ophiolite units have undergone silicification, although the carbonates appear to be more extensively silicified particularly in areas mineralized by sulphides and gold. According to Hedenquist (2004), the carbonate unit has undergone significant silicification and mineralization, especially in areas where faults intersect and in regions of extensive brecciation. Hedenquist (2004) attributed brecciation to hydrothermal activity or dissolution collapse. Mapping of alteration, i.e., "jasperoid" has in turn been interpreted in terms of original rock, with a complex pattern of supposed ophiolite. Where examined, this silicified unit appears to have had a carbonate origin (Hedenquist, 2004).

This is why special attention was given to displaced contact between carbonates and ophiolites along normal fault(s) during field mapping, as this boundary may define the upper limit of mineralization, potentially extending into the carbonate unit along feeder structures, with feeders potentially being the offsetting faults themselves.

Franck Valli (2006) had several observations regarding the relationship between structural events and gold mineralization at the Tavşan Gold Deposit and they are outlined below:

- The jasperoidized-silicified rocks occur along a thrust contact, separating micritic limestone at the bottom from an ophiolitic mélange at the top.
- The jasperoid and silicified rocks are localized along approximately north-northeast (120ºN–130ºN) vertical veins.
- A N35ºE fault acted as a channel for the silicifying fluids.

Valli (2006) proposed that gold occurrences were predominantly found along the thrust contact between massively-bedded Jurassic limestone and an overlying multi-lithic ophiolite sequence. The karstic network within the limestone and the matrix between the blocks of the ophiolite mélange possibly served as secondary channels for silicification and jasperoid formation within a zone of several tens of meters above and below the thrust fault contact. The area in the vicinity of the fault zone is an exception as the thrust fault is steeper than the topographic slope there. An en-échelon sinistral strike-slip fault zone might have bent and offset the gold mineralization zone. Thus, the sinistral deformation likely postdates ore deposition. Valli (2006) also suggested that this fault zone might have been a normal fault contemporaneous with or pre-dating mineralization, later re-activated as a strike-slip structure. The thickest gold-bearing jasperoidized-silicified unit is observed in the vicinity of a N35ºE-trending fault zone. Accordingly, Eğrigöz granite is proposed as the potential source of gold in Tavşan prospect, with fluids expelled from the granitoid. Fluids possibly circulated along the N35ºE-trending fault zone into thrust contact along which gold-rich jasperoidized rocks were formed.

Sally Goodman (2007) suggested that:

- At the Tavşan prospect, gold mineralization is hosted in jasperoid that has developed along the faulted contact between limestone and ophiolite, with minor occurrences observed in the footwall rocks.
- Recent geological mapping has produced and accurately surveyed and geometrically viable interpretation of the area; however, the structural interpretation and the relationship between structural development and mineralization remain poorly understood.

- Cross sections through the Satellite Zone indicate that E-W fault segments exhibit lower angles compared to the NNE-SSW segments. Despite this variation, jasperoid formation occurs along faults in both orientations, suggesting that these faults acted as linked structures during the movement phase associated with silicification.
- One hypothesis is that a regional-scale E–W low-angle thrust and an oblique lateral ramp at Tavşan accounts for the offset along NNE–SSW-trending satellite zone. This large-scale geometry is consistent at the prospect-scale.
- The Main zone and Sivritepe zone could potentially be reinterpreted as a ramp-flat geometry rather than a fold.
- Thicker jasperoid development appears to occur on the steeper segments of the fault zone, whereas the greatest thickness is observed at end of the satellite zone where the overall fault trend shifts from E–W to NNE–SSW.
- Gold deposition might have occurred significantly later than the thrusting and the silicification responsible for jasperoid formation. In this scenario, the silicified rocks act as a brittle host for the gold-bearing veinlets.

Şener et al. (2009) described the Tavşan deposit as an epithermal Au-Ag-Sb system situated within the Dağardı Antimony Province in western Turkey. Gold mineralization occurs primarily in jasperoid developed at the thrust contact between Jurassic limestone and Upper Cretaceous ophiolites. The mineralized jasperoid spans an 8 km strike length and is accompanied by minor gold occurrences in both the ophiolite and limestone. Structurally, the jasperoid forms along a low-angle thrust fault with a three-dimensional geometry comprising a roof thrust, NW-trending imbricate thrusts, and NE-trending lateral ramps. Late-stage NW-trending fractures postdate the thrusting, hosting crustiform quartz veinlets and controlling higher-grade gold and antimony distribution.

The mineralization process involved jasperoidization of limestone and silicification of overlying ophiolites, accompanied by iron oxide formation (e.g., hematite and limonite) and localized brecciation. Gold occurs as fine grains (~1–150 μm), often

within late-stage quartz veinlets or iron oxide-stained porous cement. The ore exhibits a typical Ag:Au ratio of 3:1, with associated sulphides such as pyrite, marcasite, and stibnite, although sulphide content is generally low (<1%). Gold mineralization is interpreted to have occurred post-jasperoid formation and is temporally linked to the nearby Eğrigöz granitoid intrusion in the Miocene.

Şener et al. (2009) emphasized the role of thrust faults and NW-oriented extensional structures as key controls on mineralization. They also suggested that the ophiolite units acted as effective aquitards, focusing fluid flow along thrust surfaces and enhancing mineralization at carbonate-ophiolite boundaries. Tavşan was highlighted as part of a regional continuum of mineralization associated with Miocene magmatism and tectonics in western Anatolia.

There are many other companies reports by either academic experts or company geologists reporting several observations regarding the relationship between geological structures and gold mineralization but because of confidential issues, they are not presented here.

1.6 Regional Geology

Türkiye is geologically divided into four main tectonic units: Pontides, Anatolides, Taurides and Border folds (or Arabian Platform) (Figure 1.5; Ketin, 1966). In general, geological evolution of Türkiye and eastern Mediterranean is attributed to the opening and closure of two oceans, namely Palaeotethys, existed between Laurasia and Gondwana and Neotethys, which overlapped both in time and in space. More recently, Okay and Tüysüz (1999) defined four major continental fragments in Türkiye: the Pontides (includingthe Strandja, the İstanbul and the Sakarya zones), the Anatolide-Tauride block, the Kırşehir Massif and the Arabian Platform; these tectonic units separated by major Tethyan sutures (Figure 1.5). The Pontides show Laurasian affinities and appear to have been sutured to the Eurasian continent during the closure of the Neotethys, while the others are of Gondwanan origin (e.g., Okay,

2008). Continent-continent collision between Pontides and Anatolide-Tauride occurred during the Late Palaeocene to Early Eocene time interval and has resulted in the closure of the İzmir-Ankara-Erzincan branch of the Neotethys Ocean (e.g., Şengör and Yılmaz, 1981; Okay and Tüysüz, 1999; Sharp & Robertson, 2006). Şengör and Yılmaz (1981) has been largely revised in light of subsequent studies, particularly Kaymakçı et. al. (2003) emphasizes the significance of Late Cretaceous to Paleocene collision-induced deformation and demonstrates how regional stress patterns evolved, culminating in Late Miocene closure through a combination of compression, transpressional faulting, and eventual extensional regimes. This event resulted in the development of corresponding suture zones (e.g., Okay and Tüysüz, 1999; Sharp & Robertson, 2006). Subduction of the southern Neotethys and the subsequent collision between Afro-Arabia and Eurasia (or Tauride-Anatolides) drove this closure, which culminated around the Late Miocene. Subduction of the African plate under Eurasia led to the ultimate closure of the northern Neotethys from Late Cretaceous to Late Miocene.

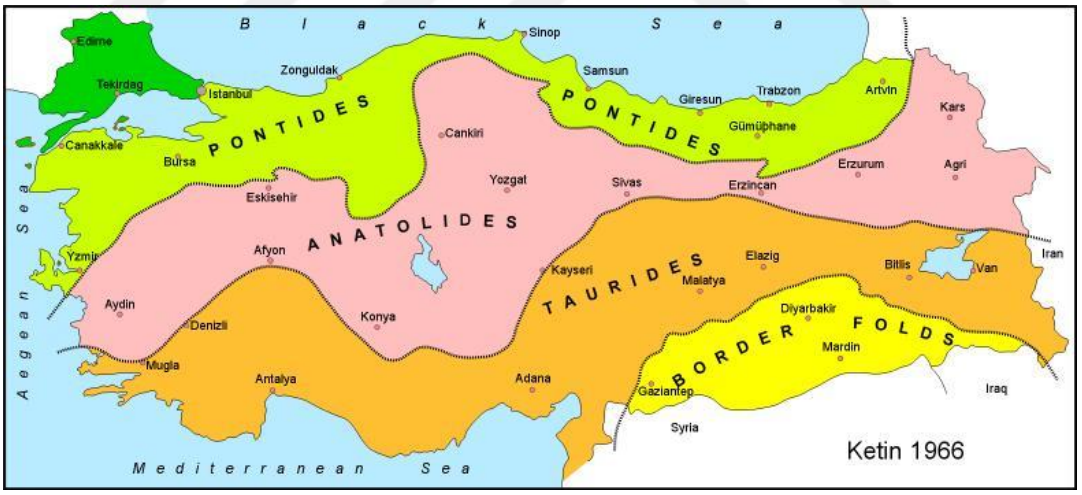

Figure 1.5. Geographic subdivision of Türkiye (Ketin, 1966).

Post-subduction and collision-related magmatism with porphyry and epithermal type mineralization are common in Türkiye (e.g., Richards, 2015; Yiğit, 2009). The transition to post-orogenic extensional tectonism throughout Anatolia and associated periods of magmatism and related hydrothermal mineralization events during the occurred during the Cenozoic (Catlos et al., 2012). Back-arc spreading induced by

the rollback and south-westward migration of the Aegean-Cyprian slab is a widely accepted causative mechanism for post-orogenic extension in western Türkiye (e.g., Yılmaz et al., 1997, 1991; Bozkurt, 2003; Bozkurt and Mittwede, 2001; van Hinsbergen, 2010; Jolivet et al., 2013; Uzel et al., 2015 and other references cited therein).

Overall, the tectonic evolution of Western Anatolia reflects a dynamic interplay of compressional and extensional processes, driven by the subduction and eventual closure of the Neotethys Ocean, followed by post-collisional extension (Figure 1.6). The ongoing tectonic activity, particularly in the form of extensional faulting, continues to shape the region's landscape and contribute to its seismic activity and mineral resource distribution.

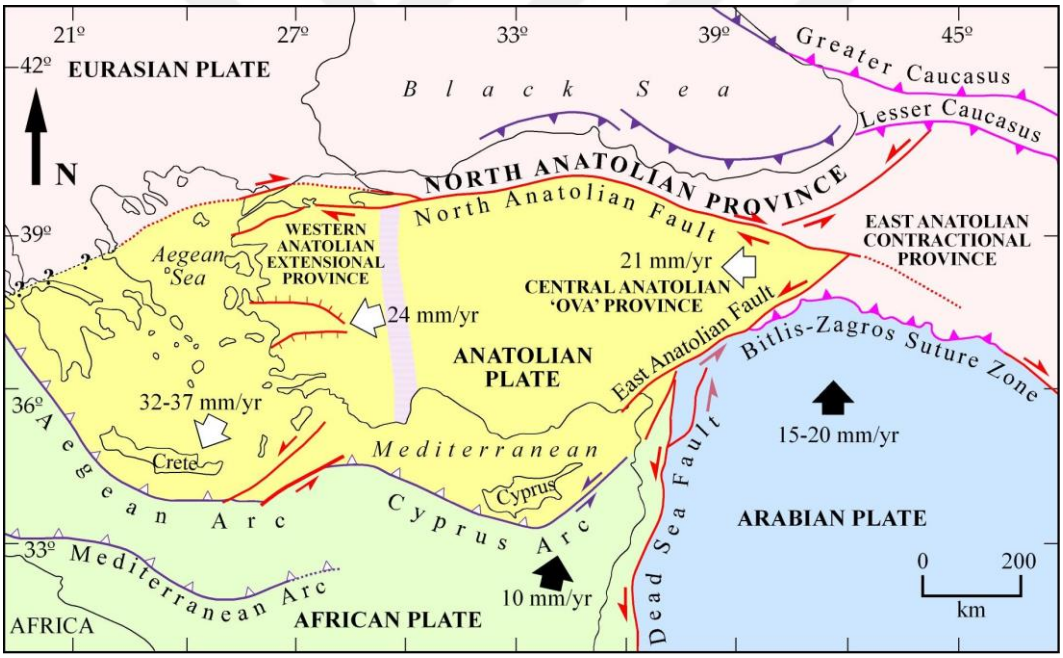

Figure 1.6. Simplified tectonic map of Türkiye showing major neotectonic structures and provinces (from Bozkurt, 2001).

Anatolia-Tauride block to the south of İzmir-Ankara Suture in western Anatolia comprises six main tectonic units: the Tavşanlı Zone, the Afyon Zone, the Menderes Massif, the Bornova Flysch Zone, and the Lycian Nappes (Figure 1.7; Okay and

Tüysüz, 1999). The study area is located at the contact zone between the Tavşanlı Zone to the north and the Afyon Zone to the south (Figure 1.7).

The Tavşanlı Zone occurs at the northern margin of the Anatolide-Tauride Block to the south the İzmir-Ankara Suture. It has experienced high pressure-low temperature metamorphism during the Cretaceous. To the south, it is bounded by the rocks of the Afyon Zone). The Afyon Zone is represented by metasedimentary rocks that have undergone low-grade regional HP/LT metamorphism and overprinting greenschist facies (Okay, 2011). Common presence of carpholite is reported as evidence of HP metamorphism in the Afyon Zone (Candan et al., 2005).

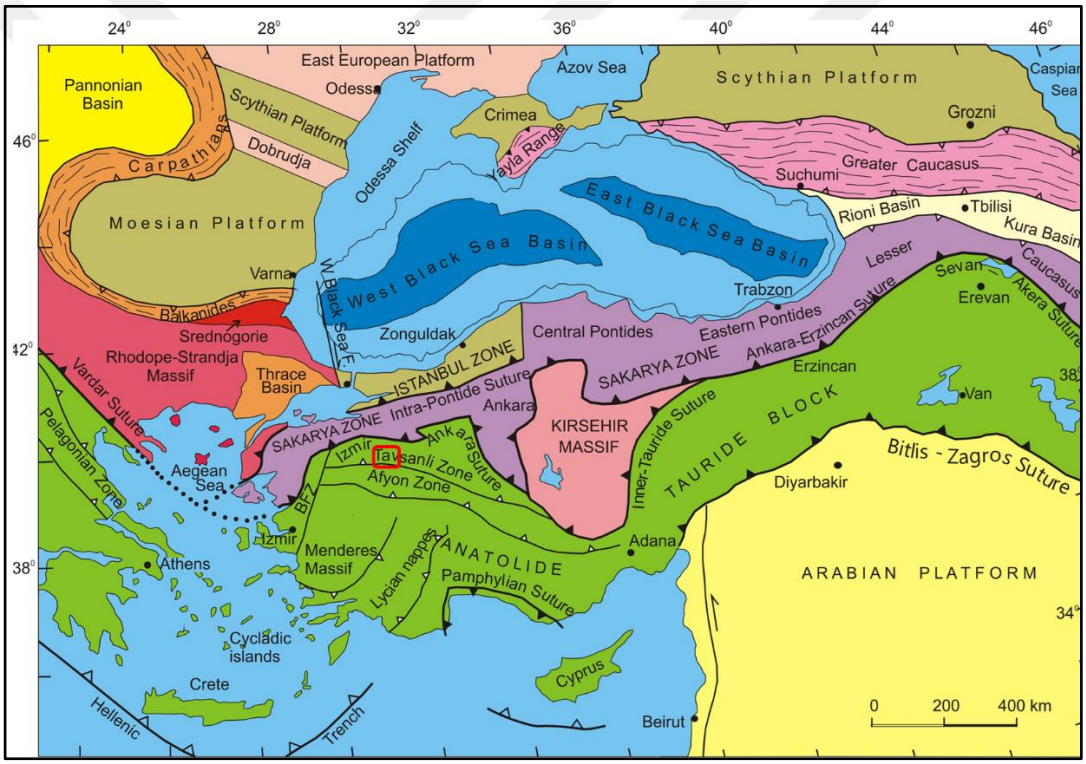

Figure 1.7. Tectonic map of north-eastern Mediterranean region showing the major sutures and continental blocks. Sutures are shown by heavy lines with the polarity of former subduction zones indicated by filled triangles. Izmir-Ankara Suture (IAES), Northern (NAFZ) and Eastern Anatolian Fault Zone (EAFZ), and Bitlis Suture (BS). (from Okay, 2008). Study area is highlighted with red rectangle.

The Tavşanlı Zone consists of several tectonostratigraphic units, including the Cretaceous ophiolitic mélange, blueschists, and sedimentary sequences that record the closure of the Neotethys Ocean (Figure 1.8 and Figure 1.9; Okay & Tüysüz,

1999; Okay et al., 2013). The ophiolitic mélange is composed of peridotites, serpentinites, and basalts, alongside with deep-marine sediments such as radiolarian cherts and pelagic limestones (e.g., Okay, 1984; Pourteau et al., 2010). This mélange represents oceanic lithosphere of the northern Neotethys material that was obducted onto the continental margin during the Late Cretaceous (Plunder et al., 2013).

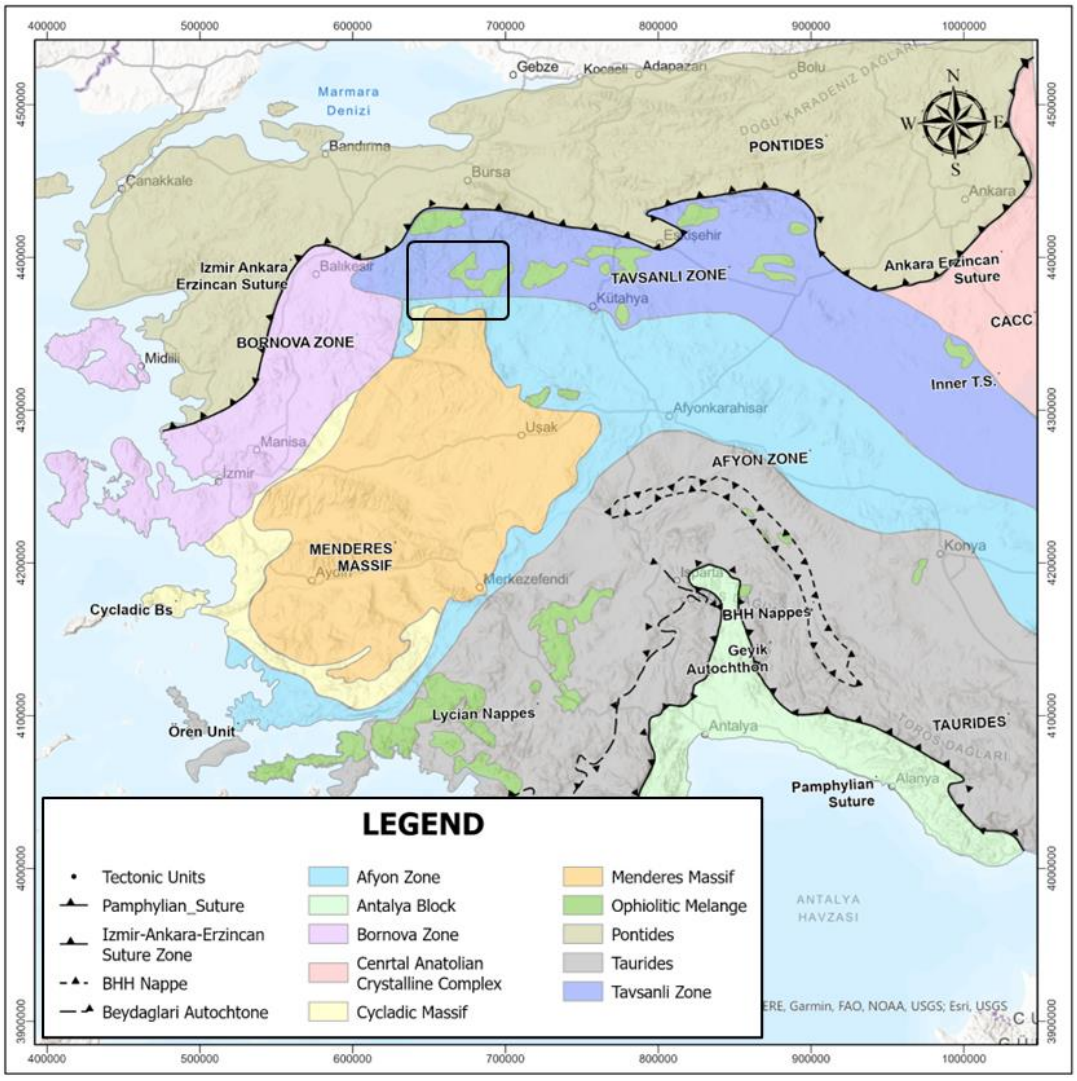

Figure 1.8. The main tectonic units of the Anatolides in western Anatolia are from north to south; the Tavşanlı Zone, the Afyon Zone and the Menderes Massif. Taurides are Lycian Nappes, Beydağları and Geyik Autochthone (redrawn from Pourteau et al., 2015). Black rectangle includes location of the study area.

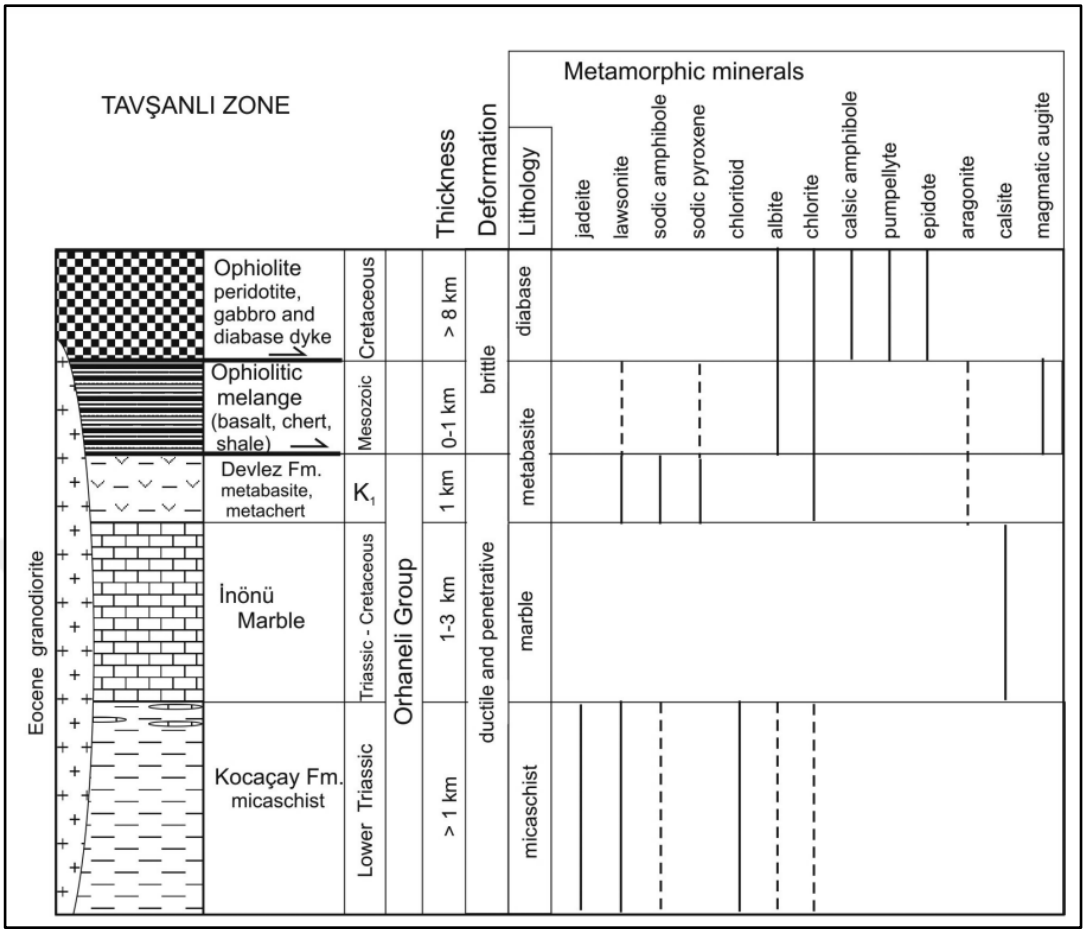

Figure 1.9. Tectonostratigraphic units of Tavşanlı Zone (from Okay et. al. 2013).

The Eğrigöz Granitoid, the most extensive intrusive body within the Tavşanlı Zone, is situated less than two kilometres from the Tavşan gold deposit (Figure 1.2). This composite batholith comprises a variety of lithologies, including granite, monzogranite, quartz monzonite, granodiorite, and aplite. Its mineral assemblage is dominated by quartz and K-feldspar (orthoclase and microperthite), with subordinate plagioclase, biotite, sericite, zircon, and opaque minerals (Catlos et al., 2012). Geochronological analyses constrain its emplacement age through multiple methods: 20 Ma ($^{40}Ar/^{39}Ar$ mica age; Işık et al., 2004), 19.4 ± 4.4 Ma (U-Pb zircon age; Hasözbek et al., 2010a), 18.77 ± 0.19 Ma (Rb-Sr mica age; Hasözbek et al., 2010a), and a broader range of 20-19 Ma.

The genesis of the Eğrigöz Granitoid is closely tied to the post-collisional extensional tectonic regime, driven by slab rollback and retreat of the Hellenic subduction zone.

These processes induced lithospheric thinning, creating favourable conditions for mantle upwelling and partial melting of the lower crust and subduction-modified mantle lithosphere (Pourteau et al., 2010; Jolivet et al., 2013). The resultant magmatism reflects decompression melting during lithospheric extension and represents a key feature of the post-collisional tectonic environment (Plunder et al., 2015).

Structurally, the emplacement of the Eğrigöz Granitoid is controlled by extensional fault systems that developed during the gravitational collapse of overthickened orogenic crust formed in the preceding compressional phase (Akay, 2009; Hasözbek et al., 2014). These fault systems, including normal and detachment faults, served as conduits for magmatic ascent from deeper crustal levels (Okay et al., 2010; Hasözbek et al., 2014). The granitoid's emplacement and its spatial association with extensional structures provide significant insights into the interplay between tectonic processes and magmatism in the evolution of the Tavşanlı Zone.

The geological evolution of the Tavşanlı Zone is a complex story of subduction, obduction, and exhumation, driven by the closure of the Neotethys Ocean and the collision between the Anatolide-Tauride Block and the Eurasian margin (Figure 1.10, Okay et al., 2010; Pourteau et al., 2010). The sequence of tectonic events that shaped the Tavşanlı Zone began with the northward subduction of the Neotethyan oceanic lithosphere beneath the continental margin of the Anatolide-Tauride Block during the Late Cretaceous (Okay, 1982 and 1984; Okay & Tüysüz, 1999). As subduction progressed, the continental margin was dragged down into the subduction zone, resulting in the deep burial and metamorphism of rocks within the Tavşanlı Zone (Plunder et al., 2013).

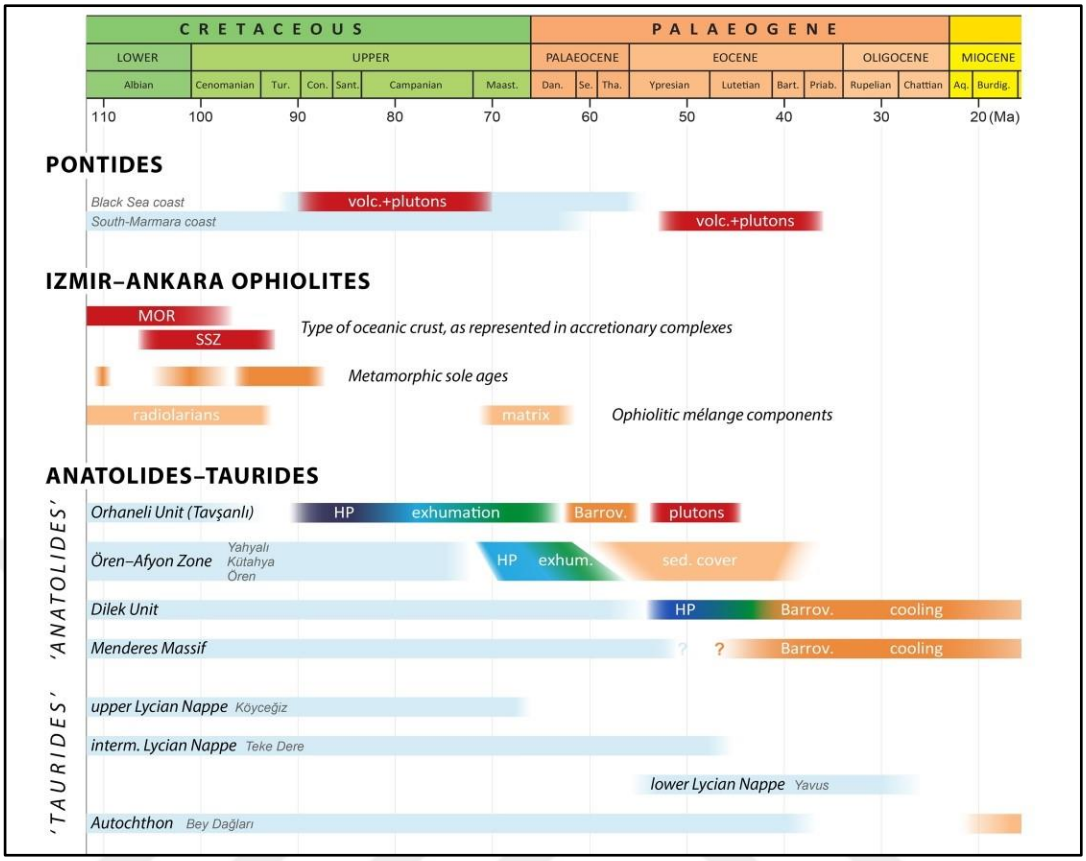

Figure 1.10. Time scale showing the age of sedimentation, timing of magmatism and metamorphism in the various tectonic units of Western Anatolia (from Plunder et. al., 2016).

CHAPTER 2

GEOLOGY OF TAVŞAN GOLD DEPOSIT

Tavşan gold deposit is situated in the Dağardı region of north-western Anatolia, which is located in the central part of the Tavşanlı Zone.

Six rock units are exposed around the Tavşan gold deposit. They, from bottom to top, are Kırkbudak formation, Budağan formation, İmranlar formation, Dağardı ophiolitic mélange and an ophiolite unit; all of these units are intruded by the Eğrigöz granitoid. Lower Miocene Taşbaşı formation unconformably overlies the older rock associations. Quaternary alluvium forms the youngest sediments (Figure 2.1). These lithological units and formations will be described in following sections.

The contact relationships of formations stand out as key components that shape the region's geology and mineralization. This chapter provides, based on field observations and thin section studies (featuring cross-polarized light (XPL) or plane-polarized light (PPL) views under the microscope), characteristics of each unit and mineralized outcrops, discusses characterization of mineralization and structural geology, and presents geologic map (Figure 2.2) and cross-sections (Figure 2.3 and Figure 2.4) of the deposit area. The Tavşan gold deposit, geologically, lies at the tectonic contact between the underlying Budağan limestones and the overlying Dağardı ophiolitic mélange (Figure 2.1).

To illustrate the regional geology and structural elements of the Tavşan gold deposit, northwest–southeast- and northeast–southwest-oriented cross-sections A–A′ and B–B′, based on field observations and approximate thicknesses of the geological units from diamond drilling data, have been constructed.

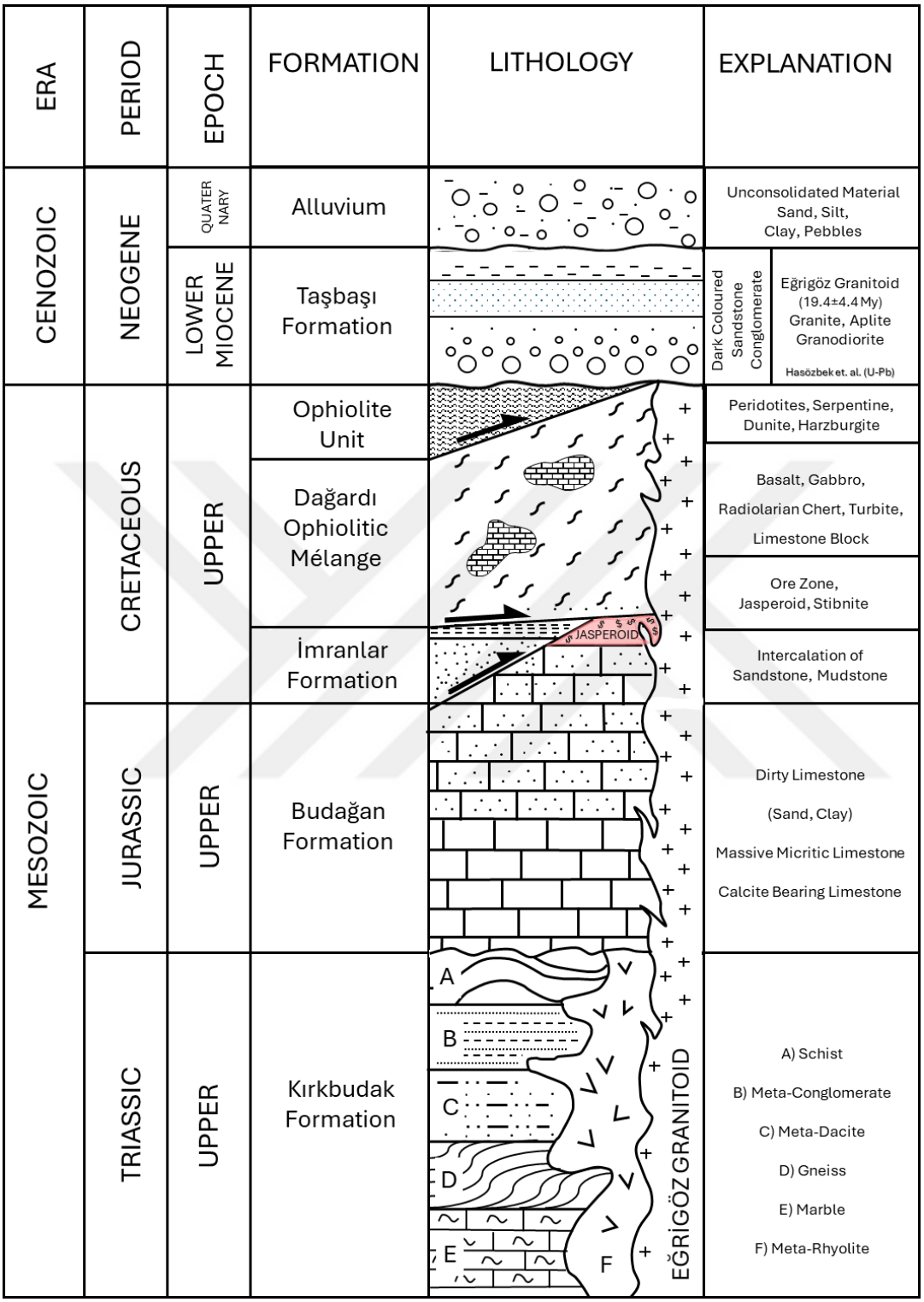

Figure 2.1. Columnar section of Tavşan gold deposit (redrawn from Explanatory Booklet of the MTA 1:100 000 Scale Geological Map of Türkiye I21 Sheet and Ersoy et al., 2014).

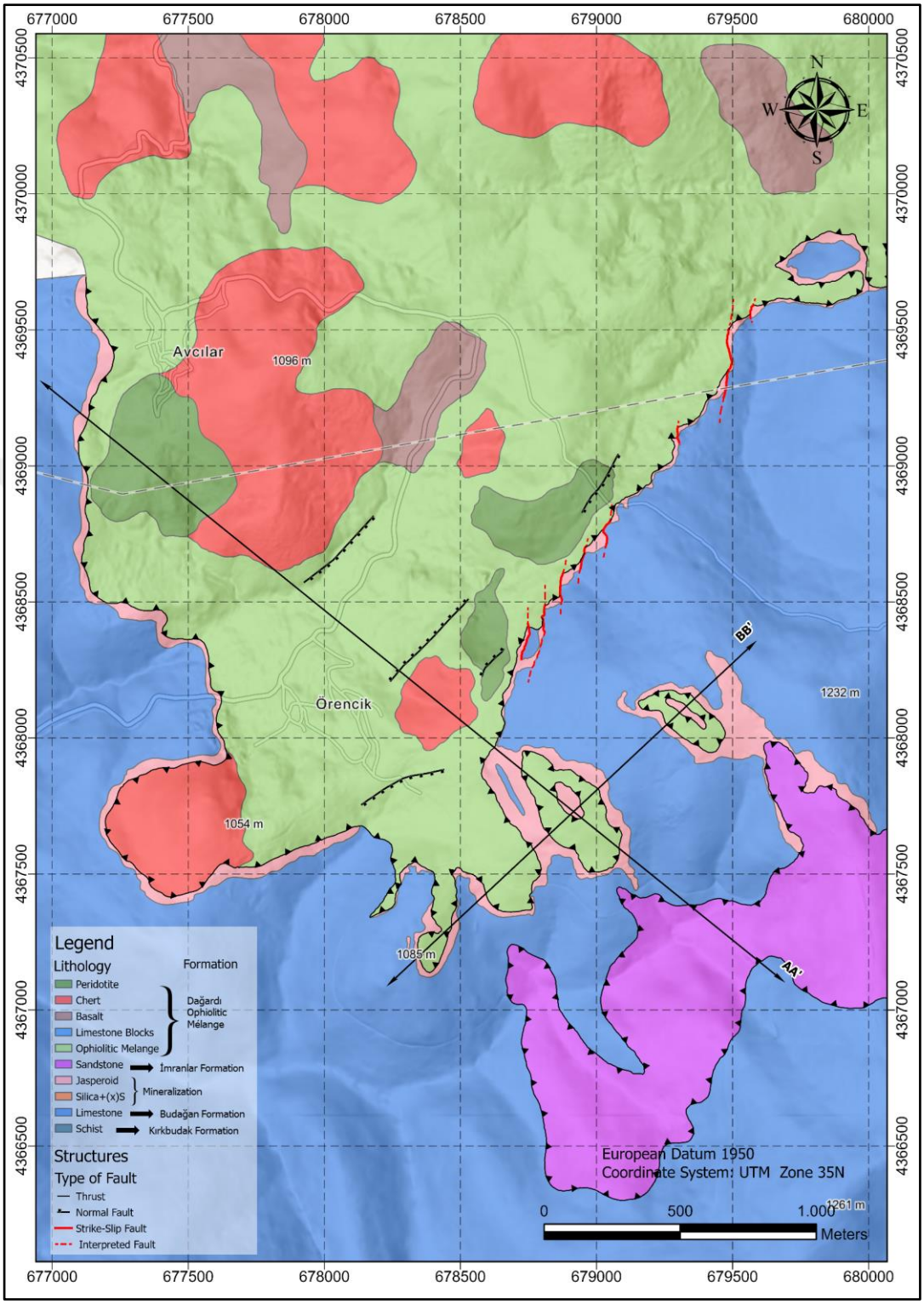

Figure 2.2. Geological map of the Tavşan gold deposit created in thesis studies.

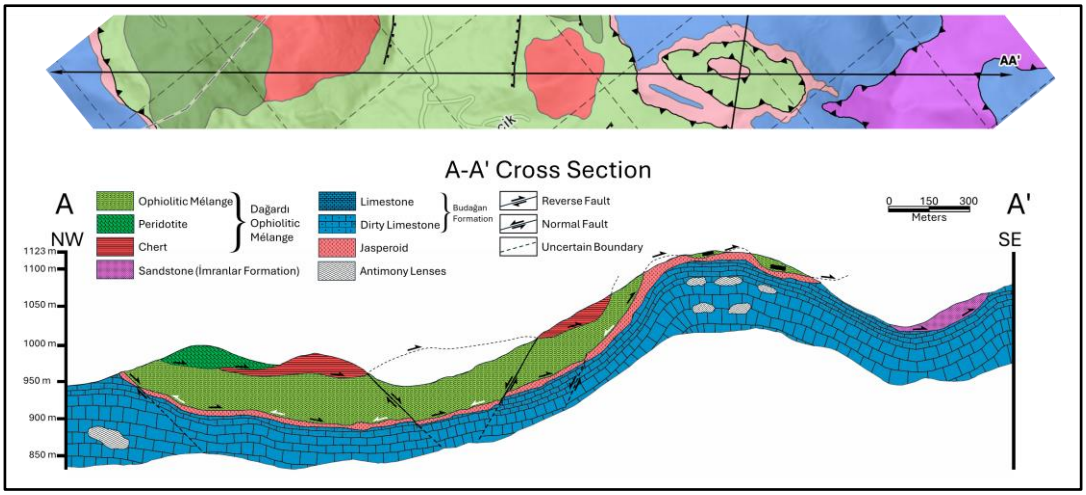

Figure 2.3.NW–SE cross Section along A-A'. The section line is shown on Figure 2.2.

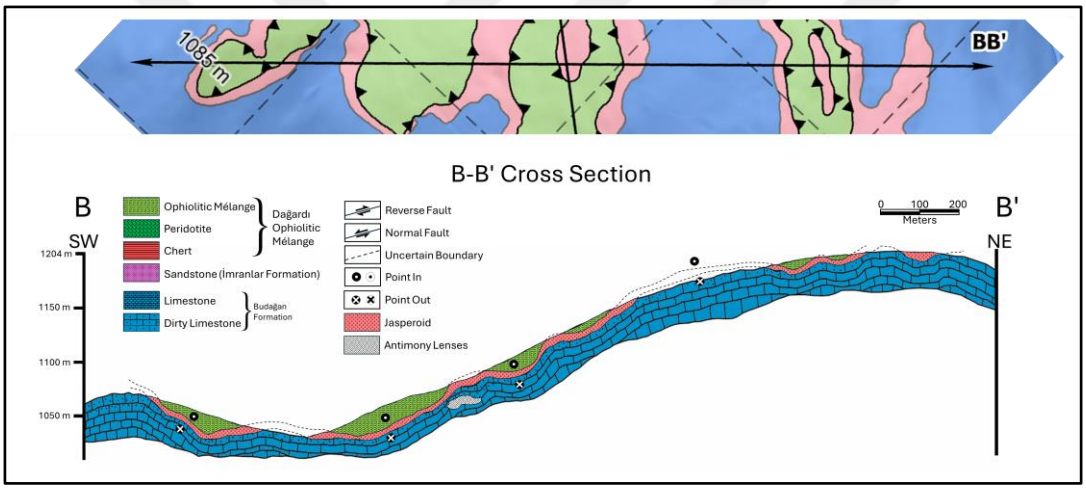

Figure 2.4. NE–SW cross Section along B-B'. The section line is shown on Figure 2.2.

Field observations illustrate that the ophiolitic melange is composed of a chaotic mixture of several lithologies (see Section 2.4). During field mapping, 2000 waypoints have been taken in order to determine and locate lithological features in the study area. 1150 outcrops (Figure 2.5) have been mapped to interpolate the final geological map (Figure 2.2).

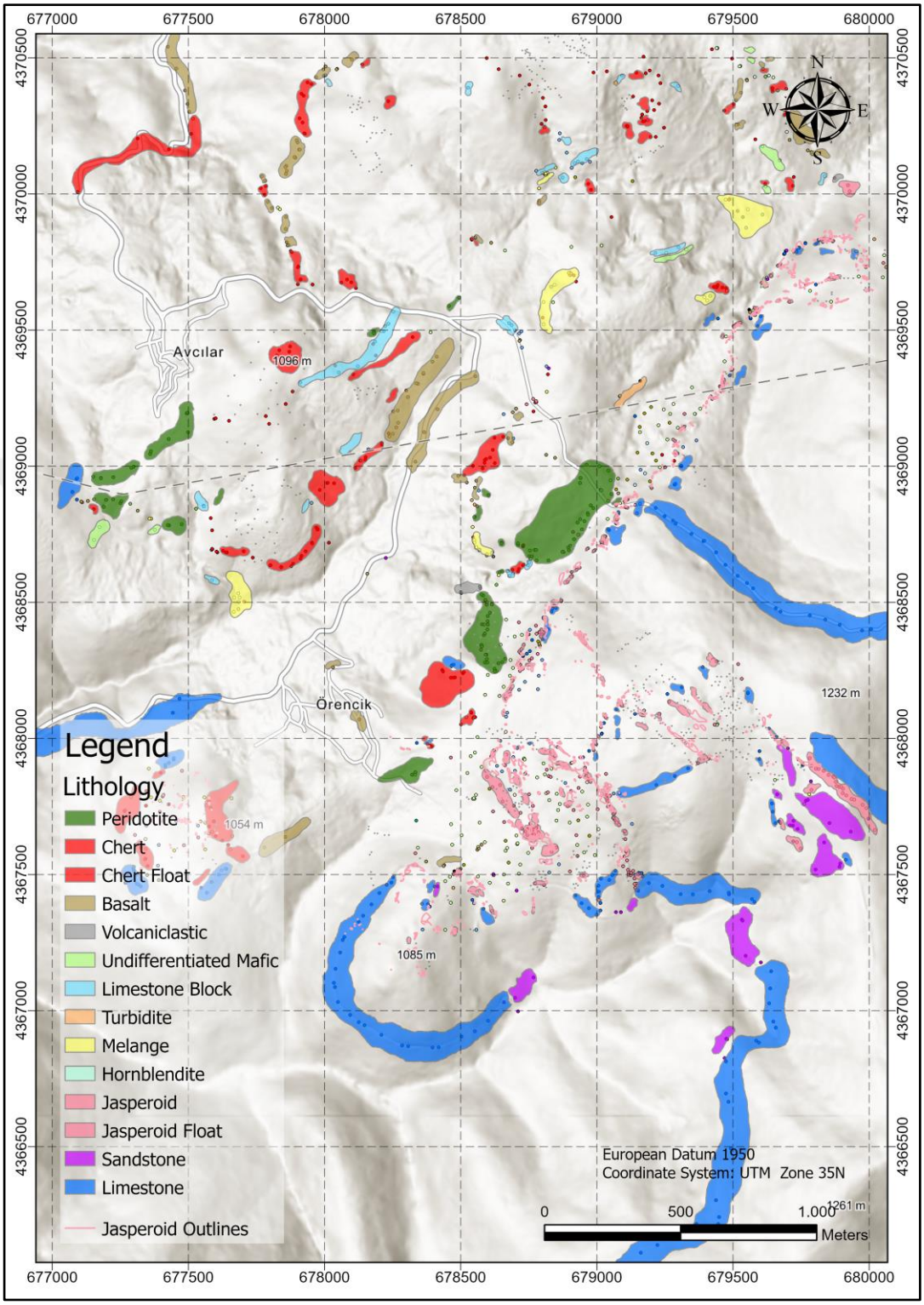

Figure 2.5. Outcrop map of the study area.

2.1 Kırkbudak Formation

Kırkbudak Formation is generally composed of low-grade meta-clastic rocks, such as alternation of meta-conglomerate-quartzite-schist-recrystallized limestone, and meta-volcanics in its upper parts. The unit was first defined by Akdeniz and Konak (1979).

Widespread outcrops of the formation occur in the south of Alaçam Mountains. It also outcrops in northeast of the study area. The foliation is readily recognizable in typically brown, grey, green, cream in coloured and bedded low-grade metamorphics (Figure 2.6 and Figure 2.7). Upward in the sequence, metavolcanics are also involved in this alternation. Metavolcanics and algal limestones within the unit are distinguished at the member level. The unit was deposited in a terrestrial to shallow marine (shelf) environment (Explanatory Booklet of the MTA 1:100 000 Scale Geological Map of Türkiye J21 Kütahya Sheet, Bilgiç, 2018).

Based on fossil content of (Palaeodasycladus, Teutloporella, Thecosmilia, Involutina, Triasina), the age of the Kırkbudak formation is assigned as Early–Middle Triassic (Konak et. al, 1980). In addition, the age of the metavolcanics is determined as Middle Triassic (243-240 Ma) by radiometric data (Akal et. al, 2012; Candan et. al, 2016).

The Kırkbudak formation unconformably overlined by the upper Jurassic–Cretaceous Budağan formation (MTA 1:100 000 Scale Geological Map of Türkiye J21 Kütahya Sheet Bilgiç, 2018).



Figure 2.6. Field view of the low-grade schists from the Kırkbudak formation. Note well-developed schistosity. Hammer is 38 cm long.



Figure 2.7. Close-up view from a schist hand specimen belonging to Kırkbudak formation.

2.2 Budağan Formation

A shallow-marine (coastal shelf) carbonate sequence of neritic recrystallized limestone, massive limestone, and micritic limestones are named as the Budağan Formation (Kaya, 1972; Akdeniz and Konak, 1979). The formation starts with greyish medium-thick bedded recrystallized limestone, grades upwards to dark grey-coloured, fossil-rich, densely folded recrystallized limestone and ends with thin- to thick-bedded, red micritic cherty pelagic limestones. Nodular cherty recrystallized limestones are rare. The thickness of the unit, which has a folded structure, is 600 m at most.

The age of the formation is, as based on its fossil content of Haurania, Valvulina, Nautiloculina, Pseudocyclammina, Textularia, Glomospira, Cuneolina, Cuneolina, Orbitoides, Lepidorbitoides, Siderolites, Ompholacyclus, and assigned as Jurassic–Cretaceous (Explanatory Booklet of the MTA 1:100 000 Scale Geological Map of Türkiye J22 Kütahya Sheet, Elibol et. al., 2018).

The Budağan formation unconformably overlies the Kırkbudak formation, while it is tectonically overlain by İmranlar formation and Dağardı ophiolitic mélange.

Budağan formation is represented by grey coloured massive limestones, recrystallized micritic limestones, and brecciated recrystallized limestones within the study area (Figure 2.8). At the bottom of the unit, there is greyish, medium-thick bedded massive limestones, while it becomes dark grey (dirty), fossiliferous, intensely folded at the upper parts of the formation (Figure 2.9). Calcite veinlets displaying stockwork structure are observed in core samples (Figure 2.9).



Figure 2.8. Views from the thick-bedded to massive micritic limestones of the Budağan formation. (B) and (C) are hand specimen and core samples, respectively.



Figure 2.9. (A) A view of the Budağan formation, a dirty limestone outcrop; this horizon is characterized by calcite veinlets. (B) Core sample shows sand size bedded sediments in limestone (see section bounded by orange lines). Limestone is also brecciated (encircled by green line) and is cut by a calcite veinlet (encircled by blue line).

2.3 İmranlar Formation

The olistostromal unit containing chaotic mixture of various blocks was named the İmranlar formation (Akdeniz and Konak, 1979). It encompasses a diverse lithological assemblage, including grey, taupe, green, and brown conglomerates, sandstones, siltstones, claystone, and limestone alternations, interspersed with blocks of various compositions and sizes. Notable among these blocks are metamorphics such as marble and schist, Permian–Triassic limestone, and ophiolite blocks. The İmranlar formation is about 200–300 m thick.

The age of the formation, as based on its fossil content including Globotruncana, Rugoglobigerina, Stomiosphaera, is assigned as Turonian–Maastrichtian (Late Cretaceous) (Explanatory Booklet of the MTA 1:100 000 Scale Geological Map of Türkiye I21 Kütahya Sheet, Okay et. al., 2018). Late Cretaceous İmranlar formation is attributed to the closure of the İzmir-Ankara-Erzincan Ocean (Explanatory Booklet of the MTA 1:100 000 Scale Geological Map of Türkiye J21 Kütahya Sheet; Bilgiç, 2018). The İmranlar formation displays thrust faulted contact relationships with overlying Dağardı ophiolitic mélange and unconformable contact with the underlying Budağan formation.

İmranlar formation is observed as large outcrops in the southern part of the study area (Figure 2.2) and comprises mainly sandstone with some mudstone intercalations (Figure 2.10).

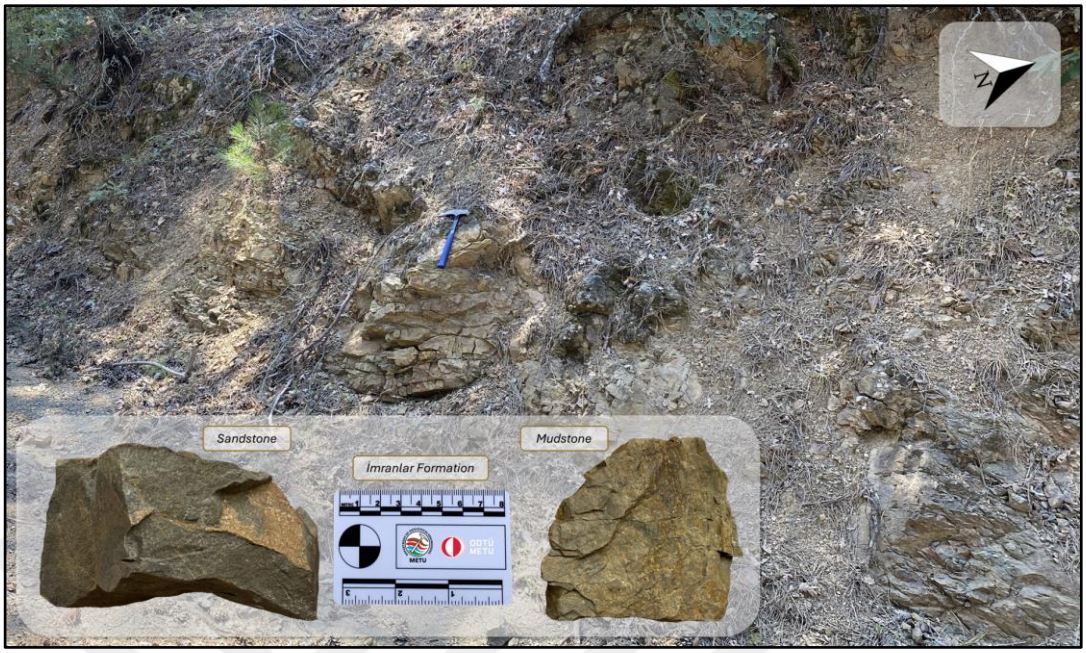

Figure 2.10. Field view from sandstones of the İmranlar formation. Hand specimens of sandstone and mudstone.

2.4 Dağardı Ophiolitic Mélange

Chaotic mixture of submarine basic rocks (basalt, gabbro, diabase, spilite, tuff, and basalt), grey, green, and brown ultrabasic rocks (peridotite, dunite, serpentinite, and pyroxenites), tuffs, turbidites, pelagic-neritic limestone and radiolarites – is named the Dağardı ophiolitic mélange (Akdeniz and Konak, 1979). The ultramafic-mafic rocks form ophiolitic slices, radiolarites and limestones that occur as blocks within a greenish, brownish, and pinkish purple sedimentary rocks. Red colour of radiolarites is typical; they also alternate with limestones. The tuffites are typically green and occasionally display massive character. Limestone blocks are white-grey, massive, recrystallized, coarse-grained with very large calcite crystals, display sugary texture; dolomitic limestone blocks are also reported.

The maximum thickness of the unit reaches to approximately 700–750 meters. The mélange tectonically overlies the Budağan and İmranlar formations along a marked thrust fault while it is unconformably overlain by the Miocene formations (Figure

2.2). The ophiolite suite can be considered an aquitard for siliceous fluids using the thrust as a conduit. A varying degree of metamorphism commonly affects all rock units described below, often overlapping due to intense deformation.

Dağardı ophiolitic mélange is interpreted as an ophiolitic mélange nappe emplaced onto the Anatolide-Tauride platform in the south and attributed to the closure of the northern branch of Neo-Tethys (the İzmir-Ankara-Erzincan Ocean) at the end of the Late Cretaceous.

2.4.1 Radiolarian Chert

Radiolarian chert forms a characteristic component of the mélange and forms several outcrops within the study area. The chert is a siliceous, hard, fine-grained homogeneous sedimentary rock and is predominantly composed of microscopic radiolarian remains (Figure 2.11).



Figure 2.11. Field view from radiolarian chert in the central part of the study area.

A core sample showing alternation of chert and mudstone layers (ID: D94_20.5) is selected for polished thin section studies. The sample shows phacoidal domains within cleaved mudstone and displays a preserved texture that allows the identification of radiolarians (Figure 2.12). The mudstone is siliciclastic, contain quartz and clays, and is mostly oxidized with hematite; calcification is also present. The radiolarian chert is variably replaced by carbonates and oxides, similar to the mudstone. The presence of cleavage in mudstones provides evidence for deformation.



Figure 2.12. View from radiolarian chert hand specimen (A) and core samples (B). (C) Phacoidal domains of chert within mudstone. Note that the radiolarians are readily recognizable at the uppermost part of the photo (PPL view).

2.4.2 Peridotites

Peridotites are sheared and form common components of the mélange in both northern and southern parts of the study area. They form dark coloured exposures with variable extent in the study area (Figure 2.2). Peridotite is composed primarily of olivine with significant amounts of pyroxenes (both clinopyroxene, and orthopyroxene).

Peridotites in the study area include serpentinized harzburgite and dunite (Figure 2.13 and Figure 2.14). In some samples, olivine is totally altered to serpentine. Orthopyroxene is also entirely altered and appears as bastite pseudomorphs while clinopyroxene is relatively better preserved and appears as colourless, subhedral/anhedral grains with high birefringence. There is evidence for intense carbonatization.

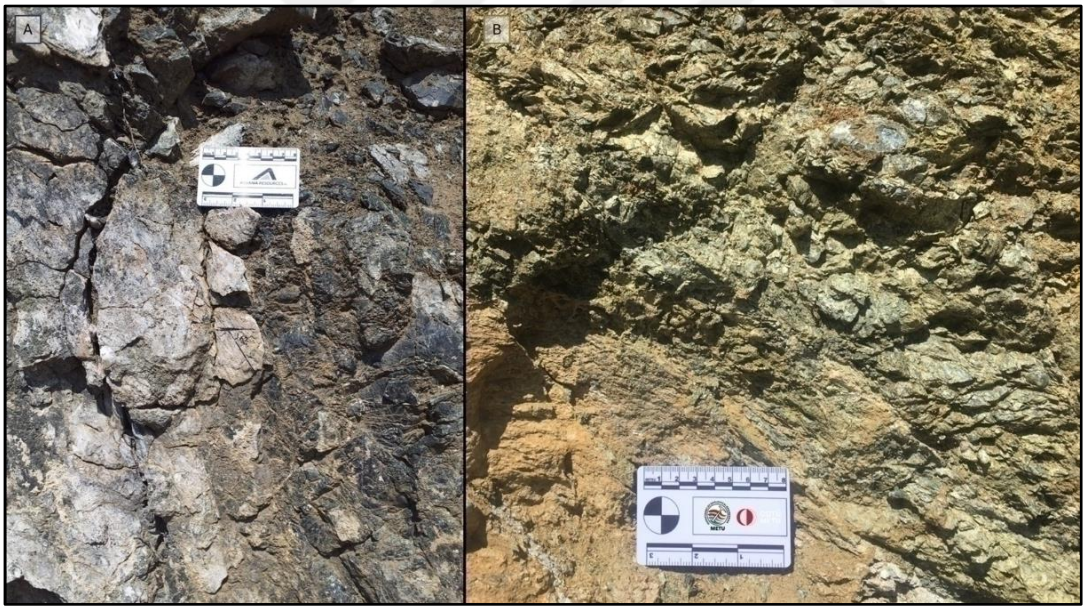

Figure 2.13. Field views from sheared peridotites in the northern side of study area. (A) Harzburgite and (B) serpentinized dunite.

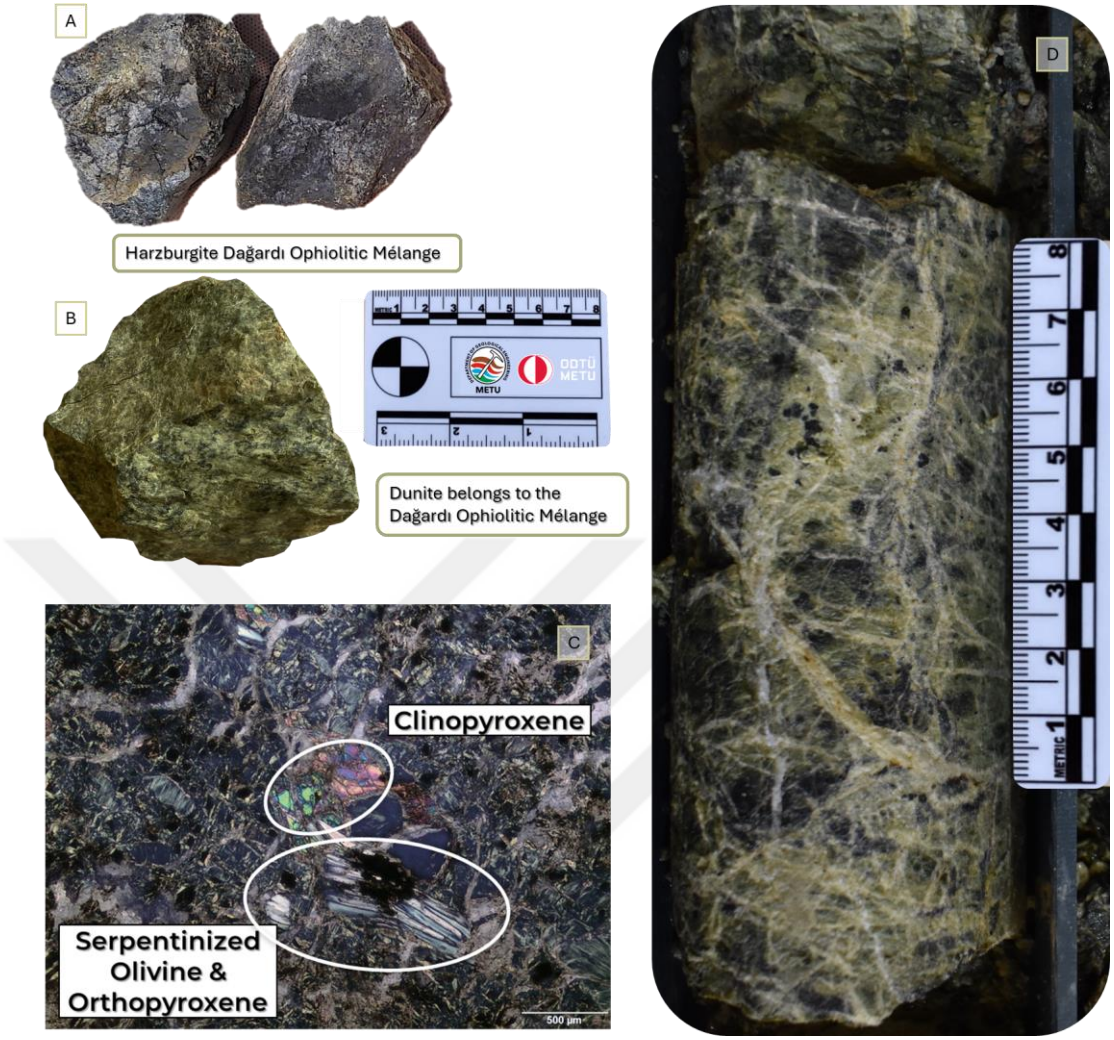

Figure 2.14. Hand specimens of harzburgite (A) and dunite (B). (C) Polished thin section of serpentinized harzburgite under the microscope with XPL view. The rock is mainly composed of olivine, clinopyroxene, and orthopyroxene but primary phases are hardly recognizable (see encircled areas) since intense alteration destroyed most of them: olivine is totally altered to serpentine, orthopyroxene is also entirely altered and appears as bastite pseudomorphs while clinopyroxene appears as colourless, subhedral/anhedral grains with high birefringence. The sample is intensely carbonatized. (D) A view from core sample of a serpentinized harzburgite.

2.4.3 Limestone Blocks

Massive, coarse-grained, white to grey coloured dolomitic limestone blocks are also common within the Dağardı ophiolitic mélange (Figure 2.15 and Figure 2.16). Large calcite crystals and sugary texture form main characteristics of the limestone blocks.



Figure 2.15. Field views from dolomitic limestone block of the Dağardı ophiolitic mélange in the northern (A) and southern (B) parts of the study area.

Owing to dolomitic nature of the limestone blocks, their magnesium content is pronounced as observed in the portable X-ray fluorescence analysis (pXRF). The Mg content is used as one of the most diagnostic features of the blocks and used as a criteria to distinguish them from the Budağan formation limestones because the latter show no evidence of Mg presence due to low dolomite contents.



Figure 2.16. Views of hand specimens (A) and core samples (B) of recrystallized dolomitic limestone blocks in Dağardı ophiolitic mélange.

2.4.4 Basalt

The Dağardı ophiolitic mélange consists basaltic rock outcrops as well (Figure 2.17). Basalts are weathered and characterized by low silica and high iron-magnesium contents, and brownish colour (Figure 2.17).



Figure 2.17. Field view from weathered submarine basalt outcrop in Dağardı ophiolitic mélange, pillow lavas brownish in colour.

Fresh basalts are dark grey and show both aphyric and porphyritic textures (Figure 2.18). Aphyric basalts are probably represent the groundmass separated from the larger porphyritic clasts. Basalts are composed primarily of olivine, clinopyroxene, and plagioclase. Olivine and clinopyroxene represent the phenocryst phases, while groundmass consists of clinopyroxene and plagioclase (altered to zeolite) (Figure 2.18). In altered samples, olivine is totally replaced by saponite (Figure 2.18). Clinopyroxene displays pinkish colours and appears to be Ti-augite. Cleavage is well-developed. There are mafic volcaniclastic blocks as well and they contain basalt and glass fragments.

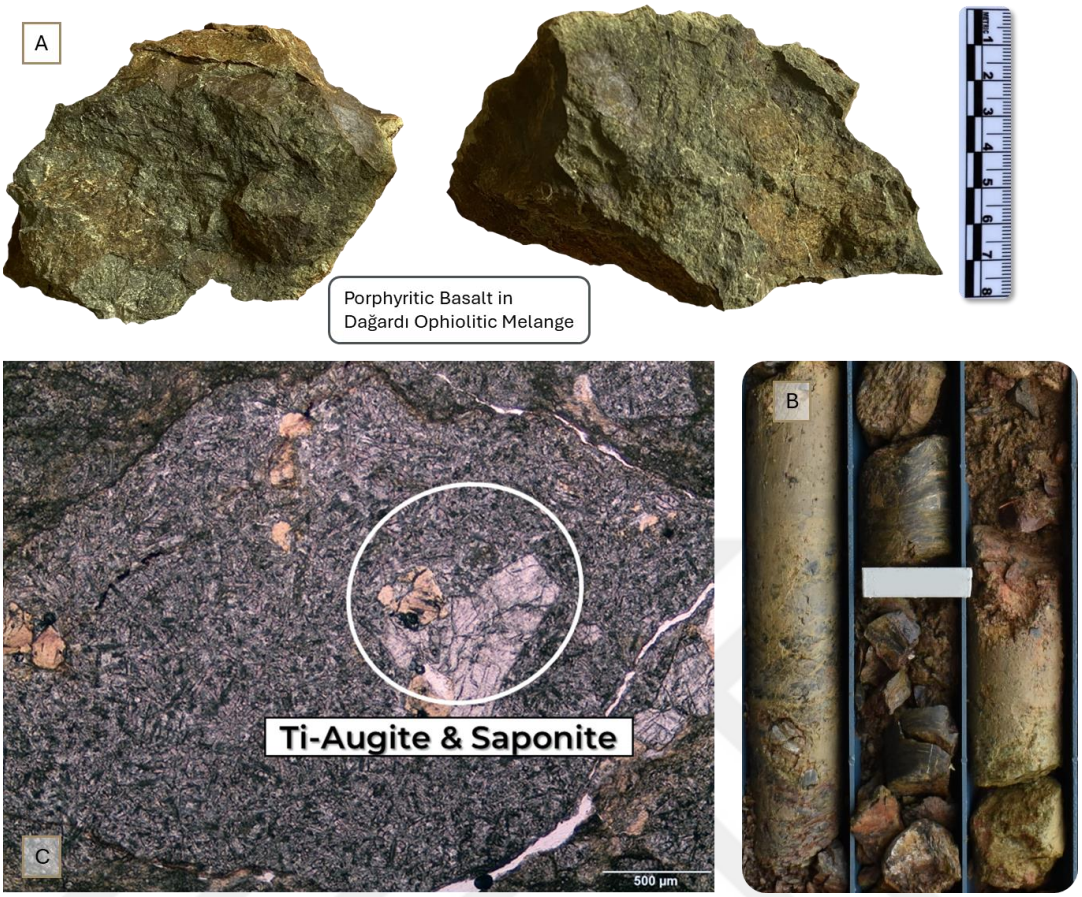

Figure 2.18. Views of hand specimens (A), core samples (B) of basalts and (C) volcaniclastics (C). Note porphyritic basalt clast with brownish-coloured Ti-rich augite and olivine phenocrysts in "C". There olivine crystal is entirely altered to saponite (PPL view).

2.4.5 Turbidites

There are outcrops of turbidites in the Dağardı ophiolitic mélange (Figure 2.19). These consist of upwards fining repeated sedimentary cycles. There are coarse conglomerates or breccias at the bottom of each cycle in places and they gradually evolve upwards into sandstone and shale/mudstone alternation.



Figure 2.19. Field view from a turbidite outcrop in Dağardı ophiolitic mélange.

Turbidites typically consists of a sequence of laminated siliceous/calcareous shales/mudstones rhythmically interbedded with thin, hard, greywacke-like sandstones (Figure 2.20A). Typically, the shales do not contain many fossils, while the coarser sandstones often have fractions of micas and glauconite (Figure 2.20B).

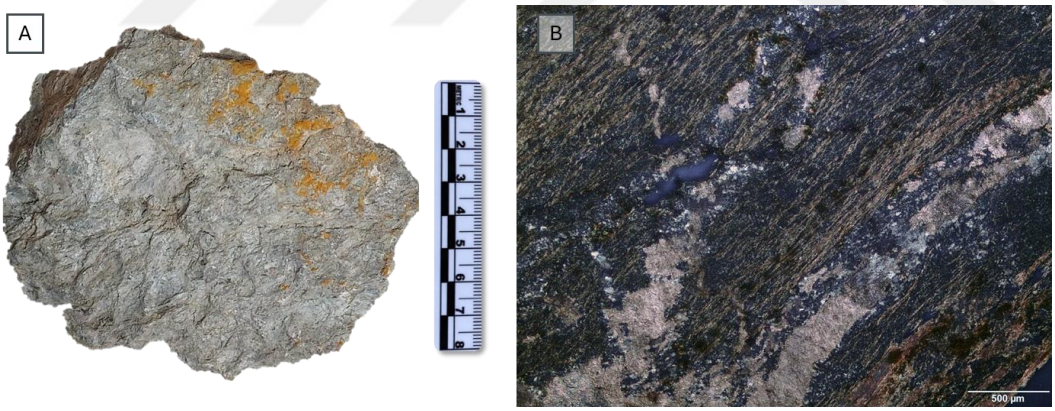

Figure 2.20. A view from (A) a turbidite hand specimen and (B) polished thin section under microscope with XPL view. Small, flaky grains are micas that have grown in response to low-grade metamorphism. Note that they are preferably aligned, defining foliation in the sample.

2.4.6 Volcaniclastics

Volcaniclastic unit forms a mappable exposure in the Dağardı ophiolitic mélange (Figure 2.2). Lack of continuous bedding is characteristic. These are composed mostly of sand-sized basalt fragments and aggregates of pyroxenes within a fine-grained deformed matrix (Figure 2.21).

There are chert, basalt, limestone, and peridotite clasts derived from various lithologies of the Dağardı ophiolitic mélange (Figure 2.22). The basalt fragments are aphyric/porphyritic. In porphyritic fragments, the phenocryst phase is augitic clinopyroxene. It generally displays subhedral/euhedral outlines and moderately/well-developed cleavages. Fractures are common. Some grains show twinning. Groundmass is initially glassy, which is now entirely altered. Aphyric fragments are also glassy and share similar features with the mesostasis of the porphyritic ones. Mineral clusters are clinopyroxenitic, consisting solely of clinopyroxene grains. (Figure 2.22). These grains show identical features to clinopyroxene phenocrysts, indicating a cogenetic origin. The sample is intensely veined, including calcite and quartz. Thin calcite and quartz veins in basalt fragments are also common.



Figure 2.21. Field view of volcaniclastic outcrop in the northern part of the study area.

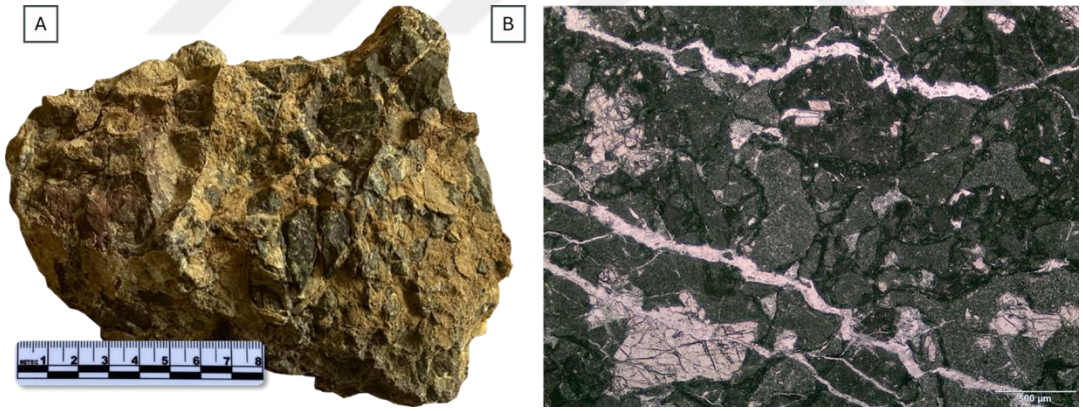

Figure 2.22. Views from (A) hand specimen of volcaniclastic unit with chert, mafic and ultramafic clasts; (B) basalt fragments and clinopyroxene aggregates, which are cut by thin veins of calcite and quartz (PPL view).

2.4.7 Dikes

In the study area, a hornblendite dike has also been observed. It is characterized by a mineral assemblage rich in hornblende with minor plagioclase (Figure 2.23 and

Figure 2.24A). Cross-cutting relationship with the Dağardı ophiolitic mélange is evident.

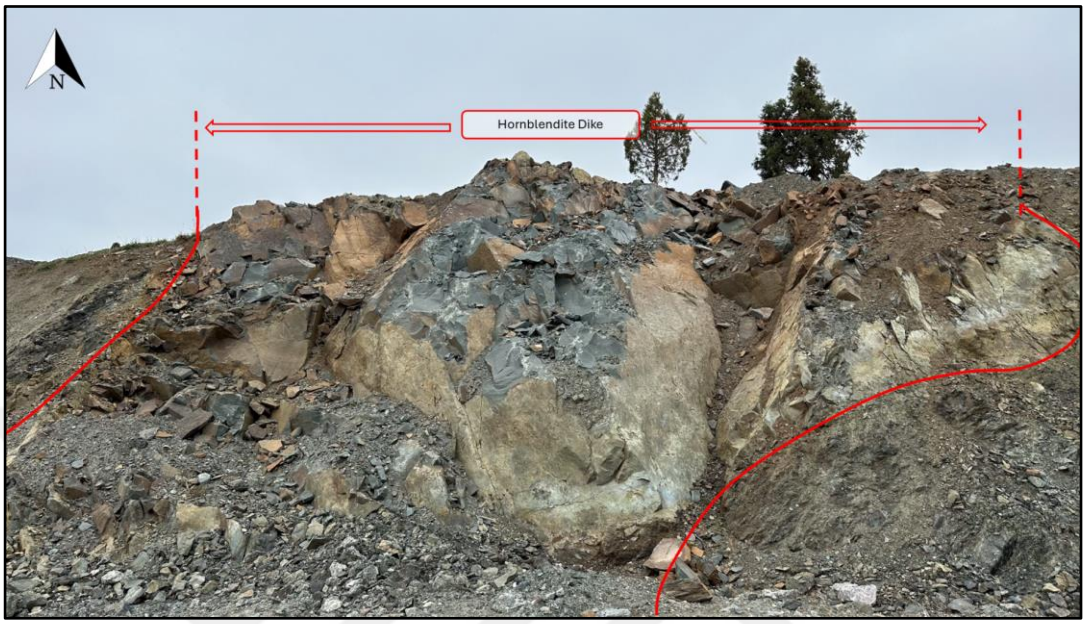

Figure 2.23. Field view form the hornblendite dike (marked with red line) intruding the ultramafics of the Dağardı ophiolitic mélange.

The rock is medium-grained phaneritic. Alteration appears to have disrupted the primary mineralogy in places. Hornblende is relatively well-preserved and occurs mostly as subhedral crystals; pleochroic with tones of brown is characteristic (Figure 2.24). Cleavage is well-developed, and basal sections (with two sets of cleavages) can be recognized. Hornblende is variably replaced by prehnite, zeolite, Ti-bearing

phases, and opaques. No relict plagioclase is found. Plagioclase has been entirely altered into prehnite, sericite, and epidote. Apatite occurs as an accessory phase.

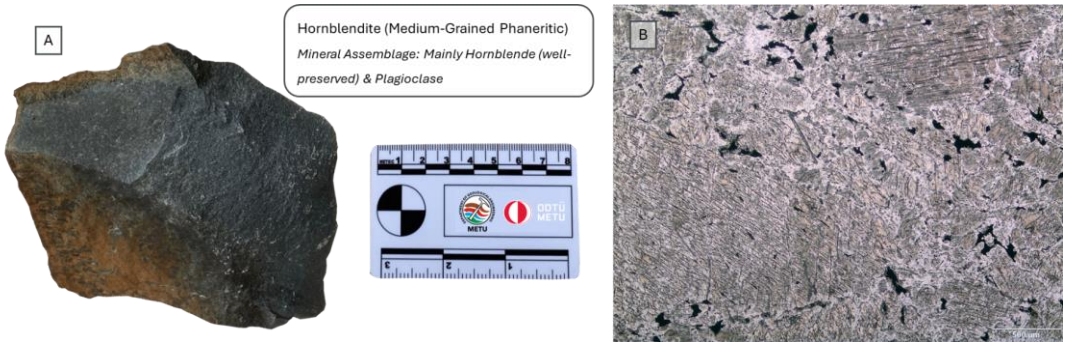

Figure 2.24. Views from hornblendite hand specimen (A) and thin section (B). PPL view shows hornblende crystals (green grains). Note that they are replaced by Ti-bearing phases (linear features) and opaques.

2.5 Taşbaşı Formation

The formation is originally defined in the Demirci Basin to represent lower Miocene conglomerate and sandstone outcrops (Akdeniz and Konak, 1979). It starts with burgundy, wine-red, and grey, coarse-grained, poorly-sorted, and medium-thick bedded basal conglomerates. These conglomerates contain pebbles derived from older rock units, including marble, schist, quartzite, gneiss, and granite. Basal unit grades upward into an alternation of conglomerates and sandstones. The sandstones are yellowish-grey, ungraded, and thin to medium bedded. The formation unconformably overlies the older units. The estimated thickness of the formation in the study area is approximately 250 meters. The age of the formation is assigned as Early Miocene (Explanatory Booklet of the MTA 1:100 000 Scale Geological Map of Türkiye I21 Sheet and Ersoy et al., 2014).

2.6 Tavşan Gold Deposit

In the Tavşan deposit, gold mineralization is mainly limited to jasperoid formed along the low-angle fault contact of the Dağardı ophiolitic mélange and the Budağan

formation, while ophiolite and limestones lack significant gold mineralization (Figure 2.25). Ophiolite suite hosts yellow iron-oxide rich clay which is identified along the fault contact with jasperoid (Figure 2.26).

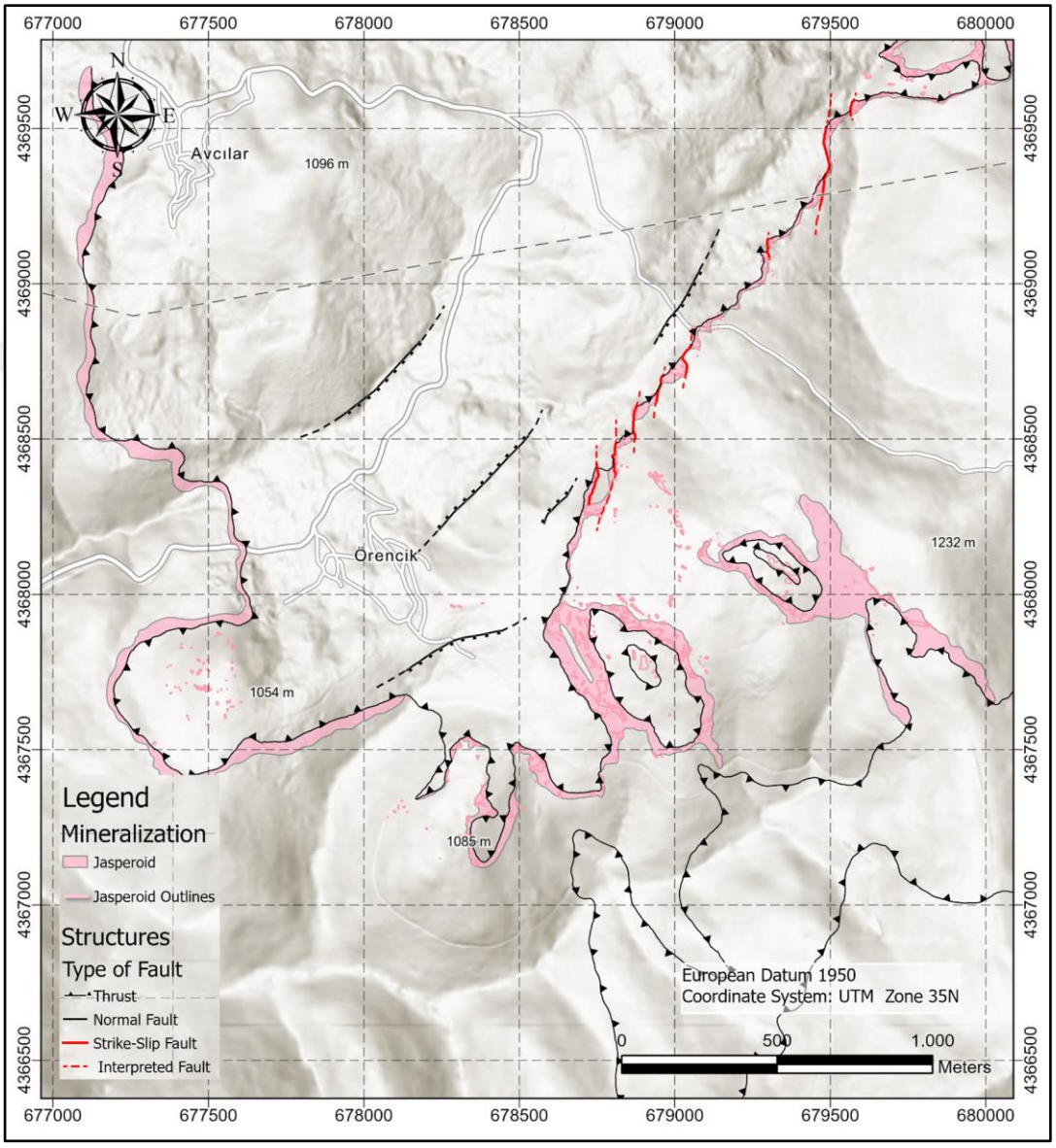

Figure 2.25. Map showing distribution of the jasperoid mineralization and outlines of Tavşan gold deposit.

There is evidence for multiple silicification events. There are no traceable interbeds and no primary structures within the jasperoid. Jasperoid in the southern part of the deposit seems more prone to leached textures, whereas those in the northern part

shows liesegang banding, (nested rings or bands caused by rhythmic precipitation within a fluid saturated rock). Because of its fine-grained to sugary silicification, jasperoid is resistant to weathering (Figure 2.26).

Field observations confirm presence of fracture-controlled solution cavities (jasperoid keels) and karstic collapse breccias within the massive micritic limestones of the Budağan formation (Figure 2.27 and Figure 2.28).

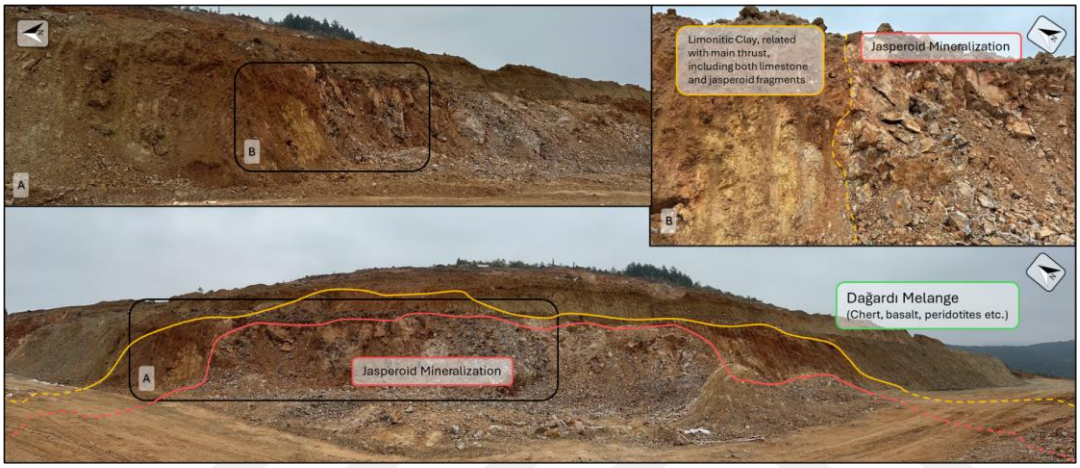

Figure 2.26. Views of low-angle fault zone consisting of main jasperoid mineralization. Yellow iron-oxide rich clay fills cavities in the limestone, low-grade metamorphosed and sheared Dağardı ophiolitic mélange.



Figure 2.27. Views of fine-grained to sugary silicification, jasperoid blocks with solution cavities.

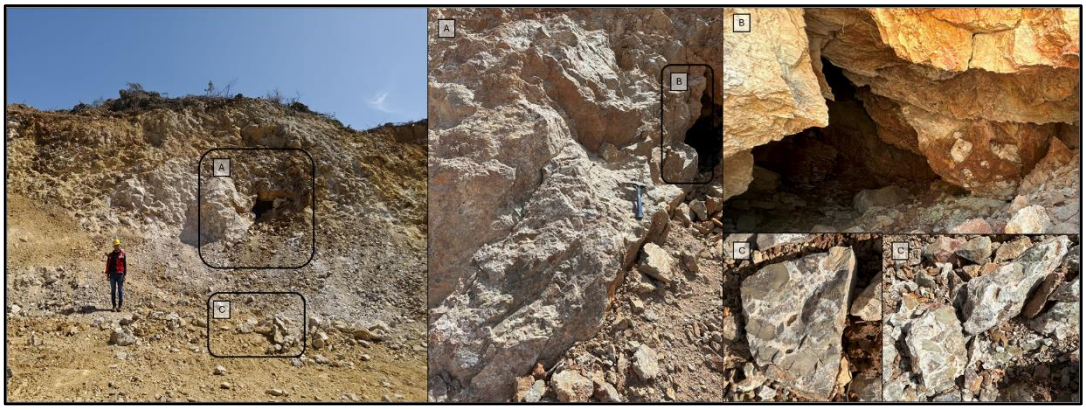

Figure 2.28. Field views of karstic cavity with breccias and silicification in the open pit.



Figure 2.29. View form core samples showing karstic cavities filled with brecciated limestone and clay-bearing sediments as a matrix. The fault zone is evident at depths between 19.80 m and 23.00 m, with fault gouge.

Detailed examination of core samples confirms sharp contact between strongly silicified jasperoid and the host limestone, where there is apparent minimal limestone recrystallization. Both the field and core observation suggest at least two stages of silicification: (i) initial pervasive silicification of host rock (including both matrix

and clasts in breccia) (Figure 2.30) and (ii) a later phase of clear quartz fracture filling with local open space filling.

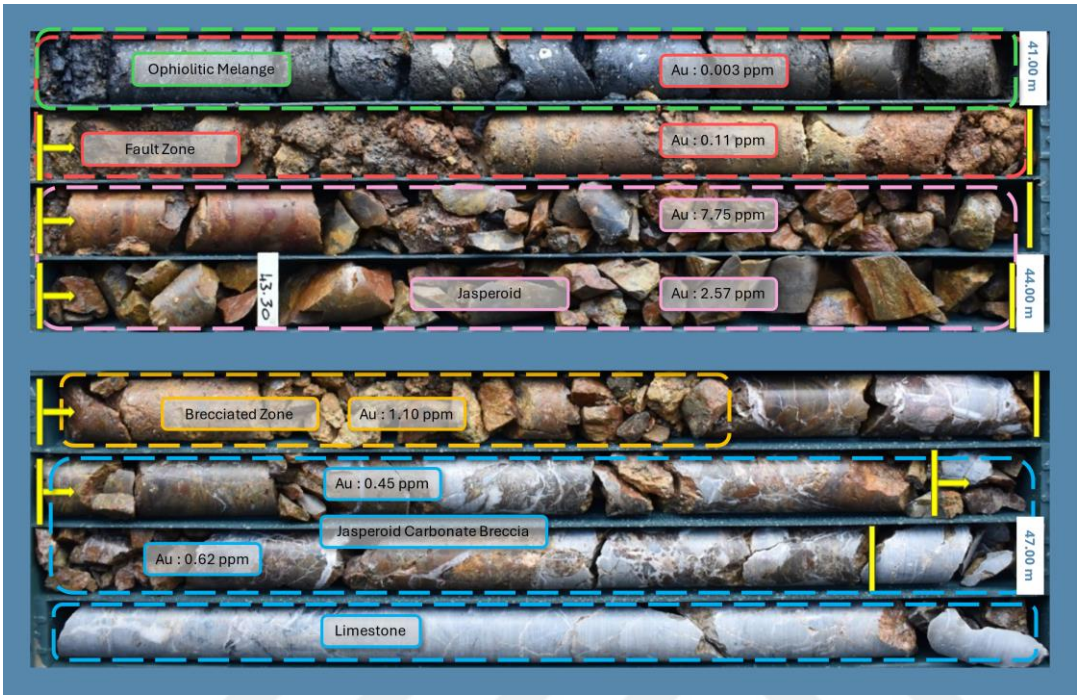

Figure 2.30. Detailed views of core samples, showing mineralization zone, as well as brecciation within ophiolitic units, jasperoid, and limestones. The fault zone is evident at depths between 41.00 m and 44.50 m, with a high concentration of gold (Au) mineralization, particularly 7.75 ppm and 2.57 ppm. The jasperoid breccia and carbonate breccia zones, visible between 44.00 m and 47.00 m, further exhibit varying levels of Au, with concentrations ranging from 0.45 ppm to 1.10 ppm. These observations suggest a complex structural framework and brecciation pattern, which are crucial for understanding the mineralization.

Another type of the mineralization is expressed by stibnite and quartz-carbonate veins, and/or fillings of drusy cavities and the cross-cutting relationship of quartz veins with jasperoid indicates that the quartz-stibnite-carbonate mineralization occurred after the jasperoid mineralization. This type of mineralization brought in antimony sulphide minerals, mostly needle-like stibnite. Some stibnites have oxidized due to weathering, turning beige in colour, but their needle-like texture has been preserved (Figure 2.31). Fine-grained sulphides include pyrite, marcasite, and stibnite (with stibiconite and kermesite detected by Electron microscope with energy

dispersive x-ray analyser (SEM_EDX)) (Teck Cominco, 1997). Sulphide content is typically less than 1% though locally it reaches 20%.



Figure 2.31. Views from stibnite minerals (metallic dark grey) with a needle-like texture developed within jasperoid. Some stibnite crystals are oxidized, turning beige while retaining the needle-like structure.

2.6.1 Reflected Light Ore Microscopy

Mineralogic and petrographic studies play a fundamental role in understanding the characteristics of the Tavşan gold deposit, especially in identifying mineral associations, textural relationships, and potential zones of mineralization. To further enhance the precision of these studies, specific high gold grade sample is selected from the study area, providing detailed minerals identification.

Figure 2.32 illustrates a hand sample from an intensely silicified zone, bearing sulphide minerals, which represents a high-grade mineralized section of the deposit. The interested area is marked on the sample, targeting areas of sulphide concentration and silicification.



Figure 2.32. Hand sample of intensely silicified, sulphide minerals bearing high-grade mineralized zone and polished mouth in the section.

Under reflected light microscopy, various mineralogical features are observed in the Figure 2.33. In view A, disseminated pyrite is seen distributed throughout the section. Views B and C highlight disseminated pyrite occurring within large epidote grains, represented by their grey colour. In view D, chalcopyrite has been partially replaced by sphalerite, a phenomenon referred to as "chalcopyrite disease." Needle-like, grey-coloured grains in view E represent rutile. Views F and G show yellow-coloured chalcopyrite grains, with covellite replacing chalcopyrite along its rims. Notably, in view G, pyrite is enclosed by chalcopyrite, which in turn is rimmed by covellite.

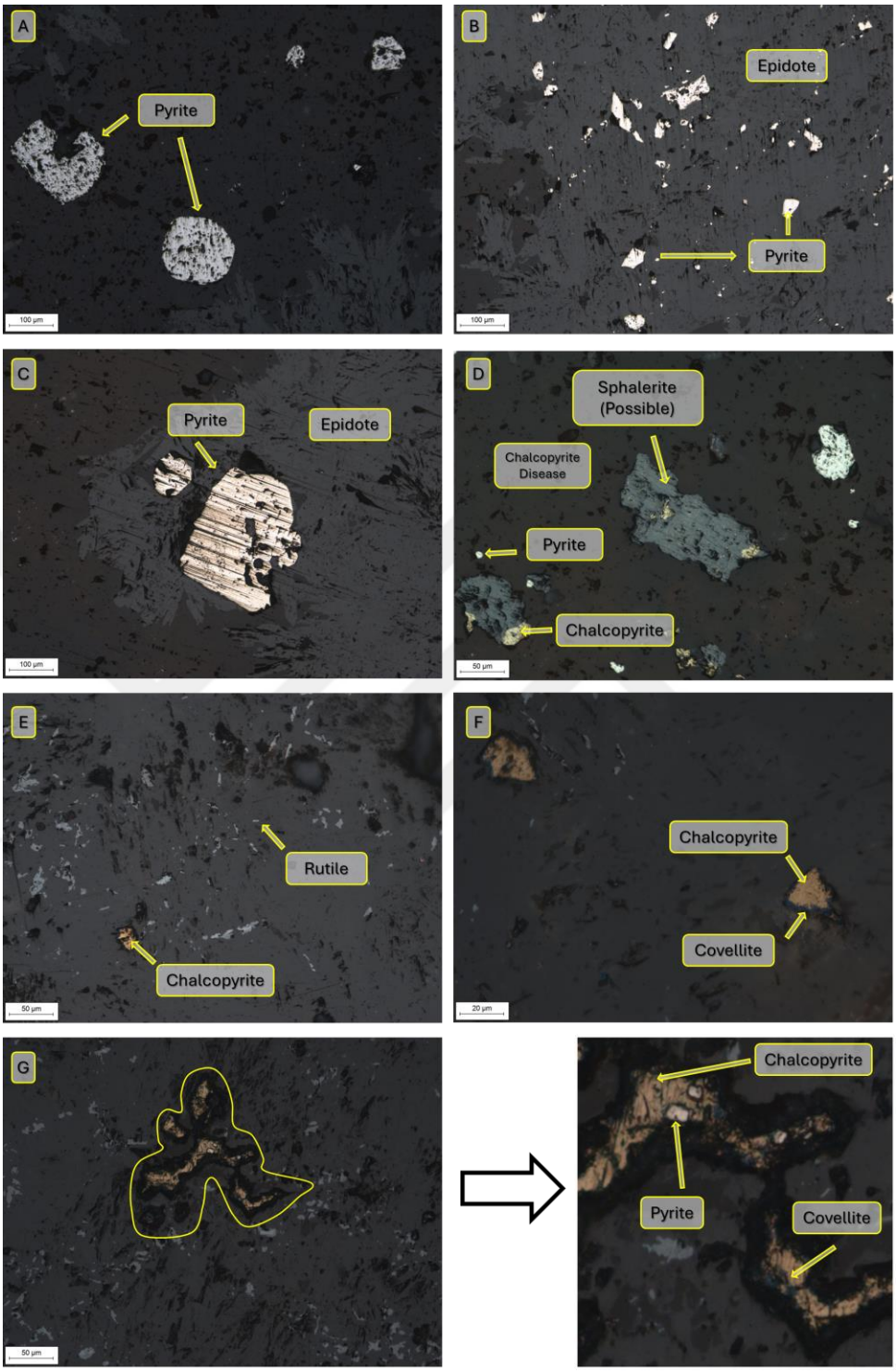

Figure 2.33. Reflected light microscopy images illustrating mineralogical features of the section: (A) Disseminated pyrite distribution, (B-C) Pyrite within large epidote grains, (D) Chalcopyrite disease with chalcopyrite replaced by sphalerite, (E) Needle-like rutile grains, (F-G) Chalcopyrite with covellite rims, and (G) Pyrite enclosed by chalcopyrite and chalcopyrite enclosed by covellite.

Microscopic studies (Figure 2.34) reveal that the mineral assemblage in these zones consists predominantly of pyrite, and chalcopyrite. Importantly, the analysis identified the presence of covellite, which occurs as both inclusions within chalcopyrite and as an alteration product along the rims of chalcopyrite grains. Of particular interest is the potential presence of gold (Au) within the chalcopyrite, concentrated along its rims in association with covellite. This suggests that gold may be spatially associated with sulphide minerals. Covellite in the sample may be supergene product and are stable under high fO_2 conditions. There is no stibnite observed in the sample but there is stibnite in the study area. Stibnite is typically not a mineral stable under high fluid fO_2. These minerals should have precipitated under strikingly different conditions.

Microscopic studies have revealed critical insights into the spatial relationships between gold-bearing phases and sulphides in the Tavşan gold deposit. Notably, the presence of gold (Au) was detected, often in association with covellite, which occurs both as inclusions within chalcopyrite and as an alteration product.

Future studies, including more extensive EPMA analysis across different zones of the deposit, will help to further refine the understanding of the mineralization processes.

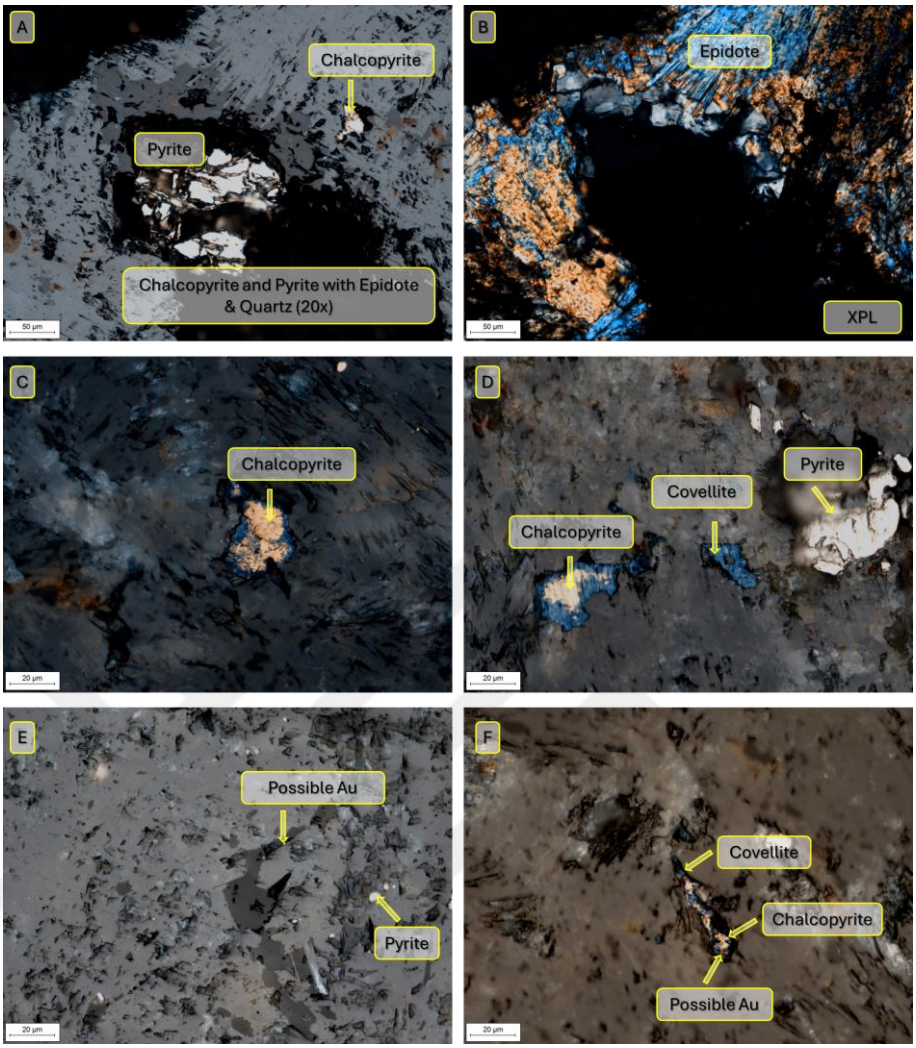

Figure 2.34. Reflected light microscopy images show pyrite, chalcopyrite, and the presence of potential Au element in the rim of chalcopyrite within covellite (F), covellite is also found as inclusions within chalcopyrite.

2.6.2 Surface Geochemistry of Tavşanlı Gold Deposit

In this section, the geochemical data obtained from soil and rock samples are analysed and interpreted to understand the mineralization processes and their relationship with lithological boundaries. This part will focus on (i) the significance of the geochemical anomalies, (ii) the correlations between key elements, and (iii) how these findings align with the geological structures identified in the region. Furthermore, the spatial distribution of the geochemical signatures will provide

insights into the study area's metallogenic potential and guiding future mineral exploration endeavours.

2.6.2.1 Soil Geochemistry

A comprehensive geochemical survey is conducted in the study area, wherein 25x25 meter grided 8,225 soil samples are analysed using portable X-ray fluorescence (pXRF) technology. The geochemical signatures derived from these analyses are provided distinct markers for different lithological units, notably the ophiolitic mélange, jasperoid mineralization, and limestone.

The elements Fe, Cr, Ni, and As are identified as key geochemical indicators for differentiating these units. Other elements, Sb, Cu, Mo, Se, Pb, Zn etc., cannot be used because of the detection limits and error intervals. A correlation matrix is constructed to assess the interrelationships among these elements. As indicated by the matrix, arsenic (As) exhibits a negative correlation with iron (Fe), chromium (Cr), and nickel (Ni), whereas Fe, Cr, and Ni are positively correlated with each other, signifying their potential association with the ophiolitic mélange (Table 2.1).

Table 2.1. Correlation matrix of selected elements.

Elements	As (ppm)	Fe (ppm)	Cr (ppm)	Ni (ppm)
As (ppm)	1	-0.12	-0.1	-0.1
Fe (ppm)	-0.12	1	0.6	0.52
Cr (ppm)	-0.1	0.6	1	0.89
Ni (ppm)	-0.1	0.52	0.89	1

The spatial distribution of these elements is mapped, revealing clear geochemical boundaries that coincide with the geological boundaries of the ophiolite unit. Figure 2.35, Figure 2.36 and Figure 2.37 illustrate the spatial distribution of Fe, Cr, and Ni anomalies respectively, highlighting the extent of the ophiolitic mélange.

It is observed that arsenic (As) anomalies have the highest values in the areas of the jasperoid exposures (Figure 2.38). For this reason, the arsenic (As) anomaly can be used as an indicator of mineralization based on soil sample results.

The following maps display anomalies using a heat map, with the zonation of high and low anomalies calculated through the inverse distance weighting (IDW) method. On the colour scale, higher or maximum values are represented by warm colours, indicated by denser scale.

It is observed that arsenic (As) anomalies have the highest values in the areas where the jasperoid unit is located on the geological map (Figure 2.38). For this reason, the arsenic (As) anomaly can be used as an indicator of mineralization based on soil sample results.

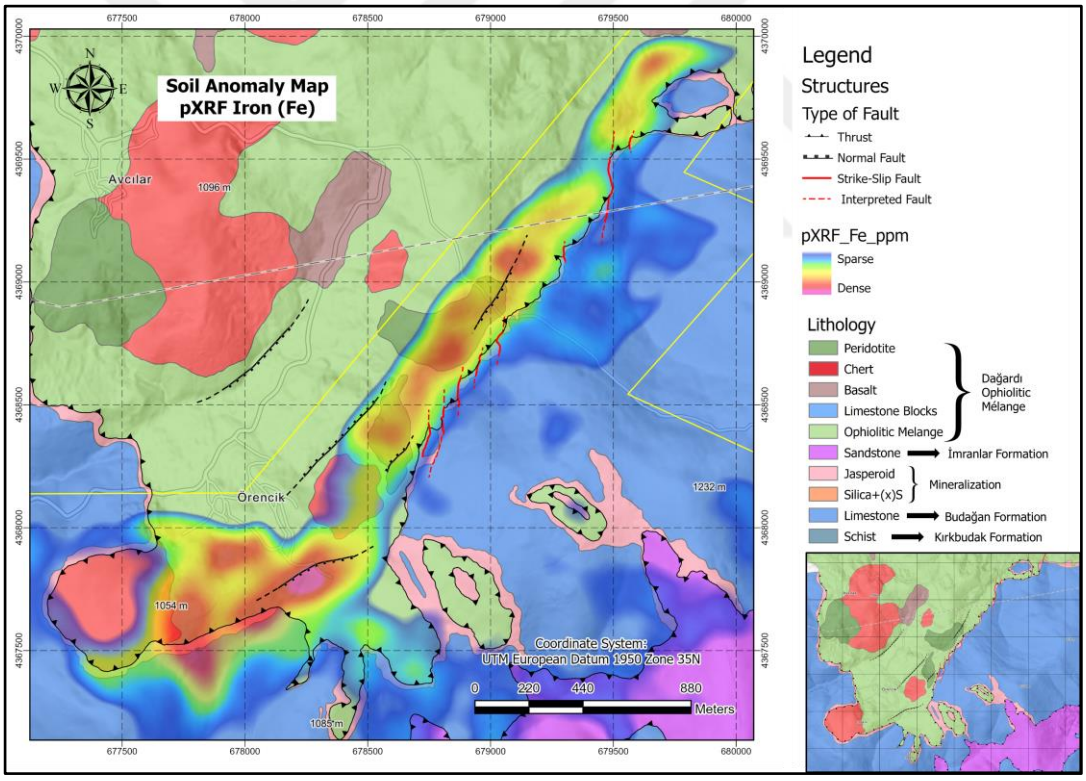

Figure 2.35. Distribution of Fe anomalies in the study area. Note that Fe anomaly along the low-angle fault contact of the Dağardı ophiolitic mélange.

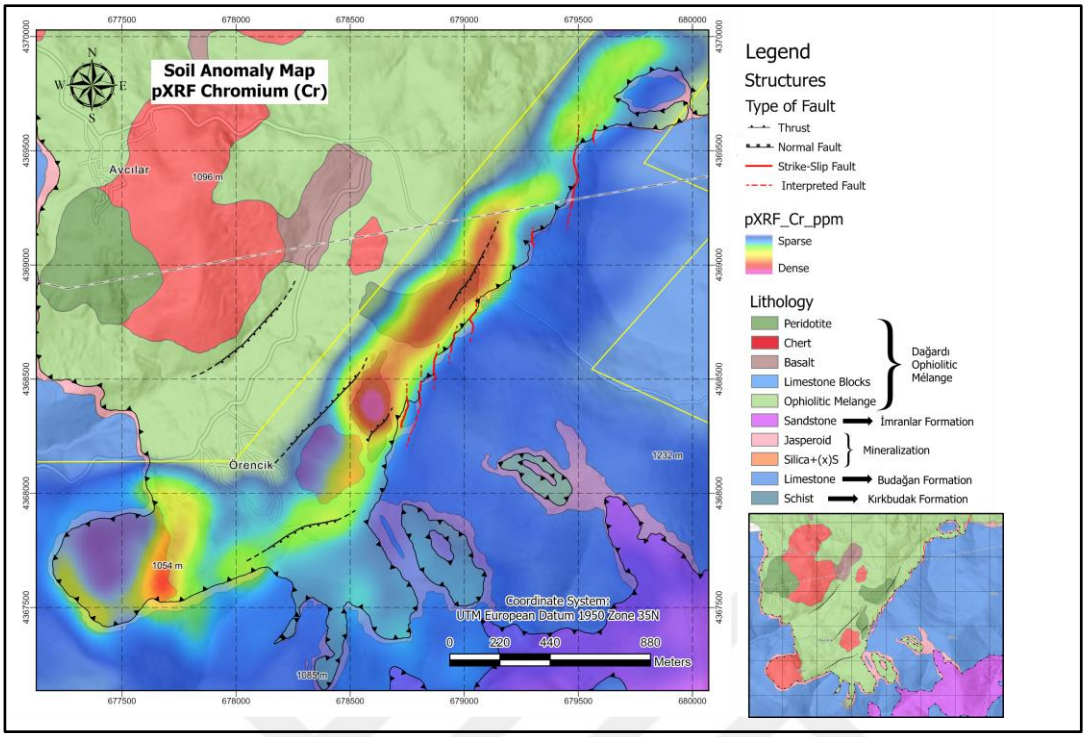

Figure 2.36. Distribution of Cr anomalies in the study area. Note that Cr anomaly along the low-angle fault contact of the Dağardı ophiolitic mélange.

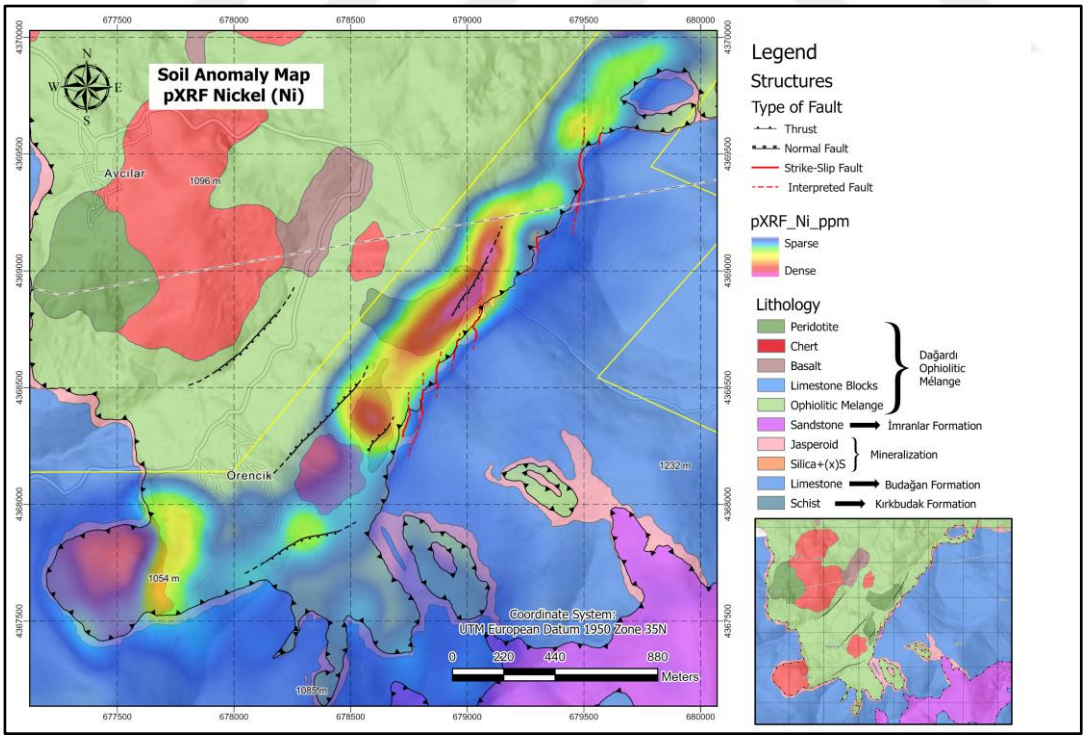

Figure 2.37. Distribution of Ni anomalies in the study area. Note that Ni anomaly along the low-angle fault contact of the Dağardı ophiolitic mélange.

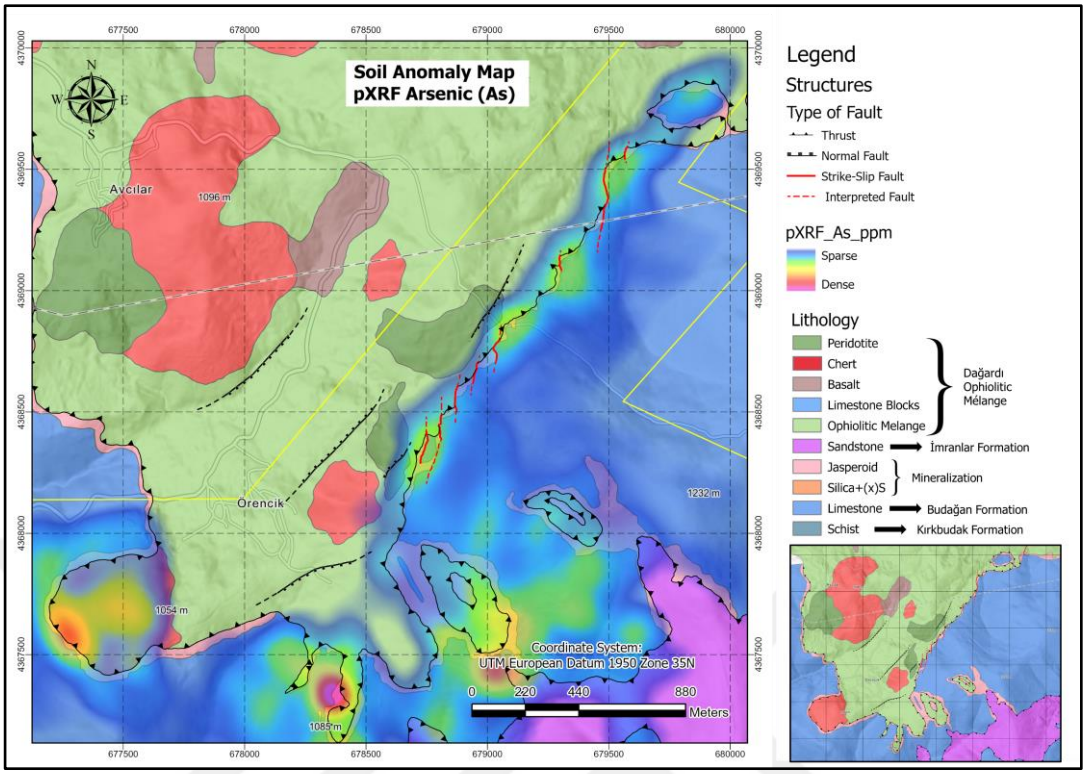

Figure 2.38. Map showing distribution of arsenic (As) anomalies from the pXRF soil samples. Anomaly boundaries indicate the jasperoid mineralization in the study area.

2.6.2.2 Rock Geochemistry

A total of 342 rock samples were collected from the jasperoid mineralization zones and ophiolitic mélange for multi-element geochemical analysis. These analyses aimed to delineate the mineralized zones and differentiate lithological units. The correlation matrix for the selected elements is presented in Table 2.2, indicating a strong positive correlation between gold (Au), arsenic (As), and antimony (Sb), with correlation coefficients of 0.52 and 0.56 respectively. Silver (Ag) also shows a positive correlation with Au, As, and Sb, whereas it is either neutral or negatively correlated with Fe, Cr, and Ni.

Table 2.2. Correlation matrix of the multi-element rock samples.

Elements	Au (ppm)	Ag (ppm)	As (ppm)	Sb (ppm)	Fe (pct)	Cr (ppm)	Ni (ppm)
Au (ppm)	1	0.5	0.52	0.56	0.04	-0.08	-0.35
Ag (ppm)	0.5	1	0.61	0.55	-0.1	0.1	0.09
As (ppm)	0.52	0.61	1	0.77	-0.24	-0.04	-0.13
Sb (ppm)	0.56	0.55	0.77	1	-0.41	-0.04	-0.17
Fe (pct)	0.04	-0.1	-0.24	-0.41	1	0.18	0.21
Cr (ppm)	-0.08	0.1	-0.04	-0.04	0.18	1	0.64
Ni (ppm)	-0.35	0.09	-0.13	-0.17	0.21	0.64	1

The geochemical anomaly maps for Au, As, and Sb (Figure 2.39, Figure 2.40, and Figure 2.41) further support the association of these elements with jasperoid mineralization. Notably, Au anomalies are predominantly confined to the jasperoid unit, with no significant anomalies detected in the ophiolitic mélange.

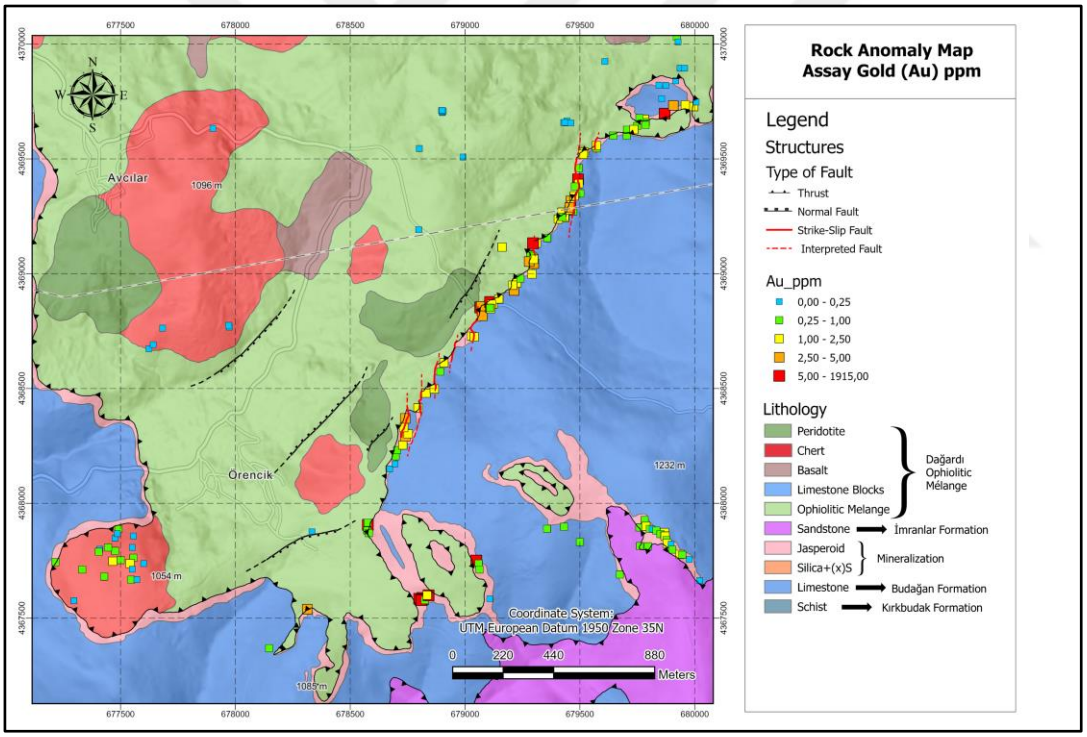

Figure 2.39. Spatial distribution of Au anomalies. Note that anomalies are concentrated within the jasperoid unit.

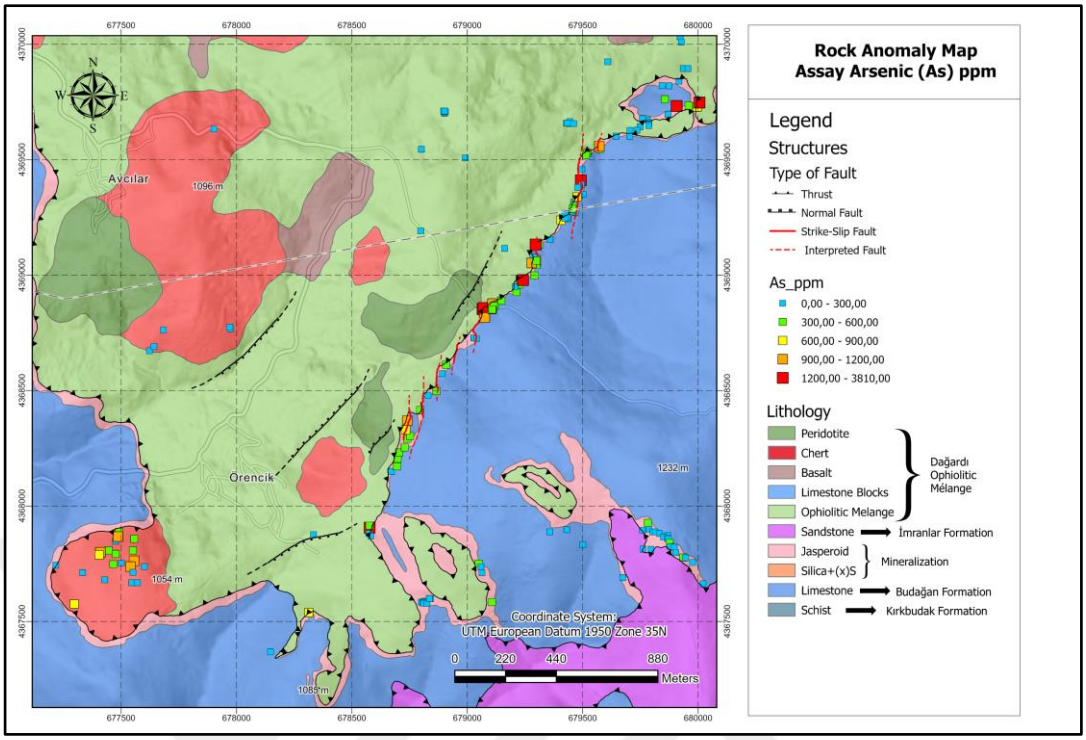

Figure 2.40. As anomaly distribution, aligned with the jasperoid unit, showing no significant presence in the ophiolitic mélange.

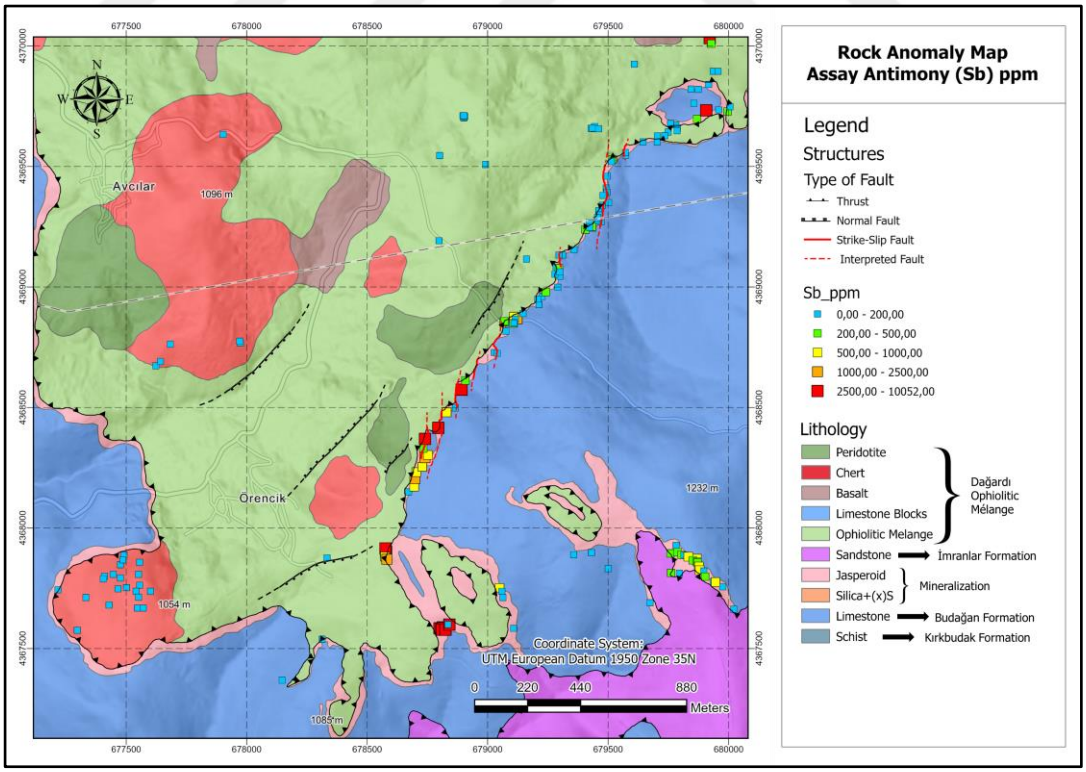

Figure 2.41. Sb anomalies, observed near the main jasperoid zone.

2.6.2.3 Multi-Element Geochemical Analysis

The multi-element geochemical analysis provided significant insights into the lithological classification and structural controls within the study area. To classify lithologies, IoGas software is used. Principal component analysis and cluster analysis are applied and mentioned in Methodology section.

The plot in Figure 2.42 shows the vectors of elements from the multi-element analysis results. It also depicts the distribution of rock samples along with their classifications and their relative positions to these vectors. In this plot, jasperoid is represented by the pink cluster, which is characterized by Au, Ag, As, and Sb elements. The ophiolitic unit is represented by the green cluster, predominantly containing Fe, Cr, Ni, Co, and Mg elements.

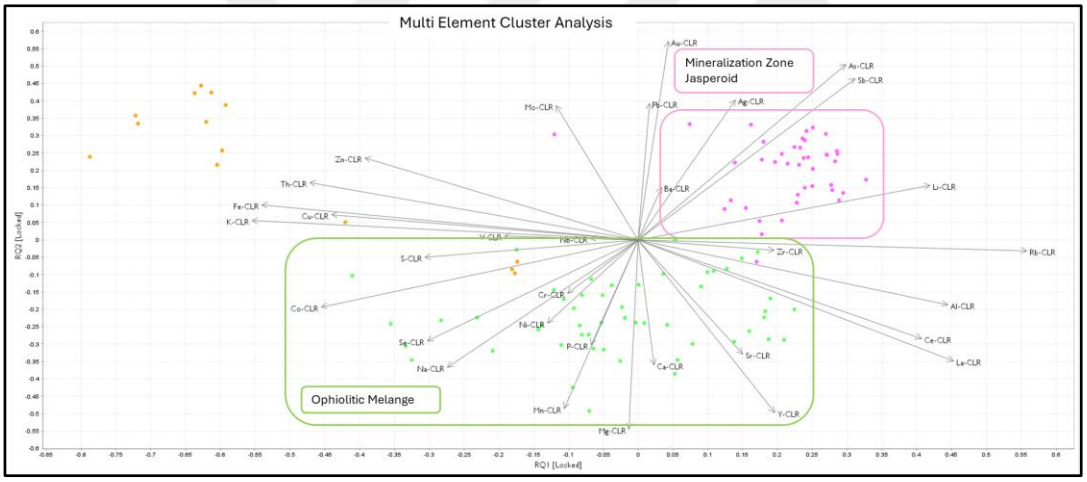

Figure 2.42. Elemental vectors illustrating the distribution of dominant geochemical clusters within the study area.

According to the cluster distributions in the subsequent map (Figure 2.43) illustrates the lithologies corresponding to these clusters. The pink cluster represents the jasperoid, intersecting the jasperoid unit in the geological map. Conversely, the green cluster, indicative of the ophiolitic unit, aligns with the ophiolite on the geological map. This study confirms that the lithological boundaries between the ophiolite and jasperoid mineralization are marked by a thrust fault.

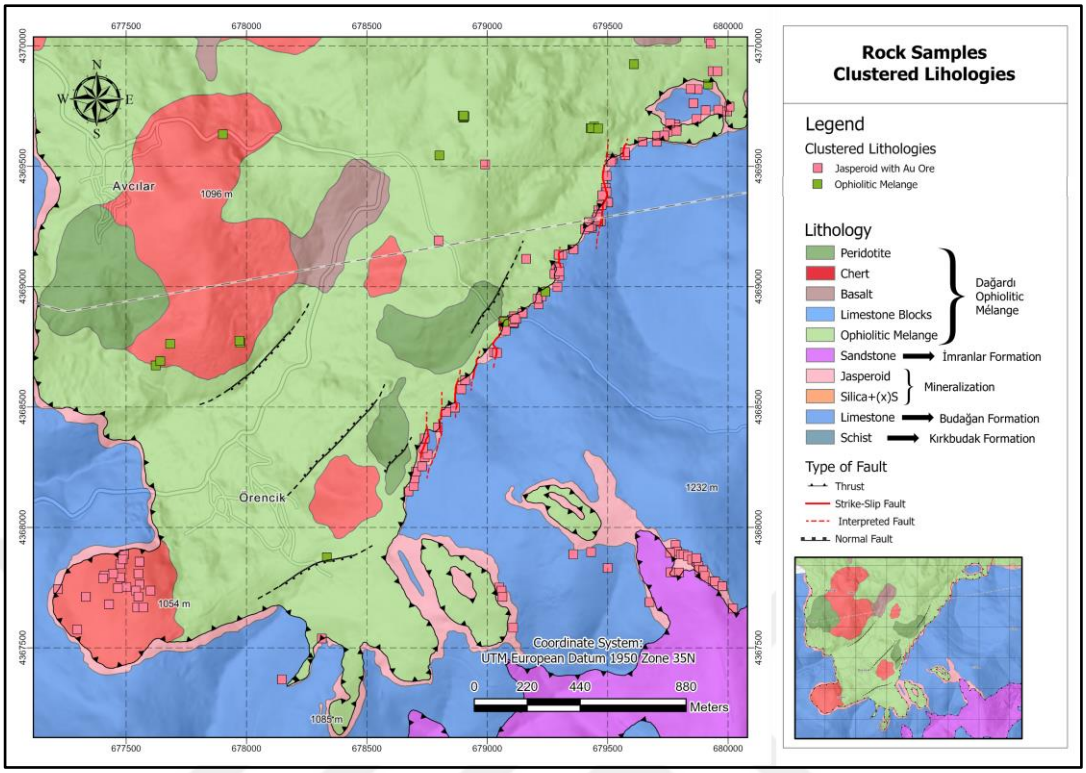

Figure 2.43. Map showing the lithological classification based on the geochemical clusters within jasperoid zone. Note how ophiolite units are distinctly separated.

2.6.2.4 Implications of Surface Geochemistry

The single-element arsenic (As) geochemical analysis and anomaly map have provided insights into the structural controls influencing jasperoid mineralization, as the distribution of arsenic (As) is directly correlated with these structures. The anomaly distribution (Figure 2.44) illustrates close association of low-angle faulting, jasperoid occurrence and As distribution. As anomalies show distinct discontinuities where the jasperoid anastomosing patterns diverge and separate. The continuity of As distribution is interrupted by north–south-trending faults and that the anomalies are therefore bounded by these structures. N–S faults cut and offset both the low-angle fault and associated jasperoid mineralization (Figure 2.44). Also, ENE–WSW-striking and southeast-dipping Örencik fault distinctly separates areas with high arsenic anomalies.

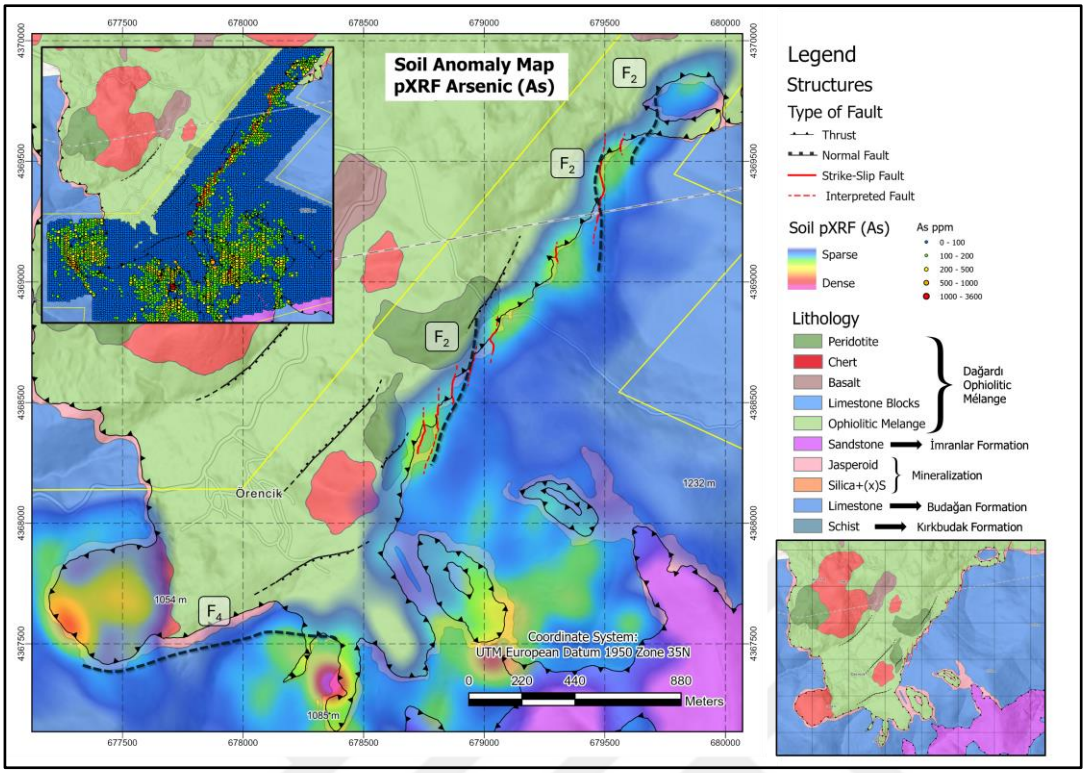

Figure 2.44. Anomaly map showing the distribution of arsenic (As) across five potential faults. The first three faults, oriented N-S, display arsenic (As) anomaly discontinuities, while the fourth fault represents a wider anomaly zone. The fifth fault, oriented E-W, separate s areas with higher arsenic (As) anomalies.

CHAPTER 3

STRUCTURAL GEOLOGY

This chapter will provide detailed information about both macro- and micro-scale geological structures. According to site observations, there occurs three distinct common structures in the Tavşan gold deposit; these are: (i) bedding, (ii) foliation, (iii) low- and high-angle faults. The characteristics of these structures will be given in the following subsections (Table 3.1).

Table 3.1. Number of measures and dominant orientation of structures.

Structure	Sets	# of Measures	General Orientation	Mean Dip Amount (°)
Bedding Plane	B1	18	WNW – ESE	23
	B2	10	NE – SW	33
Foliation	FL	119	NNW – SSE	23
Faults	F1	13	NE – SW	36
	F2	12	NNE – SSW	55
	F3	27	NE – SW	10
	F4	5	ENE – WSW	49
	F5	27	NW – SE	63
	F6	6	NNE – SSW	65

Directional data of structures are presented as rose diagrams, stereonet of the planes plotted as great circles and poles to the planes and counter graph of poles to the planes. Schmidt lower hemisphere equal-area projection of the structures also shows Bingham best fit planes and mean plane, including eigen vectors. Rose diagrams consist of wedges with lengths proportional to number of data, spanning angles representing the classes.

The attitude of fault planes and where observable, the rake of the slickenlines are all measured for kinematic analysis. The structural data are subsequently analysed by using *Dips and IoGas software*. The raw data are given in Appendix B, C and D.

Both the spatial and temporal relationships between gold mineralization and faults are explored (Figure 3.1). It is therefore important to determine if there is a change in gold grade in relationship to the structure(s). Kinematic indicators are also studied.

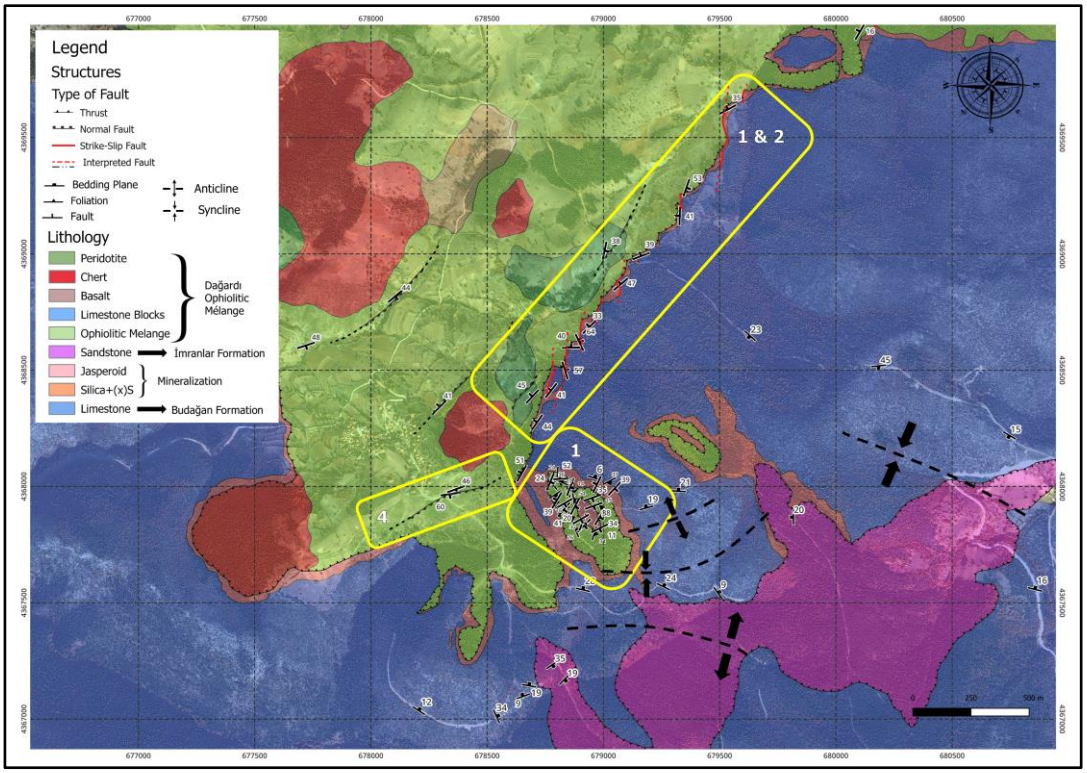

Figure 3.1. Clustered areas of interest on geological map (Appendix E).

3.1 Bedding Planes

Stratification occurs as well-developed structure in the limestones of the Budağan formation and claystone-sandstone of the İmranlar formation. These vary from medium-very thick bedded to laminated (Figure 3.2 to Figure 3.5). Bedding planes dipping at low to moderate angles. The limestones are folded as represented by several small-scale anticlines and synclines.

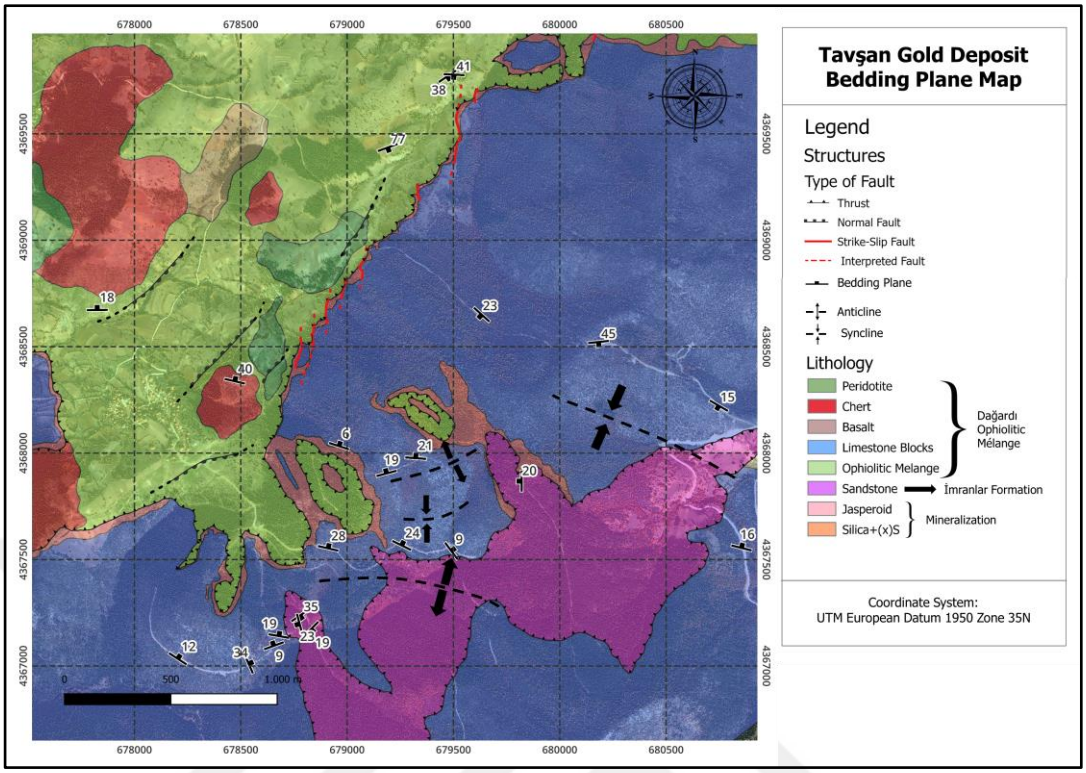

Figure 3.2. Geological map showing bedding plane orientations in limestones of the Budağan formation.

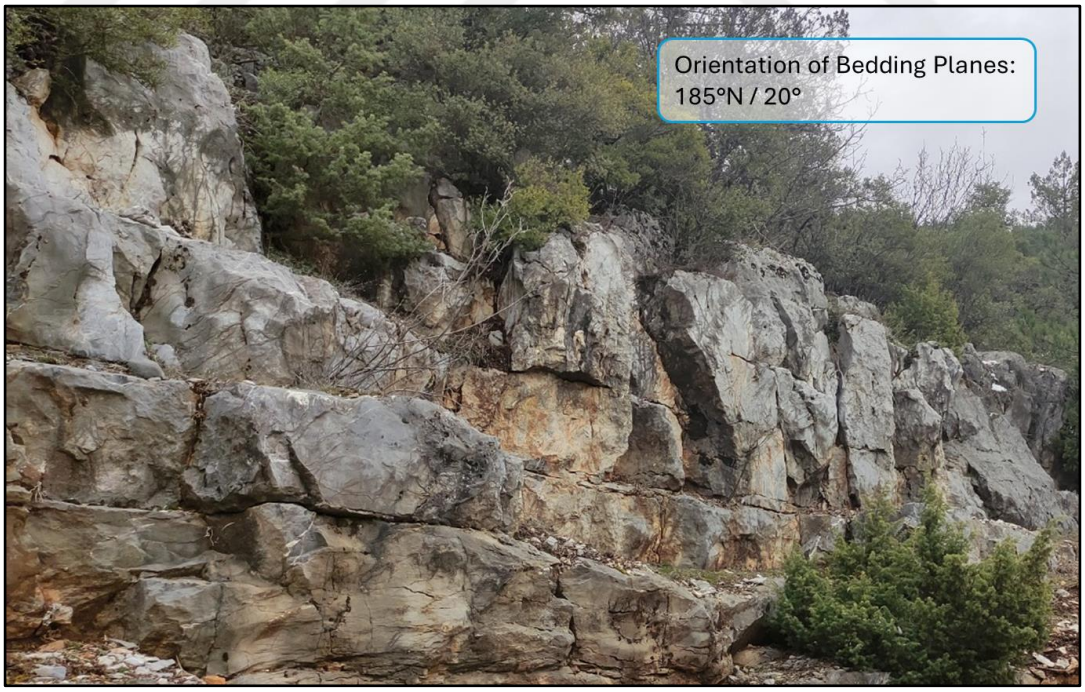

Figure 3.3. Field view from thick bedding in the limestone outcrops of the Budağan formation.

Figure 3.4 and Figure 3.5 are examples of the limestone bedding plane measurements with different orientations. Opposite dipping of beds in limestone units are shown as an example.

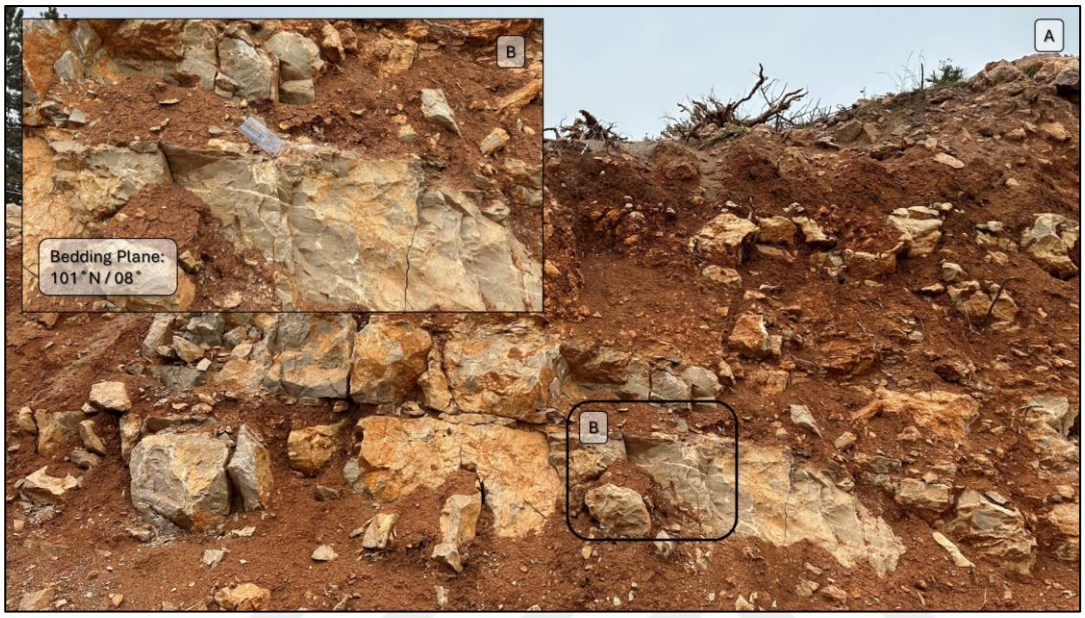

Figure 3.4. Field views from gently-dipping bedding planes in the limestones of the Budağan formation.

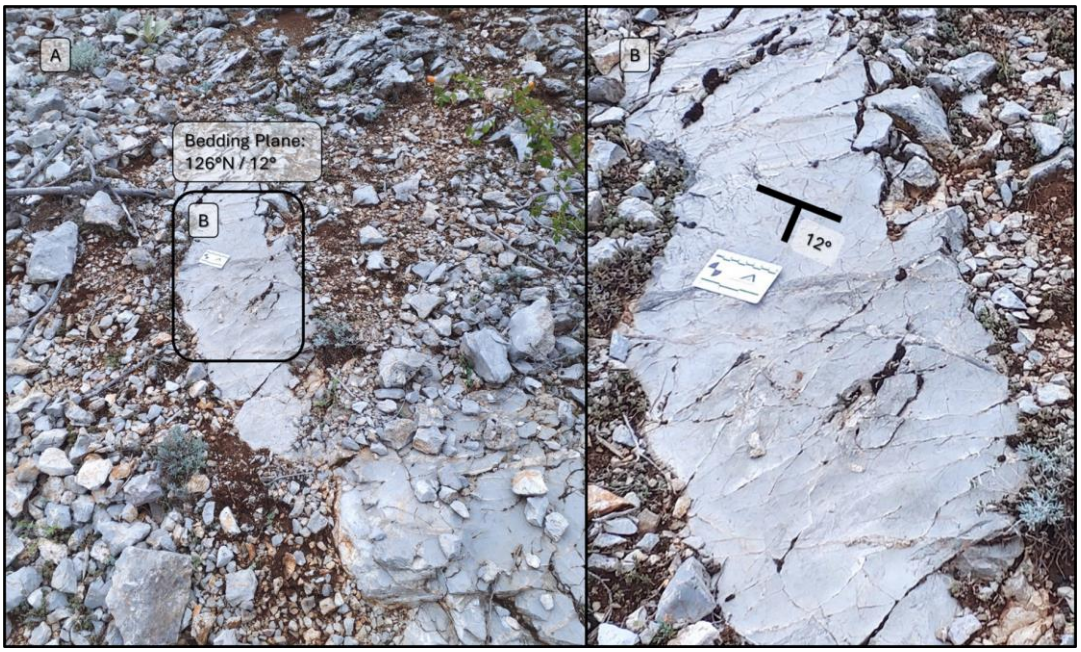

Figure 3.5. Field views from gently-dipping bedding planes in the micritic limestones of the Budağan formation.

Stereoplot of the bedding data reflects main orientations in WNW–ESE and approximately N–S directions (Figure 3.6). Collected structural data are filtered and a total of 28 measurements are analysed by using *Dips Software*; the results confirm that mean strike orientations of the bedding planes are 300–320°N and 000–020°N, and the mean dip, 30° but the dip direction changes due to folding (Figure 3.6). The dip direction and amounts may vary from one place to another; the range of dip amount is 06° and 45°.

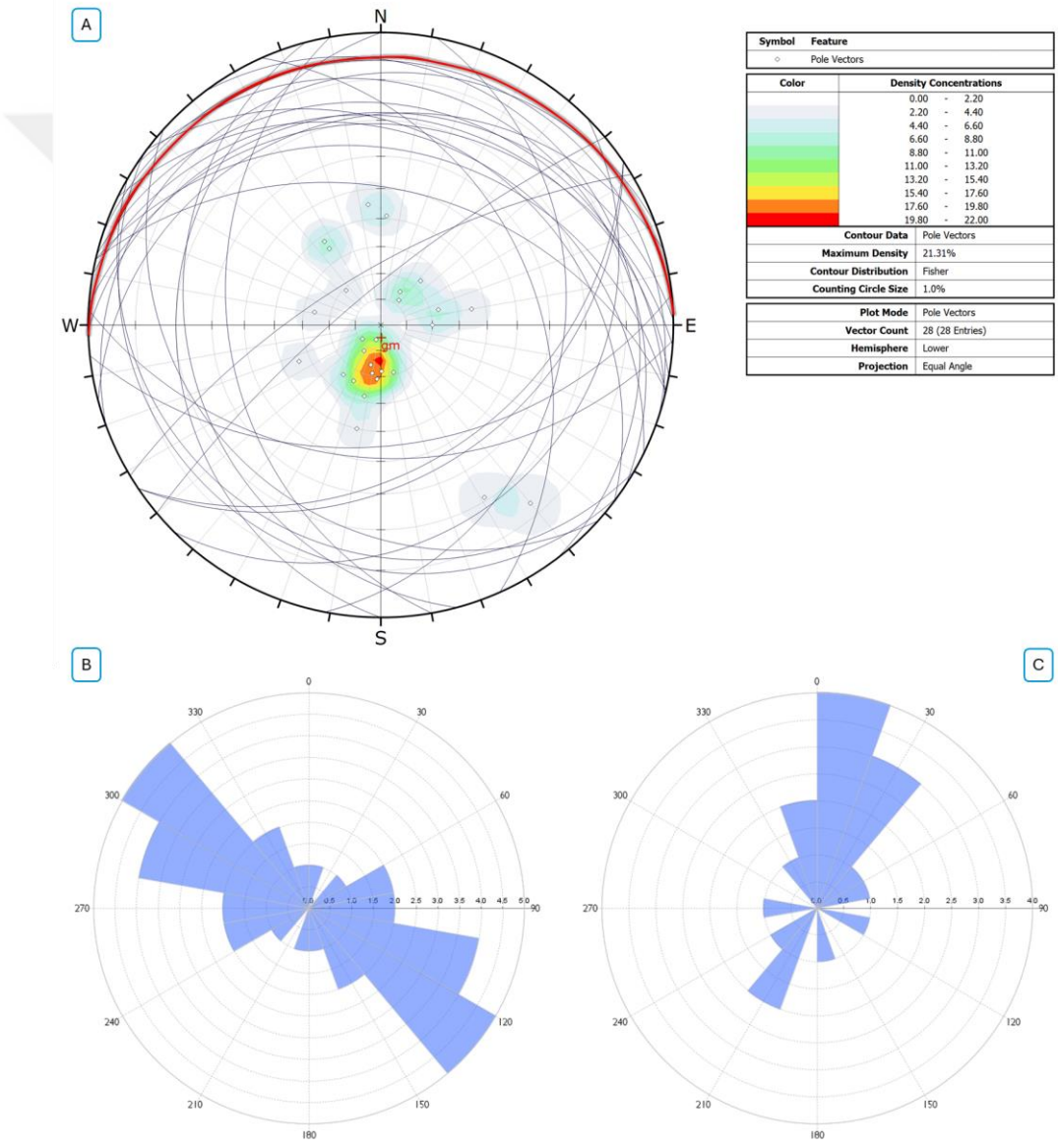

Figure 3.6. (A) Stereonet of the bedding planes, plotted as great circles, poles to planes and great circles on an equal area and contour graph of the associated poles

to the planes. The diagrams illustrate single dominant bedding orientation in the Tavşan gold deposit area. (B, C) Rose diagrams showing the geometry (strike and dip direction, respectively) of bedding planes.

3.2 Foliation

The sheared peridotites of the Dağardı ophiolitic mélange in the main zone of the open pit area typically display well-developed and penetrative foliation (Figure 3.7). The foliation measurements in the below map correspond to rectangle 1 in anomalous values in the location map created with clustered areas (Figure 3.1). In places, C-S fabrics and sigma-type augen structures are observed and they indicate top-to-the-left sense of shearing during the deformation that give rise the formation of foliation (Figure 3.8). The kinematics of the deformation is also supported by tension carbonate veins (Figure 3.9).

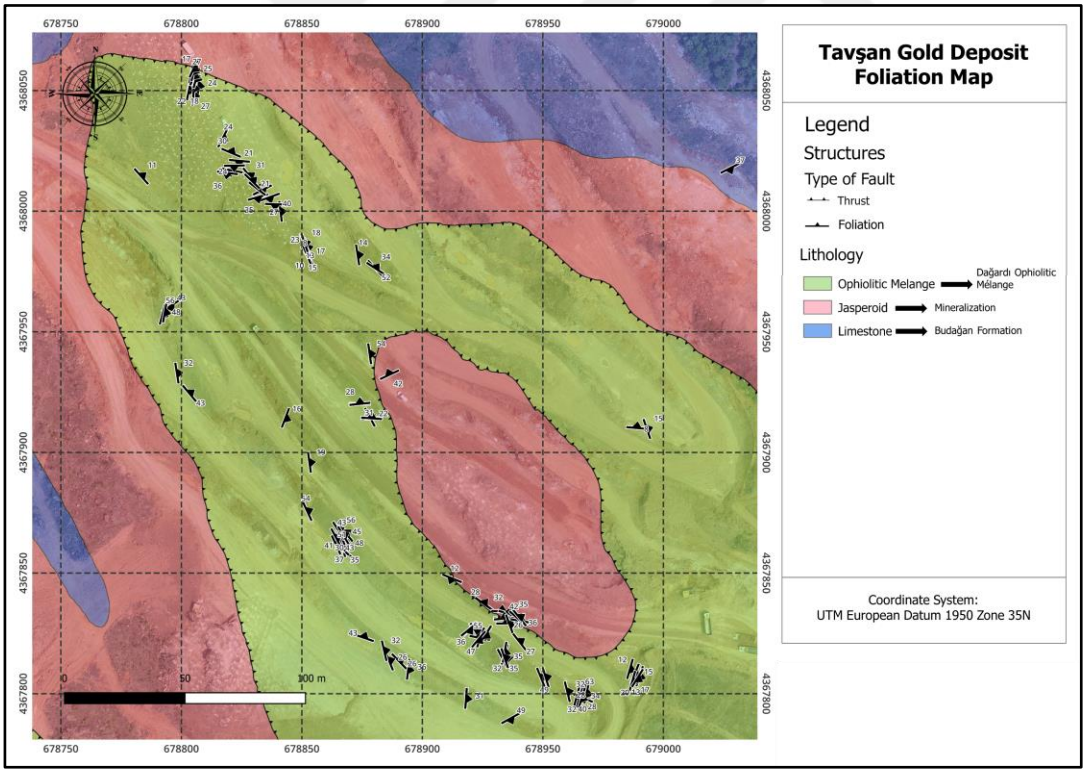

Figure 3.7. Geological map showing the location and orientation of foliation measurements.

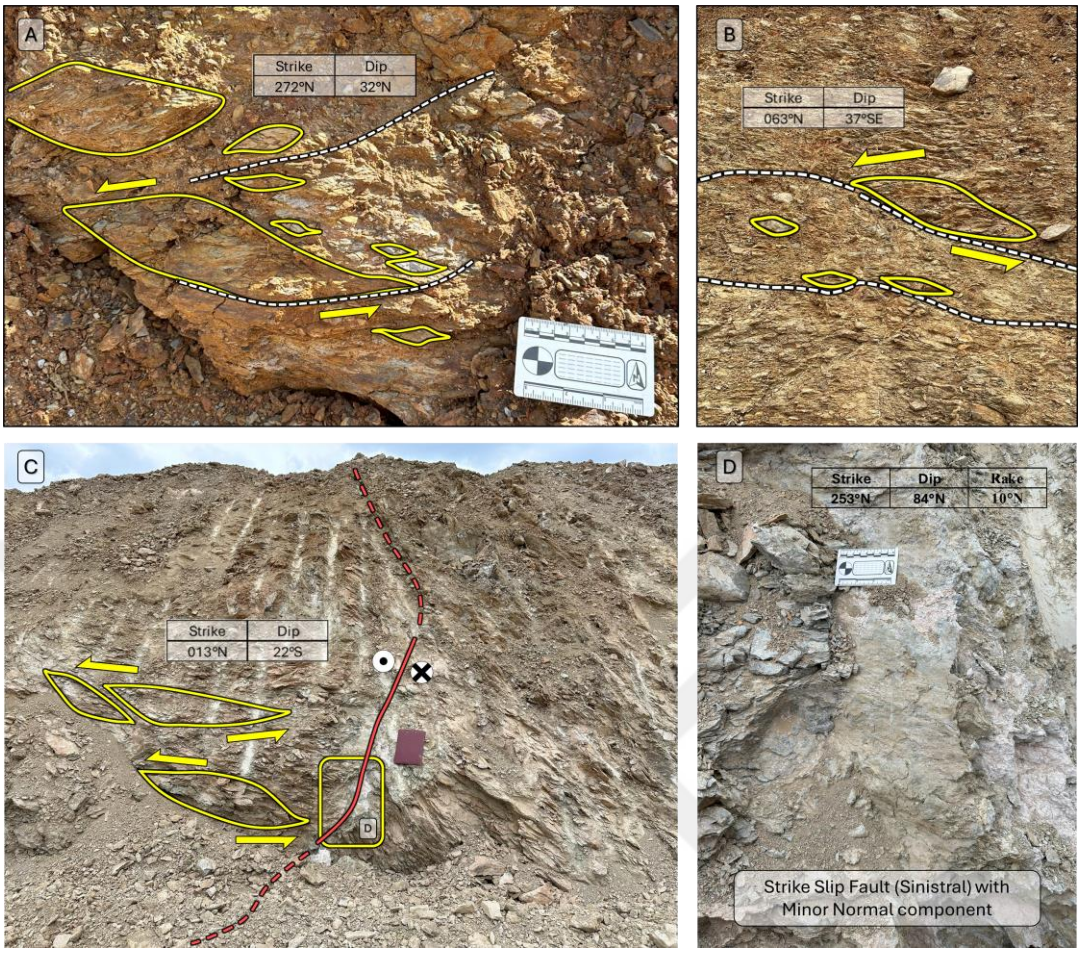

Figure 3.8. General appearance of foliation in the sheared peridotites of the Dağardı ophiolitic mélange observed in the open pit mine. Note sigma-type augen structure and C-S fabrics, indicating a top-to-the left (northeast) sense of shearing. The lower right diagram shows C-S fabrics of the foliation in the hanging-wall of a strike -slip fault.

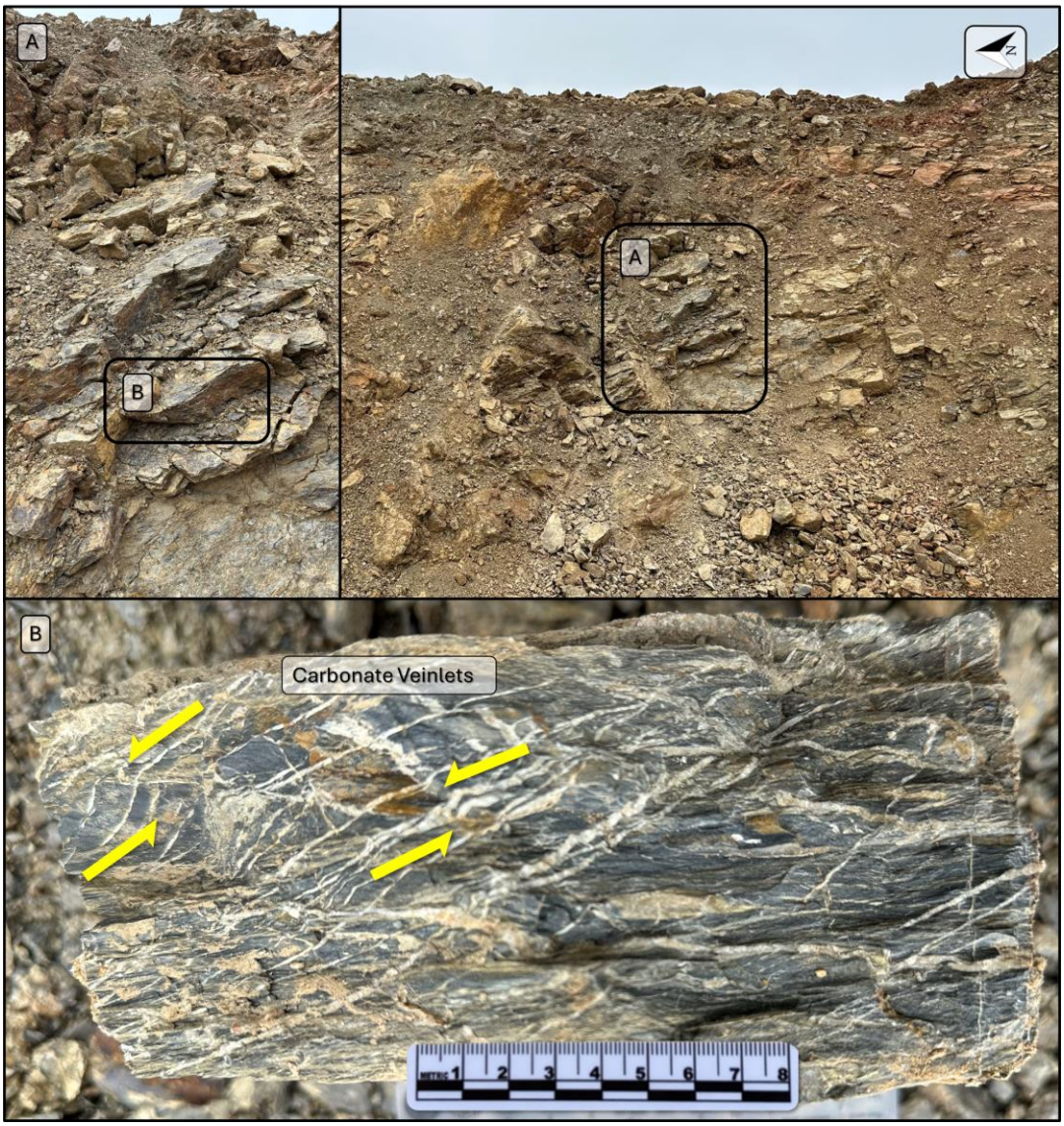

Figure 3.9. (A) field view of foliation in the sheared peridotites. (B) Field view showing carbonate veins indicating a top-to-the left (northeast) sense of shearing.

Stereoplot of the bedding data reflects two main (NW–SE, 330°N and ca. NNE–SSW, 020°N) and one relatively minor (ca. E–W) bedding orientations (Figure 3.10). Collected structural data are filtered and a total of 119 measurements are analysed by using *Dips Software*; the results confirm that mean strike orientations of the bedding planes are 320–340°N and 000–020°N, and the dip directions are NE (050°N) and ESE (120°N). The dip direction of the ca. E–W is either to north or south (Figure 3.10). The mean attitude of the foliation is 342°N/23°E.

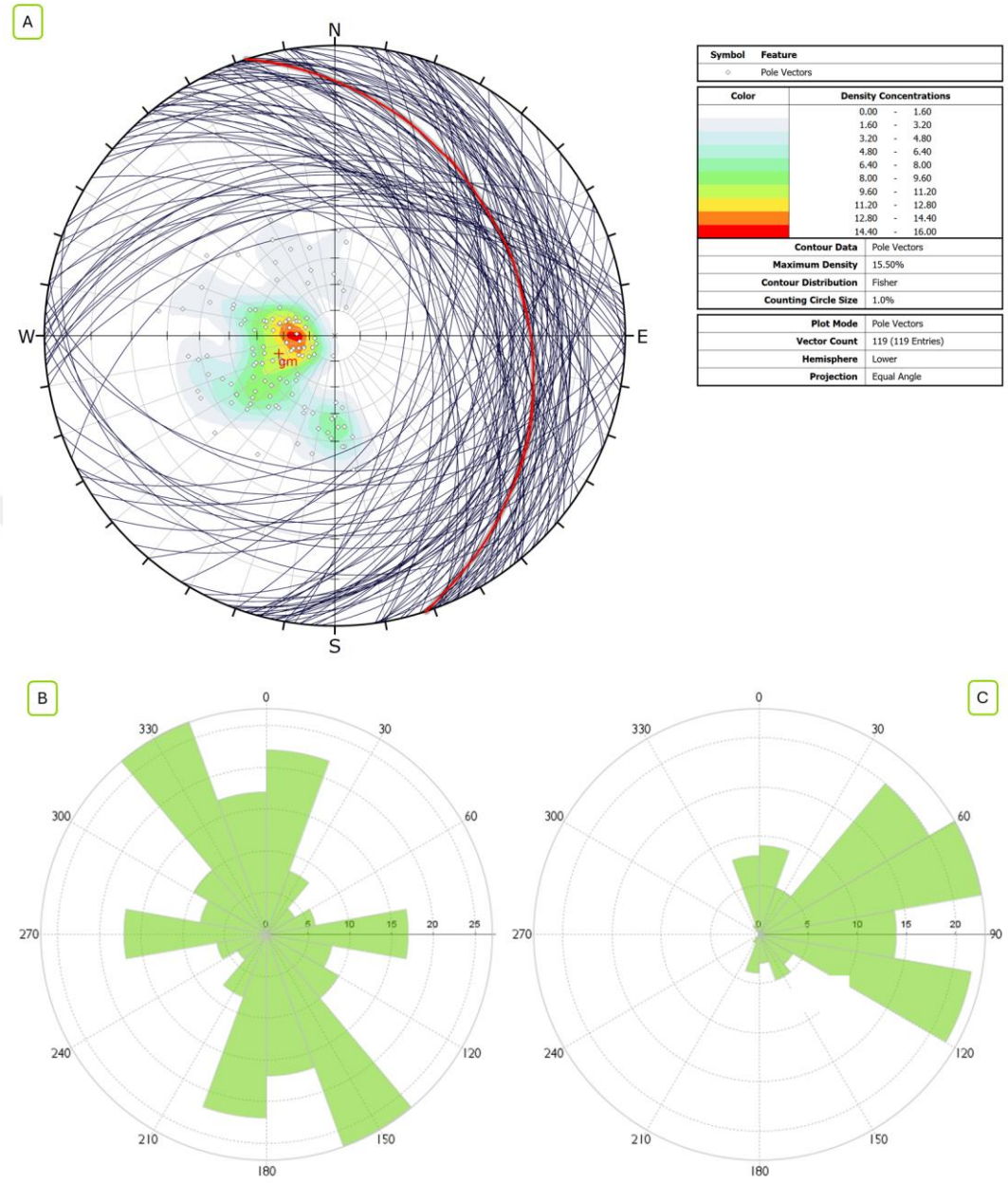

Figure 3.10. (A) Stereonet of the foliation planes, plotted as great circles, poles to planes and great circles on an equal area and contour graph of the associated poles to the planes. The diagrams illustrate single dominant foliation orientation in the Tavşan gold deposit area. Rose diagrams showing strike (B) and dip direction (C) of foliation planes.

3.3 Faults

There are four sets of systematic faults in the Tavşan gold deposit: (i) NE–SW-trending low-angle normal fault, (ii) ca. NNE–SSW-trending steeply dipping or near vertical structures, (iii) NW–SE- and (iv) ca. ENE–WSW-striking high-moderate angle faults. Collected structural data are filtered and a total of more than 105 fault measurements are analysed by using *Dips software* (Table 3.1). The common characteristics of these faults will be given in the following sub-sections.

3.3.1 Low-Angle Faults

Low-angle fault the most prominent and possibly the most important structure in the deposit area. The fault runs from southwestern corner to the northeastern corner of the mapped area (Figure 3.11). It is characterized by anastomosing structural pattern and forms the boundary of the Dağardı ophiolitic mélange in the upper plate and massive to bedded limestones of the Budağan formation. The limestones are also exposed in a tectonic window in the northeastern corner of the geological map while mélange forms a klippen in the south of the mapped area (Figure 3.11).

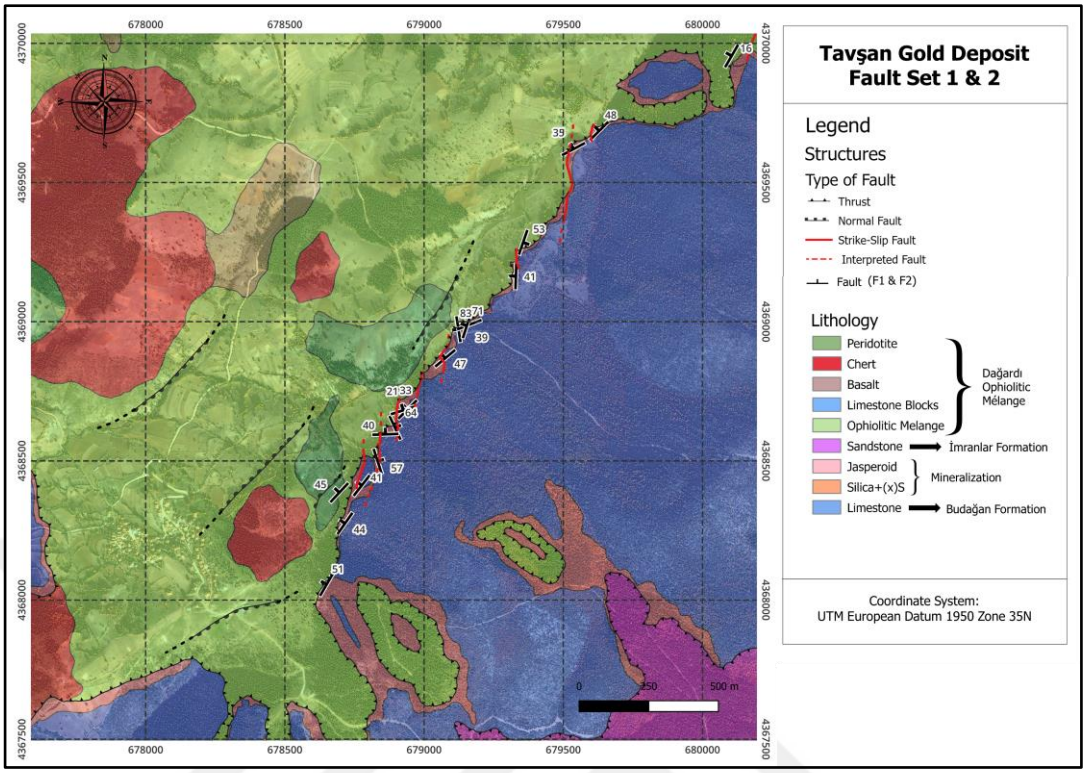

Figure 3.11. Geological map showing the location and orientation of faults in the Tavşan gold deposit.

The fault zone is marked by widespread jasperoid mineralization, which is concentrated along the low-angle fault zone (Figure 3.12 – Figure 3.13).

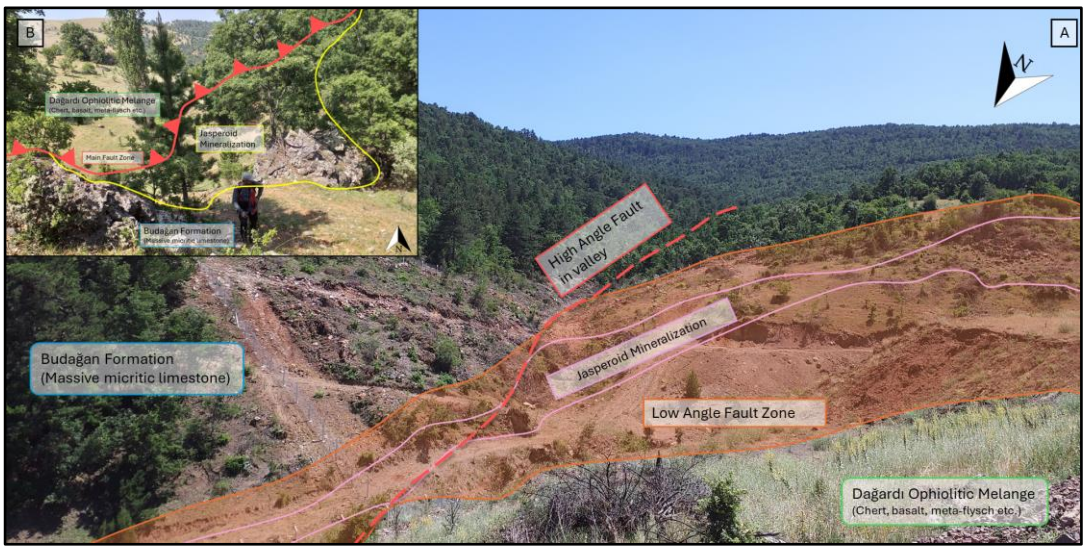

Figure 3.12. Field views from the low-angle fault zone. (B) shows the deformation zone and jasperoid mineralization associated with faulting. Note that the jasperoid

forms resistant exposures while the fault zone is characterized by an anastomosing pattern.

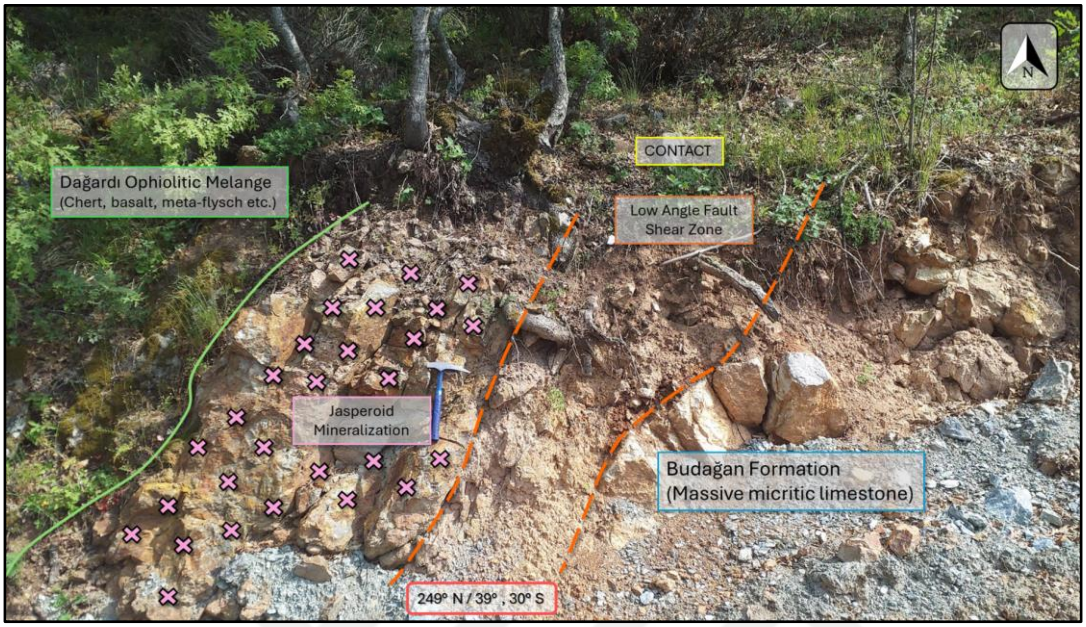

Figure 3.13. Close-up view from the low-angle fault zone between the Dağardı ophiolitic mélange in the upper plate and limestones of the Budağan formation. Note resistant jasperoid mineralization within the deformation zone of the low-angle fault.

The characteristic features of the low-angle fault and associated deformation-mineralization is well observed in the open pit area (Figure 3.14 – Figure 3.16). The fault zone is also characterized by highly-sheared and brecciated rocks, the fragments which are mostly derived from limestones, different components of the Dağardı ophiolitic mélange and jasperoid (Figure 3.14). Limonite and clay formation in the jasperoid zone are also characteristic.

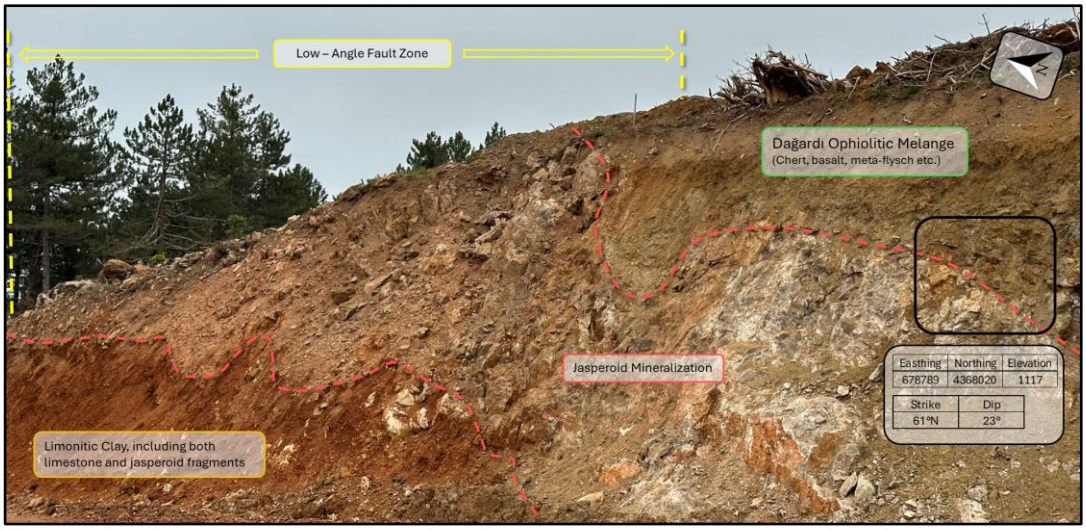

Figure 3.14. Slope cut from the open pit mine that shows the contact between mineralization and low-angle fault zone. Jasperoid zone is marked by limonitic clay; the zone also contains fragments derived from limestone, jasperoid and Dağardı ophiolitic mélange. The orientation of the fault is 061˚N / 23˚NW.

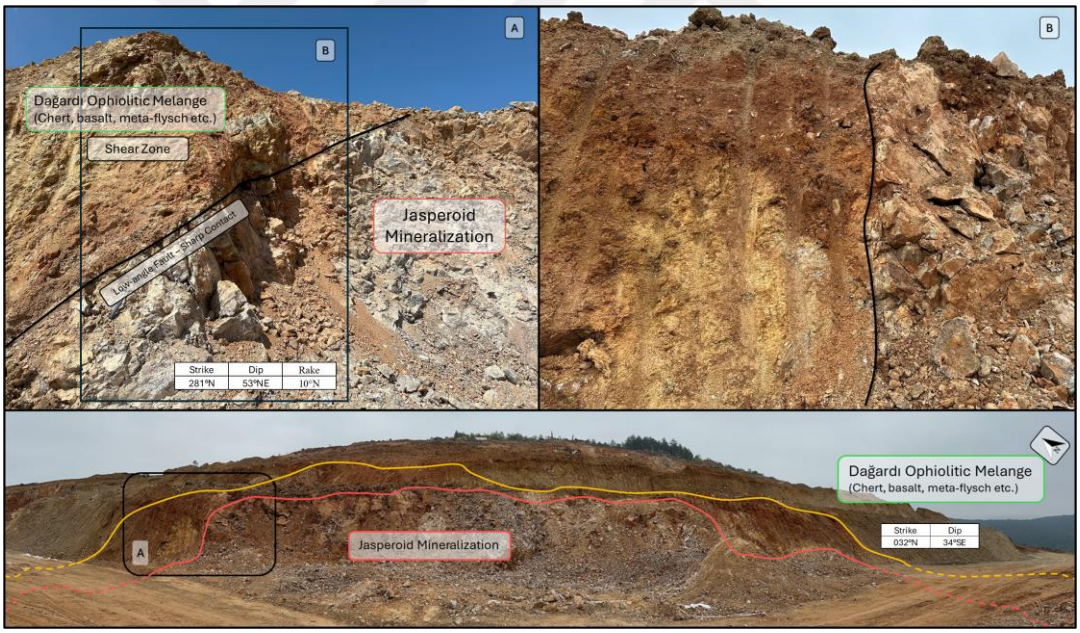

Figure 3.15. Field views showing close association of faulting and jasperoid mineralization within the ophiolitic melange. Black line represents fault surface.

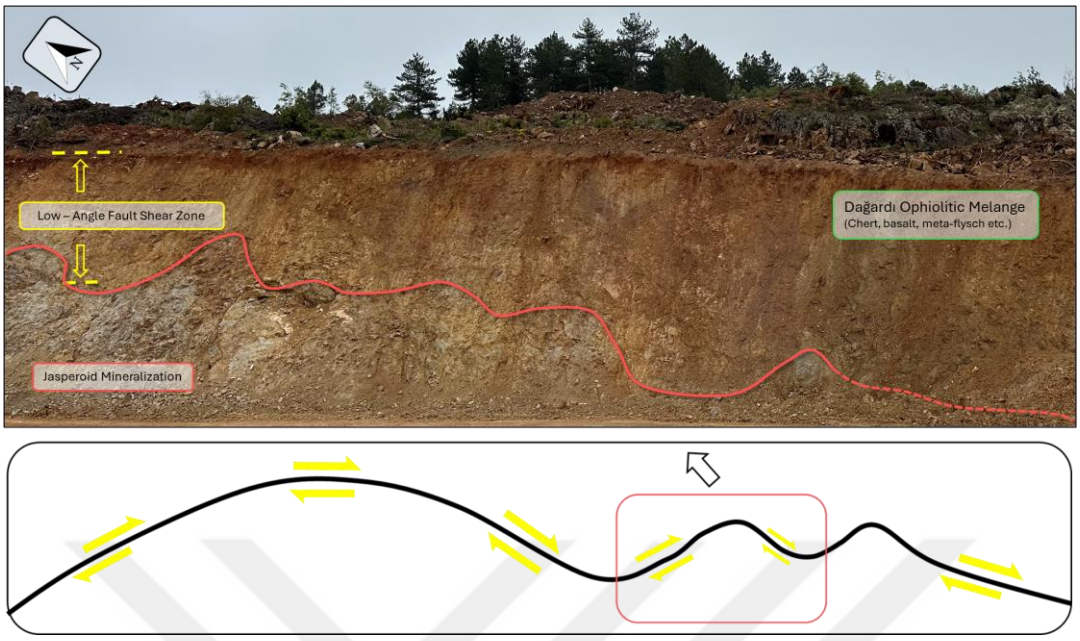

Figure 3.16. Field view and idealized sketch illustrating undulated geometry of the low-angle fault. Yellow half arrows thrust motion to SE, black arrows, the normal motion to the NW.

Along the fault zone, sheared sigma type clasts, cataclastics breccias of jasperoid and limestone unit within the oxidized clay are observed (Figure 3.17, Figure 3.18 and Figure 3.19).

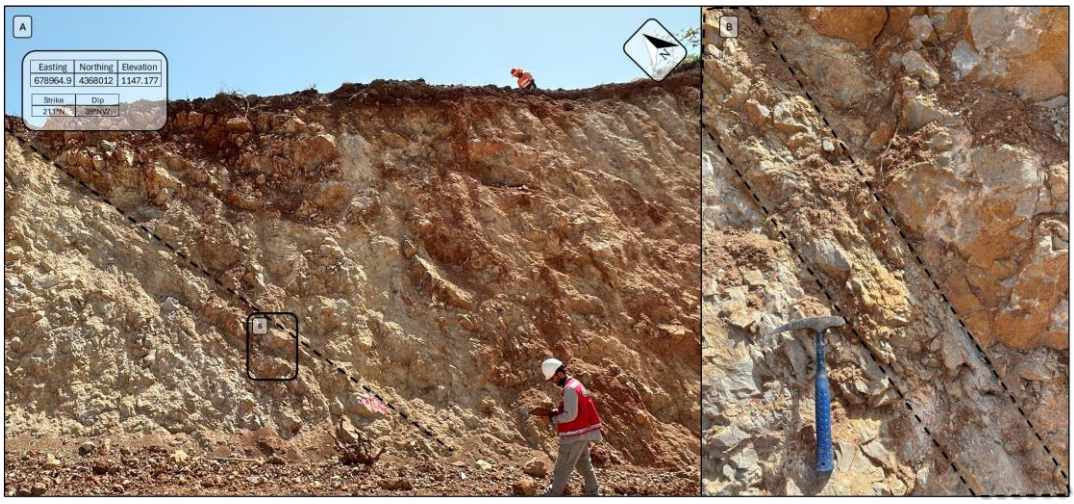

Figure 3.17. Views from a fault in the open pit mine. Note that the fault zone in close-up view (B) is marking sheared rocks and fault clay.

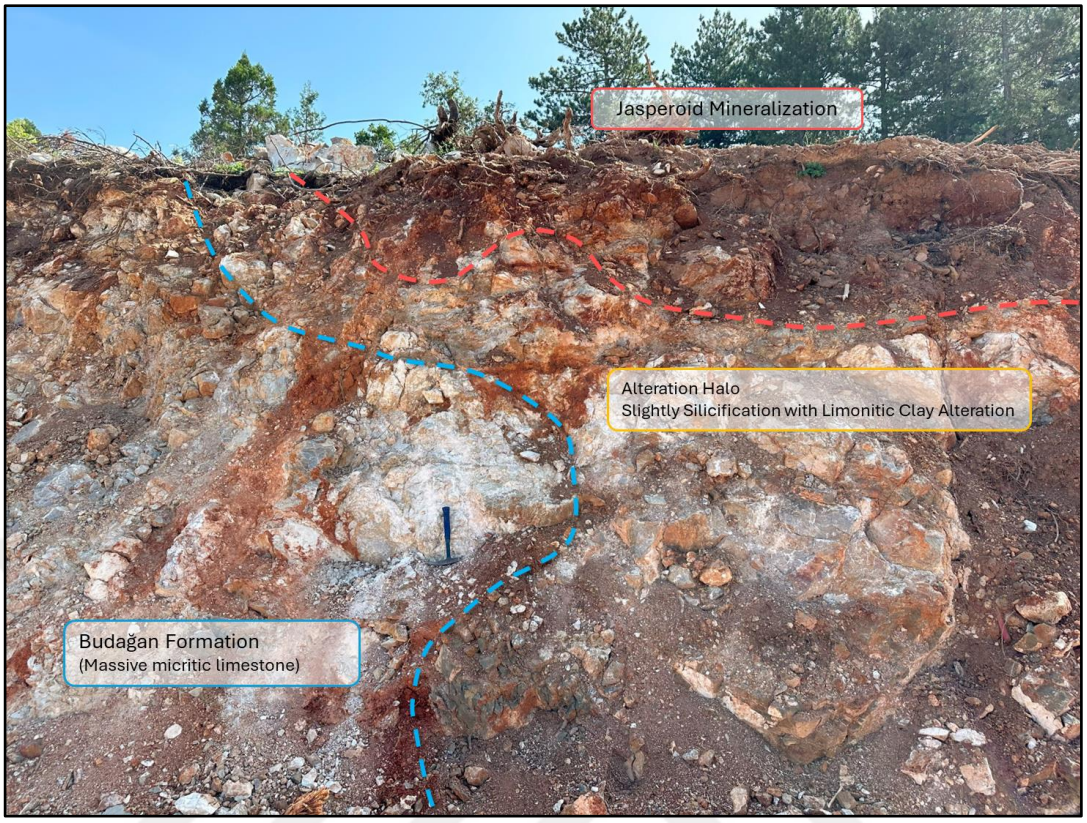

Figure 3.18. Field views showing close association of faulting, jasperoid mineralization and the Budağan Formation. Red dashed line jasperoid, blue one limestone unit.

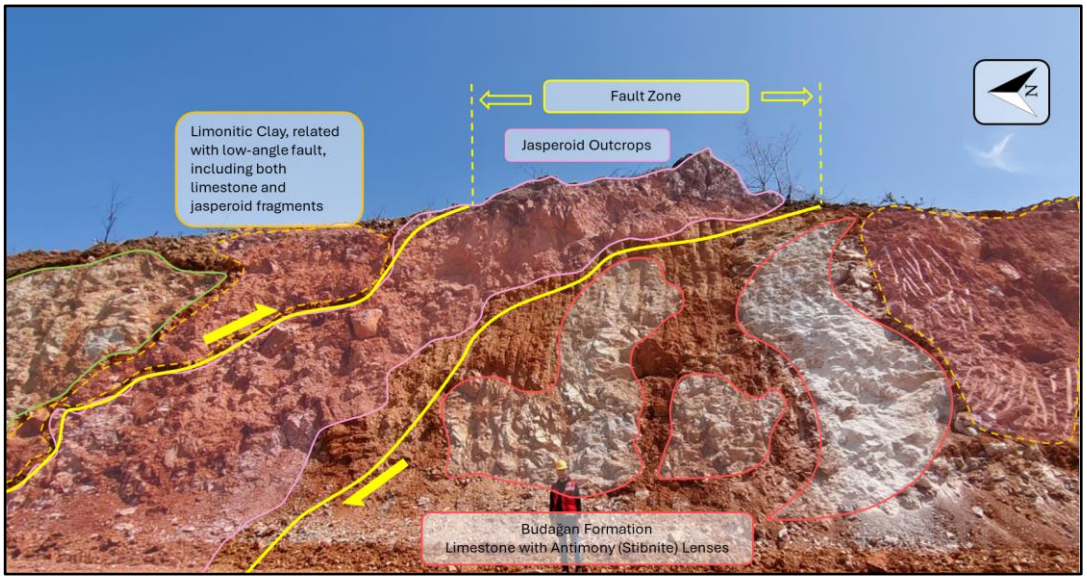

Figure 3.19. A view from the low-angle fault zone, which is interpreted to form a pathway for ore-bearing fluids. Note oxidized clay-bearing jasperoid blocks within the fault zone.

The fault measurements in the below map correspond to rectangle 1 in the location map created with clustered areas (Figure 3.1).

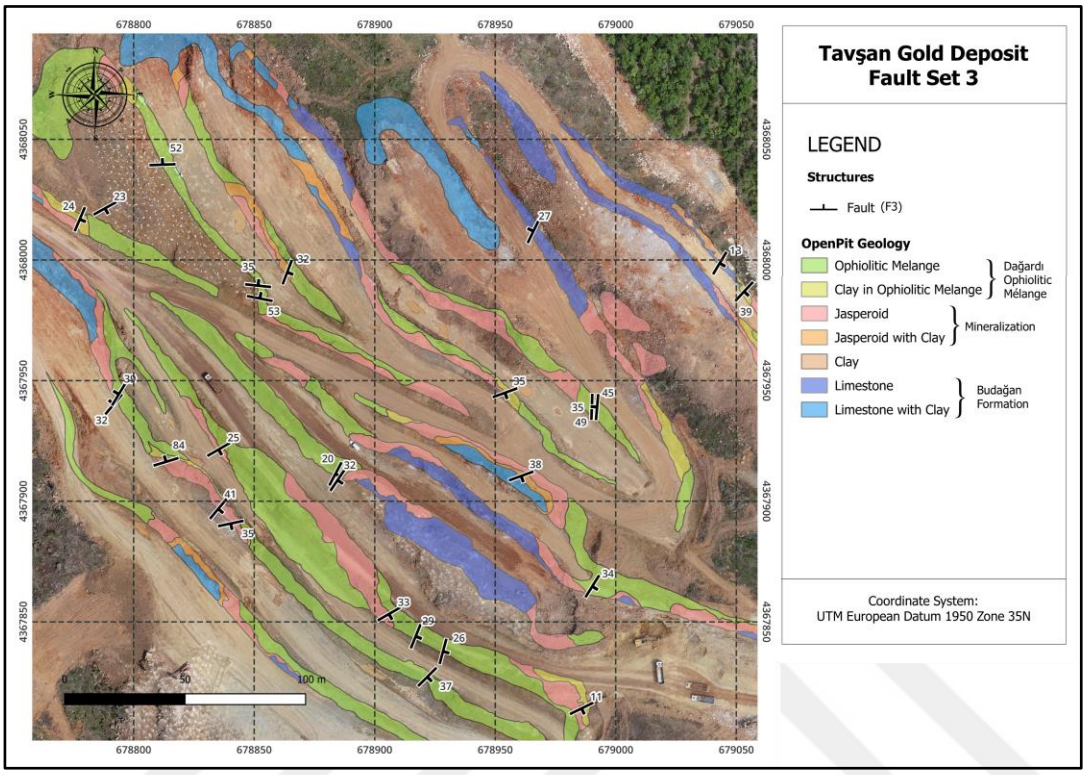

Figure 3.20. Geological map showing the location and orientation of low-angle fault measurements in the open pit mine.

Because observed low-angle fault planes, in the open pit area, dip in SE direction while those main structure cutting through the mapped area in Figure 3.11 dip NW, the measurements are analysed separately. Stereoplot of the main low-angle fault data reflects that main orientation is NE–SW where the measurements ranges between 025°N and 060°N (Figure 3.21). The data clearly shows that there are local variations in the general trend of the low-angle fault due to the existence of alternating culminations (ridges) and depressions (grooves) of variable size along their lengths. The size of undulations (corrugations) is in the order of a few centimetres to a few metres in wavelength and amplitude. Collected structural data are filtered and a total of 13 measurements are analysed by using *Dips Software*; the results confirm that mean NE–SW-trending fault planes dip in NW (310°N) direction. The mean attitude of the fault planes is 046°N/36°NW (Figure 3.21). The

corrugated nature of the low-angle fault is also well-illustrated by the fault planes observed in the open pit mine (Figure 3.22). Collected structural data (a total of 27 measurements) are analysed by using *Dips Software* and they confirm that the general trend of the low-angle fault is (E)NE–(W)SW but the dip direction is SE with some NW direction whereas it is to the NW for the main fault.

Observed low-angle fault planes are polished and ornamented by slicken lines; striations, ridge-and-grooves and gutters. The data is consistent with an oblique-slip reverse fault with minor sinistral component. The sense of shearing along the low-angle fault is top-to-the southeast and attributed to the thrust motion. There is however some evidence that this fault was reactivated and moved as a normal fault, suggesting a detachment fault motion. The tectonic significance and role of reactivation will be elaborated in the Discussion Chapter.

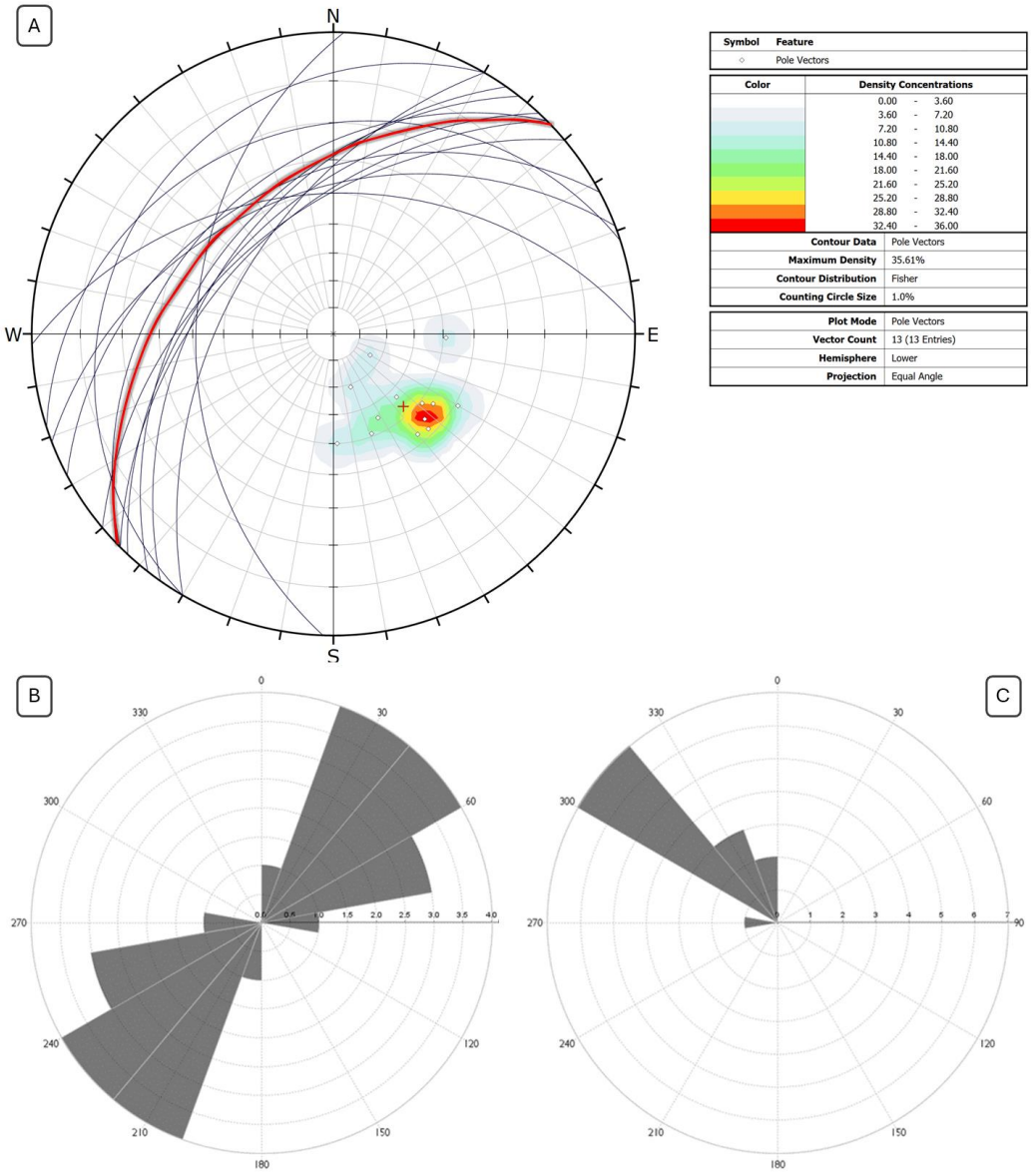

Figure 3.21. (A) Stereonet of the main low-angle fault planes, plotted as great circles, poles to planes and great circles on an equal area and contour graph of the associated poles to the planes. The diagrams illustrate single dominant fault orientation in the Tavşan gold deposit area. Rose diagrams showing strike (B) and dip direction (C) of low-angle fault planes.

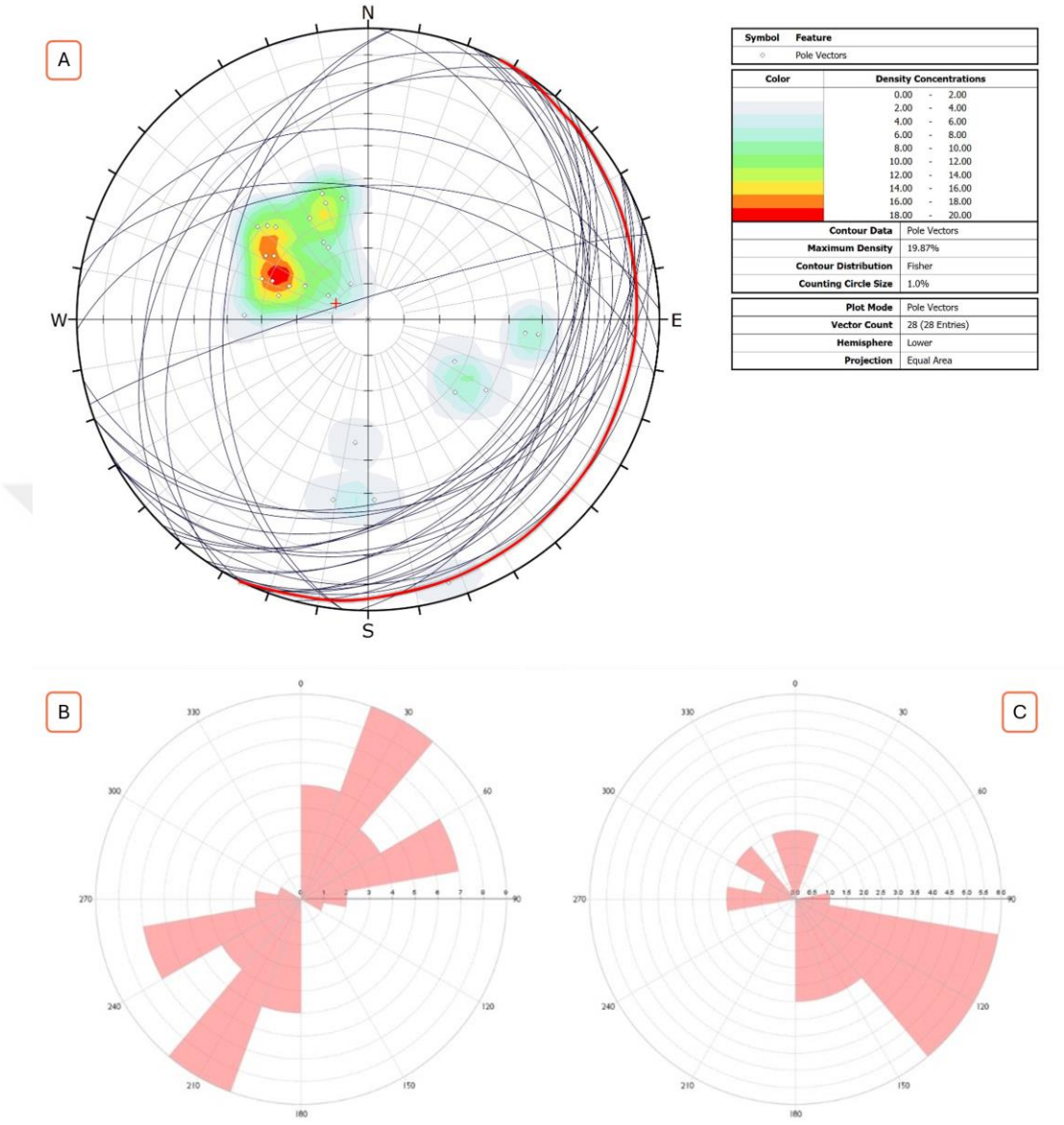

Figure 3.22. (A) Stereonet of the low-angle fault planes in the open pit mine, plotted as great circles, poles to planes and great circles on an equal area and contour graph of the associated poles to the planes. The diagrams illustrate single dominant fault orientation. Rose diagrams showing strike (B) and dip direction (C) of low-angle fault planes.

3.3.2 High-Angle Faults

Approximately NNE–SSW-trending high-angle faults are defined by juxtaposition of mélange rocks and limestones along steep structures; in map view they appear as

transfer faults offsetting the low-angle fault (Figure 3.11). They trend in 180˚N to 200˚N. Fault plane data confirm that these structures are typically oblique-slip sinistral faults with minor normal components, where rake angles range between 22˚ and 65˚ (Figure 3.23 and Figure 3.24).

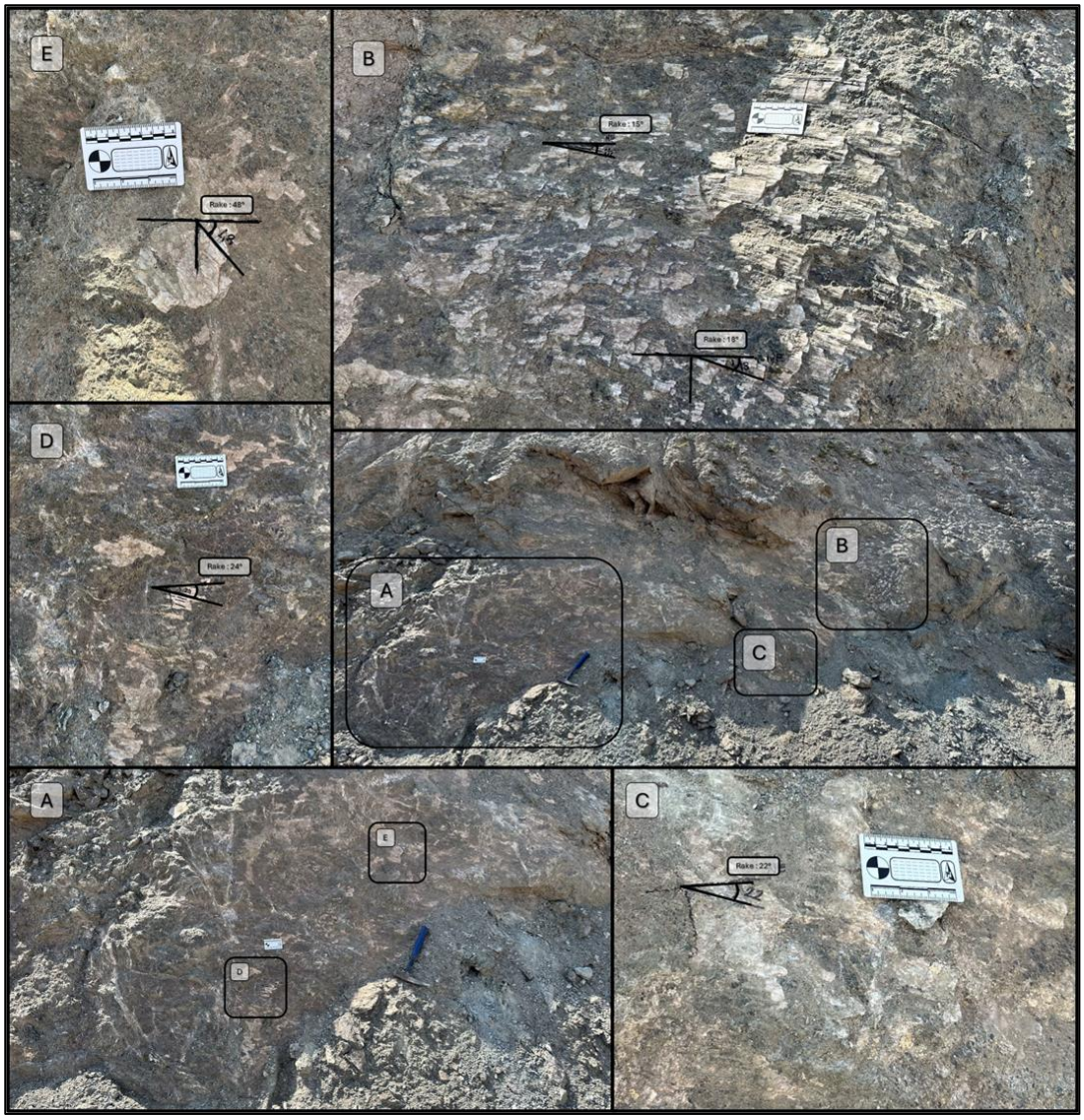

Figure 3.23. Outcrop image of high angle fault (F2) measurements. A) shows the fault surface including D and E. B) shows the chatter marks and slicken line where the measurement is taken. C) fault surface with the measurement with rake. D) closest point measurement on F2. E) fault measurement with 48˚ rake.

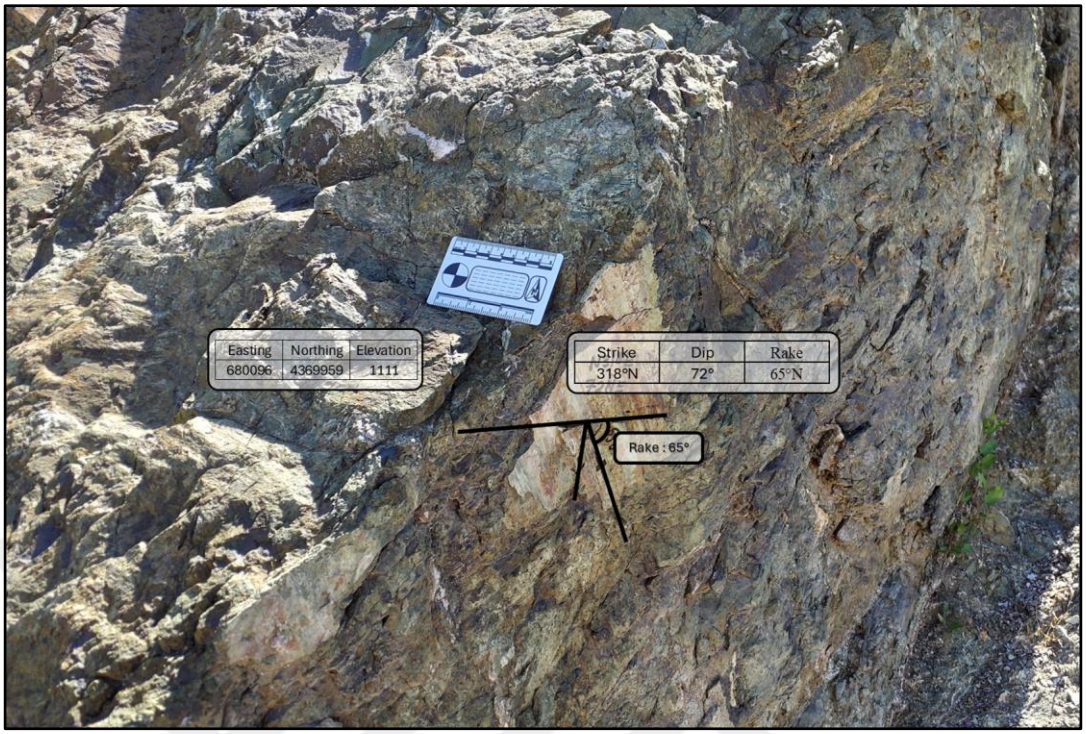

Figure 3.24. A close-up view from a NW–SE high-angle fault plane with an attitude of 318˚N/72˚E, with a rake of 65˚N. The fault is an oblique-slip normal fault with sinistral component.

Stereoplot of the main high-angle fault data reflects that main orientation is NNE–SSW where the measurements range between 000°N and 060°N (Figure 3.21). The local variation in the general trend is due to the corrugated nature of these structures. Collected structural data are filtered and a total of 12 measurements are analysed by using *Dips Software*; the results confirm that the dominant strike orientation is 000°–020°N fault planes and dip is to the ESE direction (110°N). The mean attitude of the foliation is 037°N/55°SE (Figure 3.25).

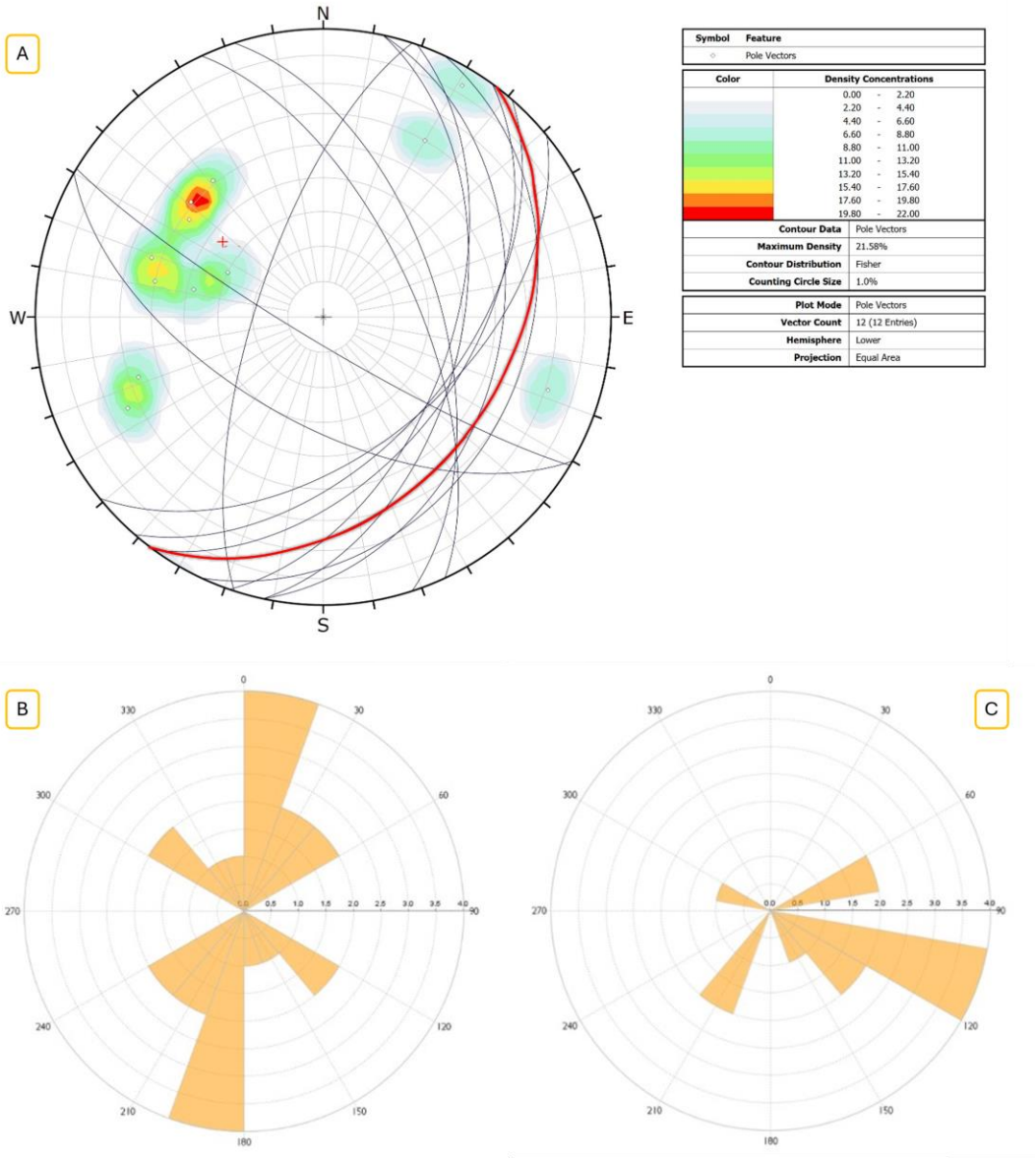

Figure 3.25 (A) Stereonet of the high-angle fault planes cutting and displacing the low-angle main fault. The planes are plotted as great circles, poles to planes and great circles on an equal area and contour graph of the associated poles to the planes. The diagrams illustrate single dominant fault orientation. Rose diagrams showing strike (B) and dip direction (C) of high-angle fault planes.

3.3.3 High to Moderate Angle Faults in Ophiolitic Mélange

These faults are mapped within Dağardı ophiolitic mélange and the limestones of the Budağan formation. They display variable strike orientations and accordingly different terminology is devised for each of them.

One these structures occur to the southeast of Örencik village and named as Örencik Fault (Figure 3.26). The fault measurements in the below map correspond to rectangle 3 in the location map created with clustered areas (Figure 3.1). It is a ENE–WSW-striking and southeast-dipping fault. Five (5) measurements have been taken from this. Where preserved, the moderately dipping fault planes are represented by polished surfaces with slickenlines. The rake angle of the slickenlines is about 27°/28° from south (Figure 3.27 and Figure 3.28). With present-day geometry, it is an oblique-slip sinistral fault with normal component. Stereoplot of the fault data reflects that mean attitude of the fault planes is 059˚N/49˚SE (Figure 3.29). The fault also potentially corresponds to discontinuity in anomalous values in the geochemical map created with arsenic (As) element values (Figure 2.38).

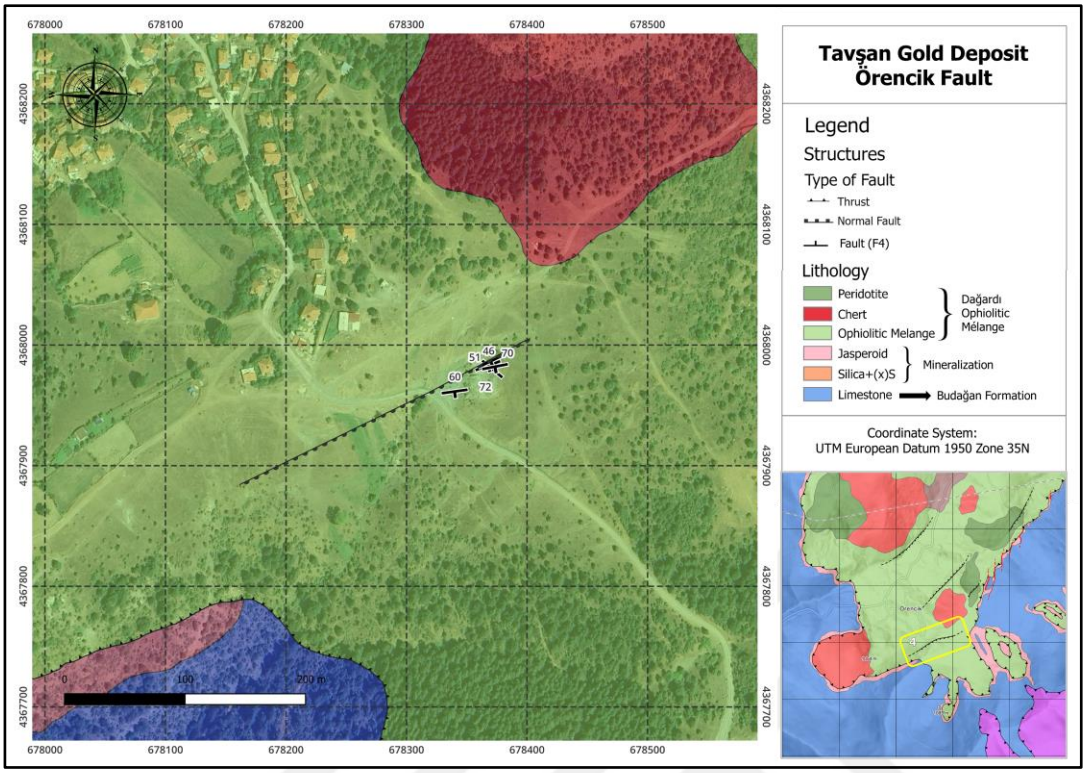

Figure 3.26. Geological map showing the location and orientation of the Örencik fault.

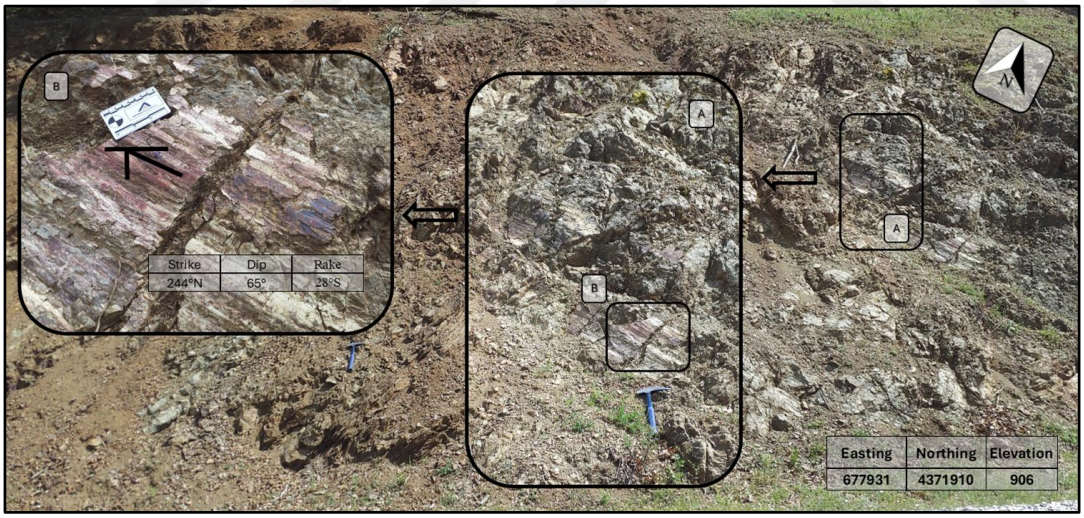

Figure 3.27. Fault measurement location and close view of fault surface in ophiolitic mélange. A) The point where the fault was measured. B) The closest point of fault measurement showing the slicken line and chatter marks with an orientation of 244˚N / 66˚W, 28˚S.

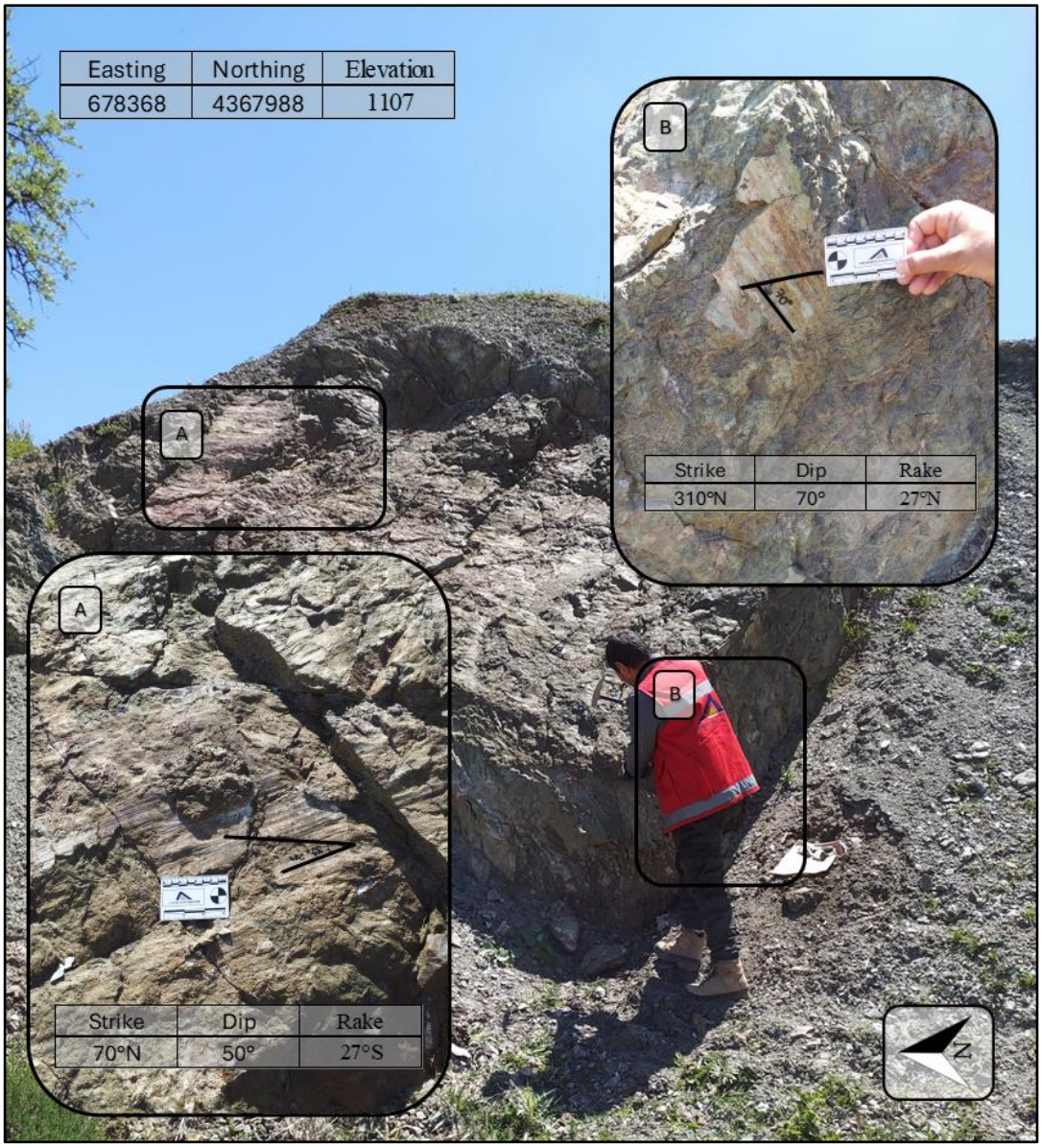

Figure 3.28. High angle fault measurement in ophiolitic mélange of As zone. A) Fault surface with chatter mark and slicken line, with an orientation of 070˚N / 50˚S, 27˚S. B) Another close image of fault surface showing different orientation of 310˚N / 70˚E, 70˚N.

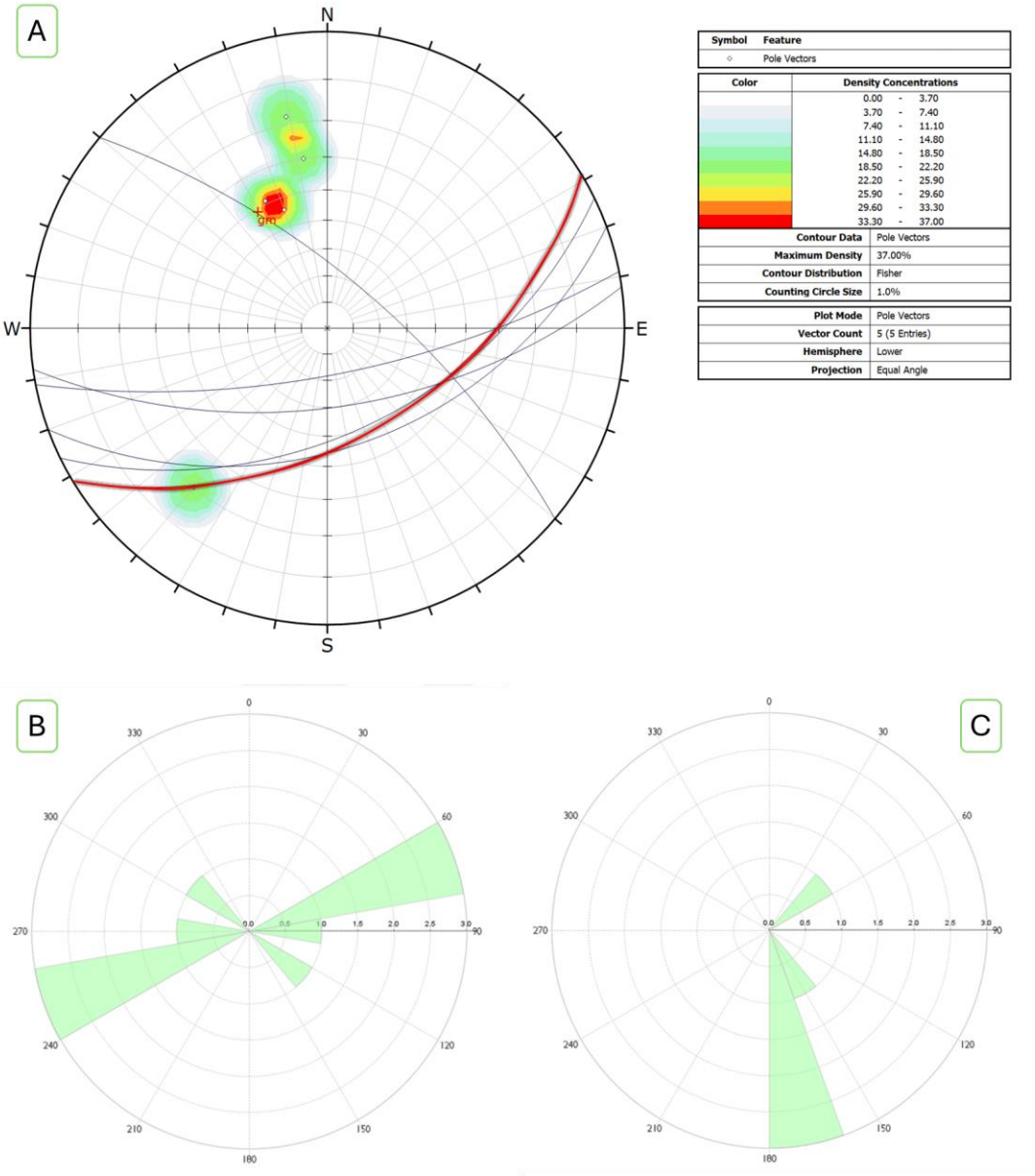

Figure 3.29. (A) Stereonet of the moderate-angle Örencik fault plane, plotted as great circles, poles to planes and great circles on an equal area and contour graph of the associated poles to the planes. The diagrams illustrate single dominant fault orientation. Rose diagrams showing strike (B) and dip direction (C) of moderate-angle fault planes.

Similarly, several high-angle faults with differing attitudes are mapped within the Dağardı ophiolitic mélange (Figure 3.30). Kinematic indicators, such as C-S fabrics, sigma-type clasts and drag folds, are common within the deformation zone (shear zones), providing valuable insights into the kinematics of faulting (Figure 3.31 –

Figure 3.34). Where preserved, the fault planes are represented by polished surfaces with slickenlines. The rake angle of the slickenlines ranges between 62° and 84° from north (Figure 3.31 and Figure 3.33) and suggest oblique-slip normal motion with sinistral/dextral component (Figure 3.31). Most structures display normal component with well-developed graben and host structures (Figure 3.32 – Figure 3.34). Twenty-seven (27) fault measurements were collected from these structures and are plotted in a stereonet (Figure 3.35). The faults mainly strike in (E)NE–(W)SW-direction but the dip direction is variable.

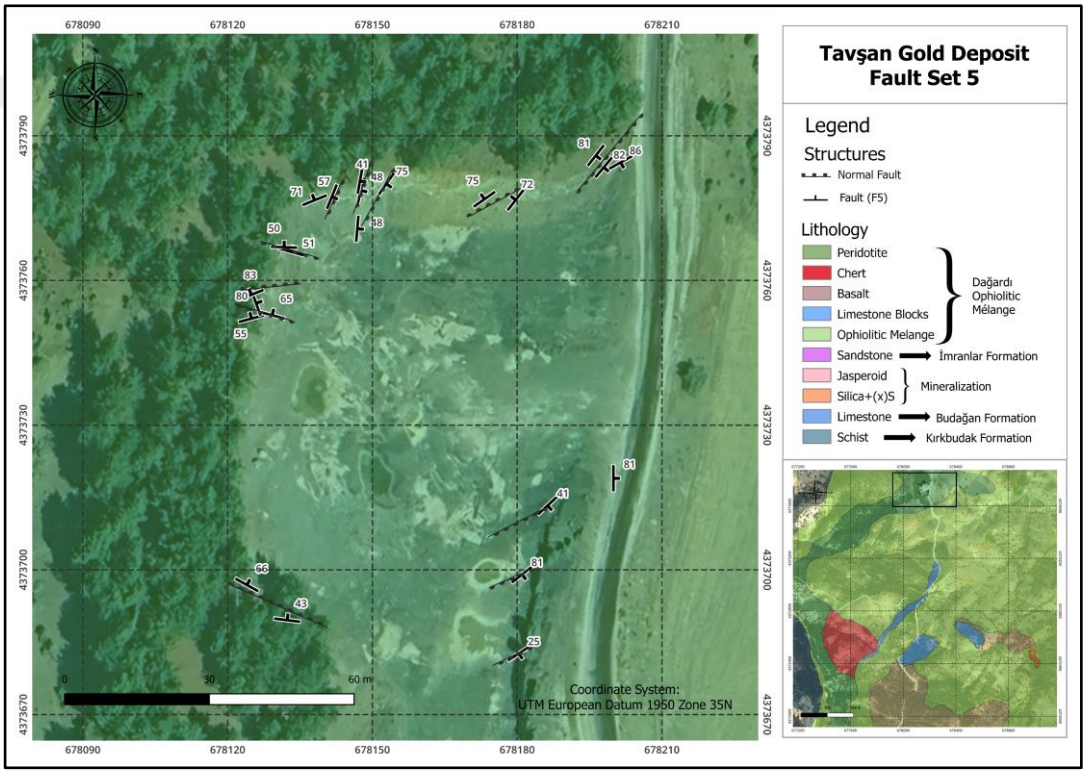

Figure 3.30. Geological map showing the location and orientation of mapped faults within the Dağardı ophiolitic mélange.

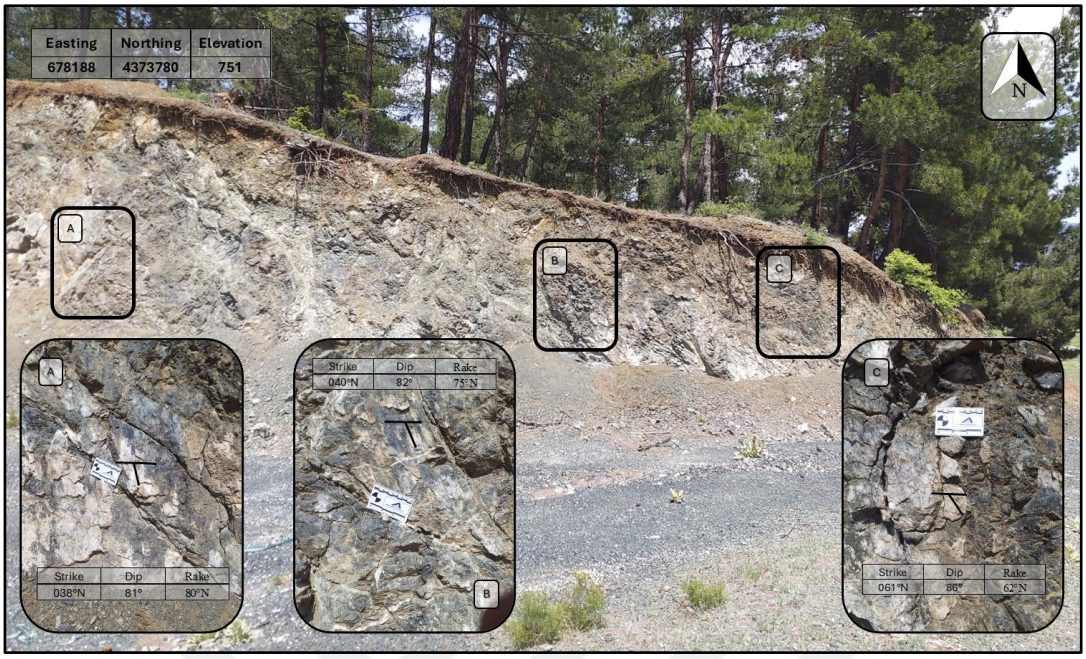

Figure 3.31. Views from high-angle fault observed within the Dağardı ophiolitic mélange. Note that the faults have dominant normal component.

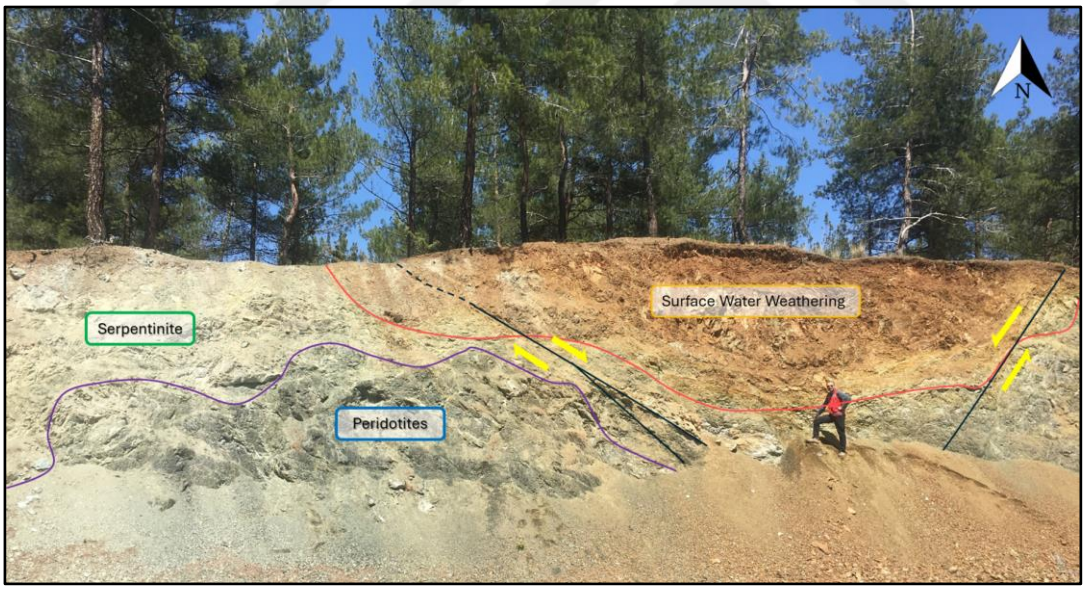

Figure 3.32. Field view from conjugate faults with normal component and a graben structure forming in-between.

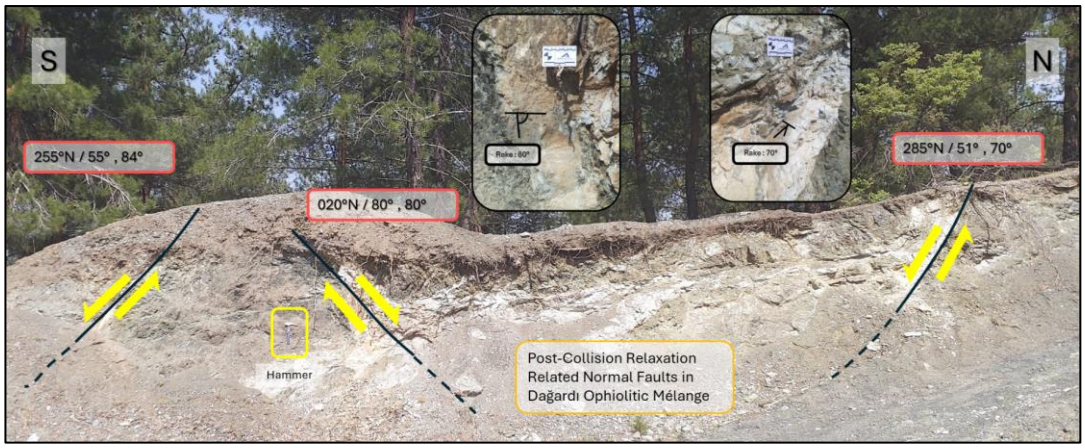

Figure 3.33. Field view from conjugate faults with normal component within the Dağardı ophiolitic mélange. Note that the fault planes are ornamented by striations with large rake angles, attesting a dominant normal faulting. The horst-and-graben structure is evident.

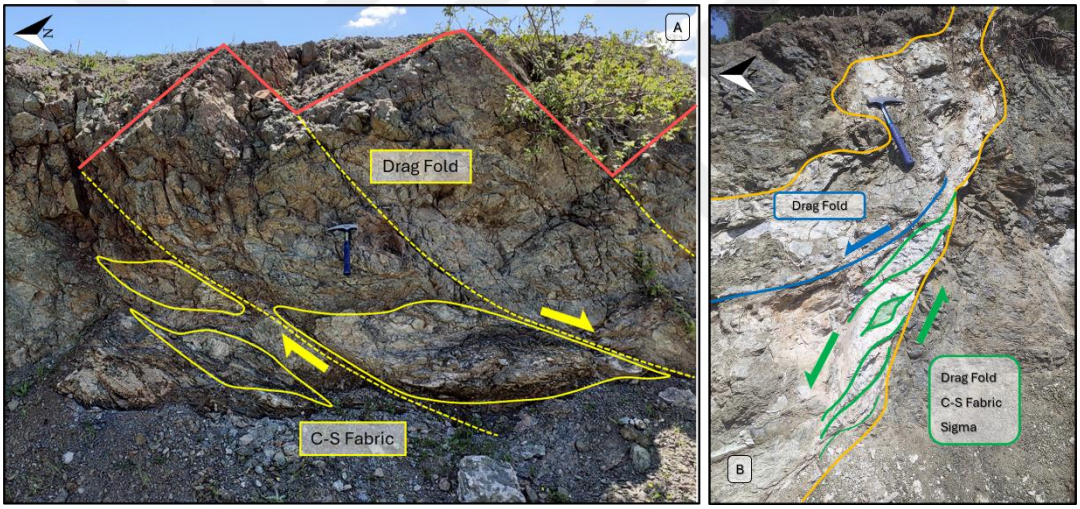

Figure 3.34. (A) A field view from pair of listric faults with normal component. Note the sigma-type structures confirm normal component of motion. (B) A view from a shear zone within serpentinized ultramafics of the Dağardı ophiolitic mélange. The C-S fabrics, sigma-type clasts and drag fold confirm normal component of the motion.

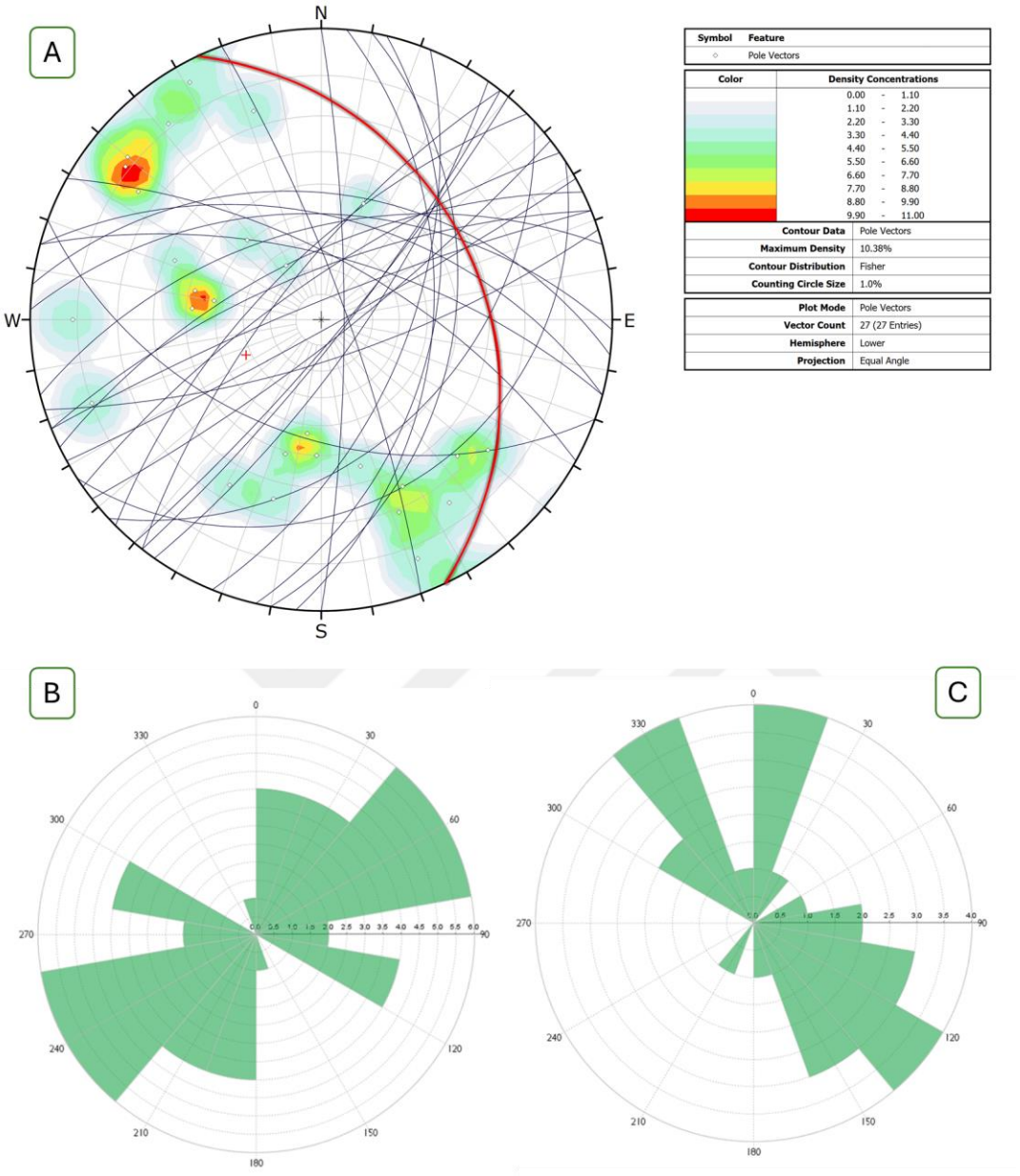

Figure 3.35. (A) Stereonet of the high-angle faults mapped within the Dağardı ophiolitic mélange, plotted as great circles, poles to planes and great circles on an equal area and contour graph of the associated poles to the planes. The diagrams illustrate single dominant fault orientation. Rose diagrams showing strike (B) and dip direction (C) of high-angle fault planes.

High-angle faults also occur within the limestones of the Budağan formation away from the mineralized zone (Figure 3.36). Measurements are focused on rectangle 4 in the location map created with clustered areas (Figure 3.1). The fault planes are

polished and ornamented by well-developed striations (Figure 3.37 and Figure 3.38). The measured 6 (six) fault planes are also plotted on a stereonet and a rose diagram (Figure 3.39). The dominant strike of the fault planes is NW–SE with dip direction is either NE by 80˚ or SW by 60˚.

Because there is no observed mineralization along these structures, they are interpreted as post-mineralizing faults.

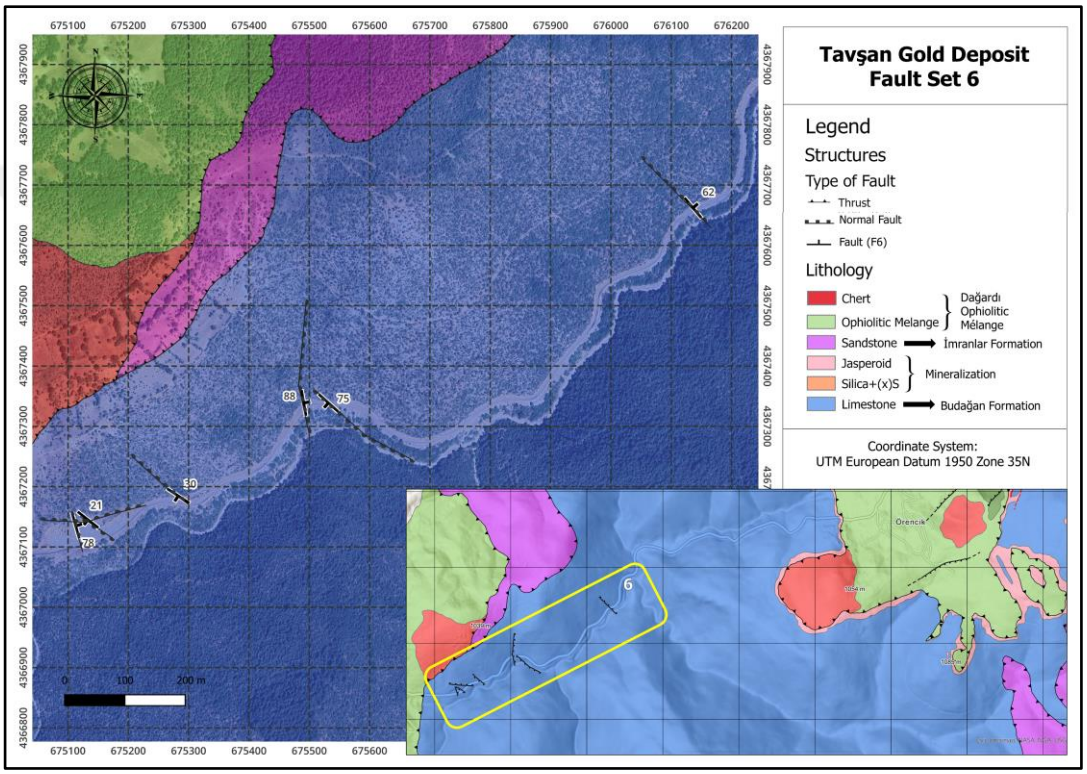

Figure 3.36. Geological map showing the location and orientation high-angle faults mapped within the limestones of the Budağan formation.

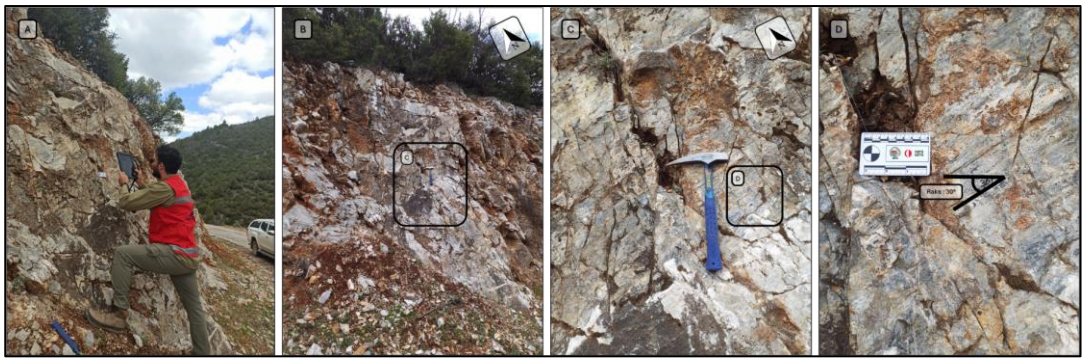

Figure 3.37. Field views from the high-angle faults mapped within the limestones of the Budağan formation. (A) General view of the outcrop while (B –D) are close-up views.

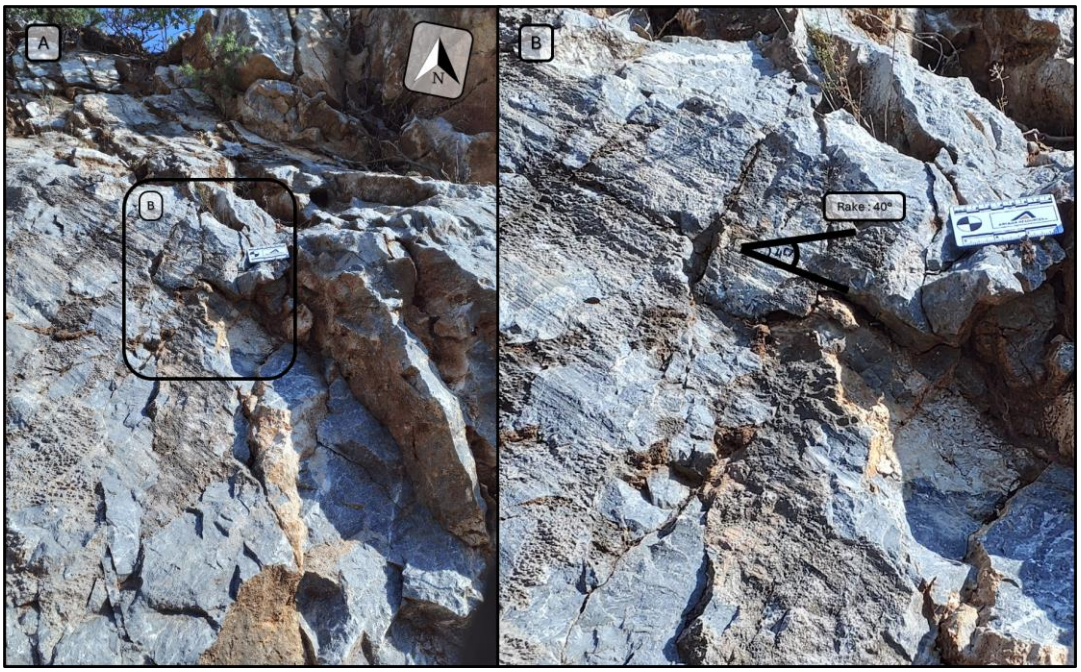

Figure 3.38. General (A) and close-up (B) views form a striated fault plane in the limestones of the Budağan formation.

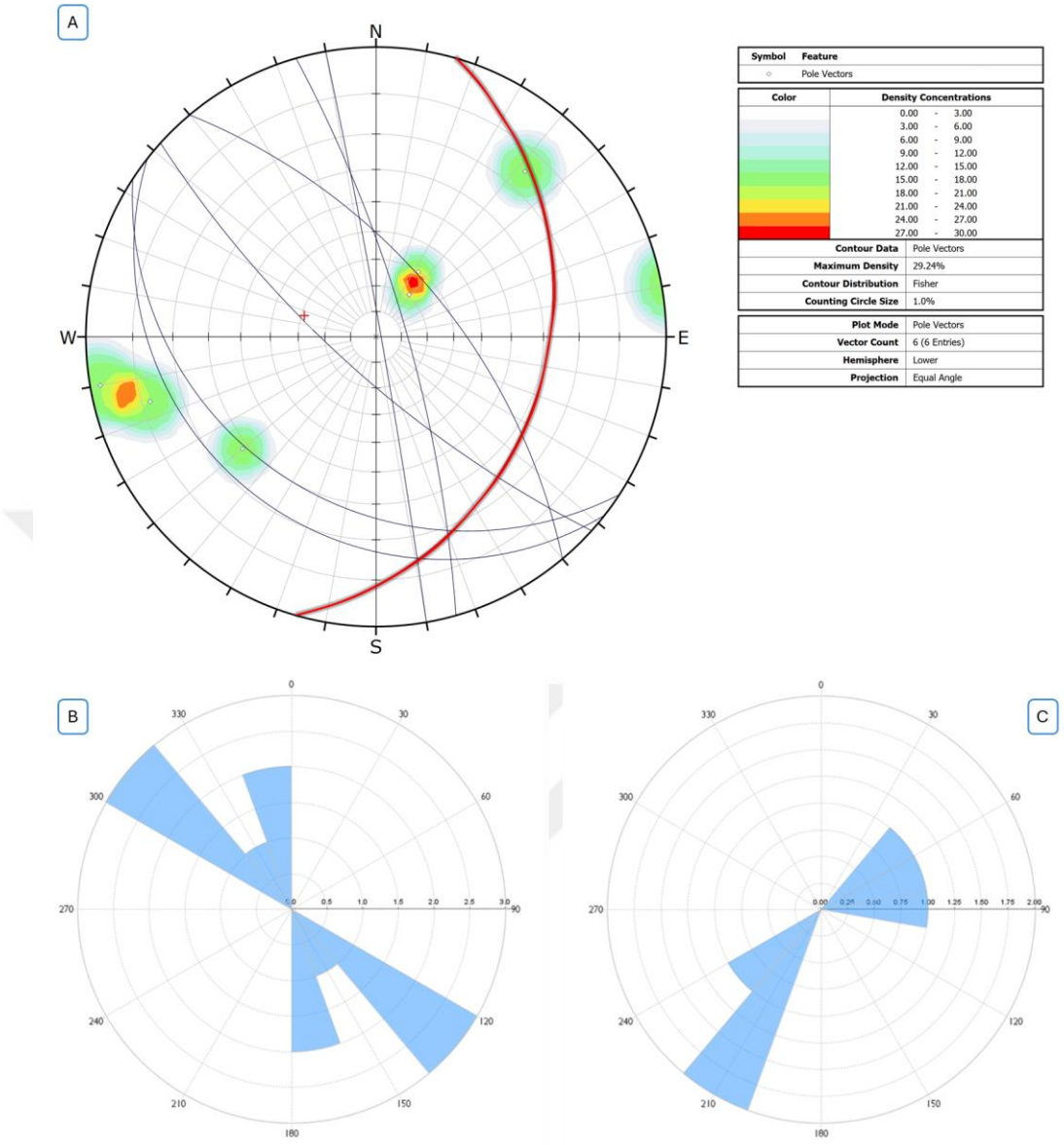

Figure 3.39. (A) Stereonet of the high-angle faults mapped within the limestones of the Budağan formation, plotted as great circles, poles to planes and great circles on an equal area and contour graph of the associated poles to the planes. The diagrams illustrate single dominant fault orientation. Rose diagrams showing strike (B) and dip direction (C) of high-angle fault planes.

3.3.4 Faulting and Mineralization: Core Sample Review

The mechanisms responsible for the formation of the Tavşan gold mineralization were investigated through field observations, fieldwork, and the examination of drill

core samples. The observations revealed that structural control plays a significant role in the mineralization process, suggesting multiple phases of ore mineralization.

The entire stratigraphic sequence can be observed in the diamond drill cores. In Figure 3.40, the core sample shows ophiolite between depths of 40.00 to 41.00 meters. A fault zone is present between 40.00 and 42.00 meters, characterized by fault gouge and breccias within the damage zone of a low-angle fault. From 42.00 to 44.00 meters, massive jasperoid is identified, while polymictic breccia is encountered between 44.00 and 44.70 meters. The jasperoid fragments, or breccias, found within the mineralization zone indicate the presence of a secondary sub-phase or episodes of mineralization. This is evident because the massive jasperoid, which is primary phase of mineralization, has undergone brecciation during a secondary phase and can now be observed within the polymictic hydrothermal breccia (Figure 3.40). Between 44.70 to 46.90 meters, a jasperoid carbonate breccia is observed, which is cross-cut by quartz carbonate veinlets. The remaining core samples represent limestone.

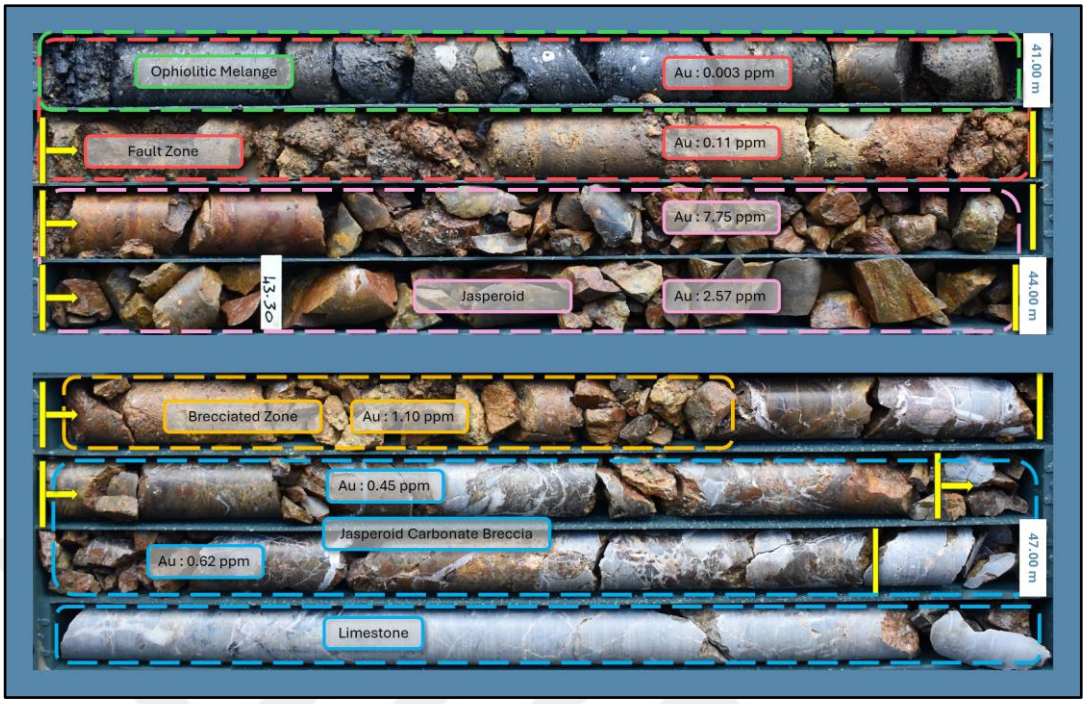

Figure 3.40. Core samples showing lithologies and their relations with mineralization and faults. Au (ppm) values are highlighted with yellow arrows for sampling intervals.

Observations of drill core samples revealed jasperoid mineralization within limestone blocks. Within the fault zone, the rocks are intensely deformed zones; ongoing cataclasis resulted in grain size reduction and consequently the formation of an impermeable clay-altered ophiolite unit. It is observed that fractures and weakness zone formed pathways for fluids to penetrate into the limestone unit. Therefore, jasperoid occurs within the limestone and, in other instances, clay infill or calcite, are observed in the drill core samples. Notably, dark brown coloured clay infill was clearly observed near the contact between jasperoid and limestone (Figure 3.41).

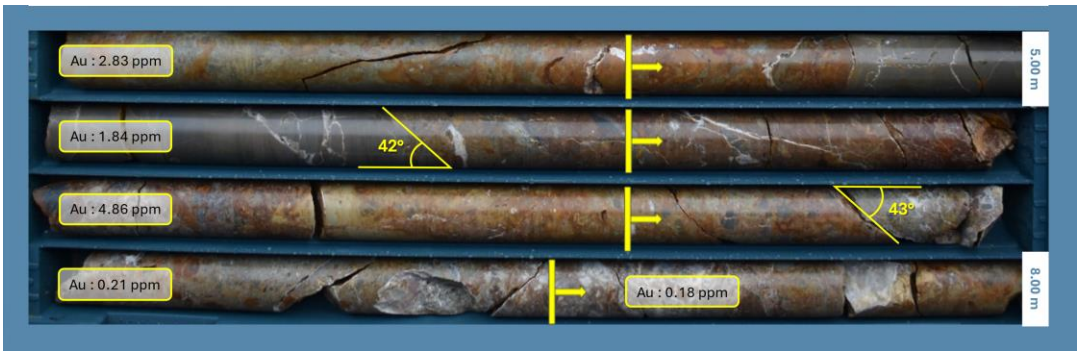

Figure 3.41. Potential high-angle faulting related jasperoid mineralization with 3.10 ppm Au. The beta angle of jasperoid contact is shown with yellow colour.

Additionally, brecciated zones were observed within limestone during fieldwork and the examination of drill core samples (Figure 3.42). These brecciated zones are composed of jasperoid and silicified limestone breccias (Figure 3.43). High Au (ppm) values, 3.48 ppm, belongs to the polymictic hydrothermal brecciated jasperoid interval (Figure 3.42).

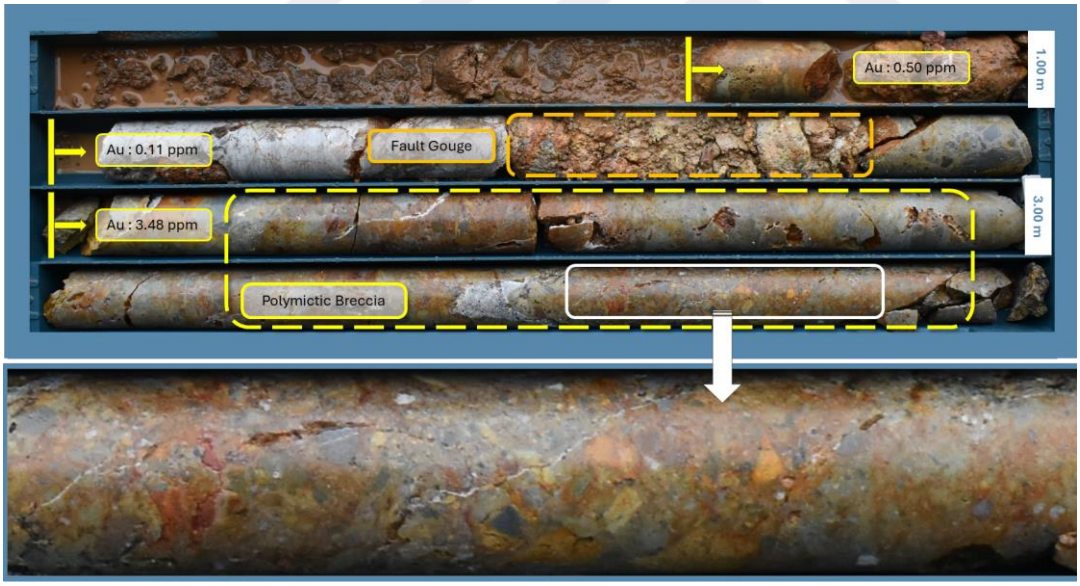

Figure 3.42. Core samples that show the polymictic hydrothermal breccia.

Within the limestone, colloform-banded silica is observed. In this zone, high-grade mineralization, around 3.85 ppm Au, is observed in core samples (Figure 3.43). Then they should have precipitated under the low-T conditions and from silica

supersaturated fluids. These silicas are potential carriers of metals into the ore system.

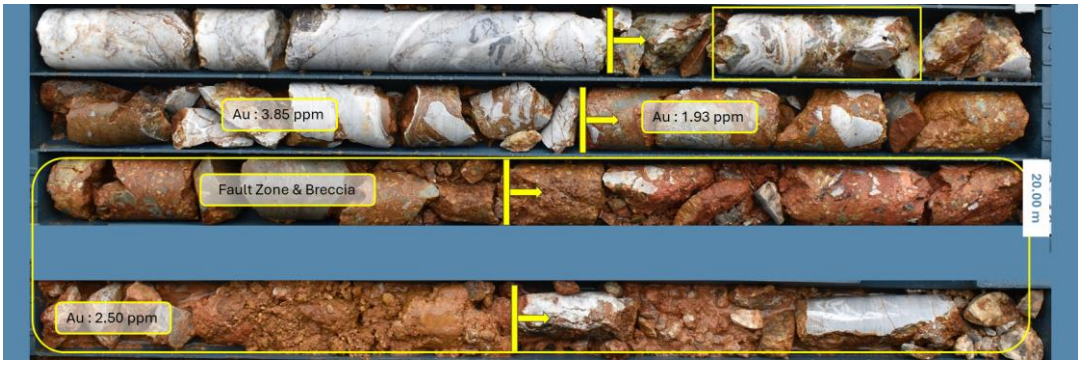

Figure 3.43. Core samples showing a void filled by reddish clay and collapse breccia.

The presence of stibnite in the field suggests a last phase of mineralization in the system. Stibnite is found in zones associated with quartz or quartz-carbonate veins, and the cross-cutting relationship of quartz veins with jasperoid indicates that the quartz-stibnite-carbonate mineralization occurred after the jasperoid mineralization. Example of this relation is shown in the core samples in below Figure 3.44.

Karstic cavities are observed within the open pit slopes and collapse breccia of jasperoid, and limestones are cross-cut by quartz carbonate veins (Figure 3.46).

The impermeable clay layer formed by the sheared ophiolite unit facilitated the deposition of stibnite within the voids in the limestone, forming lens-shaped deposits (Figure 3.47).

Hole ID	From	To	Interval	Au (ppm)	Sb (ppm)
TAV-D23-21	12.2	13.4	1.2	0.34	1176.26
	13.4	14.4	1	0.24	1199.74
	14.4	15.3	0.9	0.62	2629.53

Quartz Carbonate Epithermal Veins
- *Jasperoid Breccias*
- *Last phase of antimony bearing mineralization*

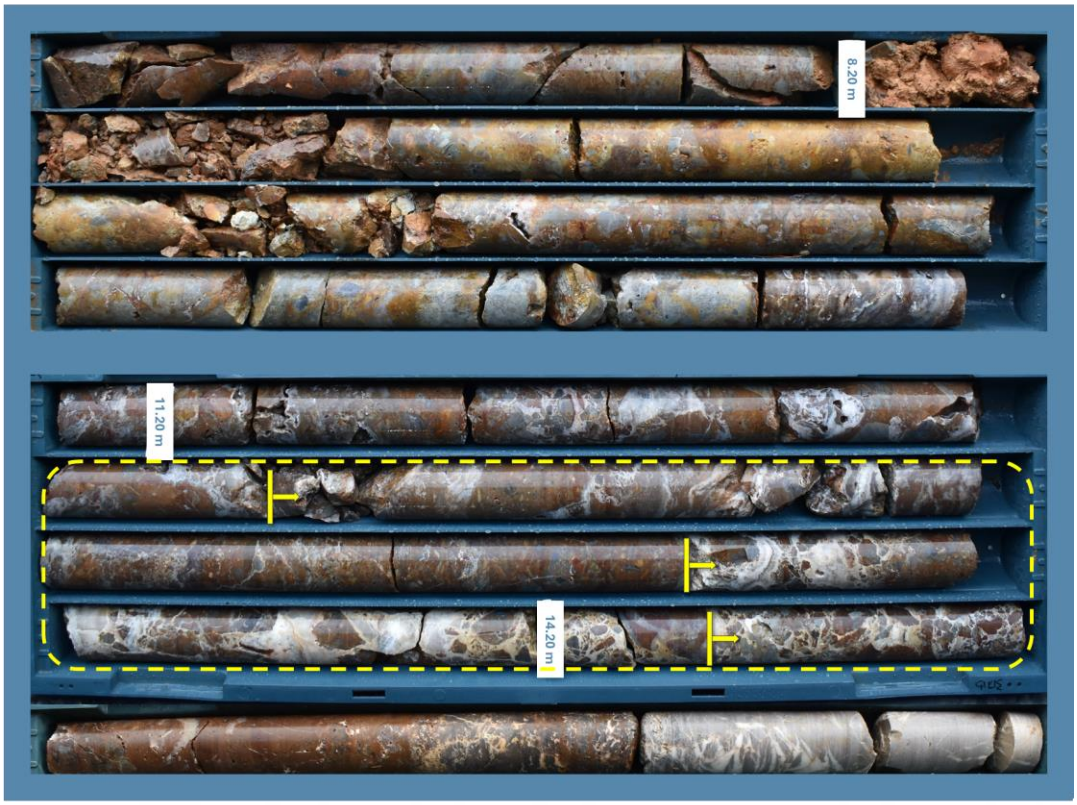

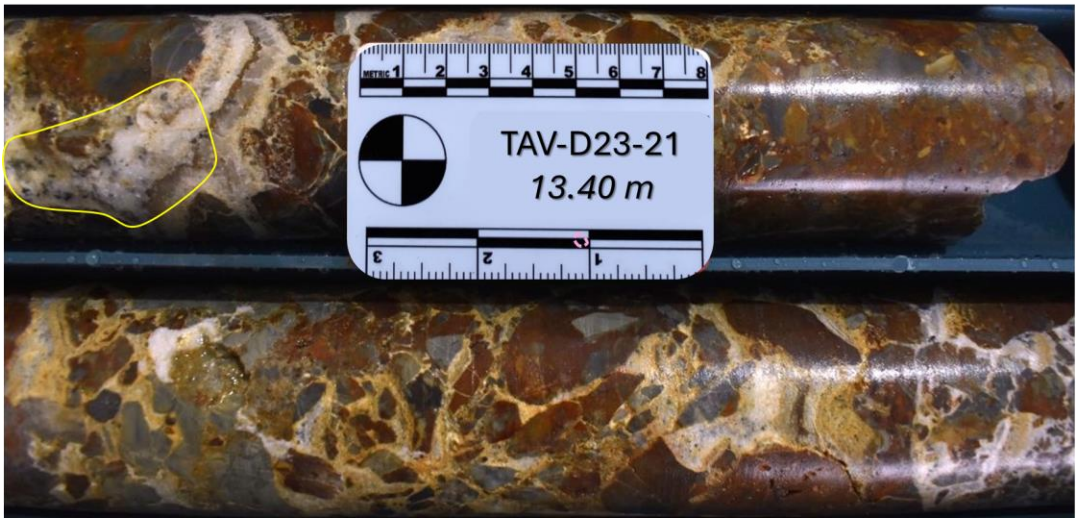

Figure 3.44. Core samples show the cross-cutting relationship between jasperoid mineralization and quartz-carbonate veins. The area indicated with yellow dash line consist of intense quartz carbonate veins and stibnite. The assay value of this zone is given above table, which includes high antimony values.

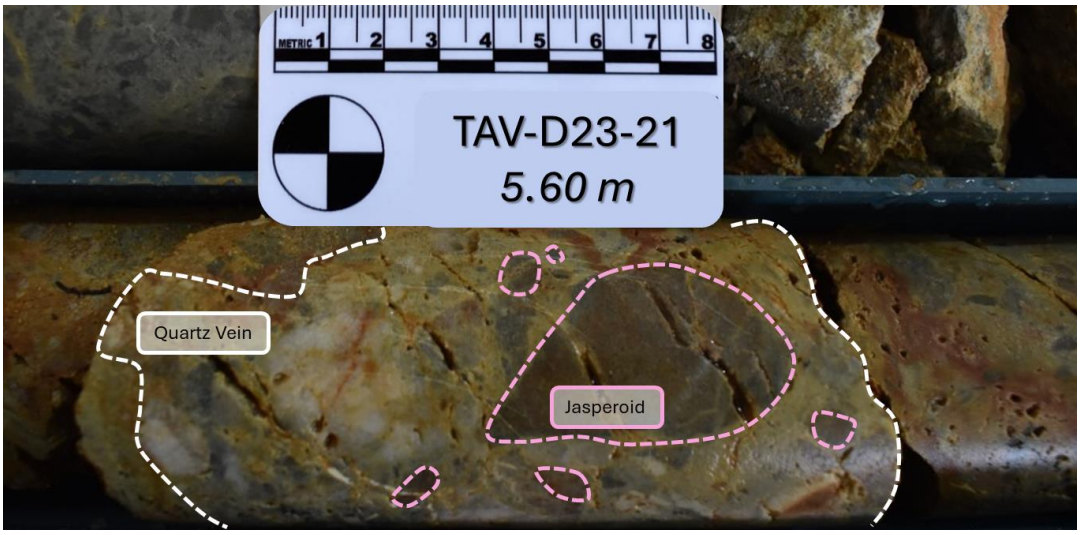

Figure 3.45. Close-up view from a brecciated jasperoid enclosed by quartz veining.



Figure 3.46. Field view from the main zone in the Budağan massive micritic limestone with cavity. The close views of (A) limestone bedding showing the cavity and brecciated limestone, (B) the cavity and (C) brecciated limestone. The breccia contains jasperoid fragments and quartz carbonate filling.

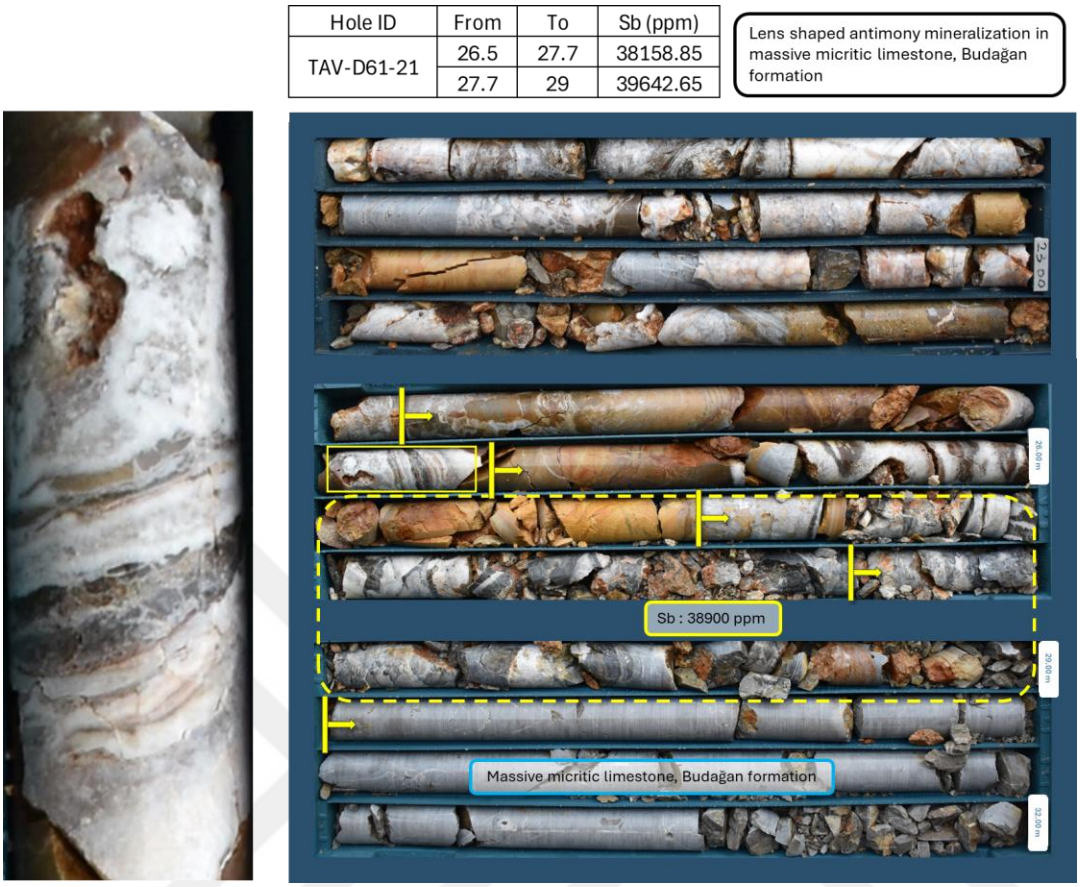

Figure 3.47. Core-samples showing very high antimony (Sb) rich lens shaped zone (represented with yellow dash line) in massive micritic limestone in Budağan formation.

The jasperoid fragments, or breccias, found within the fault zone indicate the presence of a post-mineralization fault. This is because that the low-angle fault, which initially acted as the primary pathway of mineralization and has undergone silicification. However, during another phase of deformation and jasperoid is crosscut by another fault (Figure 3.48) and brecciated which can now be observed within the fault gauge (Figure 3.48). Further studies are needed to investigate the post-mineralization fault in greater detail, as understanding its impact on both surface features and subsurface mineralization is essential.

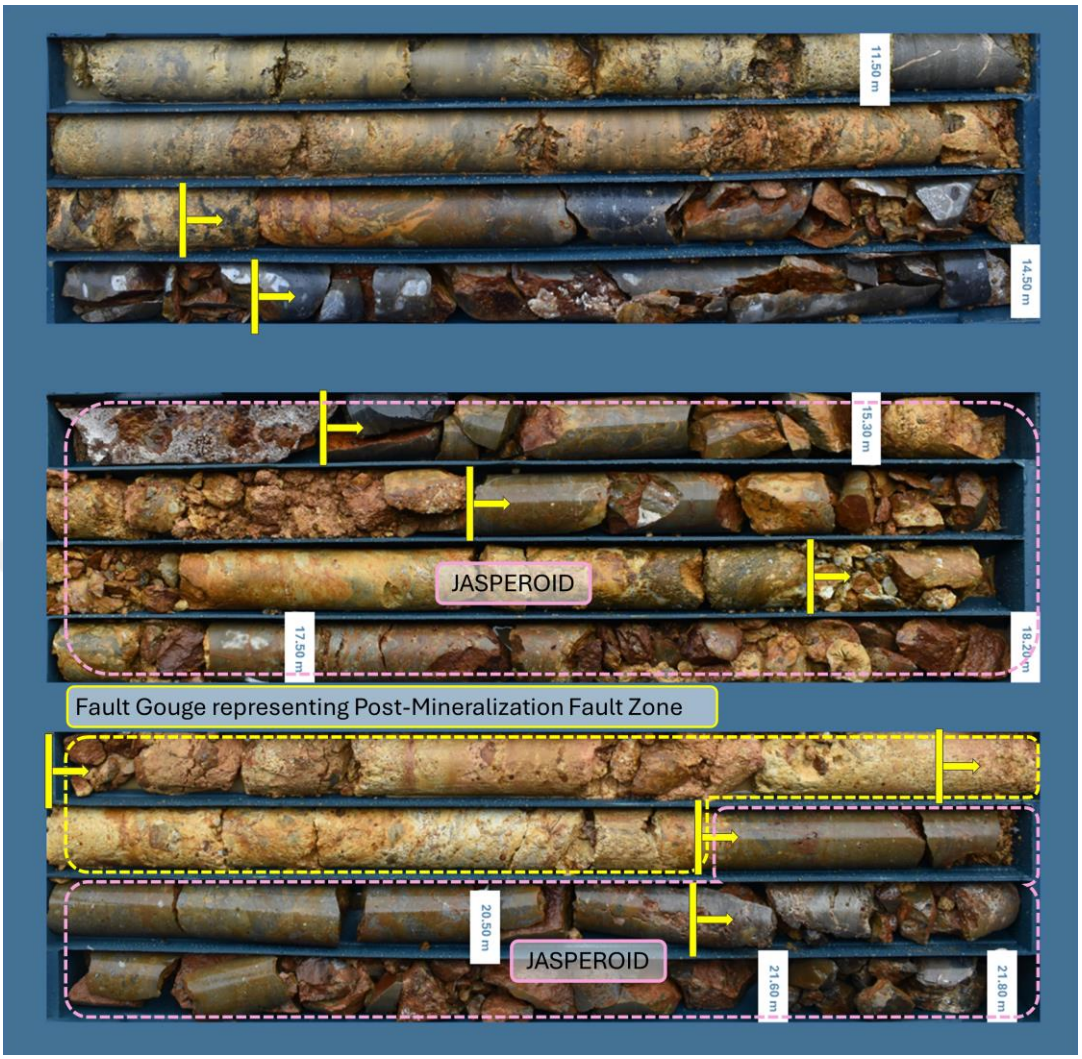

Figure 3.48. Core samples showing brecciated fault gauge belongs to post mineralization fault between massive jasperoid mineralization. In 17.80 meters of cores, Au (ppm) equivalent value is 3.34 ppm.

The sampling intervals and Au (ppm) assay results for each interval are given in Table 3.2.

Au ppm laboratory assay values for sampling intervals and intercepts.

Table 3.2. Au ppm laboratory assay values for sampling intervals and intercepts.

Hole ID	From (m)	To (m)	Au (ppm)	Intercept
TAV-D66-21	12.7	13.7	8.19	17.8 meters Au equivalent: 3.34 ppm
	13.7	14.7	9.09	
	14.7	15.9	6.31	
	15.9	17	1.9	
	17	18.2	2.6	
	18.2	19	1.32	
	19	19.7	0.982	
	19.7	20.7	1.48	
	20.7	21.9	2.22	
	21.9	23.2	3.96	
	23.2	24.5	2.54	
	24.5	25.5	3.63	
	25.5	26.5	2.84	
	26.5	27.6	1.1	
	27.6	28.6	1.775	
	28.6	29.6	4.1	
	29.6	30.5	1.645	
	30.5	31.7	0.046	
	31.7	32.8	0.75	3.7 meters Au equivalent: 0.66 ppm
	32.8	34.1	0.91	
	34.1	35.4	0.32	

An example hole is showing three different types of mineralization is shown in below Figure 3.49.

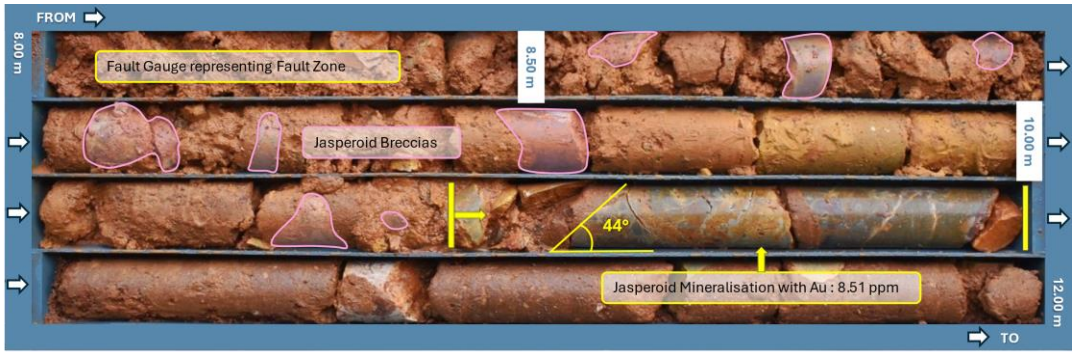

Figure 3.49. Core samples are indicating the fault zone which consist of jasperoid breccias. The contact of massive jasperoid is measured and beta angle is found as 44˚.

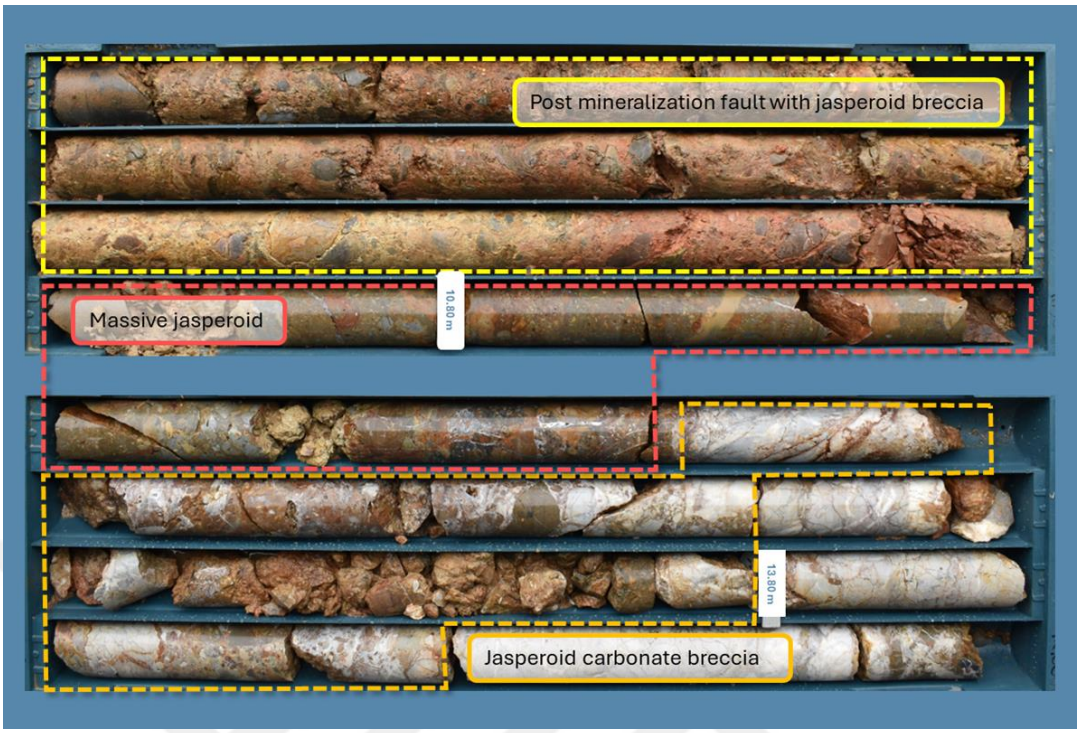

Figure 3.50. Yellow line represents brecciated jasperoid fragments in fault gauge. Red line indicates massive jasperoid while orange line belongs to the jasperoid carbonate breccia unit with quartz carbonate veinlets.

The gold grades is;

- Massive Jasperoid: Highest
- Jasperoid Breccia in Carbonates: Moderate
- Tectonic Jasperoid Breccia: Lowest

Table 3.3. Table showing the Au (ppm) and As (ppm) assay values for intervals of above drill hole.

Hole ID	From	To	Au (ppm)	As (ppm)
TAV-D35-21	7.50	8.60	0.12	1036.26
	8.60	9.60	0.14	1464.49
	9.60	10.60	0.25	1069.82
	10.60	11.90	2.59	654.46
	11.90	12.60	1.20	143.45
	12.60	13.60	0.85	203.36
	13.60	14.60	0.48	102.38
	14.60	15.30	0.34	85.77

CHAPTER 4

DISCUSSION

The Tavşan gold deposit, situated within a complex geological setting, presents a valuable opportunity to examine the relationship between structural controls and mineralization processes. The following discussion focuses on the primary research questions and aims outlined in this study, addressing the broader implications of the findings in understanding the formation of Tavşan gold deposit and the tectonic evolution of the region.

4.1 Structural Controls on Mineralization

The Dağardı ophiolitic mélange tectonically overlies the massive to thick-bedded micritic limestones of the Budağan formation (Figure 4.1). This contact was thus mapped as a thrust fault, even if it could have been reactivated by a subsequent tectonic event. Fault-plane data shows that the low-angle fault is an oblique-slip reverse fault with minor sinistral component. There is also evidence that the fault was reactivated as a normal (detachment) fault (see Section 3.3.1) for more information). The thrust faulting is attributed to nappe translation and ophiolite obduction during the closure of the northern Neotehtyan ocean along the İzmir-Ankara-Erzincan Suture Zone, while detachment faulting to the post-orogenic extension in western Anatolia.

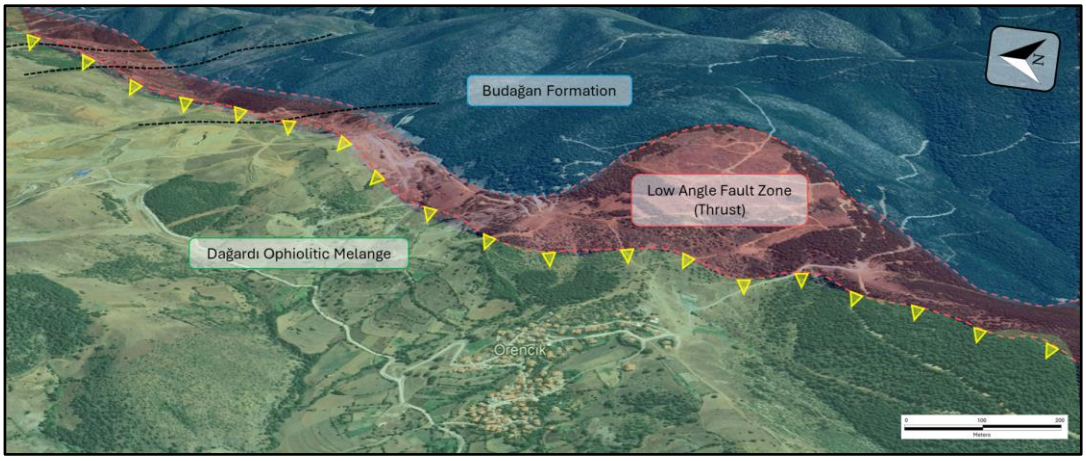

Figure 4.1. Google Earth image showing low-angle fault contact between the Dağardı ophiolitic mélange above and massive to thick-bedded micritic limestones of the Budağan formation below. The fault crosses the entire study area and forms the most prominent structure.

According to literature, there is overwhelming geological and structural evidence that the detachment fault(s) exist in this part of the Anatolia. The evidence includes presence of a low-angle fault surfaces, ductile deformation with a top-to-NE sense of shearing, and syn-kinematic granite intrusions in the footwall of the proposed detachment faults (e.g., Işık and Tekeli, 2001; Işık et al., 2004; Ring and Collins, 2005; Thomson and Ring, 2006; Sener et al., 2009; Hasözbek et al. 2010; Bozkurt et al., 2011; Catlos et al., 2012). There are also syn-kinematic granitic intrusions (Eğrigöz, Koyunoba, Alaçam) that are attributed to late Oligocene to middle Miocene magmatism during post-orogenic extension (e.g., Işık and Tekeli, 2001; Işık et al., 2004; Ring and Collins, 2005; Thomson and Ring, 2006; Akay, 2009; Catlos et al., 2012; Gessner et al., 2004 & 2017). According to these authors, the closure of the Neotethys has resulted in amalgamation and stacking of different continental blocks and crustal thickening and that following the continent-continent collision, the region has experienced post-orogenic extension due to combined effects of subduction rollback and orogenic collapse of overthickened crust. In this model, granites are interpreted as syn-extensional with respect to detachment faulting and mylonitization in their footwall. The age of mylonitization, based on $^{40}Ar/^{39}Ar$ white mica dating, is 22.9±0.5 Ma (Işık et al., 2004) whereas the Eğrigöz granite is late Oligocene to early Miocene (20.7±0.6 Ma; secondary ion mass

spectrometry (SIMS) U–Th–Pb zircon ages; Ring and Collins, 2005). The zircon and apatite fission track and (U-Th)/He apatite ages are interpreted to suggest rapid detachment fault activity and rapid exhumation/cooling during ca. 25 Ma and ca. 19 Ma interval (Thomson and Ring 2006).

The literature highlights that magmatism and detachment faulting are closely linked, suggesting thermal weakening of the over-thickened crust. This process likely triggered the reactivation of thrust faults during post-orogenic extension starting in the late Oligocene to early Miocene.

The literature also agrees that close association of magmatism and detachment faulting are closely linked, suggesting thermal weakening of the over-thickened crust. This process likely triggered the reactivation of thrust faults during post-orogenic extension starting in the late Oligocene to early Miocene (e.g., Işık and Tekeli, 2001; Işık et al., 2004; Ring and Collins, 2005; Thomson and Ring, 2006; Hasözbek et al. 2010; Bozkurt et al., 2011; Catlos et al., 2012).

It is here documented that there is both spatial and temporal relationship between low-angle faulting and jasperoid mineralization and the faulting controlled the mineralization in the Tavşan gold deposit. Field observations revealed that major mineralized zones frequently occur along low-angle faults and/or intersection-interaction of differently trending faults. Concentration of jasperoid along low-angle fault and intersection of low-angle and ca. N–S-trending high-angle faults (Figure 4.4) implies that mineralization is directly controlled and/or influenced by these structures.

In this model, low-angle faulting commenced as thrust fault, and later reactivated by during post-orogenic extensional tectonism. The weakness zone of low-angle fault zone between the serpentinites of the Dağardı ophiolitic mélange in the hanging wall and the micritic limestones of the Budağan formation allowed migration and circulation of hydrothermal solutions that come from the fissures and fractures.

Since, Tavşan mineralization is mostly confined to jasperoid (a replacement product of limestone) because the fluid could only react with limestone unit most efficiently, but not with the ophiolitic mélange. Additionally, the rheological differences between the ophiolitic mélange and the limestone resulted in varying responses to faulting and hydrofracturing. While the ophiolitic mélange experienced shearing and serpentinization during deformation, the limestone exhibited brittle deformation, such as hydrofracturing (Figure 4.2). Consequently, the sheared ophiolitic suite acted as an aquitard, forming an impermeable barrier that restricted the movement of siliceous hydrothermal fluids responsible for mineralization. The "seepage" was considered where low-angle fault-controlled fluids escape through permeable weak zones and limestone. These hydrothermal fluids were therefore confined by the sheared ophiolitic impermeable layer, leading to the precipitation of mineralization along the fault boundary. As a result, a sharp contact between the jasperoid and the ophiolite has formed. Another observation is that the jasperoid mineralization is not deformed like the ophiolitic mélange and limestone (Figure 4.2). It shows massive characterization and forms beneath the radiolarian cherts in the ophiolitic mélange. These observations provide further evidence that mineralization occurred after the deformation.

Following mineralization, they are cut and displaced by N00ºE to N20ºE-trending near vertical faults (Figure 4.4).

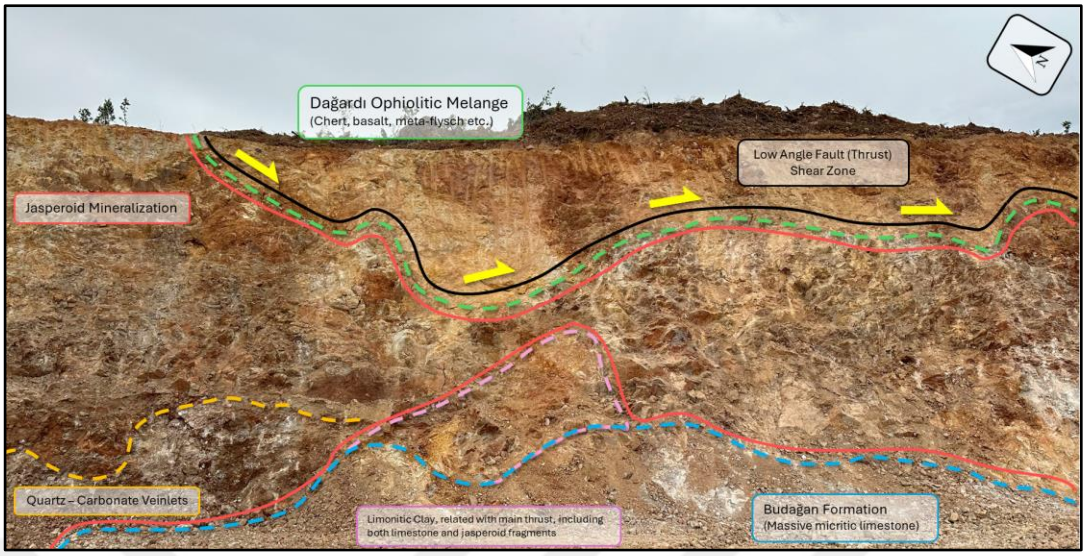

Figure 4.2. Field view illustrating association of Dağardı ophiolitic mélange, jasperoid and limestone within the damage zone of the low-angle fault. Green dashed line indicates the contact of the Dağardı ophiolitic melange and jasperoid, which is the thrust that indicated with black line. Blue dashed line represents the boundary between jasperoid and limestone. Pink dashed line shows limonitic clay related with shearing; orange dashed lines mark boundary of late-stage quartz-carbonate veins cross-cutting the adjacent units.

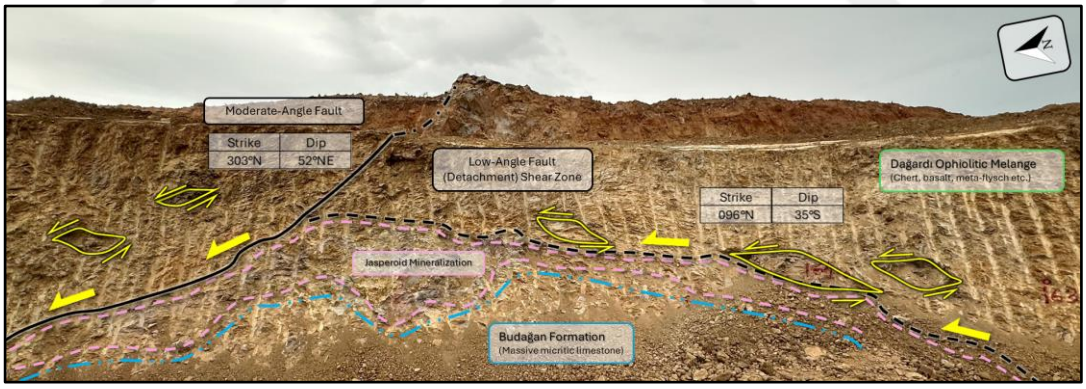

Figure 4.3. A view from low-angle fault zone with C-S fabrics and sigma-type clasts, all indicating a top-to-the-NW motion. At present configuration, the fabrics are interpreted to suggest a normal motion along the low-angle fault. Similar information about the sense of motion along the fault is interpreted to suggest that the original thrust fault is later reactivated as a detachment fault.

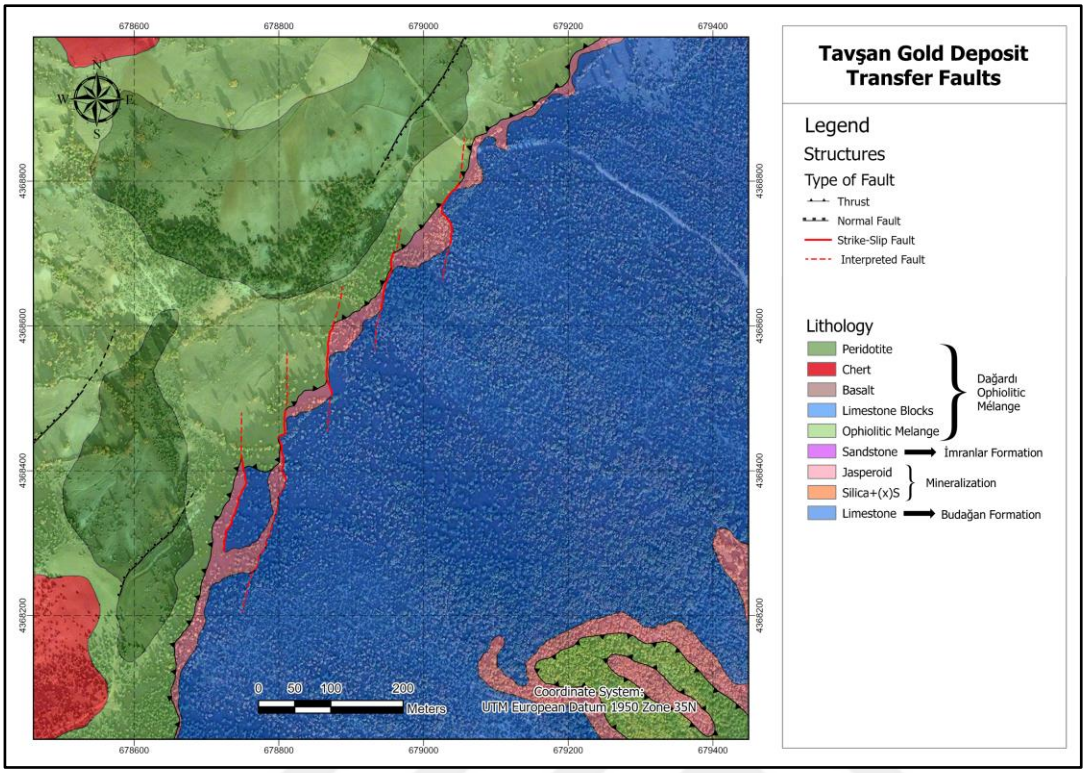

Figure 4.4. Geological map showing off set of mineralized jasperoid along strike-slip (transfer) faults.

4.1.1 Timing of Structures and Its Relationship with Mineralization

The structural evolution of the Tavşan gold deposit played a pivotal role in controlling the timing, localization, and nature of mineralization events. Understanding the sequence of structural episodes is essential to unravel the complexities of how mineralizing fluids were emplaced and how different geological processes contributed to the formation of the deposit. This section outlines the major structural events that occurred before, during, and after mineralization, focusing on the relationships between thrusting, normal faulting and the hydrothermal activity responsible for the deposition of gold, stibnite, and associated minerals. Each episode is closely linked to the tectonic evolution of the region, with distinct phases of deformation and fluid movement contributing to the overall mineralization process.

4.1.1.1 Pre-Mineralization Events

Collisional Period

During the pre-mineralization phase, the collisional event between the Anatolide-Tauride Block and the Pontides initiated a significant thrusting event. Low-angle faulting caused emplacement of the Dağardı ophiolitic mélange which overlain the micritic limestones of the Budağan formation. The structural deformation during this phase was primarily driven by compressional forces related to the closure of the northern Neo-Tethys Ocean, which resulted in extensive ophiolite obduction. The mechanical disruption of the rock units, intensely deformed shear zones, especially along the contact between the ophiolite mélange and limestone, provided critical structural controls that would later serve as pathways for mineralizing fluids.

4.1.1.2 Syn-Mineralization Events

Extension Period & Intrusion of Miocene Granitoid

Following the continent-continent collision, the region has experienced post-collisional extensional tectonics, commenced by late Oligocene–early Miocene time. This has resulted in the collapse of the over-thickened crust and reactivation of the thrust faults as low-angle normal (detachment) faults.

During the Miocene, the emplacement of the Eğrigöz granitoid occurred in the footwall of the detachment fault. The detachment faults formed critical pathways for hydrothermal fluids migration and circulation, and in turn leading to the formation of jasperoid mineralization. Hydrothermal fluids circulated through this zone, creating favourable conditions for the deposition of jasperoid, particularly along the sections of the detachment fault where secondary porosity and permeability are well pronounced.

In this model, ca. N–S-trending near vertical strike-slip faults played a crucial role in accommodating lateral motion of both the detachment and associated

mineralization. In this model, these faults are interpreted as transfer faults (Figure 4.5). The interaction between the high-angle faults and the detachment fault may have helped re-open pre-existing pathways or created new fluid channels, allowing mineralizing fluids to flow into structurally prepared zones. This reactivation enhanced jasperoid formation and the development of polymictic hydrothermal breccias, as well as creating localized zones of increased permeability where fluids could concentrate and precipitate mineralization.



Figure 4.5. Field view and sketch illustrating the N00ºE to N20ºE-trending fault, displacing the jasperoid mineralization.

At least two episodes of mineralization occurred during this period. The first one is the emplacement of massive jasperoid within the host rocks, specifically through the de-carbonatization of limestone units. This process involved the removal of carbonate material, which led to the formation of massive jasperoid bodies. The jasperoid was emplaced along fault zones, utilizing the detachment-related faults as pathways for fluid migration. As hydrothermal fluids ascended through these fault networks, the interaction between the fluids and the carbonate-rich host rocks triggered silicification, resulting in the replacement of carbonate minerals with silica

and the formation of extensive jasperoid. This stage of mineralization was closely linked to the structural preparation provided by the earlier thrusting and extensional events, which opened fractures and brecciated zones, facilitating fluid flow and silicification.

The second one involved the formation of polymictic hydrothermal breccias, which contained jasperoid as well as clasts of ophiolitic melange. These breccias were likely formed by the hydrothermal reworking of earlier thrust or detachment-related structures. The second phase continued the deposition of jasperoid within the brecciated zones, further enriching the mineralization. The repeated cycles of fluid injection and brecciation created highly porous and permeable zones, allowing for continued hydrothermal activity and further concentration of mineralization.

4.1.1.3 Post-Mineralization Events

Post Mineralization Faulting

A subsequent phase of tectonic activity or deformation caused the jasperoid bodies to have been cross-cut and disrupted by later faults. The presence of brecciated jasperoid fragments within the fault gauge (the fine-grained material within a fault zone) supports this contention. The jasperoid, which is product of silicification during the earlier mineralization phase, was mechanically broken down and incorporated into the fault gouge as breccia clasts, indicating that this later faulting occurred after the primary mineralization event. The brecciation of jasperoid within the fault zone demonstrates a complex structural history where multiple phases of faulting and mineralization occurred.

Quartz-Antimony-bearing Mineralization Phase

After the primary jasperoid mineralization, the post-mineralization event introduced stibnite and quartz-carbonate mineral phases. Stibnite, a key indicator of temperature

conditions below 200 °C and late-stage hydrothermal activity, formed within quartz and quartz-carbonate veins that crosscut the earlier jasperoid bodies (Figure 4.6). This phase is deposited within prepared karst, observed in the open pit slopes (Figure 3.46) and also, the fluids that precipitated stibnite caused further dissolution (Figure 3.44). The stibnite, along with clay infill, was often deposited within brecciated jasperoid zones and karstic spaces within the limestone. These lens-shaped karstic voids acted as repositories for late-stage mineralizing fluids.

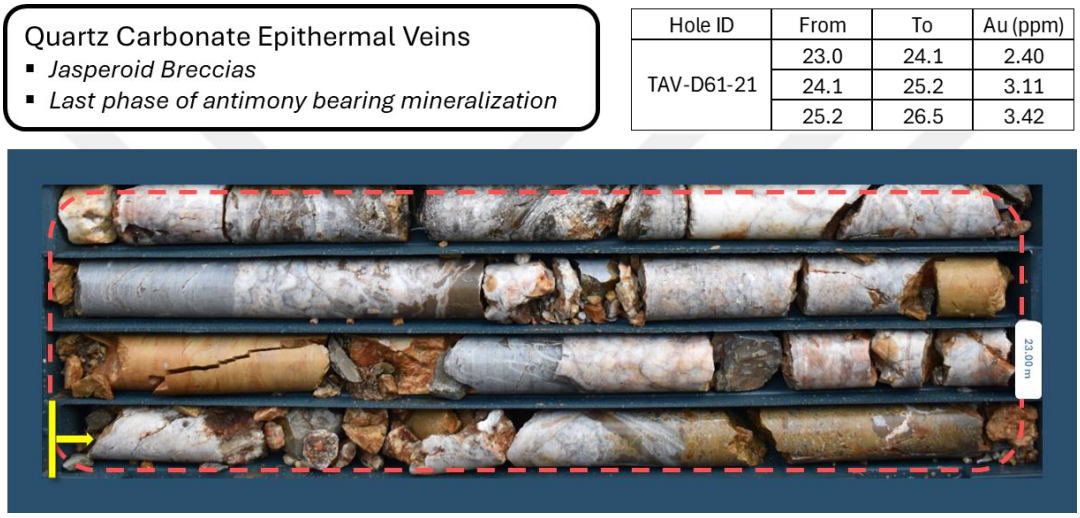

Hole ID	From	To	Au (ppm)
TAV-D61-21	23.0	24.1	2.40
	24.1	25.2	3.11
	25.2	26.5	3.42

Figure 4.6. Core-samples showing antimony (Sb) rich lens shaped zone and quartz carbonate epithermal veins (represented with red dash line) in Budağan formation.

It is important to note that the precipitation of quartz and stibnite may not have been simultaneous. Quartz likely precipitated first, with stibnite following later in response to a change in the chemistry of the hydrothermal fluids. This potential temporal separation between quartz and stibnite deposition suggests a complex fluid evolution, which should be considered in further studies to better understand the sequence of post-mineralization events.

4.2 3-D Geological Model of Tavşan Gold Deposit

4.2.1 Deposit Scale Geological Model

3-D modelling is created to consider the relationship of lithology, mineralization and structure. The geological model therefore combines huge amount of data in order to visualize and discuss of all the collected data during field work and diamond drill holes. It is aimed to understand and verify the structural control on mineralization. The 3D geological model utilizes field observations, structural data, geological map, re-logged core lithology.

Model is created by using Leapfrog Geo software. To start with, topography of the study area was generated by using of point cloud data which is taken from topographer team, and geological map is imported to link geology and topography in order to explore the effect of morphology on geology (Figure 4.7).

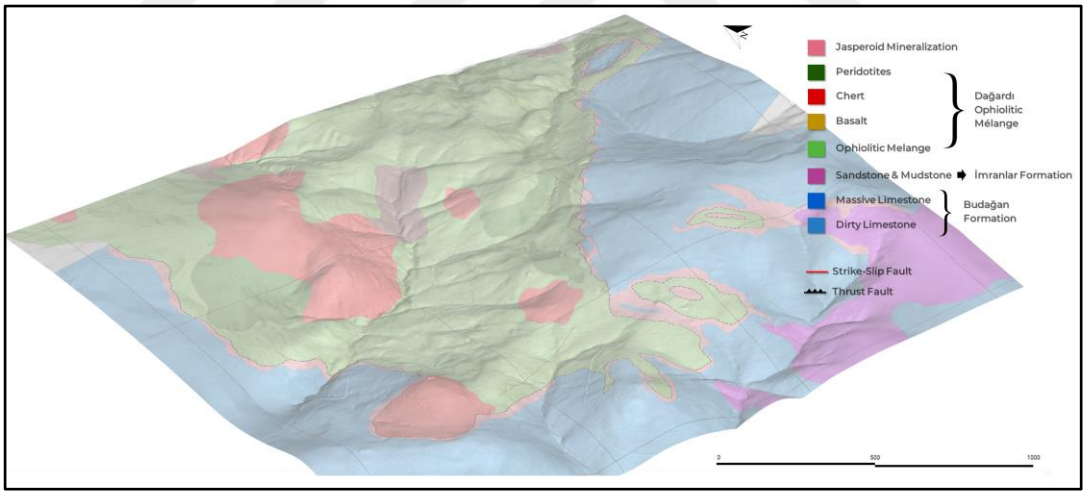

Figure 4.7. Topography of the study area and draped surface geological map in oblique view.

Structural measurement and all structural observations are integrated into the geological map. Besides, drillhole lithology and core assay results are selected and evaluated in 3-D model building. The fault measurement and lithological unit boundaries were placed on topography (Figure 4.8).

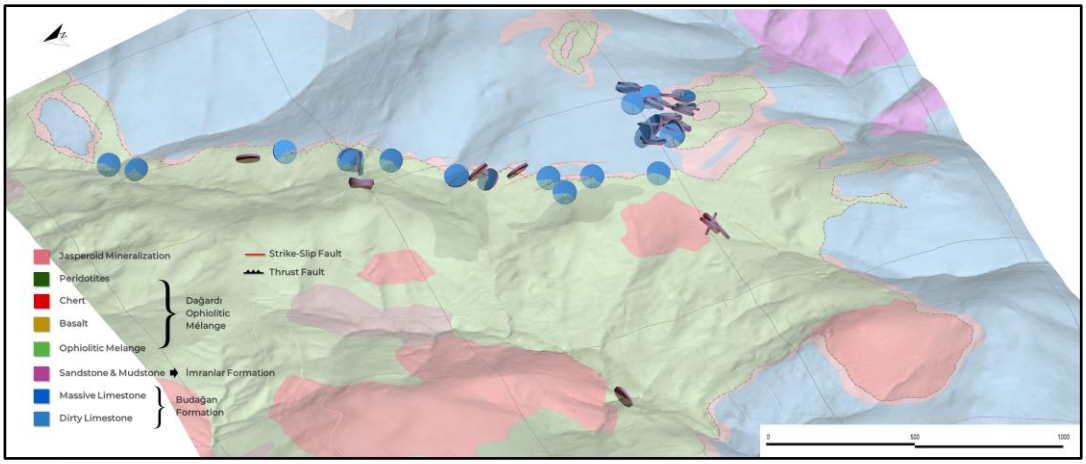

Figure 4.8. Structural measurements are combined to the geological map. Fault measurements are seen as a disk shape, which all oriented according to the strike and dip direction.

For the geological model of the Tavşan gold deposit, 381 drillholes are used for the lithological modelling and 18853.20 meters are relogged for the geological model. 8332 core sample assay results are used for the determination of the ore zone with the grade.

For the drillhole interpretation in 3-D, re-logged lithology, assay values from the geochemical analysis, collar data are all incorporated (Figure 4.9). The location of drillhole and survey data that indicate the direction of drillholes in specific depth were imported to the software program (Figure 4.10 and Figure 4.11).

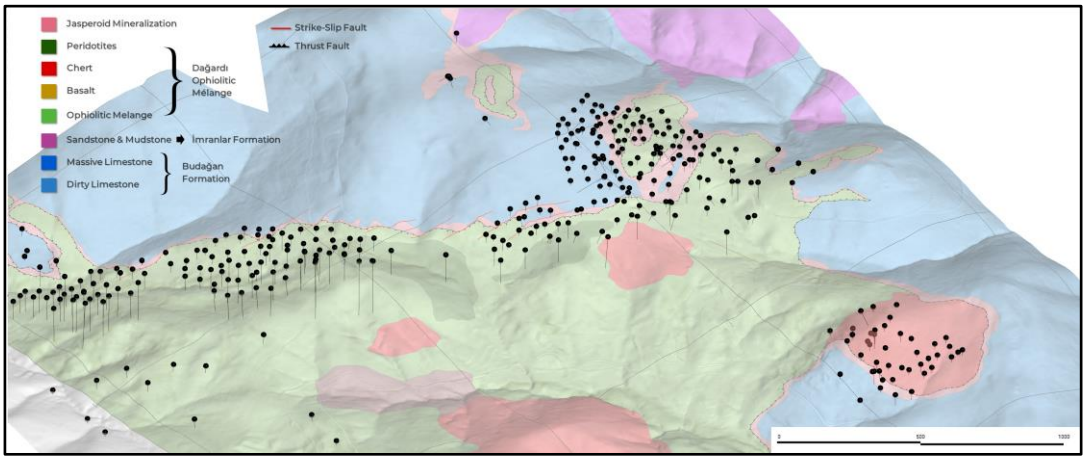

Figure 4.9. Showing the collar and traces of the drillholes location of the study area on the geological map and topography.

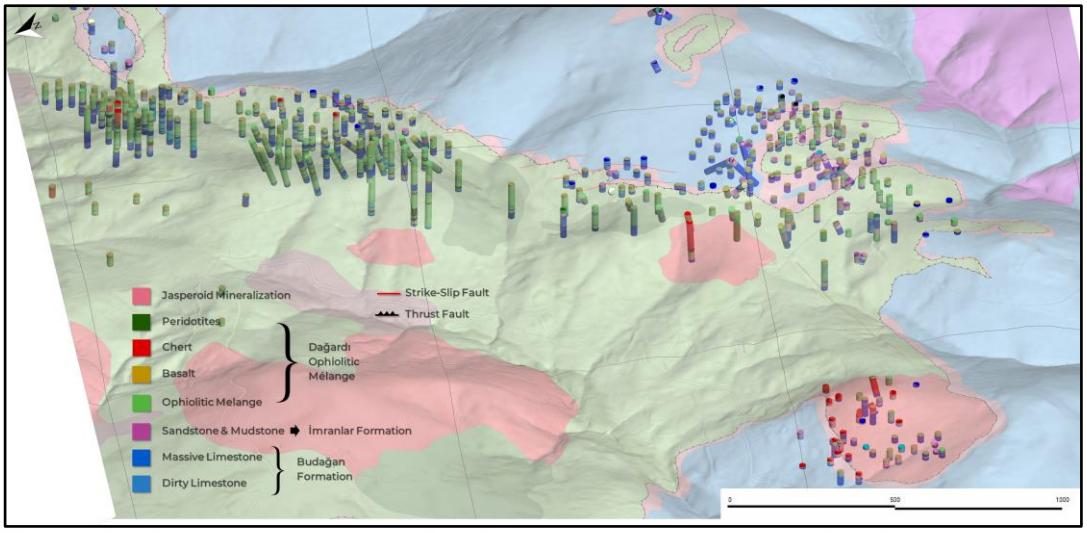

Figure 4.10. Showing the lithologically classified and color-coded state of the drillholes.

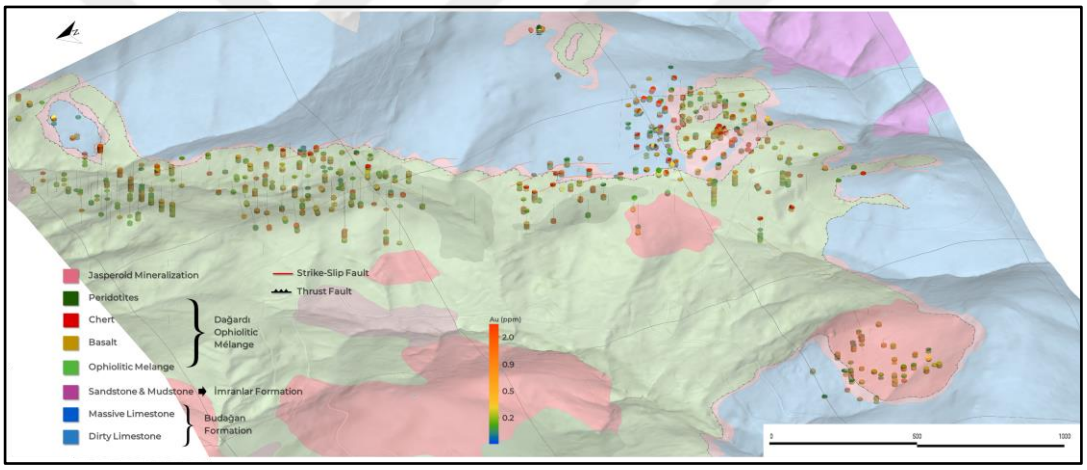

Figure 4.11. Classified zones in the drillhole based on Au ppm values in drillholes on geological map. In the legend, red colour shows the high values of Au, while the blue colour is the low values.

After the drillhole information and geology map are formed in 3-D, the lithological data from the drilling records were cross verified against the surface geological map. By comparing the lithology indicated in core logging of the drillholes with the lithologies identified on the geological map, the lithological consistency of the regional geology was confirmed (Figure 4.12). Comparison and correlation of data deduced from the drillhole core logging and surface geological mapping is also performed for (i) ophiolitic mélange, chert, limestone and jasperoid (Figure 4.13)

and (ii) chert and limestone within jasperoid mineralization zone, separately. It is observed that lithologies are consistently correlated (Figure 4.14).

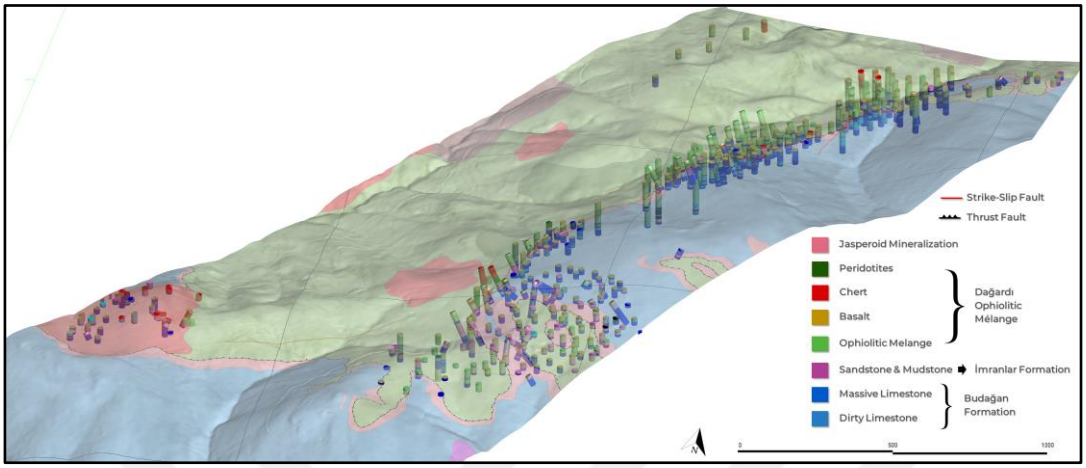

Figure 4.12. Correlation and comparison lithology distribution as indicated by core logging and surface geological mapping in the Tavşan gold deposit.

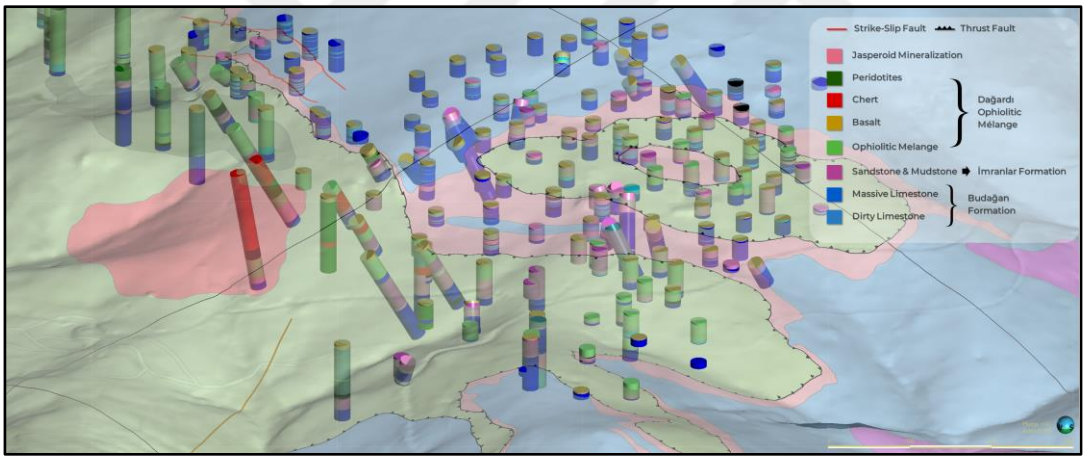

Figure 4.13. Correlation of logging data with surface geological mapping of Main Zone.

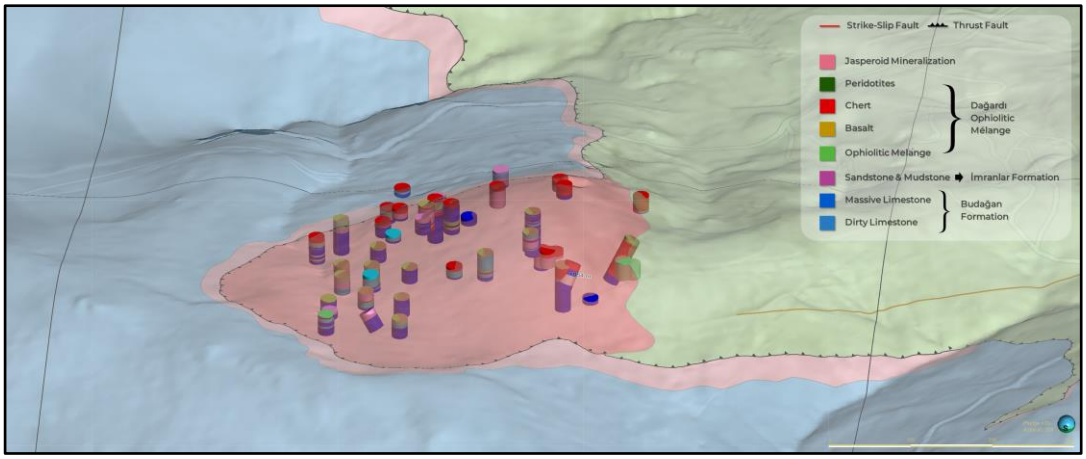

Figure 4.14. Chert unit of geological map and logged chert unit are correlated in West Zone.

The construction of the 3-D geological model involves an iterative process of synthesizing available data and geological interpretations (Figure 4.15) within the context of a field-derived geological framework. Consequently, the accuracy and reliability of the model are closely linked to the data from surface geological mapping (lithology and geological structures), topographic features and diamond drillhole lithologic logging. The 3-D lithological model is compared with surface geological map and shown in the Figure 4.16.

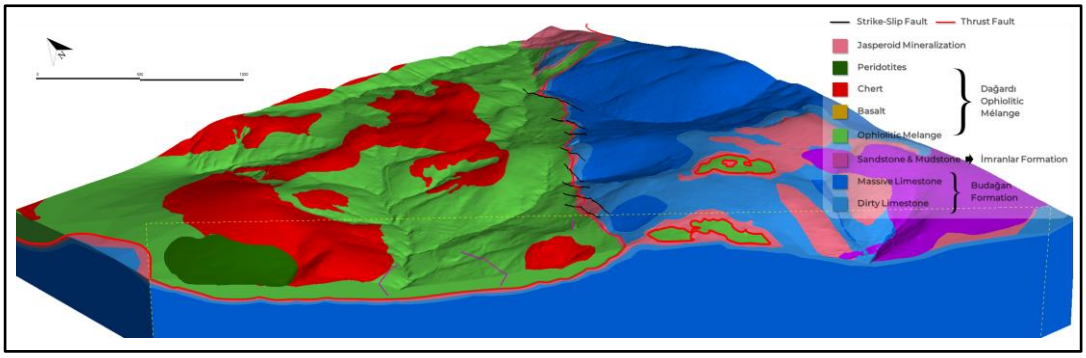

Figure 4.15. Solid model within the context of a field-derived geological framework.

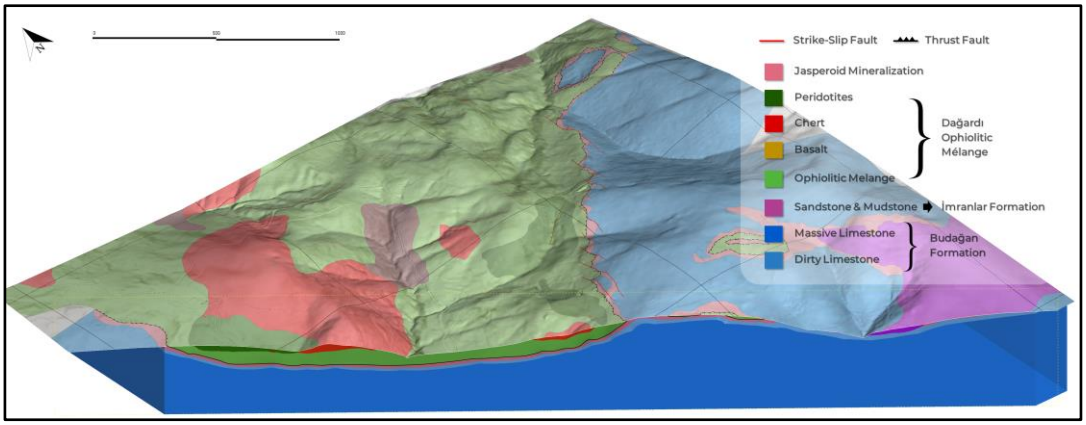

Figure 4.16. Comparison of 3-D lithological model with surface geological map.

The grade model for gold (Au) in the drillhole samples, applying a 0.5 ppm cut-off, is illustrated through the yellow panels in Figure 4.17. The diagram highlights the distribution and spatial extent of gold mineralization across the deposit, providing a clear representation of the zones that meet or surpass the defined cut-off criteria. This approach ensures a focused analysis on economically significant mineralization.

In the Figure 4.18, zones identified as jasperoid in the core samples were used to construct a detailed lithological model. The pink model visually represents the distribution and geometry of the jasperoid zones. Furthermore, this jasperoid model has been cross-referenced and compared with the grade model to assess the spatial relationship between lithology and ore mineralization. The figure also illustrates the influence of geological structures, particularly low-angle detachment and high-angle strike-slip (transfer) faults. The diagram (Figure 4.18) also illustrate distribution and continuity of the jasperoid zones within the model, highlighting how the structural features impact the overall geological framework. Offsets caused by the strike-slip faults are visibly present in the jasperoid lithological model, where displacement along these faults has shifted sections of the jasperoid zones. These structural displacements are key to interpreting the spatial arrangement of the jasperoid units. Furthermore, the model allows us to observe the influence of the strike-slip faults on the overlying mineralization zones (Figure 4.18 and Figure 4.19). Structural controls, such as faulting, play a significant role in shaping the distribution, continuity, and geometry of the mineralized zones. The model also demonstrates how these

geological features can either compartmentalize or extend the mineralization along certain pathways. This model highlights the critical relationship between structures and mineralization, emphasizing the role of transfer faults in controlling the localization and extent of ore zones.

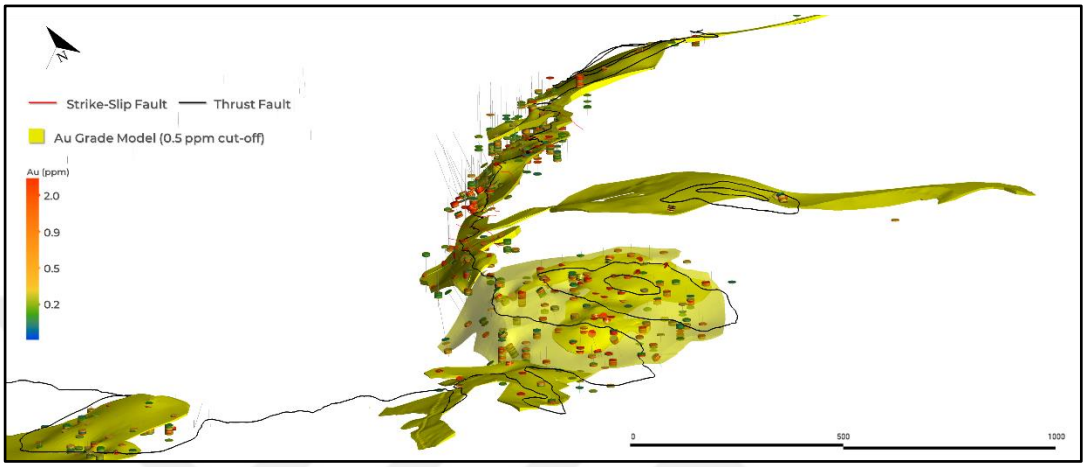

Figure 4.17. Grade model built with Au 0.5 ppm cut-off containing the drillhole assay Au values. Yellow panel represent the grade model of Au.

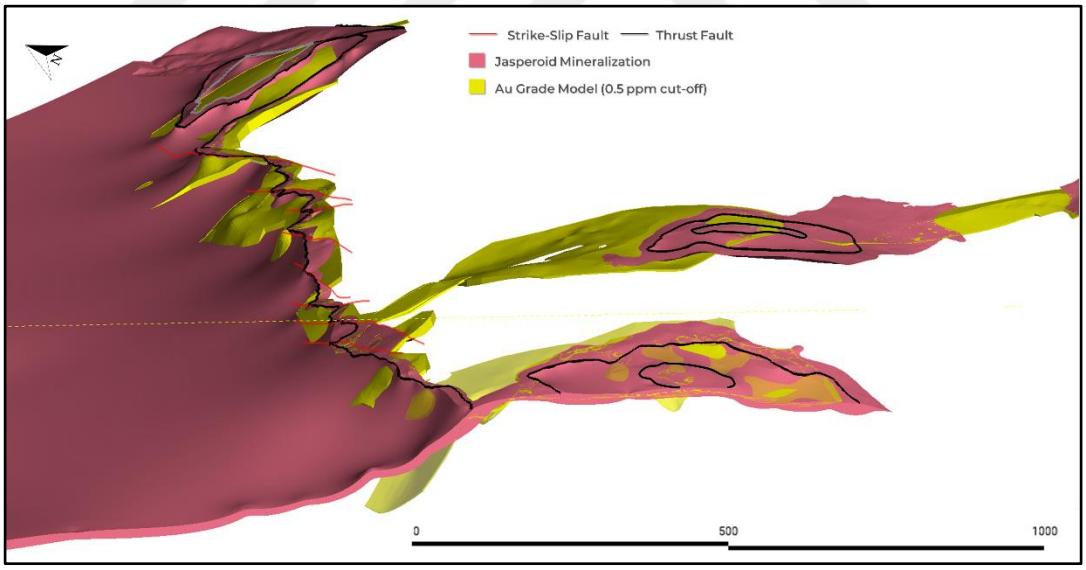

Figure 4.18. Jasperoid lithological model and Au grade model combination. Pink panel represents the jasperoid model building from lithologies of drillhole data while the yellow panel is the grade model of Au. Low-angle fault (black line) and strike-slip fault (red line) effect the jasperoid mineralization.

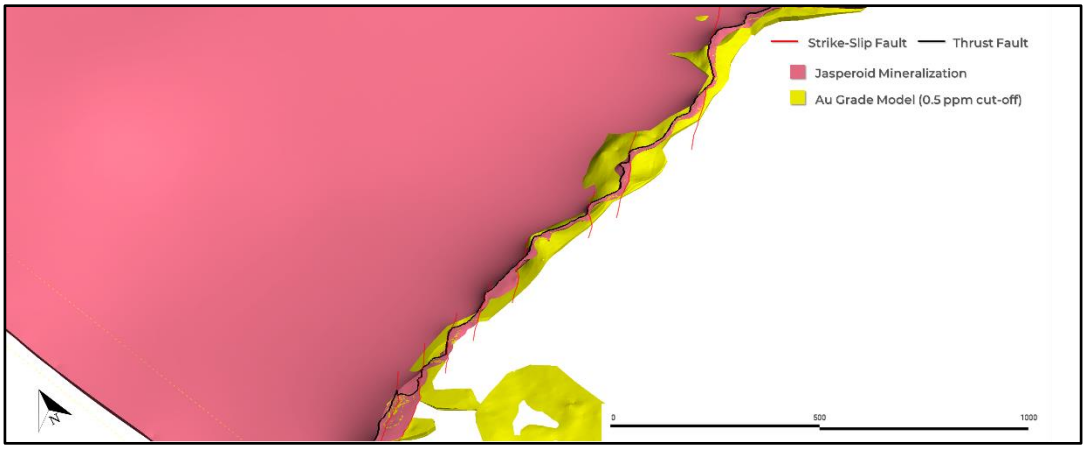

Figure 4.19. Displacement along the strike-slip (transfer) faults has shifted sections of the jasperoid zones.

The 3-D geological modelling of the Tavşan gold deposit provides valuable insights into the relationships between lithology, mineralization, and structural controls within the study area. By integrating extensive field data, including geological maps, drillhole lithology, assay results, and structural observations, the model offers a detailed understanding of the deposit's geometry. The use of Leapfrog Geo software allowed effective combination of surface mapping, topography, and subsurface drill data, enhancing the accuracy of the lithological and grade models.

The lithological model, constructed using relogged drillhole data and surface mapping, demonstrated strong consistency between surface geology and subsurface interpretations. Furthermore, the grade model, applying a 0.5 ppm cut-off for gold, effectively highlighted the economically significant mineralized zones within the deposit. The comparison of the jasperoid lithological model with the grade model revealed the influence of geological structures, particularly thrust, detachment and transform faults, on the continuity and distribution of both jasperoid units and mineralized zones.

Overall, the model underscores the critical role of structural controls, such as faulting, in shaping the spatial arrangement of mineralization. These structural features not only displace lithological units but also impact the extent and continuity

of ore zones, emphasizing the importance of understanding geological structures in resource estimation and exploration strategies (Figure 4.20).

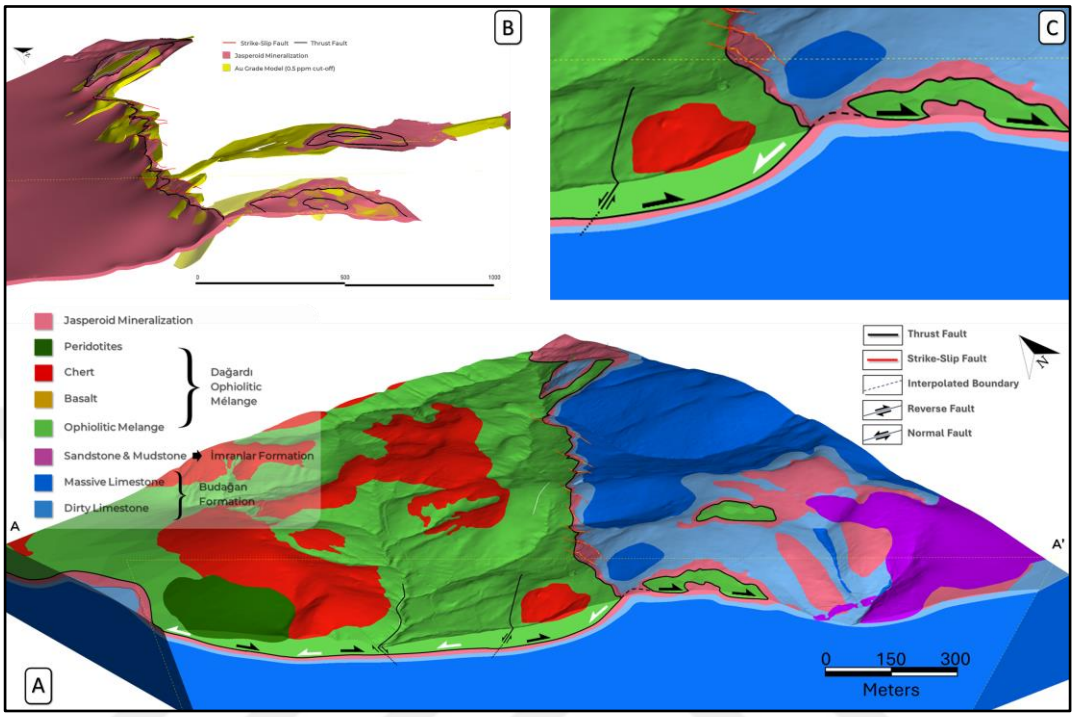

Figure 4.20. (A) Final geological model of Tavşan gold deposit. Black line with bold half arrows represents the low-angle fault whereas the black line with double half arrows the strike-slip faults. Black and white arrows are representative of sense of motion for thrust and detachment faulting, respectively. (B) Combined Au grade and jasperoid mineralization model and the strike-slip faulting. (C) Relationship between strike-slip fault and the low-angle fault.

4.2.2 Pit Scale Geological Model

The 3-D model aimed at developing a deposit-scale geological model were undertaken to conduct a more detailed investigation of the Tavşan gold mineralization, focusing specifically on the open-pit area. In the detailed geological modelling of the open pit, particular emphasis was placed on analysing the influence of structural controls on the mineralization process.

Within the scope of the study, the open-pit area was selected as the location for developing the geological model, and the focus was narrowed to this specific area to

allow for detailed analysis. Open pit slope geological mapping was carried out at a 1:100 scale, focusing on lithological contacts, mineralization zones, related features; the data is recorded within the coordinates (Figure 4.21). This mapping provided critical surface data for the open-pit area, which was used to correlate subsurface information from diamond drill holes. Key lithological units identified include ophiolitic mélange, limestone, and jasperoid bodies, with the latter being closely associated with gold mineralization. These observations were initially digitized and transferred into a two-dimensional format using ArcGIS software, enabling precise spatial representation and analysis.

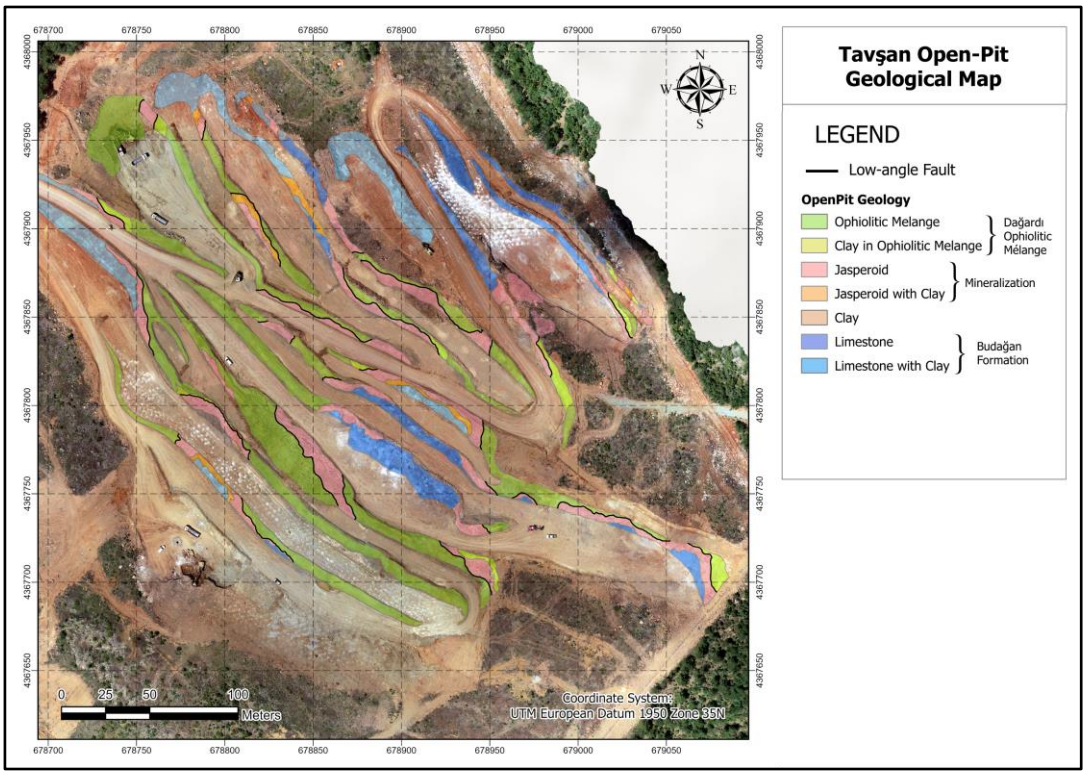

Figure 4.21. Tavşan open-pit geological map showing the alteration and lithology related features.

Open cut mapping was completed as part of this study, with all lithological contacts and observed features detailly mapped and incorporated into the final map. To further refine the geological model, the collected data, including the slope map and lithological observations, were integrated into a three-dimensional environment using Leapfrog Geo software. This integration also involved the combination of the

geological data with the mine's topography to create a comprehensive 3-D model. The topographical data for the open cuts were generated using high-resolution drone imagery, which provided a detailed and accurate representation of the terrain. This approach allowed for a robust analysis of the spatial relationships and structural controls within the open-pit environment, contributing significantly to the overall understanding of the deposit geology (Figure 4.22).

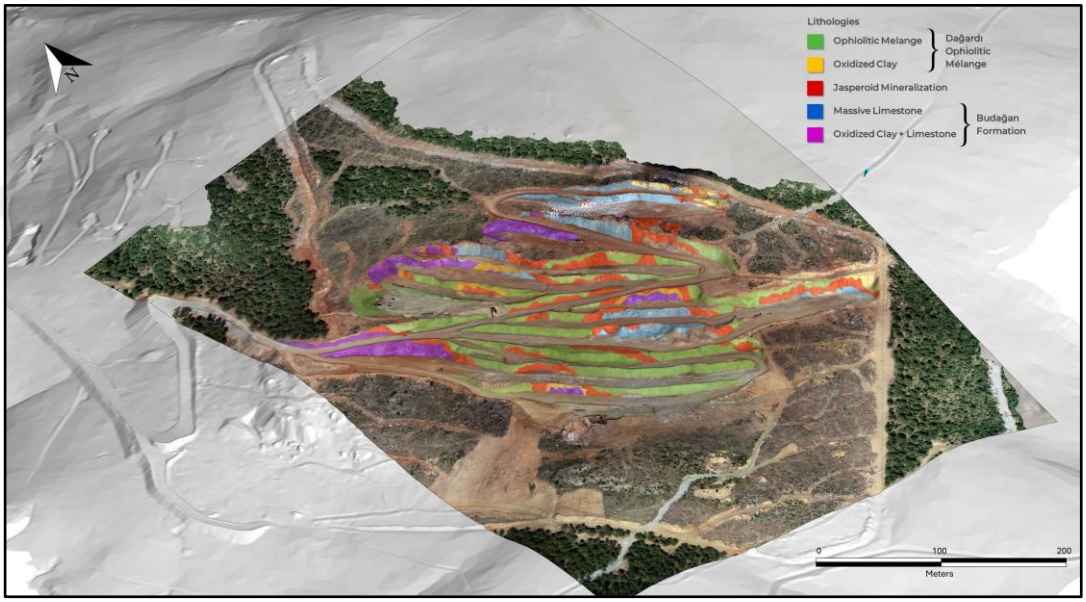

Figure 4.22. High-resolution topography and drone imagery of the open pit area. Geological map is draped on the topography.

A total of 105 drill holes are located within the study area, and these holes were integral to the research (Figure 4.23). Lithological logs from these drill holes provided valuable subsurface information, allowing for the identification of lithological boundaries and the correlation of these boundaries with surface geological features. The lithological logs were incorporated into the 3-D geological model, which enhanced the understanding of the subsurface continuity of key units such as jasperoid and limestone.

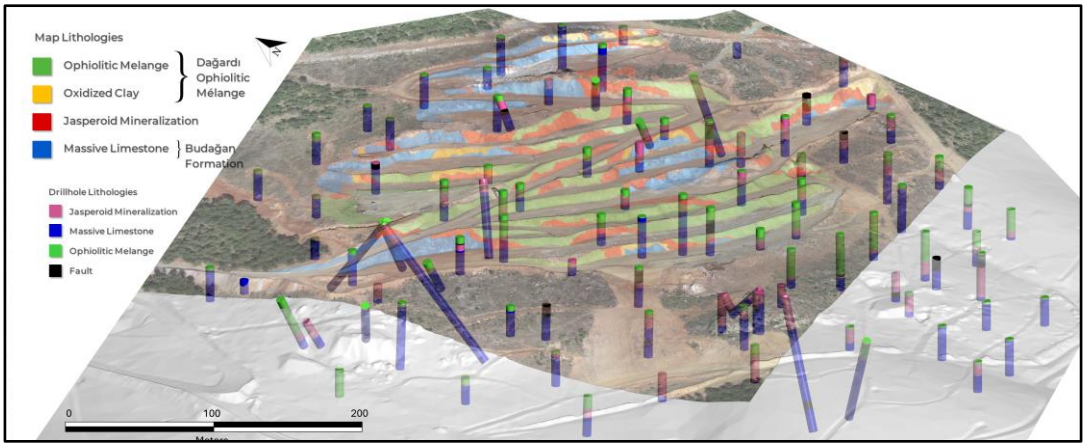

Figure 4.23. Diamond drill holes within the lithologically classified and color-codes and open-pit slope geology.

The assay data from diamond drill holes, particularly for gold (Au) and silver (Ag), was used to develop a grade model within the 0.5 ppm Au cut-off (Figure 4.24). A total of 1,634 assay results were incorporated into the model. These results provided the spatial distribution of gold and silver mineralization within the pit and were essential for the creation of the grade model, which visually highlights economically significant mineralization zones. The integration of assay data into the 3-D grade model enabled a more localized understanding of ore distribution.

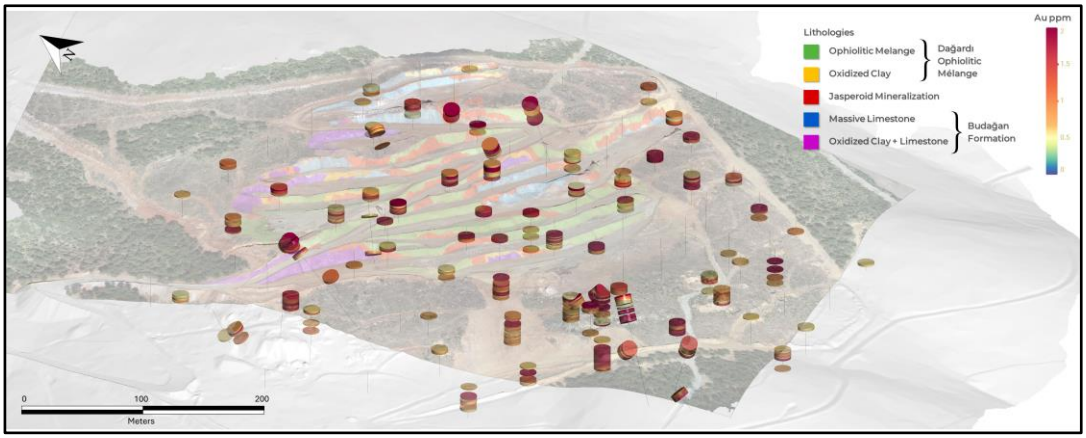

Figure 4.24. Diamond drill hole assay in accordance with Au ppm values within the 0.5 ppm cut-off.

During the fieldwork, measurements of faults, foliation patterns, contacts, and ore orientations were meticulously collected from the open-pit slopes to enhance the accuracy and detail of the 3-D geological model. Slickensides, striations, and other

kinematic indicators such as C-S fabrics and drag folds were observed and recorded (Figure 4.25). These structural measurements were critical in identifying the reactivation of thrust faults into normal faults, which provided significant pathways for hydrothermal fluids responsible for mineralization. The collected data on fault orientation and foliation were digitized and incorporated into the 3-D model to better understand the geometry and influence of structural controls on ore distribution.

These measurements, which are systematically presented in the "Structure" section of the thesis, along with the foliation and fault orientations (Figure 4.25 and Figure 4.26), emphasized the role of low-angle faulting in mineralizing processes, confirming that thrust reactivation played a major role in the emplacement of jasperoid and gold-bearing fluids.

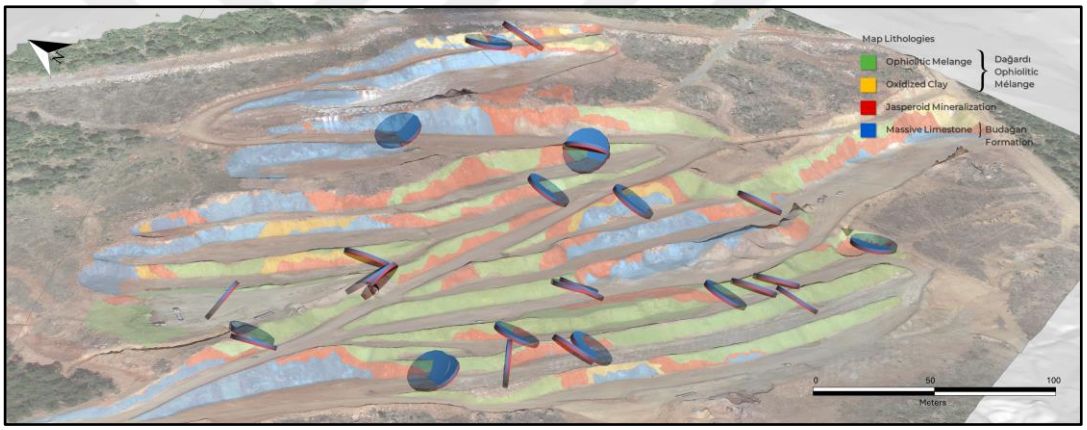

Figure 4.25. Fault orientation measurements from pit slopes plotted on open pit geological map. Fault measurements are seen as a disk shape, which all are oriented according to the dip and dip direction.

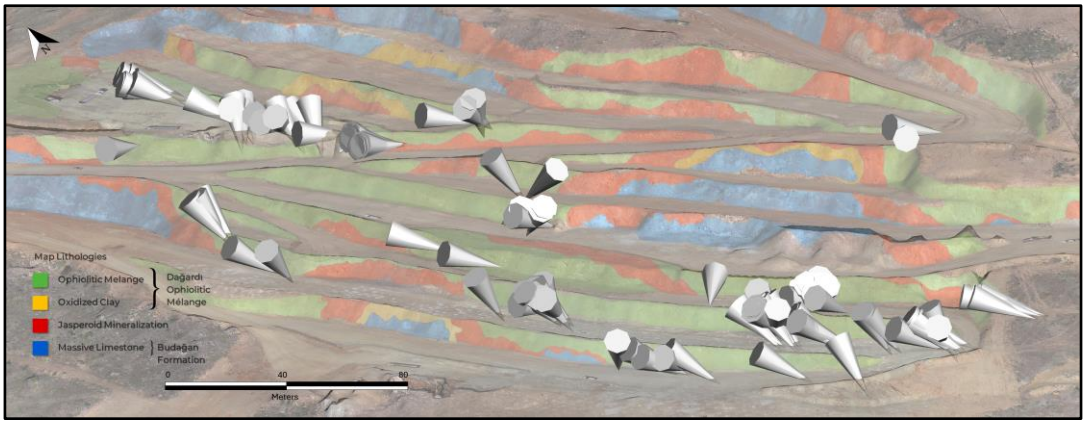

Figure 4.26. Foliation orientation measurements from pit slopes plotted on the open pit geological map. Foliation measurements are seen as a cone shape, which all are oriented according to the dip and dip direction.

Using Leapfrog Geo software, a deposit-scale 3D geological model was developed by integrating all previously mentioned datasets. The model illustrates a consistent stratigraphic sequence from top to bottom, consisting of ophiolitic mélange, jasperoid mineralization, and limestone, respectively. Additionally, the model clearly delineates the undulating nature of the low-angle fault within the jasperoid, which plays a key role in controlling the mineralization (Figure 4.27). Due to the modification of the original topography by mining activities, the model also reflects the presence of klippe and tectonic windows, representing remnants of autochthonous and allochthonous units, respectively. These structural features are well-observed in the model, providing insight into the complex tectonic and depositional history of the deposit. In Figure 4.28 below, the E–W cross sections of the geological model provide a closer and more detailed view of the relatively thick jasperoid ore zone and the continuous stratigraphic sequence.

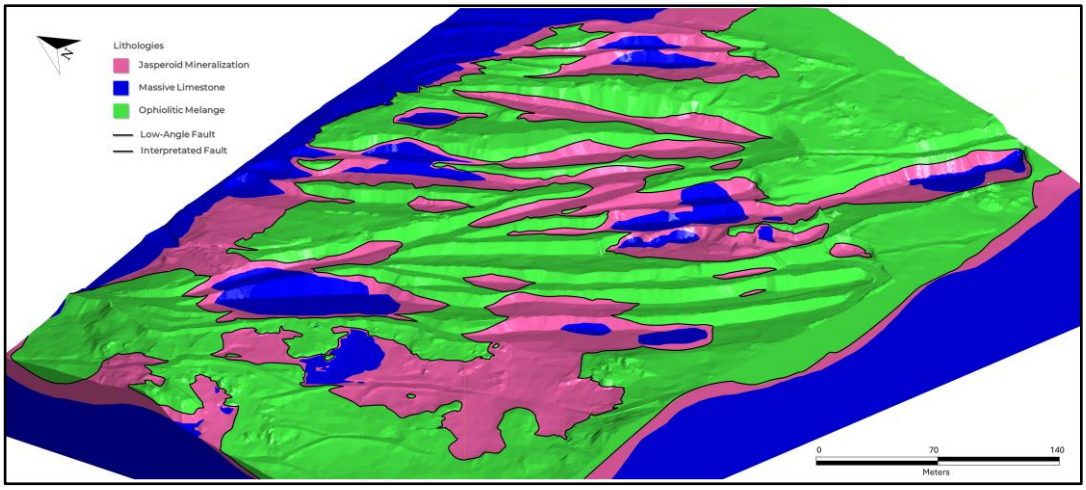

Figure 4.27. 3-D geological model of the Tavşan open-pit.

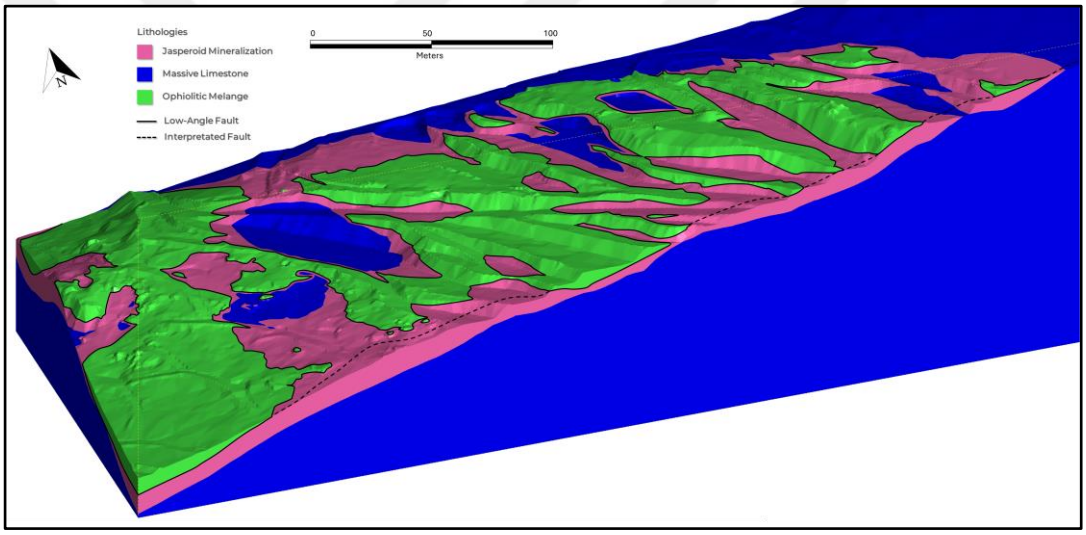

Figure 4.28. East–West cross section of 3-D geological model of open pit.

The surface geological map was compared with the 3-D geological model to verify the accuracy of the subsurface interpretations. This comparison highlighted a strong correlation between surface-mapped lithologies and those identified in the subsurface model. For instance, the continuity of the jasperoid body along low-angle fault was confirmed in both surface mapping and the 3-D model, illustrating the structural control on mineralization in the open-pit area.

Below figures illustrate a NW–SE- and ENE–WSW-oriented 3-D cross-sections, showing the comparison between the geological model and the surface geological

map (Figure 4.29 and Figure 4.30). The continuity of key lithological units, particularly the jasperoid body, is clearly visible and strongly correlates between these two separate studies (Figure 4.29). The structural control exerted by low-angle fault is well represented, confirming the accuracy of the subsurface model. Separate legends and colour codes for the map and model ensures clarity in visualizing the distribution of units, reinforcing the consistency of the geological interpretation across both datasets (Figure 4.30).

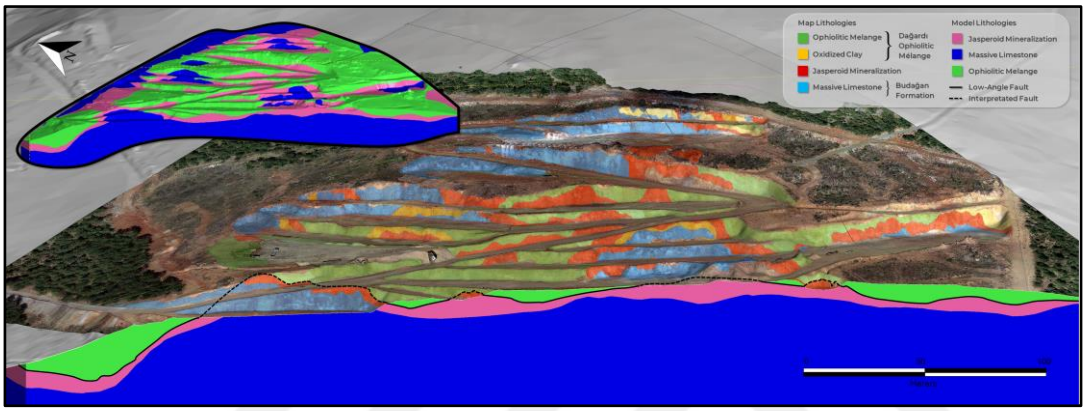

Figure 4.29. NW–SE-oriented 3-D cross-section comparing the geological model and surface geological map. Two separate legends and colour codes are used to differentiate between the lithologies in the geological map and those in the 3-D model.

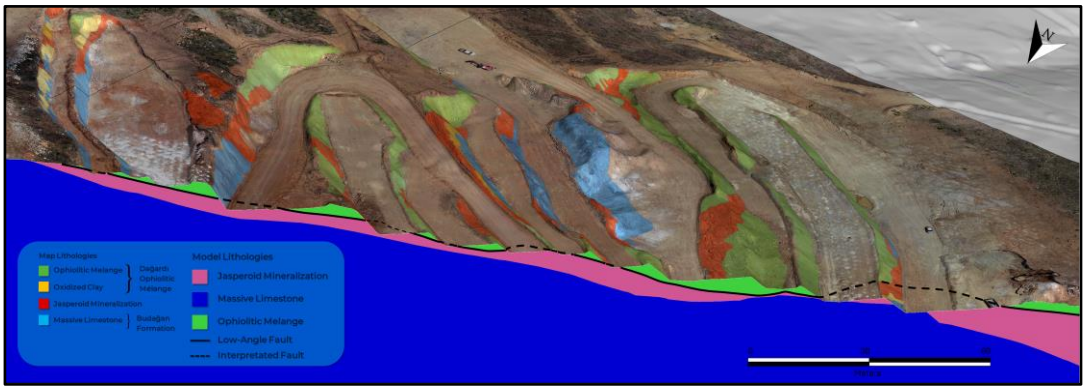

Figure 4.30. ENE–WSW-oriented 3-D cross-section showing the lateral extent of mineralization and the distribution of lithological units.

The gold ore zone grade model was generated by utilizing assay values derived from diamond drill core samples. To accurately define the geometry and distribution of mineralization, the search ellipsoid was designed with careful consideration of the

nature of gold mineralization within the deposit. The structural measures, such as fault orientations and foliation data, were integrated into the model to better align the geometry of the ore zones with the known structural controls on mineralization.

Two cut-off grades were applied in the grade model: a 1.5 ppm Au cut-off to define high-grade domains and a 0.5 ppm Au cut-off for low-grade domains. The use of these cut-off values allowed for the clear identification of both high-grade and low-grade zones of gold mineralization. The higher cut-off was particularly useful for focusing on the most economically significant parts of the ore body, while the lower cut-off provided a broader view of the mineralized zones. This approach ensured that the model could capture the full range of grade variability, offering valuable insights into the distribution of gold mineralization within the deposit.

Figure 4.31 offers a comprehensive view of the entire ore zone, highlighting the gradational changes in grade across different parts of the deposit. The colour-coded scale facilitates an easy comparison of high-grade ore zones with lower-grade areas, aiding in the understanding of the lateral extent of mineralization throughout the ore body.

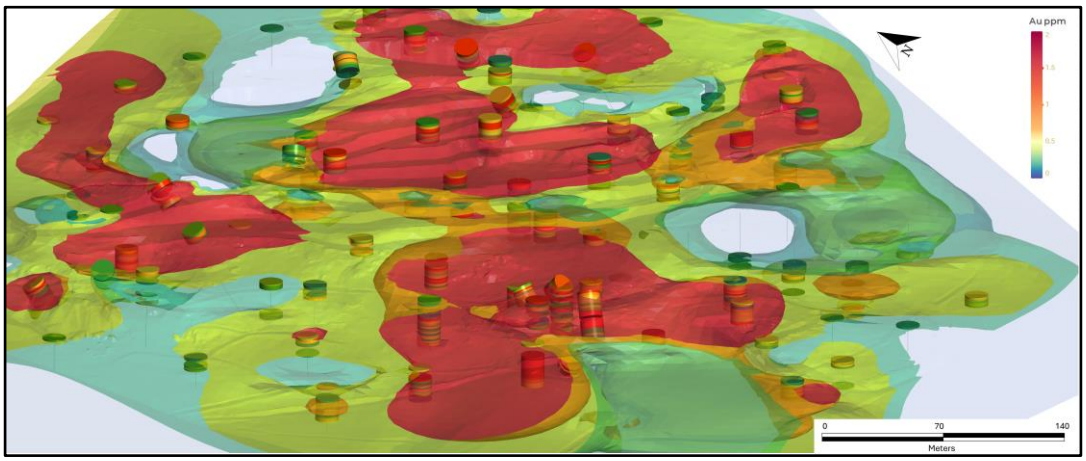

Figure 4.31. The gold grade model, depicted with a colour-coded scale, illustrates the spatial distribution of gold grades throughout the deposit. Red zones represent high-grade areas where Au values exceed 1.5 ppm, while blue zones indicate areas with gold below 0.25 ppm. The intermediate grades are represented by green (0.25 to 0.5 ppm) and orange (0.5 to 1.5 ppm) colours. The gradual colour transition from red to blue provides a visual representation of how gold mineralization decreases across the deposit.

The spatial correlation between high assay values from core samples and the modelled high-grade zones confirms the continuity of rich mineralized zones within the deposit (Figure 4.32).

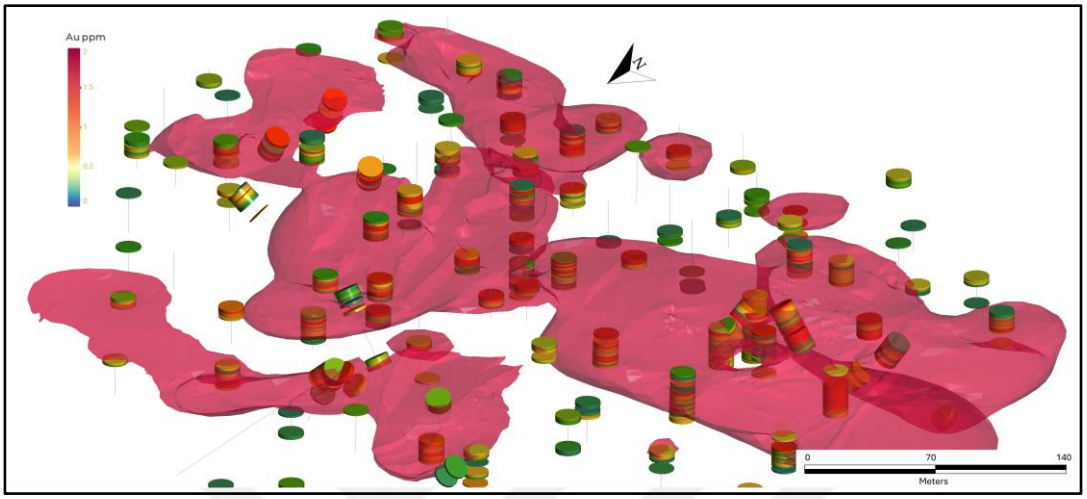

Figure 4.32. The high-grade mineralization zones within the deposit, showing areas where assay values exceed 1.5 ppm Au. The figure focuses on these high-grade zones, indicated in red, alongside assay data from the diamond drill holes.

The comparison between the grade model and the geological map demonstrates a strong correlation between the geological boundaries, fault contacts, and the distribution of mineralized zones within the deposit. The shallow and gently dipping orientation of both the grade model and the lithological units shown on the geological map aligns closely with the low-angle faulting system. This consistency reinforces the structural control on mineralization, particularly in relation to the jasperoid bodies that are closely associated with fault lines. The data presented in this figure not only supports the presence of both high-grade and low-grade zones but also reinforces the geological interpretation that these zones are structurally controlled, primarily associated with jasperoid bodies along fault lines. The comparison of the grade model with both the geological map and the 3-D geological model underscores the critical role that structural features, particularly faults, play in localizing mineralization and influencing the geometry of the ore zones.

The Figure 4.33, illustrates how the mineralized zones, both high-grade and low-grade, align with the mapped lithological boundaries and fault contacts, confirming

the structural control of mineralization. The jasperoid bodies associated with gently dipping structures are evident in both the geological map and the grade model (Figure 4.34).

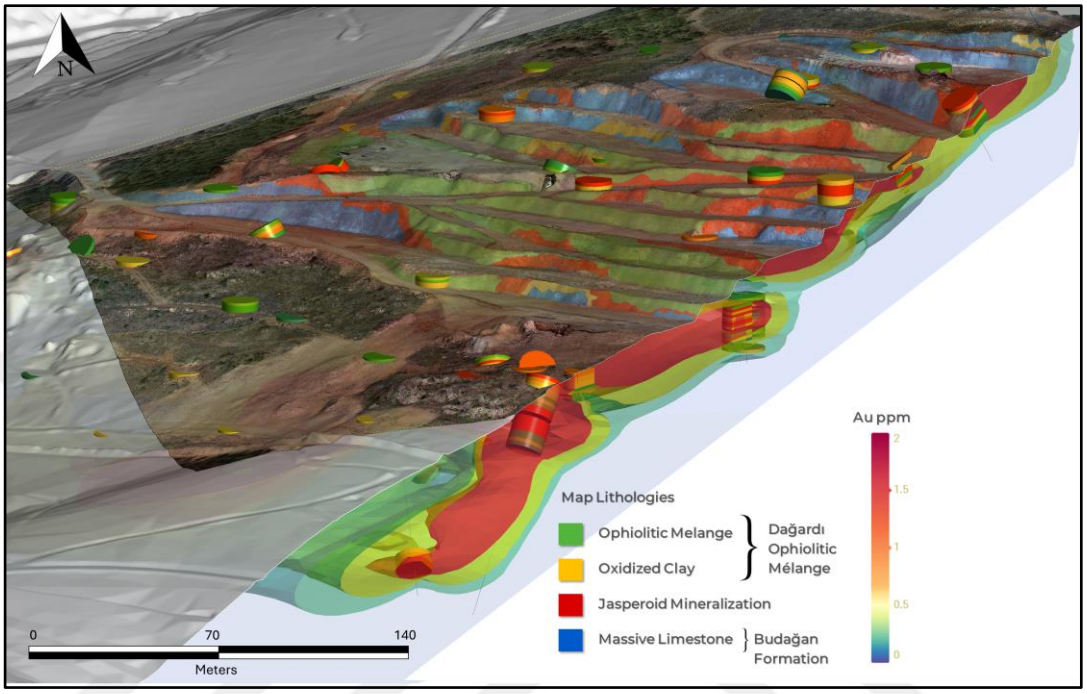

Figure 4.33. NE–SW-oriented cross-section of the grade model, showing the correlation between the shallow-dipping ore zones and the geological map of the open-pit area.

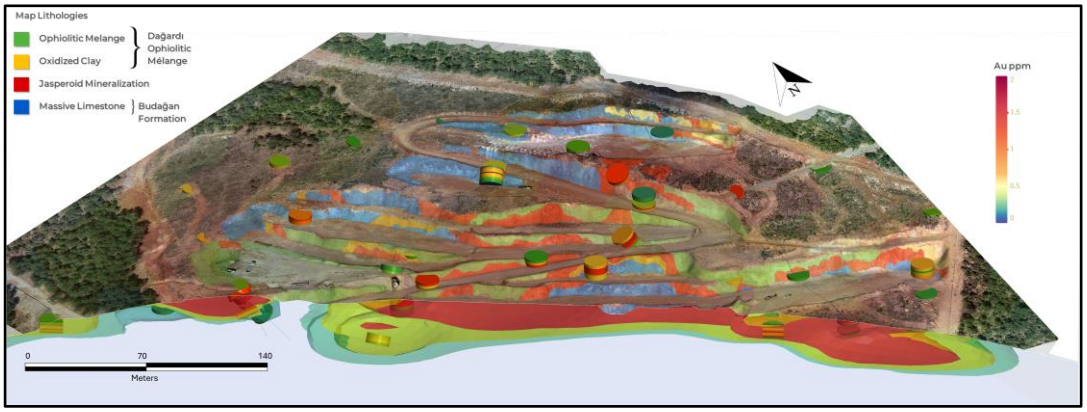

Figure 4.34. NW–SE-oriented cross-section of the grade model, depicting the same correlation between shallow-dipping ore zones and the geological map.

Additionally, the final phase of mineralization is associated with quartz-carbonate veins, which crosscut the earlier jasperoid mineralization and typically contain

antimony, primarily in the form of stibnite. This phase of mineralization was modelled separately to better understand its relationship with the gold mineralization in the ore zones. The spatial distribution of gold (Au) and antimony (Sb) in the model provides insight into how these two mineralizing events are interconnected. The Au-Sb model is illustrated in Figure 4.35, highlighting the distinct but related nature of these mineralization phases.

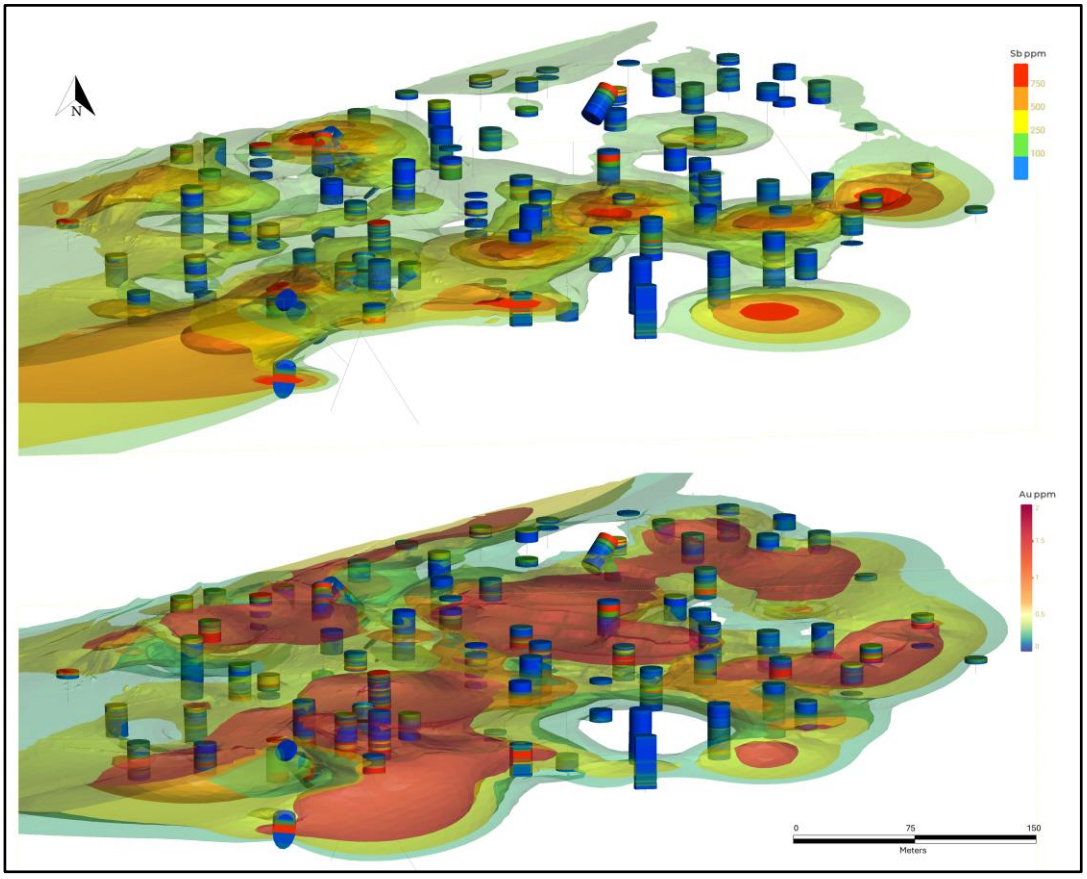

Figure 4.35. The spatial distribution of gold (Au) and antimony (Sb) in the grade model.

The integration of detailed geological, structural, and assay data into the open-pit model provides a robust framework for ongoing resource development and future exploration. The understanding of lithological continuity, fault control on mineralization, and grade distribution will aid in optimizing pit design, targeting new drill holes, and refining resource estimates.

4.3 Mineralization Style of the Tavşan Deposit

The Tavşan Gold Deposit is a geologically complex system that has been the focus of various studies, resulting in multiple classifications and interpretations of its mineralization style. The characteristic of the deposit is aligning with several deposit types -such as epithermal, Carlin-type, and listwanite-hosted systems. This section synthesizes previous research and integrates observations from this study to provide a comprehensive understanding of the deposit's classification and formation. However, to determine the precise type of deposit, further studies are needed.

The Tavşan Prospect can be broadly categorized as a sediment-hosted epithermal gold deposit, with several distinctive characteristics (cf. Armstrong, 2006; Bektaş, 2020), incorporating the following basic features:

- Sedimentary host rock (predominantly limestone).
- The presence of trace elements such as arsenic (As), antimony (Sb), mercury (Hg), and thallium (Tl) is notable.
- Mineralization occurs in lithologically-controlled jasperoid-hosted formations at shallow levels, while deeper mineralization is structurally controlled and rich in silica.
- Extensional faulting plays a significant role in creating conduits for mineralization.
- Similar-age intrusive possibly nearby (heat, fluid and/or metal source).

Additionally, researchers (Larson & Erler, 1993), have classified Tavşanlı prospect as an epithermal gold deposit based on specific features:

- An Au-associated epithermal trace element litho-geochemical signature -characterized by elements such as Au, Ag, As, Sb, and Zn- is evident at Örencik.
- Host rocks are compressively deformed mélange rocks, including serpentine and greywacke; the local stress regime is apparently

compressional, and the major mineralization controlling structure is a low angle thrust fault along which extensive brecciation, which is not obvious. Although more local brecciation is restricted to silicified areas.

- Silicification and Sb metallisation, both present at Örencik, are permissive to epithermal mineralization.
- In other mélange terrains such as that represented by the Franciscan of the Coastal Ranges in California, USA, epithermal mineralization is more Hg-rich and alteration is silica-carbonate rather than silicification (Shields, 2019).
- However, neither the Sb metallization nor the silicification alteration is, in the absence of other criteria, definitive of epithermal conditions.
- The similarity of litho-geochemical trace element signatures at Örencik is convincing evidence that the Au-Sb mineralization at Örencik formed under epithermal conditions.

Another classification (Kuşcu, 2020), suggests that Tavşan prospect could be a Carlin-type Mineral deposit, with features such as:

- Largely replacement bodies with visually subtle alteration dominated by decarbonatization and silicification (jasperoid) of dirty carbonate means silty carbonate host rocks.
- Containing Au in solid solution or as submicron particles in disseminated pyrite or marcasite.
- Occurrence along the rifted cratonic margin (passive margin evolution) within a variably carbonaceous sequence comprised of basal siliciclastic rocks and overlain predominantly by carbonate rocks.
- Shelf-slope sequence contains a large mass of thin-bedded, pyritic, and carbonaceous silty dolomitic limestone and marl, which are the primary host rocks.

- The presence of ore is often linked to extensional faults and various types of contractional structures, such as thrusts and folds. These structures are typically reactivated from earlier geological events, particularly regional compression, and thrusting occurrences.
- Secondary permeability and porosity are generated through the dissolution of carbonate along these faults, leading to the formation of collapse-solution breccias and karstic cavities. This facilitates the flow of fluids and contributes to the development of strata-bound orebodies (J. W. Hedenquist & Lowenstern, 1994; White & Hedenquist, 1995).
- The gold mineralized zone is predominantly hosted within sedimentary formations and is structurally controlled. Notably, there is no indication of associated magmatic activity in close proximity to the mineralization.

The example of Carlin Type Mineral Deposit in Türkiye (Kuşcu, 2020);

- Tavşan Gold & Silver Deposit (Dağardı, Kütahya)
- Söğüt Gold Deposit (Dudaş, Bilecik)
- Mollakara Gold Deposit (Diyadin, Ağrı)

Yiğit (2005, 2009) reviewed previous research and stated that Tavşan prospect is a listwanite-hosted deposits, hosted by ophiolitic ultramafic rocks, mainly serpentinites, are associated with thrust faults, normal faults, and shear zones, which are favourable loci for high-fluid flow and related mineralization with silica-carbonate alteration (listwanitization). Gold mineralization typically post-dates the serpentinization process (Uçurum, 2000). The Tethyan ophiolitic mélanges, of course, control the distribution of the deposits Kaymaz, Tavşan, Karaağac, and Narman. An intimate Sb-Au association is present in some prospects, such as at Tavşan in the Dağardı Sb district (2.5 Mt at 5.75% Sb; Ersecen, 1989) and Karaağac in Muratdağı Sb district. On the other hand, the Au-Sb association is a characteristic feature of many low-temperature mineralizing systems, and it is also strongly linked

to epizonal orogenic gold deposits, as discussed by Groves and Goldfarb (2015). Groves and Goldfarb (2015) identified epizonal orogenic gold deposits as systems forming in shallow crustal levels, often characterized by a strong Au-Sb association. These deposits typically develop in compressional to extensional tectonic regimes, where structural controls, such as thrust faults and folds, facilitate fluid flow and mineral deposition. The Au-Sb association in such deposits is attributed to the similar solubility and mobility of gold and antimony in hydrothermal fluids, enabling their co-precipitation under low-temperature and low-pressure conditions (Groves and Goldfarb, 2015).

According to this thesis study, classification of the Tavşan gold deposit can be a ***carbonate replacement type deposit***. The Tavşan gold deposit exhibits several characteristics that strongly align with those observed in carbonate replacement type (CRT) deposits, suggesting that this classification is the most appropriate for this deposit. CRT deposits typically form through the interaction of mineralizing fluids with carbonate rocks, leading to the replacement of these rocks by mineralized zones rich in metals like gold, silver, and base metals. The Tavşan gold deposit shares many key features with CRT deposits, particularly in terms of its mineralization patterns, structural controls, and lithological associations.

One of the most compelling arguments for classifying the Tavşan gold deposit as a CRT deposit is its carbonate-rich host rock, predominantly limestone, which is typical of such deposits. The replacement of carbonate by jasperoid, a key alteration product, is a hallmark of CRT deposits, as evidenced in the Tavşan gold deposit where jasperoid formation is pervasive, particularly along fault zones and contacts with ophiolitic units. The jasperoid bodies are structurally controlled, forming along thrust and detachment faults, which have facilitated the movement of mineralizing fluids. This replacement process has been well-documented in similar CRT deposits worldwide, where mineralization tends to be localized in structurally prepared zones, including fault planes and brecciated zones within carbonate sequences.

Furthermore, the geochemical signature of the Tavşan gold deposit, with elevated concentrations of elements such as gold (Au), antimony (Sb), and arsenic (As), is consistent with CRT deposits, where these elements are commonly associated with mineralized zones. The presence of replacement textures in the Tavşan gold deposit where the original carbonate matrix is replaced by silica-rich jasperoid and mineralized with gold, also mirrors the replacement-style mineralization typical of CRT systems.

Moreover, the structural control on the mineralization at Tavşan gold deposit, particularly the role of low-angle faults, is another feature aligning it with CRT deposits. The formation of collapse breccias and karstic cavities due to carbonate dissolution along fault zones, as observed in Tavşan, is a key mechanism that enhances the porosity and permeability of the host rock, allowing for extensive fluid flow and mineral deposition. This fluid interaction is characteristic of CRT deposits, where the dissolution of carbonate creates secondary porosity, leading to the formation of ore bodies along these fault-controlled pathways.

Kuşçu (2020) proposed that the Tavşan gold deposit aligns with Carlin-type mineral deposits. While both Carlin and CRT deposits share similar characteristics such as carbonate-rich host rocks and structural controls, CRT deposits are more strongly associated with jasperoid formation and the replacement of carbonate by silica and sulfide mineralization. The critical distinction lies in the role of associated magmatic activity. CRT deposits frequently exhibit evidence of proximal magmatic influence, such as the nearby Eğrigöz granitoid in Tavşan gold deposit, which likely provided heat and fluids driving mineralization. In contrast, Carlin-type deposits typically lack such a magmatic connection and are primarily linked to rifted cratonic margin settings, which are not explicitly evident at Tavşan.

While the main phase of mineralization at Tavşan aligns with carbonate replacement processes, the final phase of mineralization, represented by quartz-carbonate veining and the deposition of antimony (Sb), suggests an epithermal system overprint the earlier CRT mineralization. This epithermal phase is characterized by the presence

of stibnite and other antimony-bearing minerals within the quartz-carbonate veins, which crosscut the jasperoid mineralization.

The geological and structural setting of the quartz-carbonate veins at Tavşan is consistent with epithermal mineralization, which often forms in extensional environments where faults and fractures provide conduits for mineralizing fluids. In the case of Tavşan gold deposit, these veins are hosted within the jasperoid-altered limestone and are spatially associated with structural zones, indicating that they formed in response to continued hydrothermal activity after the primary phase of gold mineralization. The antimony mineralization observed within these veins is also characteristic of epithermal systems, as Sb is commonly associated with low-temperature, shallow-level hydrothermal processes. The evidence, such as the colloform banding and crystalline textures of quartz in the veins, supports the idea that this final phase of mineralization is distinct from the earlier CRT phase, representing a separate hydrothermal event and epithermal mineralization.

In summary, while the Tavşan gold deposit primarily exhibits features consistent with carbonate replacement type mineralization, the quartz-carbonate veining and antimony mineralization represent a subsequent phase of epithermal mineralization. The deposit thus reflects a complex mineralization history with both deep-seated carbonate replacement processes and later, shallow-level epithermal activity, providing a comprehensive example of multi-phase mineralization typical of structurally complex ore deposits.

CHAPTER 5

CONCLUSIONS

The Tavşan gold deposit has been the focus of detailed geological studies to unravel its complex mineralization processes. This thesis employed a combination of field geological mapping, core logging, structural analysis, geochemical interpretations, petrography and Electron Probe Micro-Analysis (EPMA), integrated into a comprehensive 3-D geological model to achieve a comprehensive understanding of the deposit. These methodologies have provided a robust framework for understanding the mineralization patterns, structural controls, and depositional mechanisms at the Tavşan gold deposit, with implications for both academic research and practical exploration strategies.

- Detailed **geological mapping** was conducted at a scale of **1:5000**, identifying the key lithological units, including the **Dağardı ophiolitic mélange**, **micritic limestones of the Budağan formation**, and **jasperoid mineralization**.
- **Petrographic studies** examined thin sections from each rock type in the region and mineralized zones, revealing the textural relationships between ore minerals and host rocks, helping to establish the type of lithologies.
- **Geochemical surface sampling** across the deposit provided a comprehensive understanding of the distribution of key trace elements such as **gold (Au)**, **antimony (Sb)**, **arsenic (As)**, and **mercury (Hg)**, which are closely associated with the mineralization process.
- The geochemical analysis identified distinct **elemental anomalies** (Au, As, Sb), which were mapped and correlated with **structural features**. Faults

acted as conduits for **hydrothermal fluids**, controlling the distribution of jasperoid and the associated mineralization.

- **Open Pit Slope Mapping** at a **1:100 scale** offered high-resolution structural data, capturing critical features such as **fault zones**, **jasperoid extensions**, **mineralized breccias, and their relations**, directly observable due to ongoing mining activities.
- **Diamond drill core logging** provided detailed insights into the subsurface geology and the spatial distribution of mineralization. Relogging of **18,853 meters** of drill core and analysis of **8,332 core assays** were critical for constructing the **3-D geological model** and the **grade model** for the mineralization.
- Structural measurements from fault planes, bedding, and foliations revealed a complex fault system, dominated by **low-angle faults, primary thrust, reactivated as detachment fault**. These faults played a critical role in channelling hydrothermal fluids, facilitating **mineralization** within **jasperoid bodies**.
- The thrust faults were later reactivated by extensional tectonics, forming **detachment faults**, which further localized mineralization. **Kinematic indicators** such as C-S fabrics and slickensides confirmed the structural movement along these faults.
- Fault reactivation during subsequent tectonic events facilitated the formation of mineralized breccias, further localizing mineralization along pre-existing fault zones.
- A **3-D geological model** was constructed using **Leapfrog Geo** software, integrating **drill core data, assay results, and structural measurements**. The model confirmed the continuity of **jasperoid mineralization** along thrust and detachment faults, highlighting the structural controls on the deposit.

- The model demonstrated the role of fault reactivation in localizing mineralization and showed that the **grade distribution** of gold was aligned with the major **structural zones**.

The Tavşan gold deposit can be classified as a **carbonate replacement type (CRT) deposit**, characterized by the following features:

- **Jasperoid replacement of carbonate rocks**, particularly along fault zones, driven by hydrothermal fluids that precipitated gold.
- **Fault-controlled mineralization**, where **low-angle thrust, and detachment faults** served as the primary conduits for the fluids responsible for jasperoid and gold deposition.
- **Replacement textures**, where the original carbonate rock was replaced by **silica** (jasperoid) and mineralized with gold, showing evidence of structural control.
- **Multistage mineralization**, where an initial CRT phase was followed by an **epithermal overprint**, characterized by quartz-carbonate veining and antimony mineralization.

Future studies should focus on:

- **Further geochemical analysis** across different mineralized zones to refine the understanding of trace element distributions and their relationship to ore deposition.
- Further studies are needed to investigate the **post-mineralization fault** in greater detail, as understanding its impact on both surface features and subsurface mineralization is essential
- Expanding the **3-D geological model** to incorporate additional drill data, structural interpretations and measures.

The integration of structural, geochemical, and geological data in this study offers a framework for understanding **similar mineral deposits** in the region. The identification of structural controls on mineralization provides valuable guidance for future **exploration strategies** in the Tavşanlı Zone and other structurally complex terrains in Anatolia.

REFERENCES

Akay, E. (2009). Geology and petrology of the Simav Magmatic Complex (NW Anatolia) and its comparison with the Oligo-Miocene granitoids in NW Anatolia: implications on Tertiary tectonic evolution of the region. *International Journal of Earth Sciences*.

Akdeniz, N., & Konak, N. (1979). Simav-Emet Tavşanlı-Dursunbey-Demirci yörelerinin jeolojisi. *Mineral Research and Exploration*.

Akgün, E., & Özden, S. (2019). Plio-Quaternary stress states along the Kütahya Fault and surroundings, NW Turkey. *Turkish Journal of Earth Sciences*.

Alexandre, P. (2021). *Practical Geochemistry*.

Angelier, J., Lybéris, N., Le Pichon, X., Barrier, E., & Huchon, P. (1982). The tectonic development of the hellenic arc and the sea of crete: A synthesis. *Tectonophysics*, *86*(1–3). https://doi.org/10.1016/0040-1951(82)90066-X

Ariana Resources. (1996). *Red Rabbit Project: The Tavsan Sector – Prospect Summary*

Ariana Resources. (2012). *The Tavsan Sector – Prospect Summary*. *44*(0).

Ariana Resources. (2016). *RNS Results from Tavsan Scoping Study*.

Ariana Resources. (2016). *Tavsan Scoping Study*.

Ariana Resources. (2017). *RNS Tavsan Exploration Targets*.

Ariana Resources. (2017). *Significant Resource Development Upside at Tavsan*. 110265(February), 110493.

Ariana Resources. (2018). *RNS Tavsan Resource*.

Ariana Resources. (2018). *Tavsan Resource Update*. 11(1), 1–5. http://link.springer.com/10.1007/978-3-319-59379-1%0Ahttp://dx.doi.org/10.1016/B978-0-12-420070-8.00002-

7%0Ahttp://dx.doi.org/10.1016/j.ab.2015.03.024%0Ahttps://doi.org/10.1080/07352689.2018.1441103%0Ahttp://www.chile.bmw-motorrad.cl/sync/showroom/lam/es/bike/urb

Ariana Resources. (2019). *Tavşan RockSaw Sampling Report*. October

Ariana Resources. (2020). *RNS Tavsan Channel Sampling Results*.

Ariana Resources. (2020a). *50% Increase in Tavsan Resource* (Issue June 2020).

Ariana Resources. (2020a). *RNS Tavsan Channel Sampling Results.*

Ariana Resources. (2020b). High-Grade Zones Identified At Tavsan (Vol. 25, Issue 1.) http://dx.doi.org/10.1016/j.jss.2014.12.010%0Ahttp://dx.doi.org/10.1016/j.sbspro.2013.03.034%0Ahttps://www.iiste.org/Journals/index.php/JPID/article/viewFile/19288/19711%0Ahttp://citeseerx.ist.psu.edu/viewdoc/download?doi=10.1.1.678.6911&rep=rep1&type=pdf%0Ahtt

Ariana Resources. (2020b). *RNS Tavsan Resource Increase.*

Armijo, R., Meyer, B., Hubert, A., & Barka, A. (1999). Westward propagation of the North Anatolian fault into the northern Aegean: Timing and kinematics. *Geology*, *27*(3), 267–270. https://doi.org/10.1130/0091-7613(1999)027<0267:WPOTNA>2.3.CO;2

Armstrong, T. (2006). *Technical Report and Resource Estimate On The Tavşan Gold Property West Central Turkey* (Issue 123).

Arpart, E. (1969). The rift system of the Western Turkey; thoughts on its development. *Bulletin of the Mineral Research and Exploration Institute of Turkey*, *October*, 85–106.

Arpat, E., & Bingöl, E. (1969). The Rift System of the Western Turkey; Thoughts on It's Development.

Aydin, B. (2007). Koyunoba Plutonu (Simav-Kütahya) Karakoca Yöresi Polimetalik Damar Tipi Cevherleşmesinin Jenetik İncelenmesi. 1-60

Bacak, G. (2003). 2003, Bacak - Dağardı Güneyi (Kütahya) Ofiyolitinin Jeolojisi ve Jeokimyasal Özellikleri. *İTÜ Dergisi*.

Barka, A. A. (1988). Strike-Slip Fault Geometry in Turkey & It's Influence on Earthquake Activity. *Tectonics*, *7*(3), 663–684.

Baş, H. (1986). Domaniç-Tavşanlı-Kütahya- Gediz Yöresinin Tersiyer Jeolojisi. *Geological Engineering*, *17*.

Bektaş, R. (2020). *Tavsan Mineral Resources Estimate 2020 Review* (Vol. 110, Issue i.)

Bektaş, R. (2020). *Tavsan Resource Tecnical Report*.

Boucher, K. (2016). The structural and fluid evolution of the Efemçukuru epithermal gold deposit, Western Turkey (Issue June).

Bozkurt, E. (2000). Timing of extension on the Buyuk Menderes Graben, western Turkey, and its tectonic implications. *Geological Society Special Publication*, *173*, 385–403. https://doi.org/10.1144/GSL.SP.2000.173.01.18

Bozkurt, E. (2001). Neotectonics of Turkey-a synthesis. *Geodinamica Acta*

Bozkurt, E. (2003). Origin of NE-trending basins in Western Turkey. *Geodinamica Acta*, *16*(2–6), 61–81. https://doi.org/10.1016/S0985-3111(03)00002-0

Bozkurt, E. (2007). Extensional vs. Contractional origin for the southern Menderes shear zone, SW Turkey: Tectonic and metamorphic implications. *Geological Magazine*, *144*(1), 191–210. https://doi.org/10.1017/S0016756806002664

Bozkurt, E., & Graham Park, R. (1999). The structure of the palaeozoic schists in the southern menderes massif, western Turkey: A new approach to the origin of the main menderes metamorphism and its relation to the Lycian Nappes. *Geodinamica Acta*, *12*(1), 25–42. https://doi.org/10.1080/09853111.1999.11105329

Bozkurt, E., & Mittwede, S. K. (2001). Introduction to the Geology of Turkey - A

synthesis. *International Geology Review*, *43*(7), 578–594. https://doi.org/10.1080/00206810109465034

Bozkurt, E., & Mittwede, S. K. (2005). Introduction: Evolution of continental extensional tectonics of Western Turkey. *Geodinamica Acta*, *18*(3–4), 153–165. https://doi.org/10.3166/ga.18.153-165

Bozkurt, E., & Oberhänsli, R. (2001). Menderes Massif (Western Turkey): Structural, metamorphic and magmatic evolution - A synthesis. *International Journal of Earth Sciences*, *89*(4), 679–708. https://doi.org/10.1007/s005310000173

Bozkurt, E., & Sözbilir, H. (2004). Tectonic evolution of the Gediz Graben: Field evidence for an episodic, two-stage extension in western Turkey. *Geological Magazine*, *141*(1), 63–79. https://doi.org/10.1017/S0016756803008379

Bozkurt, E., & Sözbilir, H. (2006). Evolution of the large-scale active Manisa Fault, southwest Turkey: Implications on fault development and regional tectonics. *Geodinamica Acta*, *19*(6), 427–453. https://doi.org/10.3166/ga.19.427-453

Bozkurt, E., Satır, M., & Buğdaycıoğlu, Ç. (2011). Surprisingly young Rb/Sr ages from the Simav extensional detachment fault zone, northern Menderes Massif, Turkey. *Journal of Geodynamics*, *52*(5), 406–431. https://doi.org/10.1016/j.jog.2011.06.002

Bozkurt, E., Winchester, J. A., Mittwede, S. K., & Ottley, C. J. (2006). Geochemistry and tectonic implications of leucogranites and tourmalines of the southern Menderes Massif, southwest Turkey. *Geodinamica Acta*, *19*(5), 363–390. https://doi.org/10.3166/ga.19.363-390

Bozkurt, E., Winchester, J. A., Ruffet, G., & Rojay, B. (2008). Age and chemistry of miocene volcanic. Rocks from the Kiraz Basin of the Küçük menderes graben: Its significance for the extensional tectonics of Southwestern Anatolia, Turkey. *Geodinamica Acta*, *21*(5–6), 239–257. https://doi.org/10.3166/ga.21.239-257

Burchfiel, B. C. (2008). The Aegean: A natural laboratory for tectonics. *IOP Conference Series: Earth and Environmental Science*, *2*, 012001. https://doi.org/10.1088/1755-1307/2/1/012001

Candan, O., Çetinkaplan, M., Oberhänsli, R., Rimmelé, G., & Akal, C. (2005). Alpine high-P/low-T metamorphism of the Afyon Zone and implications for the metamorphic evolution of Western Anatolia, Turkey. *Lithos*, 102-124.

Catlos, E., Jacob, L., Oyman, T., & Sorensen, S. (2012). Long-Tern Exhumation of an Aegean Metamorphic Core Complex Granitoids in the Northern Menderes Massif Western Turkey. *American Journal of Science*, 534-571.

Corbett, G. (2002). Epithermal Gold for Explorationists. *Applied Geoscientific Practice and Research in Australia, February*, 1–26.

Çiftçi, N. B., & Bozkurt, E. (2008). Folding of the Gediz Graben fill, SW Turkey: Extensional and/or contractional origin. *Geodinamica Acta*, *21*(3), 145–167. https://doi.org/10.3166/ga.21.145-167

Çiftçi, N. B., & Bozkurt, E. (2009a). Evolution of the Miocene sedimentary fill of the Gediz Graben, SW Turkey. *Sedimentary Geology*, *216*(3–4), 49–79. https://doi.org/10.1016/j.sedgeo.2009.01.004

Çiftçi, N. B., & Bozkurt, E. (2009b). Pattern of normal faulting in the Gediz Graben, SW Turkey. *Tectonophysics*, *473*(1–2), 234–260. https://doi.org/10.1016/j.tecto.2008.05.036

Çiftçi, N. B., & Bozkurt, E. (2010). Structural evolution of the Gediz Graben, SW Turkey: Temporal and spatial variation of the graben basin. *Basin Research*, *22*(6), 846–873. https://doi.org/10.1111/j.1365-2117.2009.00438.x

Delibaş, O., Moritz, R., Chiaradia, M., Selby, D., Ulianov, A., & Revan, M. K. (2017). Post-collisional magmatism and ore-forming systems in the Menderes massif: new constraints from the Miocene porphyry Mo–Cu

Pınarbaşı system, Gediz–Kütahya, western Turkey. *Miner Deposita*, 1157-1178.

Ellero, A., Frassi, C., Göncüoğlu, M. C., Lezzerini, M., Marroni, M., Ottria, G., Pandolfi, L., Sayit, K., & Tamponi, M. (2021). Geological, Structural and Mineralogical Approach to Investigate the Evolution of Low- and very Low-Grade Metamorphic Units from the Intra-Pontide Suture Zone, Central Pontides, Turkey. In *Journal of Earth Science* (Vol. 32, Issue 6, pp. 1512–1527). https://doi.org/10.1007/s12583-021-1445-8

Ersoy, Y., Helvaci, C., Sözbilir, H., Erkül, F., & Bozkurt, E. (2008). A geochemical approach to Neogene-Quaternary volcanic activity of western Anatolia: An example of episodic bimodal volcanism within the Selendi Basin, Turkey. *Chemical Geology*, *255*(1–2), 265–282. https://doi.org/10.1016/j.chemgeo.2008.06.044

Etzel, T. M., Catlos, E. J., Cemen, I., Ozerdem, C., Oyman, T., & Miggins, D. (2020). Documenting Exhumation in the Central and Northern Menderes Massif (Western Turkey): New Insights from Garnet-Based P-T Estimates and K-Feldspar 40Ar/39Ar Geochronology. *Lithosphere*.

Exploration, M. R. (n.d.). *Explanatory Booklet of J21 Kütahya.* Mineral Research and Exploration.

Gessner, K., Collins, A. S., Ring, U., & Güngör, T. (2004). Crustal fluid flow in hot continental extension: Tectonic framework of geothermal areas and mineral deposits in western Anatolia. *Geological Society, London, Special Publications, 453(1), SP453.7*. https://doi.org/10.1144/SP453.7

Gessner, K., Markwitz, V., & Güngör, T. (2017). Structural and thermal history of poly-orogenic basement: U-Pb geochronology of granitoid rocks in the southern Menderes Massif, Western Turkey. *Journal of the Geological Society, 161(1), 93–101*. https://doi.org/10.1144/0016-764902-166

Glodny, J., & Hetzel, R. (2007). Precise U-Pb ages of syn-extensional Miocene

intrusions in the central Menderes Massif, western Turkey. *Geological Magazine, 144(2), 235–246.* https://doi.org/10.1017/S0016756806003025

Goodman, S. (2007). *Kiziltepe, Kinik, Tavsan Structural Memo* (Issue April).

Graham, M. L. (2016). Stratigraphic And Petrographic Characterization of Hs Epithermal Au-Ag Mineralization at The Tv Tower District, Biga Peninsula, NW Turkey.

Groves, I. (2016). *MEMO Tavşan*.

Groves, I. (2018). *Tavşan Quick Review and Work Program*. Figure 1, 10–27.

Göncüoğlu, M. C. (2008). Geology.

Göncüoğlu, M. C. (2010). Introduction To The Geology Of Turkey: Geodynamic Evolution Of The Pre-Alpine And Alpine Terranes.

Göncüoğlu, M. C. (2018). *Geology* (pp. 57–73). https://doi.org/10.1007/978-3-319-64392-2_5

Göncüoğlu, M. C. (2019). A review of the geology and geodynamic evolution of tectonic terranes in Turkey. In *Modern Approaches in Solid Earth Sciences* (Vol. 16, pp. 19–72). Springer International Publishing. https://doi.org/10.1007/978-3-030-02950-0_2

Göncüoğlu, M. C. (n.d.). Mineral Resources of Turkey. https://doi.org/10.1007/978-3-030-02950-0

Hasözbek, A., Akay, E., Erdoğan, B., Satır, M., & Siebel, W. (2010). Early Miocene granite formation by detachment tectonics or not? A case study from the northern Menderes Massif (Western Turkey). *Journal of Geodynamics*, 67-80.

Hasözbek, A., Erdoğan, B., Satır, M., Siebel, W., Akay, E., Doağn, G. D., & Taubals, H. (2014). Al- in-hornblende Thermobarometry and Sr-Nd-Pb-O isotopic

compositions of the Alaçam Granite in NW Anatolia (Turkey). *Turkish Journal of Earth Science* .

Hagemann, S. G., & Brown, P. E. (2020). Exploration for Epithermal Gold Deposits. *Gold in 2000, January 2000*, 245–277. https://doi.org/10.5382/rev.13.07

Hedenquist, J. (2006). Comments on October visit to Tavsan project, Biga Peninsula, Turkey.

Hedenquist, J. W. (2004). Observations on gold prospects at Altintepe, Central Pontides, and Tavsan, Biga region, Republic of Turkey.

Hedenquist, J. W. (2006). Field observations. In *Mitteilungen der Versuchsanstalt fur Wasserbau, Hydrologie und Glaziologie an der Eidgenossischen Technischen Hochschule Zurich* (Issue 194).

Hedenquist, J. W., & Lowenstern, J. B. (1994). The role of magmas in the formation of hydrothermal ore deposits. *Nature*, *370*(6490), 519–527. https://doi.org/10.1038/370519a0

Hedenquist, J., & Arribas, A. (2000). *Exploration for Epithermal Gold Deposits*. https://www.researchgate.net/publication/228840402

Hinsbergen, D. J. J. (2010). A key extensional metamorphic complex reviewed and restored: The Menderes Massif of western Turkey. *Earth-Science Reviews*, *102*(1–2), 60–76. https://doi.org/10.1016/j.earscirev.2010.05.005

Hinsbergen, D. J. J., Dekkers, M. J., Bozkurt, E., & Koopman, M. (2010). Exhumation with a twist: Paleomagnetic constraints on the evolution of the Menderes metamorphic core complex, western Turkey. *Tectonics*, *29*(3). https://doi.org/10.1029/2009TC002596

Hinsbergen, D. J., Kaymakçı, N., Spakman, W., & Torsvik, T. H. (2010). Reconciling the geological history of western Turkey with plate circuits and mantle tomography. *Earth and Planetary Science Letters*.

Hinsbergen, D. J. J., & Schmid, S. (2012). Map-view restoration of Aegean-west Anatolian accretion and extension since the Eocene.

Hirst, J. (2013). Tavşan Property, West Central Turkey. Tetra Teck, 782, 22240112.

Hirst, J. (2018). Competent Persons Report for the Tavsan Property, West Central Turkey. www.tetratech.com

Howard, A. E., & Yüceer, C. (2005). *Tavsan Gold Property Report* (Issue June).

Howard, A. E., & Yüceer, C. (2006). *Tavsan Gold Property Report*. *September*.

Işık, V. (2004). Micro-tectonic features of Simav shear zone, northern Menderes massif, western. *Geological Bulletin of Turkey*.

Işık, V., & Tekeli, O. (2001). Late orogenic crustal extension in the Northern Menderes Massif (Western Turkey): Evidence for metamorphic core complex formation. *International Journal of Earth Science*.

Işık, V. (2012a). Orojenez ve Türkiye ' deki Tektonik Birlikler.

Işık, V. (2012b). Türkiye' deki Masifler.

Jolivet, L., Faccenna, C., Huet, B., Labrousse, L., Le Pourhiet, L., Lacombe, O., Lecomte, E., Burov, E., Denèle, Y., Brun, J. P., Philippon, M., Paul, A., Salaün, G., Karabulut, H., Piromallo, C., Monié, P., Gueydan, F., Okay, A. I., Oberhänsli, R., Driussi, O. (2013). Aegean tectonics: Strain localisation, slab tearing and trench retreat. *Tectonophysics*, *597–598*, 1–33. https://doi.org/10.1016/j.tecto.2012.06.011

Kaya, O. (1972). Tavşanlı Yöresi "Ofiolit" Sorununun Anaçizgileri.

Kaymakcı, N., Paul M. Van Dijk (2006). Neogene Tectonics of the Çankiri Basin (north Central Turkey). *The Bulletin of Turkish Association of Petroleum Geologists, Volume 13*, 27-56.

Kaymakcı, N. (2006). *Tavşanlı Report Commented*.

Kaymakcı, N., Kuşcu, İ., & Yüceer, C. (2004). *Tavşanli Gold Occurrence Field Repport*.

Ketin, İ. (1966). Geology of Turkey

Kirwin, D. J., & Royle, D. Z. (2018). Sediment-Hosted Gold Deposits in Southeast Asia. *Resource Geology*, *69*(2), 125–147. https://doi.org/10.1111/rge.12189

Kumral, M., Abdelnasser, A., & Budakoglu, M. (2016). Geochemistry of hydrothermal alteration associated with cenozoic intrusion-hosted Cu-Pb-Zn mineralization at Tavşanlı Area, Kütahya, NW Turkey. *Minerals*, *6*(1). https://doi.org/10.3390/min6010013

Kumral, M., Abdelnasser, A., Doner, Z., & Karaman, M. (2014). Geochemical investigations of Eğrigöz mineralization at the northern margin of Tauride-Anatolide platform: A case study from Tavşanli zone, Kütahya, Turkey. June.

Kuşcu, İ. (2007). Discussion on "Gold in Turkey - A missing link in Tethyan metallogeny." *Ore Geology Reviews*, *30*(2), 135–140. https://doi.org/10.1016/j.oregeorev.2006.01.004

Kuşcu, İ. (2020). Carlin-Type Gold Deposits : Characteristic Features And Exploration Systematics.

Larson, L. T., & Erler, Y. A. (1993). The epithermal lithogeochemical signature a persistent characterization of precious metal mineralization at Kursunlu and Orencik, two prospects of very different geology in western Turkey. *Journal of GeochemwalExploratton*, *47*, 321–331.

Leroux, G. M. (2016). Stratıgraphıc And Petrographıc Characterızatıon Of Hs Epıthermal Au-Ag Mıneralızatıon At The Tv Tower Dıstrıct, Bıga Penınsula, Nw Turkey. In *The Unıversıty Of Brıtısh Columbıa* (Issue May).

McKenzie, D., & Yilmaz, Y. (1991). Deformation and volcanism in western Turkey and the Aegean. *Bulletin - Technical University of Istanbul*, *44*(3–4), 345–373.

Mercier, J. L., Sorel, D., Vergely, P., & Simeakis, K. (1989). Extensional tectonic regimes in the Aegean basins during the Cenozoic. *Basin Research*, *2*(1), 49–71. https://doi.org/10.1111/j.1365-2117.1989.tb00026.x

Morrison, D. (2016). *Tavsan High Level Scoping Report*.

Odyssey Resources Limited. (2004). *Observations on gold prospects at Altintepe, Central Pontides , and Tavsan , Biga region , Republic of Turkey* (Vol. 1, Issue 613).

Okay, A. I. (1980). Mineralogy, Petrology, and Phase Relation of Glaucophane-Lawsonite Zone Blueschists Fom the Tavşanlı Region, Northwest Turkey. *Contributions to Mineralogy and Petrology*, *255*, 243–255.

Okay, A. I. (1980a). Lawsonite Zone Blueschists and a Sodic Amphibole Producing Reaction in the Tavşanll Region, Northwest Turkey. *Contrib Mineral Petrol*, *75*, 179–186.

Okay, A. I. (1980b). Mineralogy, Petrology, and Phase Relations of Glaucophane-Lawsonite Zone Blueschists From the Tavsanh Region, Northwest Turkey. *Contrib. Mineral. Petrol*, *72*, 243–255.

Okay, A. I. (1981a). Kuzeybatı Anadolu ' daki Ofiyolitlerin Jeolojisi ve Mavişist Metamorfizması (Tavşanlı - Kütahya). *Türkiye Jeoloji Kurumu Bülteni*, *24*(Şubat), 85–95.

Okay, A. I. (1981b). Lawsonite zone blueschists and a sodic amphibole producing reaction in the Tavşanli Region, Northwest Turkey. *Contributions to Mineralogy and Petrology*, *75*(3), 179–186. https://doi.org/10.1007/BF01166758

Okay, A. I. (1982). Contributions to Mineralogy and Petrology Incipient Blueschist Metamorphism and Metasomatism in the Tavşanlı Region, Northwest Turkey. *Contrib Mineral Petrol*, *79*, 361–367.

Okay, A. I. (1982). Incipient Blueschist Metamorphism and Metasomatism in the

Tavşanlı Region, Northwest Turkey. *Contributions to Mineralogy and Petrology*, 361–367.

Okay, A. I. (1984). Distribution and characteristics of the north-west Turkish blueschists. *Geological Society, London, Special Publications 1984*; v. 17; p. 455-466. doi:10.1144/GSL.SP.1984.017.01.33.

Okay, A. I. (2008). Geology of Turkey: A Synopsis. *Anschnitt*. http://jan.ucc.nau.edu/~rcb7/

Okay, A. I. (2009). Tavşanlı Zonu Anatolid-Torid Bloğunun Dalma Batmaya Uğramış Kuzey Ucu.

Okay, A. I. (2011). Tavşanlı Zone: The Northern Subducted Margin of the Anatolide-Tauride Block. *Bulletin of the Mineral Research and Exploration*, pp. 191-221.

Okay, A. I., & Tüysüz, O. (1999). Tethyan sutures of northern Turkey. *Geological Society Special Publication*, *156*, 475–515. https://doi.org/10.1144/GSL.SP.1999.156.01.22

Okay, A. I., Sunal, G., Sherlock, S., Altıner, D., Tüysüz, O., Kylander-Clark, A. R., & Aygül, M. (2013). Early Cretaceous sedimentation and orogeny on the active margin of Eurasia: Southern Central Pontides, Turkey. *Tectonics*.

P & E Mining Consultants Inc (2006). *Technical Report and Resource Estimate on The Alous Copper Silver Property Morocco for Odyssey Resources Limited*.

Pirajno ; , F., Ünlü, T., Dönmez, C., & Bahadır Şahin, M. (2019). *Modern Approaches in Solid Earth Sciences Volume 16 Mineral Resources of Turkey*. Springer.

Pirajno, F. (2000). Ore Deposits and Mantle Plumes. In *Ore Deposits and Mantle Plumes*. https://doi.org/10.1007/978-94-017-2502-6

Pirajno, F. (2009). Hydrothermal processes and mineral systems. I n *Hydrothermal*

Processes and Mineral Systems. https://doi.org/10.1007/978-1-4020-8613-7

Plunder, A., Agard, P., Chopin, C., & Okay, A. I. (2013). Geodynamics of the Tavşanlı Zone, Western Turkey: Insights into subduction/obduction processes. *Tectonophysics*, *608*, 884–903. https://doi.org/10.1016/j.tecto.2013.07.028

Plunder, A., Agard, P., Chopin, C., Pourteau, A., & Okay, A. I. (2015). Accretion, underplating and exhumation along a subduction interface: From subduction initiation to continental subduction (Tavşanli zone, W. Turkey). *Lithos*, *226*, 233–254. https://doi.org/10.1016/j.lithos.2015.01.007

Pourteau, A., Oberhänsli, R., Candan, O., Barrier, E., & Vrielynck, B. (2015). Neotethyan closure history of Western Anatolia: a geodynamic discussion. *International Journal of Earth Sciences*, *105*(1), 203–224. https://doi.org/10.1007/s00531-015-1226-7

Pourteau, A., Candan, O., & Oberhänsli, R. (2010). High- pressure metasediments in central Turkey: Constraints on the Neotethyan closure history. *Tectonics*.

Richards, J. P. (2015). Tectonic, magmatic, and metallogenic evolution of the Tethyan orogen: From subduction to collision. *Ore Geology Reviews*, *70*, 323–345. https://doi.org/10.1016/j.oregeorev.2014.11.009

Ring, U., & Collins, A. S. (2005). U–Pb SIMS dating of synkinematic granites: timing of core-complex formation in the northern Anatolide belt of western Turkey. *Journal of the Geological Society*, 289-298.

Roche, V., Bouchot, V., Beccaletto, L., Jolivet, L., Guillou-Frottier, L., Tuduri, J., Bozkurt, E., Oguz, K., & Tokay, B. (2019). Structural, lithological, and geodynamic controls on geothermal activity in the Menderes geothermal Province (Western Anatolia, Turkey). *International Journal of Earth Sciences*, *108*(1), 301–328. https://doi.org/10.1007/s00531-018-1655-1

Rossetti, F., Crespo Blanc, A., Riguzzi, F., Leroux, E., Pavlopoulos, K., Bellier, O., & Kapsimalis, V. (2018). IEREK Interdisciplinary Series for Sustainable

Development The Structural Geology Contribution to the Africa-Eurasia Geology Basement and Reservoir Structure, Ore Mineralisation and Tectonic Modelling. In *Technology & Innovation*. http://www.springer.com/series/15883

Sánchez, M. G., Mcclay, K. R., King, A. R., & Wijbrams, J. R. (2016). Cenozoic Crustal Extension and Its Relationship to Porphyry Cu-Au-(Mo) and Epithermal Au-(Ag) Mineralization in the Biga Peninsula, Northwestern Turkey*. *Special Publications of The Society of Economic Geologists*. www.segweb.org/SP19-

Sener, K., Arar, M., Wedin, F., & Goodman, S. (2009). Contrasting Styles of Epithermal Gold Mineralisation at the Kiziltepe and Tavsan Deposits, Western Turkey. Smart Science for Exploration and Mining, Proceedings of the 10th Biennial SGA Meeting of The Society for Geology Applied to Mineral Deposits, Townsville Australia, 17th - 20th August 2009, 2, 848–850.

Seyitoglu, G., & Scott, B. C. (2015). Timing of Cenozoic extensional tectonics in Western Turkey. *Geological Society*. http://jgs.lyellcollection.org/

Seyitoglu, G., Esat, K., Aktug, B., & Analysis, S. (2019). New Contributions to the Neotectonics of Türkiye : Towards an Alternative Perspective Türkiye ' nin Neotektoniğine Yeni Katkılar : Başka Bir Bakış Açısına Doğru New Contributions to the Neotectonics of Türkiye : Towards an Alternative. January.

Seyitoglu, G., Scott, B. C., & Rundle, C. C. (1992). Timing of Cenozoic extensional tectonics in west Turkey. *Journal - Geological Society (London), 149*(4), 533–538. https://doi.org/10.1144/gsjgs.149.4.0533

Sharp, I. R., & Robertson, A. H. F. (2006). Tectonic-sedimentary evolution of the western margin of the Mesozoic Vardar Ocean: Evidence from the Pelagonian and Almopias zones, northern Greece. *Geological Society Special Publication, 260*(January 2006), 373–412. https://doi.org/10.1144/GSL.SP.2006.260.01.16

Shields, J. E. (2019). *Mixed Igneous Origin and Large Range of Peak Metamorphic*

Pressure and Temperature Conditions of Blocks in a Melange.

Sillitoe, R. H. (2010). Model for Porphyry Copper Systems. *Economic Geology*, http://ezproxy.utas.edu.au/login?url=http://search.proquest.com/docview/742899977?accountid=14245%5Cnhttp://www.segweb.org/

Şengör, C. & Yılmaz, Y. (1981). *Tethyan Evolution of Turkey: A Plate Tectonic Approach*. *75*, 181–241. https://doi.org/10.1016/0040-1951(81)90275-4

Şengör, C. (1987). Tectonic of the Tethysides: Orogenic Collage Development in a Collisional Setting.

Taymaz, T., Yilmaz, Y., & Dilek, Y. (2007). The geodynamics of the Aegean and Anatolia: Introduction. *Geological Society Special Publication*, *291*, 1–16. https://doi.org/10.1144/SP291.1

Teck Cominco. (1997). *Petrography Report*.

Teck Comminco. (1997). *Tavşan Report.*

Thomson, S. N., & Ring, U. (2006). Thermochronologic evaluation of postcollision extension in the Anatolide orogen, western Turkey. *Tectonics*.

Topuz, G., & Okay, A. I. (2014). Prograde calcite to aragonite transformation in the Gümüşyeniköy micritic limestones (Tavşanlı, NW Turkey). *International Journal of Earth Sciences*, *103*(8), 2271–2272. https://doi.org/10.1007/s00531-014-1049-y

Topuz, G., Okay, A. I., Altherr, R., Meyer, H. P., & Nasdala, L. (2006). Partial high-pressure aragonitization of micritic limestones in an accretionary complex, Tavşanli Zone, NW Turkey. *Journal of Metamorphic Geology*, *24*(7), 603–613. https://doi.org/10.1111/j.1525-1314.2006.00657.x

Uçurum, A. (2000). Listwaenites in Turkey: Perspectives on formation and precious metal concentration with reference to occurrences in east-central Anatolia. *Ofioliti*, *25*(1), 15–29.

Uğurlu, B. (2019). *Kızıltepe Low-Sulphidation Epithermal Deposit (Sındırgı, Balıkesir): An Example for Relay-Ramp-Hosted Epithermal Gold Mineralization In Western Turkey*. Middle East Technical University.

Uzel, B., Sözbilir, H., & Özkaymak, Ç. (2012). Neotectonic evolution of an actively growing superimposed basin in Western Anatolia: The inner bay of izmir, Turkey. *Turkish Journal of Earth Sciences*, *21*(4), 439–471. https://doi.org/10.3906/yer-0910-11

Uzel, B., Langereis, C. G., Kaymakci, N., Sözbilir, H., Özkaymak, Ç., & Özkaptan, M. (2015). Paleomagnetic evidence for an inverse rotation history of Western Anatolia during the exhumation of Menderes core complex. *Earth and Planetary Science Letters*, *414*(April), 108–125. https://doi.org/10.1016/j.epsl.2015.01.008

Uzel, B., Özkaymak, Ç., & Sözbilir, H. (2013). Neogene-Quaternary evolution of the Manisa Basin: Evidence for variation in the stress pattern of the Izmir-Balikesir Transfer Zone, Western Anatolia. In *Journal of Geodynamics* (Vol. 65, pp. 117–135). https://doi.org/10.1016/j.jog.2012.06.004

Valli, F. (2006a). *Tavsan Geology Final Report.*

Valli, F. (2006a). *Tavşan Project Report* (Vol. 46, Issue 1). https://academic.oup.com/sleep/article/33/9/1201/2454639

Valli, F. (2006b). *Tavsan Preliminary Report.*

Valli, F. (2006b). *Tavsan Report.*

Valli, F. (2006b). *Tavşan Project Review (Issue 1).*

Valli, F. (2006c). *Tavsan Report.* https://academic.oup.com/sleep/article/33/9/1201/2454639

Volkov, A. V., Serafimovski, T., Kochneva, N. T., Tomson, I. N., & Tasev, G. (2006). The Alshar epithermal Au-As-Sb-Tl deposit, southern Macedonia.

Geology of Ore Deposits, *48*(3), 175–192. https://doi.org/10.1134/S1075701506030020

White, N. C., & Hedenquist, J. W. (1995). Epithermal Gold Deposits: Styles, Characteristics & Exploration. *SEG Discovery*, *23*, 1–13. https://doi.org/10.5382/segnews.1995-23.fea

White, N. C., & Hedenquist, J. W. (1990). Epithermal environments and styles of mineralization: variations and their causes, and guidelines for exploration. *Journal of Geochemical Exploration*, *36*, 445–474.

White, N. C., & Hedenquist, J. W. (1995). Epithermal Gold Deposits: Styles, Characteristics & Exploration. *SEG Discovery*, *23*, 1–13. https://doi.org/10.5382/segnews.1995-23.fea

Whitney, D. L., & Bozkurt, E. (2002). Metamorphic history of the southern Menderes massif, Western Turkey. *Bulletin of the Geological Society of America*, *114*(7), 829–838. https://doi.org/10.1130/0016-7606(2002)114<0829:MHOTSM>2.0.CO;2

Yiğit, Ö. (2005). Gold in Turkey - A missing link in Tethyan metallogeny. *Ore Geology Reviews*, *28*(2), 147–179. https://doi.org/10.1016/j.oregeorev.2005.04.003

Yiğit, Ö. (2009). Mineral Deposits of Turkey in Relation to Tethyan Metallogeny: Implications for Future Mineral Exploration. *Economic Geology*. www.kitco.com

Yigit, O., Nelson, E. P., Hitzman, M. W., & Hofstra, A. H. (2003). Structural controls on Carlin-type gold mineralization in the gold bar district, Eureka County, Nevada. *Economic Geology*, *98*(6), 1173–1188. https://doi.org/10.2113/gsecongeo.98.6.1173

Yılmaz, H., & Şener, A. K. (2013). Low-sulfidation epithermal Au-Ag mineralization in the Sındırgı district, Balıkesir province, Turkey. *Turkish*

Journal of Earth Sciences, *22*(4), 485–522. https://doi.org/10.3906/yer-1204-10

Yılmaz, H., Sönmez, F. N., Akay, E., Şener, A. K., & Tezel Tufan, S. (2013). Low-sulfidation epithermal Au-Ag mineralization in the Sındırgı district, Balıkesir province, Turkey. *Turkish Journal of Earth Sciences*, *22*(4), 485–522. https://doi.org/10.3906/yer-1204-10

Yılmaz, Y. (1991). Deformation and Volcanism in Western Turkey and the Aegean. https://www.researchgate.net/publication/279763211

Yılmaz, Y. (1997). Geology of western Anatolia Tectonic development of the Bitlis-Zagros suture mountains SE Anatolia View project. https://www.researchgate.net/publication/292784054

APPENDICES

A. Summary Table of Followed Methodology

Methodology	Description	Quantity
Searching & Reviewing	Company Reports	30 Reports
	Literature (papers, thesis, public reports etc.)	70 Papers
	MTA Studies & Reports	10 Old Reports
	MTA-100k Booklets	J21-J22-I21
	MTA-25k Raster Data	I21-C-3, I22-D-4, I22-D-3, J21-B-2, J21-B-3, J22-A-1,2,3,4
Digitizing	MTA-25k Vector Layers	I21-C-3, I22-D-4, I22-D-3, J21-B-2, J21-B-3, J22-A-1,2,3,4
Reviewing	Available Existing Data	Geological Maps, Assay Results, Drilling etc.
Outcrop Mapping	Lithological Layer on GIS	1100 Outcrops
GPS Point	Way Points	2000 Points
Geological Interpolation	Geological Map	Lithological, Structural Features etc.
MagSus	Results for Each Lithological Units	20 Measurements
Specific Gravity	Results for Each Lithological Units	20 Measurements
Structural Measurements	Strike/Dip/Rake Values	250 Measurements
Petrography Studies	Thin Section Images & Results	20 Polished Thin Sections
Electron Micro-Probe Analysis	Potential Mineralization	2 Ore Microscopy Samples
pXRF Analysis	36 Elements Results & GIS Layers	200 Measurements
Geochemical Rock Composite Sampling	Assay Results (FA, Multi Elements)	100 Samples
Quality Assurance & Control Measures	Laboratory Results	CRM's & Blanks
Geochemical Interpretation	Single & Multi Element- Graphs & Comments	iOGas Soil, Rock Sampling and Drilling
Cross Sections	High Resolution Long and Short Cross Sections	2 Cross Sections
Columnar Section	High Resolution Tectonostratigraphic Section	Covering All Formations
Discovering	Potential Other Mineral Occurrences	Mn, Sb, Cu, Zn, Au
Using of Leapfrog	Comparison of Grade & Geological Model	3-D Geological Model

B. Fault Measurement

Point ID	Easting	Northing	Strike	Dip	Rake	Sense	Set
TAV001	678688.57	4368392.35	223	45			Set 1
TAV002	680096.24	4369959.20	210	16			Set 1
TAV003	679158.95	4368997.91	249	39	30	N	Set 1
TAV004	678768.46	4368417.31	218	41			Set 1
TAV005	678707.92	4368280.35	215	44			Set 1
TAV006	678641.68	4368060.61	210	51			Set 1
TAV007	679621.92	4369691.86	225	48			Set 1
TAV008	679069.62	4368875.76	230	47			Set 1
TAV009	678933.97	4368691.34	225	33			Set 1
TAV010	679532.05	4369628.31	242	35			Set 1
TAV011	678922.30	4368690.86	252	21			Set 1
TAV012	678860.85	4368604.68	268	40			Set 1
TAV013	679320.28	4369163.50	182	41			Set 1
TAV014	679011.69	4369011.15	25	30	22	N	Set 2
TAV015	679011.69	4369011.15	12	50	24	N	Set 2
TAV016	679012.69	4369012.15	12	38	48	N	Set 2
TAV017	679013.24	4369015.00	41	51	18	S	Set 2
TAV018	679013.24	4369015.00	36	48	14	S	Set 2
TAV019	679013.24	4369015.00	51	51	5	S	Set 2
TAV020	680178.01	4370091.57	120	60	15	S	Set 2
TAV021	679113.98	4368971.45	121	83	60	N	Set 2
TAV022	679144.52	4368988.51	198	71			Set 2
TAV023	679364.54	4369281.87	19	53	10	S	Set 2
TAV024	678842.15	4368501.20	342	57			Set 2
TAV025	678904.05	4368622.67	335	64			Set 2
TAV026	678922.58	4367826.41	45	37	25	S	Set 3
TAV027	678790.89	4367940.88	220	32			Set 3
TAV028	678792.89	4367944.88	211	39	40	N	Set 3
TAV029	678918.03	4367843.62	22	29			Set 3
TAV030	678929.39	4367837.46	15	26			Set 3
TAV031	678884.67	4367910.83	28	20			Set 3
TAV032	678964.85	4368012.37	206	27			Set 3
TAV033	678991.18	4367939.10	2	35			Set 3
TAV034	678991.18	4367939.10	185	45			Set 3
TAV035	678991.18	4367939.10	185	49			Set 3
TAV036	678864.74	4367994.54	21	32			Set 3
TAV037	678852.54	4367985.10	281	53	10	N	Set 3
TAV038	678851.73	4367990.43	276	35			Set 3
TAV039	678811.94	4368040.58	268	52	15	S	Set 3
TAV040	678991.19	4367864.16	32	34			Set 3

TAV041	678840.52	4367889.69	78	35			Set 3
TAV042	678835.93	4367896.13	40	41			Set 3
TAV043	678813.10	4367917.38	253	84			Set 3
TAV044	678835.78	4367920.51	60	25			Set 3
TAV045	678906.45	4367852.31	60	33			Set 3
TAV046	678986.31	4367813.14	64	11			Set 3
TAV047	678885.51	4367908.15	34	32			Set 3
TAV048	679054.06	4367986.19	43	39			Set 3
TAV049	679044.09	4367998.14	31	13			Set 3
TAV050	678954.42	4367943.93	70	35			Set 3
TAV051	678961.15	4367909.44	70	38			Set 3
TAV052	678778.65	4368016.46	23	24			Set 3
TAV053	678788.65	4368020.46	61	23			Set 3
TAV054	678372.61	4367981.73	310	70	70	S	Set 4
TAV055	678368.21	4367980.82	70	46	27	S	Set 4
TAV056	678370.68	4367984.53	64	51	15	S	Set 4
TAV057	678340.21	4367959.34	82	60	10	S	Set 4
TAV058	678373.81	4367979.92	79	72	65	S	Set 4
TAV059	677552.67	4370301.51	110	46	35	S	Set 5
TAV060	677308.79	4372725.91	225	67	30	N	Set 5
TAV061	678007.83	4372891.30	244	65	28	N	Set 5
TAV062	678132.40	4373690.10	277	43	80	N	Set 5
TAV063	678124.25	4373697.34	299	66	40	N	Set 5
TAV064	678124.80	4373752.62	255	55	84	N	Set 5
TAV065	678129.34	4373753.32	285	65	85	N	Set 5
TAV066	678126.41	4373755.46	340	80	80	N	Set 5
TAV067	678124.71	4373757.54	248	83	80	N	Set 5
TAV068	678133.41	4373766.43	285	51	70	N	Set 5
TAV069	678131.71	4373767.43	272	50	60	N	Set 5
TAV070	678137.81	4373777.14	248	71	50	N	Set 5
TAV071	678142.10	4373777.16	22	57	75	N	Set 5
TAV072	678148.14	4373778.54	13	48	64	N	Set 5
TAV073	678147.42	4373770.68	5	48	53	N	Set 5
TAV074	678147.96	4373780.54	10	41	80	N	Set 5
TAV075	678153.34	4373779.72	35	75	35	S	Set 5
TAV076	678172.91	4373777.29	235	75	45	S	Set 5
TAV077	678179.27	4373777.01	218	72	30	S	Set 5
TAV078	678196.73	4373785.57	38	81	80	S	Set 5
TAV079	678198.38	4373783.11	40	82	75	N	Set 5
TAV080	678201.73	4373784.00	61	86	62	S	Set 5
TAV081	678186.67	4373712.93	47	41	64	N	Set 5
TAV082	678200.50	4373718.98	0	81	47	S	Set 5
TAV083	678181.36	4373698.61	52	81	73	S	Set 5

TAV084	678180.66	4373682.21	57	25	57	S	Set 5
TAV085	677722.43	4368598.75	72	74			Set 5
TAV086	675528.94	4367335.60	132	75	40	N	Set 6
TAV087	675495.11	4367339.59	350	88	10	N	Set 6
TAV088	675280.46	4367180.96	123	30	20	N	Set 6
TAV089	675130.46	4367141.65	128	21	20	S	Set 6
TAV090	675116.90	4367136.23	344	78	45	N	Set 6
TAV091	676139.30	4367665.05	320	62	60	S	Set 6

C. Foliation Measurement

Point ID	Easting	Northing	Elevation	Strike	Dip
TAV092	678937	4367789	1103	61	49
TAV093	678919	4367798	1102	4	31
TAV094	678891	4367814	1101	316	26
TAV095	678895	4367810	1101	7	36
TAV096	678887	4367814	1101	338	26
TAV097	678885	4367818	1101	347	32
TAV098	678876	4367824	1102	289	43
TAV099	678967	4367799	1107	292	32
TAV100	678968	4367800	1107	8	63
TAV101	678966	4367798	1107	18	32
TAV102	678969	4367800	1107	12	28
TAV103	678965	4367799	1107	15	40
TAV104	678967	4367798	1107	17	34
TAV105	678961	4367801	1106	346	28
TAV106	678950	4367807	1107	338	54
TAV107	678952	4367807	1107	343	49
TAV108	678934	4367815	1106	333	35
TAV109	678936	4367815	1106	351	28
TAV110	678935	4367816	1106	17	40
TAV111	678935	4367817	1106	10	35
TAV112	678935	4367815	1106	341	32
TAV113	678923	4367826	1107	325	37
TAV114	678923	4367826	1107	327	46
TAV115	678923	4367826	1107	323	39
TAV116	678923	4367826	1107	329	43

TAV117	678924	4367824	1107	281	45
TAV118	678925	4367823	1107	20	52
TAV119	678927	4367824	1107	32	55
TAV120	678924	4367822	1107	40	47
TAV121	678920	4367826	1106	44	31
TAV122	678920	4367826	1106	51	36
TAV123	678868	4367861	1106	350	51
TAV124	678869	4367864	1106	351	48
TAV125	678867	4367864	1106	340	33
TAV126	678868	4367860	1106	310	35
TAV127	678867	4367861	1106	313	37
TAV128	678866	4367863	1106	321	41
TAV129	678865	4367862	1106	335	43
TAV130	678868	4367866	1106	339	45
TAV131	678865	4367865	1106	332	16
TAV132	678867	4367866	1106	339	30
TAV133	678869	4367867	1106	321	56
TAV134	678866	4367868	1106	327	32
TAV135	678868	4367866	1106	329	43
TAV136	678865	4367864	1106	334	23
TAV137	678853	4367876	1106	335	54
TAV138	678804	4367925	1106	320	43
TAV139	678799	4367933	1106	351	32
TAV140	678796	4367960	1111	57	43
TAV141	678793	4367957	1111	15	48
TAV142	678794	4367958	1111	10	56
TAV143	678844	4367914	1113	21	16
TAV144	678854	4367896	1112	352	19
TAV145	678912	4367847	1112	112	12
TAV146	678926	4367838	1111	306	28
TAV147	678933	4367835	1111	272	32
TAV148	678936	4367834	1112	286	31
TAV149	678938	4367832	1112	268	35
TAV150	678934	4367832	1112	272	39
TAV151	678938	4367833	1112	262	50
TAV152	678938	4367831	1112	260	39
TAV153	678938	4367833	1112	264	35
TAV154	678935	4367830	1112	269	26
TAV155	678934	4367832	1112	265	42

TAV156	678941	4367831	1112	280	36
TAV157	678940	4367832	1112	311	23
TAV158	678937	4367829	1112	340	13
TAV159	678941	4367832	1112	321	13
TAV160	678941	4367822	1112	322	27
TAV161	678987	4367810	1112	16	12
TAV162	678989	4367808	1112	22	15
TAV163	678991	4367807	1112	18	17
TAV164	678988	4367805	1112	16	20
TAV165	678990	4367806	1112	32	13
TAV166	678879	4367915	1116	332	22
TAV167	678879	4367915	1116	266	42
TAV168	678879	4367915	1116	274	37
TAV169	678874	4367921	1116	270	31
TAV170	678874	4367921	1116	264	28
TAV171	679028	4368017	1161	63	37
TAV172	678994	4367910	1135	341	15
TAV173	678989	4367911	1134	275	8
TAV174	678881	4367977	1129	317	34
TAV175	678881	4367977	1129	303	52
TAV176	678874	4367982	1128	351	14
TAV177	678853	4367982	1122	332	10
TAV178	678853	4367982	1122	328	15
TAV179	678853	4367982	1122	337	8
TAV180	678853	4367985	1122	343	17
TAV181	678852	4367987	1122	338	13
TAV182	678852	4367987	1122	336	23
TAV183	678852	4367987	1122	341	18
TAV184	678842	4368000	1121	353	8
TAV185	678837	4368005	1122	70	27
TAV186	678839	4368002	1122	92	40
TAV187	678834	4368008	1122	63	23
TAV188	678832	4368005	1122	74	35
TAV189	678832	4368010	1121	308	35
TAV190	678829	4368015	1121	322	31
TAV191	678830	4368013	1121	314	21
TAV192	678824	4368020	1121	95	21
TAV193	678821	4368016	1121	101	18
TAV194	678819	4368015	1121	97	36

TAV195	678822	4368018	1121	89	24
TAV196	678821	4368025	1121	293	30
TAV197	678818	4368030	1121	27	24
TAV198	678808	4368052	1122	5	24
TAV199	678804	4368051	1122	10	18
TAV200	678806	4368048	1122	7	27
TAV201	678804	4368050	1122	12	22
TAV202	678806	4368051	1122	3	15
TAV203	678807	4368055	1122	15	25
TAV204	678805	4368057	1122	12	27
TAV205	678806	4368056	1122	20	19
TAV206	678806	4368058	1122	13	22
TAV207	678806	4368059	1122	25	17
TAV208	678886	4367933	1121	245	42
TAV209	678879	4367941	1121	352	54
TAV210	678784	4368015	1118	318	11

D. Bedding Plane Measurement

Point ID	Easting	Northing	Strike	Dip	Rock Type
TAV211	678473.7	4368347	283	40	Sandstone
TAV212	679194.1	4369426	250	77	Sandstone
TAV213	680182.7	4368512	84	45	Limestone
TAV214	680743	4368214	120	15	Limestone
TAV215	680857.1	4367564	284	16	Limestone
TAV216	678836.5	4367166	45	19	Sandstone
TAV217	678783.8	4367229	56	35	Mudstone
TAV218	678766.9	4367195	165	23	Mudstone
TAV219	678681.2	4367150	280	19	Mudstone
TAV220	678652.4	4367104	250	9	Limestone
TAV221	678546.3	4367014	336	34	Limestone
TAV222	678209.4	4367042	303	12	Limestone
TAV223	679498.5	4367546	323	9	Limestone
TAV224	679260.9	4367575	296	24	Limestone
TAV225	678912.8	4367562	283	28	Limestone
TAV226	679182.8	4367914	255	19	Limestone
TAV227	679810.6	4367868	180	20	Sandstone
TAV228	675000.8	4367096	126	12	Limestone
TAV229	675127.7	4367116	307	24	Limestone
TAV230	675396.7	4367227	170	35	Limestone
TAV231	677824.5	4368682	269	18	Sandstone
TAV232	674936.8	4367092	11	26	Limestone
TAV233	676830.1	4371211	239	69	Limestone
TAV234	679626.4	4368643	132	23	Limestone
TAV235	679323.3	4367986	274	21	Limestone
TAV236	679476.7	4369762	56	38	Sandstone
TAV237	679502.1	4369768	93	41	Sandstone
TAV238	678964.8	4368042	288	6	Limestone

E. Geological Maps

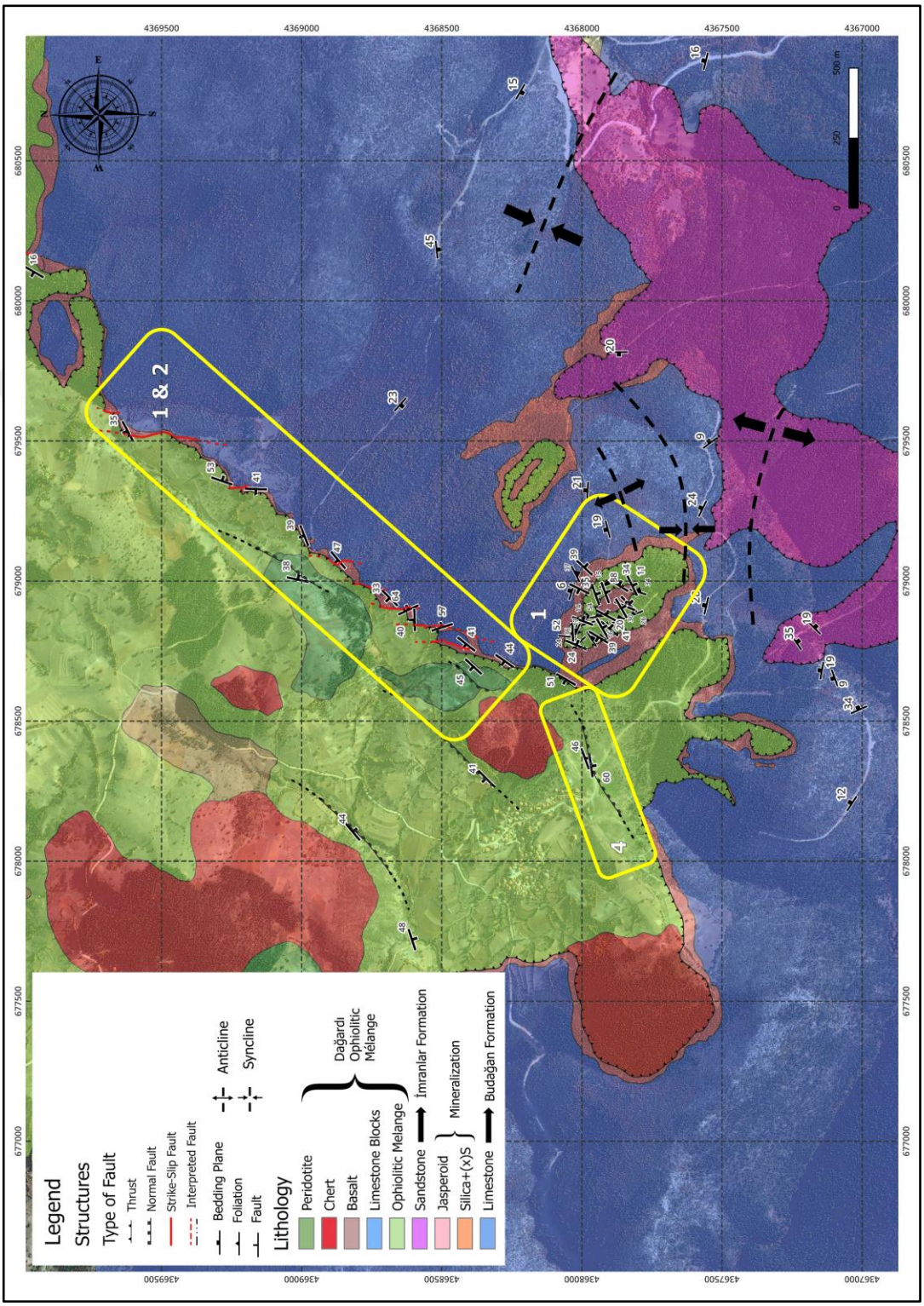

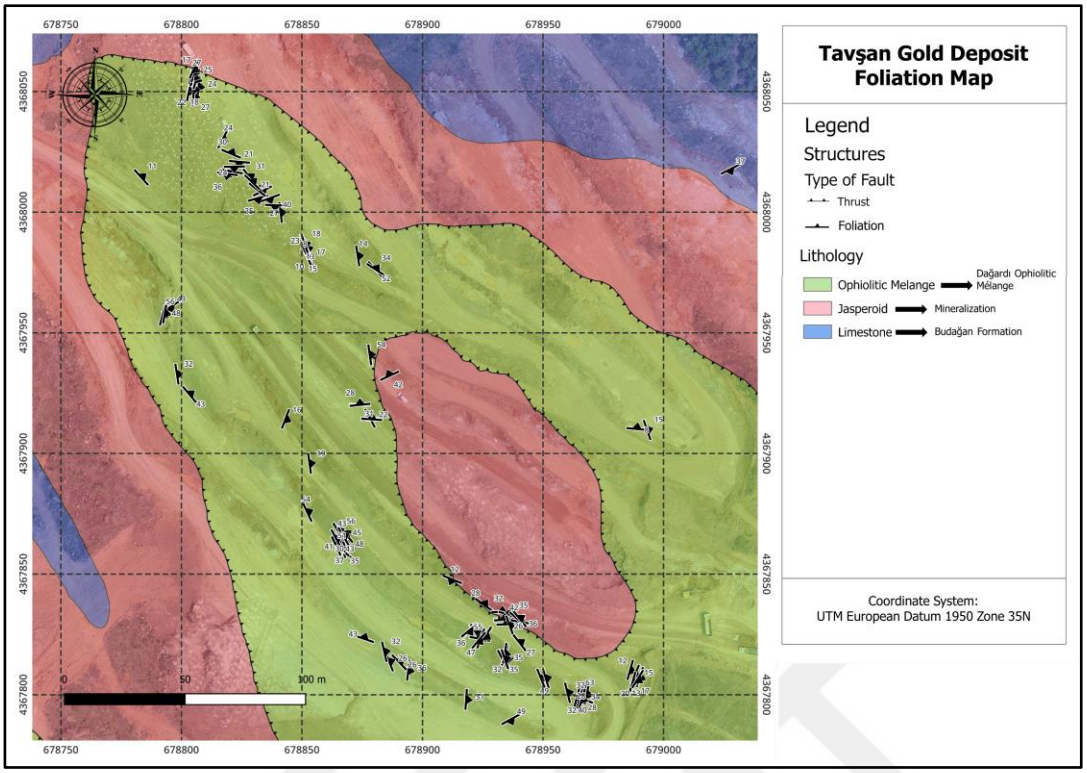
Tavşan Gold Deposit
Foliation Map
Legend
Structures
Type of Fault
Thrust
Foliation
Lithology
Ophiolitic Melange
Dağardı Ophiolitic Mélange
Jasperoid
Mineralization
Limestone
Budağan Formation
Coordinate System:
UTM European Datum 1950 Zone 35N
678750
678800
678850
678900
678950
679000
4368050
4368000
4367950
4367900
4367850
4367800
0
50
100 m

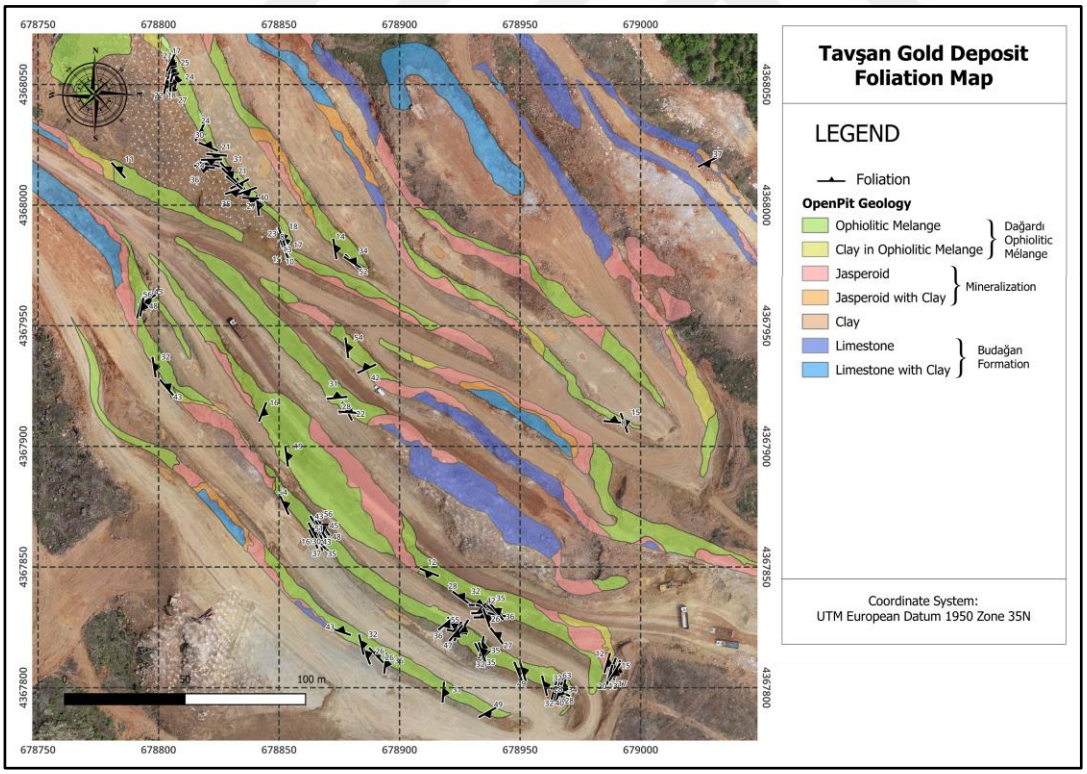
Tavşan Gold Deposit
Foliation Map
LEGEND
Foliation
OpenPit Geology
Ophiolitic Melange
Clay in Ophiolitic Melange
Dağardı Ophiolitic Mélange
Jasperoid
Jasperoid with Clay
Mineralization
Clay
Limestone
Limestone with Clay
Budağan Formation
Coordinate System:
UTM European Datum 1950 Zone 35N
678750
678800
678850
678900
678950
679000
4368050
4368000
4367950
4367900
4367850
4367800
0
50
100 m

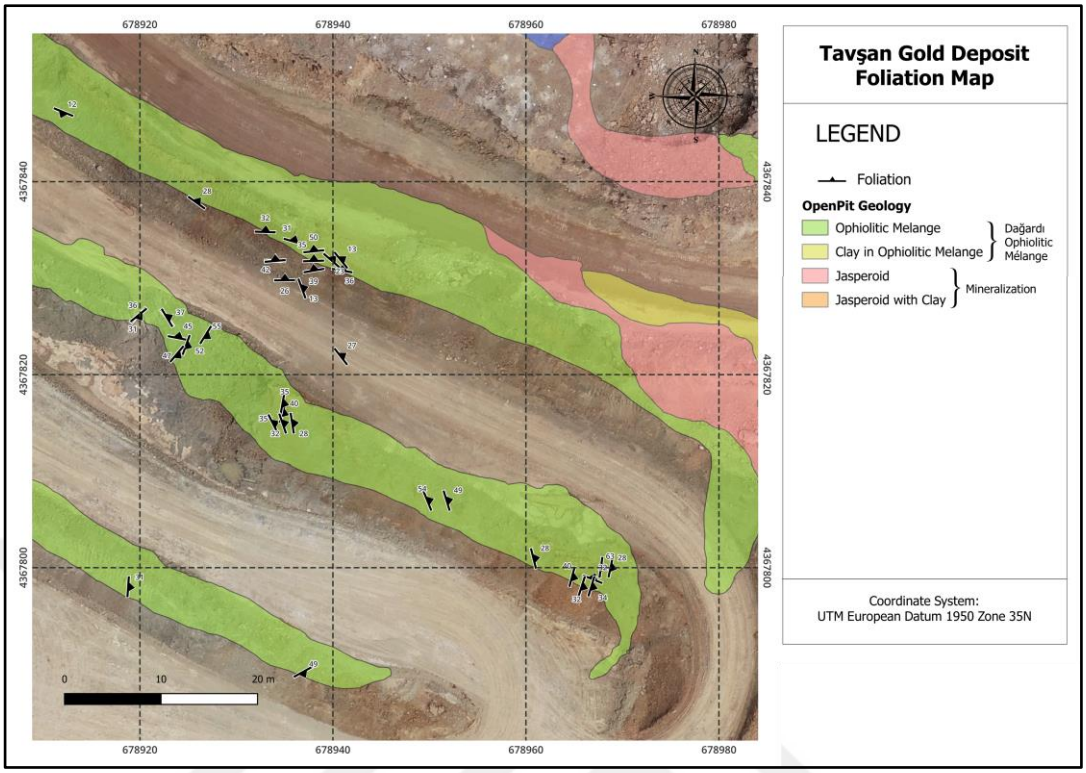
678920
678940
678960
678980
4367840
4367820
4367800
0
10
20 m
Tavşan Gold Deposit
Foliation Map
LEGEND
Foliation
OpenPit Geology
Ophiolitic Melange
Clay in Ophiolitic Melange
Dağardı Ophiolitic Mélange
Jasperoid
Jasperoid with Clay
Mineralization
Coordinate System:
UTM European Datum 1950 Zone 35N

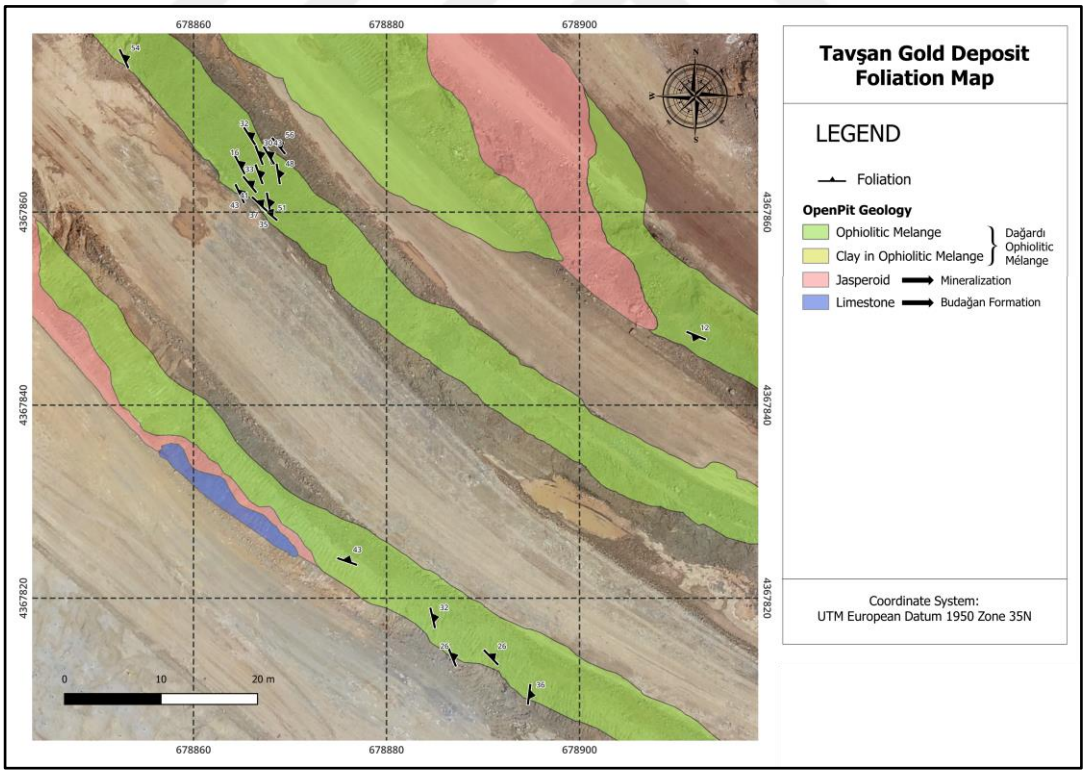
678860
678880
678900
4367860
4367840
4367820
0
10
20 m
Tavşan Gold Deposit
Foliation Map
LEGEND
Foliation
OpenPit Geology
Ophiolitic Melange
Clay in Ophiolitic Melange
Dağardı Ophiolitic Mélange
Jasperoid
Mineralization
Limestone
Budağan Formation
Coordinate System:
UTM European Datum 1950 Zone 35N

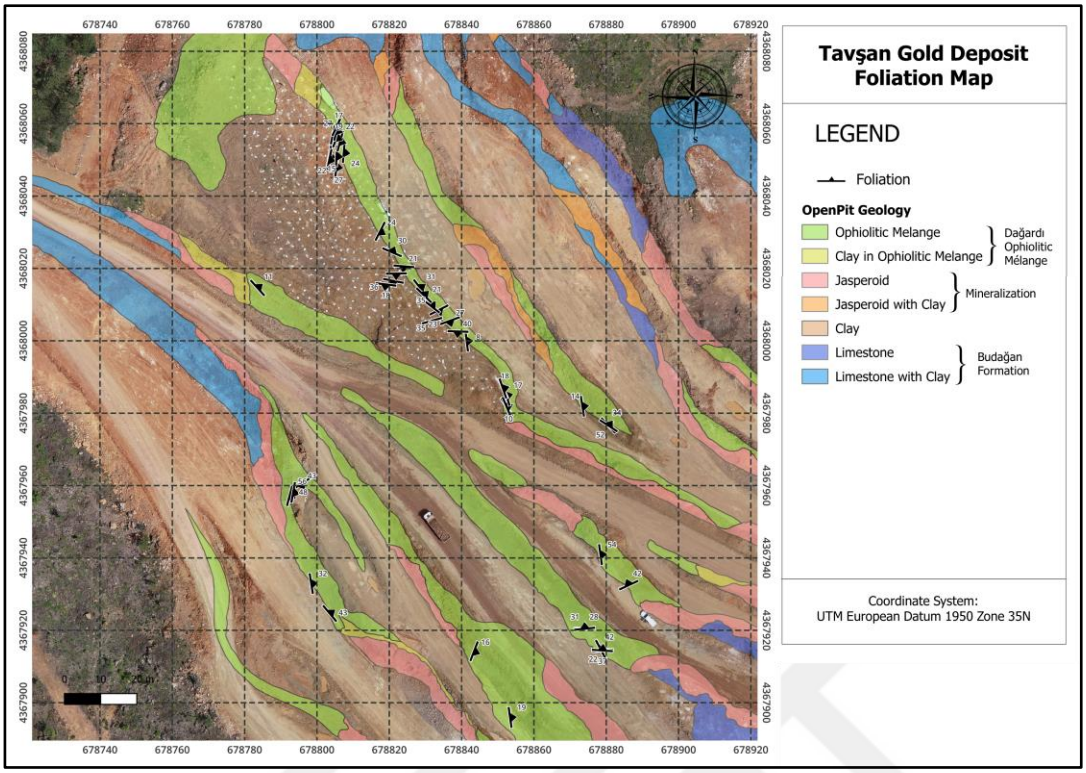
Tavşan Gold Deposit
Foliation Map
LEGEND
Foliation
OpenPit Geology
Ophiolitic Melange
Clay in Ophiolitic Melange
Dağardı Ophiolitic Mélange
Jasperoid
Jasperoid with Clay
Mineralization
Clay
Limestone
Limestone with Clay
Budağan Formation
Coordinate System:
UTM European Datum 1950 Zone 35N
678740
678760
678780
678800
678820
678840
678860
678880
678900
678920
4368080
4368060
4368040
4368020
4368000
4367980
4367960
4367940
4367920
4367900

F. Rock Assays

Easting	Northing	Au (ppm)	Ag (ppm)	As (ppm)	Sb (ppm)
678429	4366976	0.0	0.5	163.0	44.0
678181	4367481	0.4	1.0	137.0	59.0
678347	4367651	4.4	4.1	782.0	67.0
675124	4369873	0.0	0.0	638.0	53.0
675307	4369964	0.1	0.8	383.0	47.0
675331	4369953	0.1	0.9	523.0	67.0
674759	4370308	0.1	0.7	452.0	9900.0
679100	4368965	6.2	5.1	2980.0	310.0
677936	4369745	0.0	0.0	15.0	0.0
677657	4368785	0.0	0.0	10.0	0.0
677676	4368803	0.0	0.0	25.0	0.0
677717	4368875	0.0	0.0	17.0	6.0
674721	4369320	0.1	7.2	289.0	111.0
674764	4369316	0.0	0.8	85.0	120.0
674824	4369337	0.1	13.2	799.0	174.0
674843	4369368	0.0	4.5	300.0	100.0
674901	4369364	0.0	8.1	180.0	95.0
675006	4369423	0.0	1.5	151.0	71.0
675020	4369461	0.0	1.9	85.0	54.0
674961	4369440	0.0	2.1	310.0	106.0
674923	4369459	0.0	1.1	110.0	82.0
674906	4369465	0.0	1.2	130.0	76.0
674901	4369504	0.1	0.8	108.0	78.0
674811	4369422	0.0	1.7	98.0	91.0
674791	4369448	0.0	2.1	106.0	90.0
674784	4369492	0.0	0.0	100.0	577.0
674822	4369506	0.0	0.0	64.0	658.0
674822	4369506	0.0	0.5	72.0	1250.0
684680	4370852	0.1	17.7	1820.0	104.0
684680	4370870	0.1	23.0	352.0	76.0
684682	4370900	0.0	23.4	875.0	75.0
679104	4368966	1.0	4.2	1125.0	243.0
679136	4368975	1.7	5.5	562.0	119.0
679156	4368980	2.1	4.0	573.0	2410.0
679247	4369039	2.8	3.9	422.0	157.0
679260	4369072	1.5	7.9	322.0	150.0
679331	4369176	2.8	3.4	1010.0	87.0
679318	4369195	0.4	3.6	246.0	90.0
679330	4369190	0.5	5.9	166.0	224.0
679469	4369356	1.3	4.6	176.0	117.0
679505	4369383	0.3	1.5	76.0	112.0
679495	4369385	0.5	44.5	82.0	156.0
679495	4369390	0.9	4.3	256.0	119.0
679491	4369394	1.3	15.2	439.0	189.0
679495	4369410	1.6	32.0	265.0	165.0
679495	4369424	0.8	7.4	181.0	134.0
679495	4369429	2.8	10.4	236.0	154.0
679118	4366391	0.1	6.7	330.0	108.0
679123	4366400	0.1	3.8	258.0	51.0
679123	4366421	0.0	4.9	68.0	118.0
679119	4366424	0.1	4.3	188.0	104.0
679076	4366360	0.0	0.0	550.0	8.0
679059	4366385	0.0	0.0	323.0	8.0
679059	4366396	0.0	0.0	624.0	10.0

679054	4366395	0.0	0.0	1365.0	22.0
679055	4366399	0.0	0.5	644.0	9.0
679047	4366400	0.0	0.0	1015.0	10.0
679082	4366435	0.1	8.1	381.0	67.0
679102	4366466	0.1	7.8	283.0	60.0
679118	4366437	0.0	5.1	80.0	93.0
679119	4366420	0.0	8.6	68.0	159.0
684710	4370806	0.0	34.1	1210.0	124.0
684717	4370802	0.1	7.5	2860.0	153.0
684699	4370807	0.0	10.5	381.0	73.0
684694	4370826	0.0	7.9	114.0	96.0
684667	4370846	0.1	18.3	481.0	82.0
684656	4370872	0.3	22.8	1080.0	97.0
684663	4370882	0.1	21.5	768.0	120.0
684673	4370859	0.1	22.9	1920.0	75.0
684680	4370852	0.1	18.2	1770.0	133.0
684692	4370847	0.1	17.3	1540.0	130.0
671878	4372235	0.0	0.0	1500.0	12.0
671886	4371751	0.0	0.0	0.0	30.0
671893	4371785	0.0	0.0	0.0	7.0
671893	4371779	0.0	0.0	0.0	6.0
671583	4372555	0.0	0.0	465.0	0.0
671587	4372557	0.0	1.1	587.0	0.0
671617	4372770	0.0	0.0	19.0	138.0
671579	4372564	0.4	4.1	3670.0	1520.0
680493	4369939	0.2	7.9	110.0	79.0
680596	4369985	0.4	5.0	72.0	88.0
680586	4369973	0.4	8.3	111.0	126.0
680626	4369986	0.2	3.9	87.0	68.0
680627	4370007	0.0	1.3	12.0	16.0
680632	4370001	0.0	1.8	16.0	28.0
680168	4369855	0.0	0.0	509.0	5.0
677426	4366410	6.6	6.1	747.0	1080.0
678706	4368262	0.2	6.4	136.0	0.0
678729	4368284	0.3	6.7	341.0	502.0
678732	4368317	0.7	4.5	376.0	1465.0
678738	4368344	0.4	4.9	309.0	649.0
678763	4368366	1.2	9.3	461.0	665.0
678774	4368404	2.8	3.6	345.0	1725.0
678786	4368415	2.1	6.0	457.0	615.0
678767	4368442	1.6	20.8	661.0	225.0
678774	4368482	3.2	2.0	949.0	2620.0
678829	4368528	1.2	11.6	587.0	3120.0
678864	4368592	1.2	21.4	97.0	778.0
678900	4368610	1.1	21.1	507.0	143.0
678926	4368686	0.7	33.4	215.0	2880.0
678942	4368724	1.6	7.6	444.0	280.0
679062	4368840	1.1	5.4	174.0	84.0
679074	4368837	1.6	16.8	208.0	122.0
679104	4368970	5.0	4.6	1370.0	257.0
679143	4368989	6.6	3.4	1030.0	644.0
679181	4369002	1.4	4.9	425.0	96.0
679242	4369062	1.8	2.7	261.0	178.0
679275	4369091	0.4	3.9	1735.0	222.0
679325	4369111	1.8	5.6	534.0	149.0
679333	4369156	3.0	19.8	302.0	164.0
679345	4369245	2.5	6.6	516.0	162.0
679392	4369267	0.3	4.8	129.0	101.0

679440	4369350	1.7	3.4	776.0	255.0
679467	4369362	1.5	3.0	276.0	247.0
679496	4369411	2.3	12.7	363.0	143.0
679536	4369462	1.0	6.2	265.0	127.0
679526	4369523	7.0	3.7	1550.0	145.0
679529	4369505	1.4	3.0	215.0	142.0
679553	4369642	2.1	7.8	542.0	498.0
679607	4369658	0.9	6.8	333.0	108.0
679679	4369714	0.9	10.6	129.0	167.0
679738	4369714	0.9	4.1	191.0	131.0
679783	4369755	0.5	4.3	79.0	122.0
679815	4369785	1.5	11.0	205.0	87.0
679908	4369932	0.2	27.6	216.0	98.0
679951	4369952	0.2	36.4	172.0	98.0
679821	4369773	1.0	5.6	200.0	104.0
679903	4369809	6.3	5.9	298.0	405.0
679941	4369845	4.9	0.9	1395.0	4090.0
679993	4369847	1.7	4.6	567.0	159.0
680030	4369840	1.1	0.7	634.0	413.0
680195	4369918	0.6	3.0	134.0	117.0
680263	4370015	0.3	5.6	132.0	25.0
680250	4370020	0.2	8.1	134.0	26.0
680245	4370029	0.1	14.2	152.0	22.0
680272	4370056	0.0	16.6	351.0	23.0
680283	4370068	0.0	0.3	32.0	0.0
680875	4370016	0.1	8.5	54.0	36.0
680726	4370035	0.1	6.2	32.0	70.0
680697	4370046	0.4	30.8	138.0	131.0
680633	4370014	0.0	0.6	12.0	27.0
680586	4370025	0.4	5.3	128.0	391.0
680531	4370032	0.5	12.1	70.0	134.0
680510	4370009	0.0	0.3	20.0	13.0
680528	4370005	0.0	0.5	28.0	21.0
680450	4369992	0.1	3.0	142.0	62.0
680347	4370098	0.4	0.9	313.0	114.0
680395	4369995	1.0	7.1	180.0	55.0
680388	4370005	0.6	6.9	207.0	44.0
680380	4370002	0.9	16.8	185.0	112.0
680362	4370005	0.3	5.2	140.0	46.0
680370	4370008	1.1	3.8	413.0	39.0
680362	4370023	0.7	9.8	174.0	15.0
680360	4370038	0.1	11.3	90.0	22.0
680360	4370067	0.6	22.1	94.0	48.0
681169	4370004	0.1	5.8	0.0	0.0
681202	4369981	0.0	7.2	0.0	0.0
681257	4370001	0.0	1.0	0.0	0.0
677590	4367970	0.1	4.1	421.0	23.0
677585	4367920	0.1	0.7	555.0	20.0
677590	4367875	1.0	0.0	1108.0	85.0
677575	4367850	1.9	0.8	1060.0	131.0
677635	4367850	0.1	0.0	21.0	0.0
677535	4367865	0.5	2.5	104.0	19.0
677510	4367905	0.5	0.4	465.0	38.0
677500	4367860	1.0	0.6	402.0	66.0
677480	4367920	0.4	0.6	326.0	114.0
677510	4367960	0.2	0.6	276.0	22.0
677525	4368000	0.4	0.9	354.0	33.0
677520	4367980	0.2	1.2	1028.0	87.0

677580	4367780	0.5	1.0	284.0	74.0
677605	4367780	0.2	0.6	266.0	42.0
677585	4367825	0.2	0.5	236.0	42.0
680375	4370030	0.7	4.0	157.0	76.0
680375	4370030	0.4	2.3	99.0	35.0
680385	4370005	0.7	0.6	118.0	26.0
680405	4369960	1.2	2.1	153.0	16.0
680490	4369980	0.2	2.6	55.0	10.0
680530	4369950	0.3	3.6	83.0	18.0
680540	4369950	0.5	3.8	68.0	13.0
680580	4370010	0.6	6.8	93.0	57.0
680585	4370020	0.3	1.8	58.0	18.0
680640	4370015	0.1	6.3	29.0	15.0
680740	4369995	0.2	2.9	27.0	8.0
680750	4370000	0.3	4.5	45.0	8.0
680770	4370020	0.2	1.2	37.0	6.0
680860	4370050	0.1	1.8	29.0	5.0
680855	4370050	0.1	23.6	13.0	28.0
681040	4370060	0.1	1.7	45.0	8.0
681030	4370060	0.2	1.8	91.0	27.0
681130	4370035	0.1	3.1	48.0	10.0
681120	4370035	0.1	2.0	64.0	10.0
680600	4370050	0.1	1.0	19.0	7.0
680290	4370049	0.7	2.2	194.0	37.0
680229	4370073	0.1	3.7	15.0	0.0
680040	4369860	0.1	1.4	1600.0	11.0
679606	4369670	2.1	13.0	948.0	51.0
679820	4369760	0.3	0.0	53.0	48.0
679793	4369790	0.7	4.1	155.0	33.0
679195	4369228	1.9	6.2	207.0	62.0
679110	4368929	2.9	0.7	1200.0	146.0
679025	4369620	0.1	2.1	0.0	0.0
679534	4367944	0.6	11.5	170.0	48.0
679465	4368010	0.4	4.1	145.0	8.0
679391	4368001	0.6	4.5	210.0	89.0
679795	4367926	0.3	12.7	111.0	239.0
679793	4368007	0.4	8.3	179.0	264.0
679830	4367925	0.8	7.2	276.0	170.0
679902	4367985	1.1	4.2	173.0	555.0
680231	4370146	0.4	2.6	109.0	19.0
678832	4369304	0.1	1.2	18.0	0.0
677463	4367793	0.6	0.7	100.0	29.0
677367	4367824	0.3	1.1	267.0	64.0
677331	4367688	0.1	12.5	809.0	103.0
677444	4367912	0.1	1.1	949.0	103.0
677439	4367901	0.8	0.6	733.0	149.0
679330	4369245	9.0	6.2	1364.0	141.0
679313	4369165	4.0	2.3	1043.0	73.0
679333	4369175	1.3	4.6	306.0	75.0
679456	4369380	1.3	3.3	164.0	124.0
679457	4369359	0.7	2.2	134.0	20.0
679486	4369390	1.6	1.4	286.0	38.0
679490	4369400	2.7	3.3	344.0	54.0
679509	4369451	2.0	4.5	724.0	74.0
679512	4369492	0.5	3.3	221.0	41.0
679530	4369572	0.5	5.2	194.0	36.0
679548	4369632	2.5	2.7	344.0	103.0
679739	4369739	1.0	2.8	200.0	39.0

679769	4369740	1.1	4.2	279.0	47.0
677251	4367856	0.3	150.0	110.0	61.0
679890	4369874	0.1	44.8	344.0	65.0
679878	4369933	0.1	37.8	190.0	44.0
679970	4370007	0.1	3.8	114.0	19.0
679990	4370007	0.2	7.6	76.0	11.0
679149	4368979	1.8	2.7	591.0	28.0
678000	4367523	0.0	0.3	0.0	0.0
678037	4367490	0.1	0.8	0.0	0.0
678052	4367490	0.0	0.3	0.0	0.0
678070	4367466	0.1	0.5	0.0	0.0
678110	4367423	1.5	1.6	0.0	0.0
678143	4367387	0.5	2.6	0.0	0.0
678175	4367345	0.1	0.3	0.0	0.0
678212	4367313	0.0	0.3	0.0	0.0
678248	4367270	0.0	0.3	0.0	0.0
678283	4367233	0.0	0.3	0.0	0.0
678320	4367195	0.5	2.7	0.0	0.0
678354	4367159	0.0	0.3	0.0	0.0
678386	4367122	0.0	0.3	0.0	0.0
678430	4367085	0.0	0.3	0.0	0.0
678085	4367450	0.1	1.4	0.0	0.0
678090	4367445	0.1	0.3	0.0	0.0
678096	4367439	0.1	0.6	0.0	0.0
678102	4367430	0.1	1.9	0.0	0.0
678127	4367416	0.3	5.0	0.0	0.0
678152	4367380	0.3	1.3	0.0	0.0
678083	4367806	0.0	0.3	0.0	0.0
678103	4367784	3.0	11.4	0.0	0.0
678106	4367779	0.0	0.3	0.0	0.0
678157	4367727	0.4	3.6	0.0	0.0
678190	4367694	0.0	0.3	0.0	0.0
678208	4367675	0.2	2.8	0.0	0.0
678214	4367669	0.0	0.3	0.0	0.0
678227	4367651	0.2	1.6	0.0	0.0
678269	4367610	0.1	0.8	0.0	0.0
678282	4367589	1.0	0.0	0.0	0.0
678290	4367580	0.0	0.3	0.0	0.0
678315	4367575	0.2	0.5	0.0	0.0
678320	4367572	0.9	13.0	0.0	0.0
678330	4367562	0.0	0.3	0.0	0.0
678331	4367545	0.2	2.6	0.0	0.0
678329	4367533	0.0	0.3	0.0	0.0
678375	4367499	0.0	0.3	0.0	0.0
678400	4367470	0.9	2.8	0.0	0.0
678411	4367453	0.6	1.9	0.0	0.0
678411	4367446	0.6	3.2	0.0	0.0
678421	4367439	1.4	4.5	0.0	0.0
678423	4367432	0.8	5.2	0.0	0.0
678456	4367407	0.1	0.3	0.0	0.0
678465	4367398	0.1	0.3	0.0	0.0
678464	4367392	0.3	0.3	0.0	0.0
678492	4367371	0.0	0.3	0.0	0.0
678510	4367358	0.1	0.8	0.0	0.0
678513	4367347	0.2	4.1	0.0	0.0
678518	4367348	0.1	3.6	0.0	0.0
678519	4367344	0.7	1.7	0.0	0.0
678576	4367298	0.0	0.3	0.0	0.0

678605	4367259	0.0	0.3	0.0	0.0
678243	4367996	0.0	0.3	0.0	0.0
678243	4367996	0.0	0.3	0.0	0.0
678263	4367975	0.0	0.3	0.0	0.0
678242	4367956	0.0	0.8	0.0	0.0
678358	4367864	0.1	0.3	0.0	0.0
678386	4367827	0.3	4.9	0.0	0.0
678390	4367823	0.3	3.1	0.0	0.0
678394	4367819	1.6	3.2	0.0	0.0
678398	4367815	0.5	2.7	0.0	0.0
678402	4367811	1.4	6.9	0.0	0.0
678416	4367792	0.2	1.8	0.0	0.0
678420	4367789	0.2	3.5	0.0	0.0
678421	4367786	0.5	2.5	0.0	0.0
678424	4367783	0.6	2.8	0.0	0.0
678427	4367780	0.9	2.0	0.0	0.0
678434	4367773	0.1	1.7	0.0	0.0
678437	4367769	0.5	9.9	0.0	0.0
678442	4367764	2.0	3.5	0.0	0.0
678445	4367761	0.4	3.8	0.0	0.0
678448	4367758	0.4	3.8	0.0	0.0
678464	4367742	0.0	0.3	0.0	0.0
678473	4367731	0.0	0.3	0.0	0.0
678475	4367728	0.0	0.3	0.0	0.0
678539	4367632	0.4	2.6	0.0	0.0
678575	4367606	0.5	2.4	0.0	0.0
678584	4367593	0.1	0.3	0.0	0.0
678592	4367588	0.1	6.7	0.0	0.0
678597	4367586	0.1	0.5	0.0	0.0
678600	4367581	0.3	2.6	0.0	0.0
678606	4367578	0.6	2.0	0.0	0.0
678613	4367567	0.1	4.1	0.0	0.0
678614	4367567	0.4	5.4	0.0	0.0
678615	4367568	0.1	3.7	0.0	0.0
678616	4367569	2.0	4.9	0.0	0.0
678620	4367563	0.9	2.5	0.0	0.0
678624	4367562	0.2	3.4	0.0	0.0
678622	4367555	0.4	2.0	0.0	0.0
678626	4367550	0.5	3.7	0.0	0.0
678629	4367549	0.2	1.2	0.0	0.0
678630	4367545	0.0	0.3	0.0	0.0
678651	4367523	0.0	0.3	0.0	0.0
678691	4367481	0.0	0.3	0.0	0.0
678704	4367471	0.1	1.1	0.0	0.0
678705	4367467	0.1	4.3	0.0	0.0
678706	4367462	0.1	4.0	0.0	0.0
678714	4367451	0.0	2.1	0.0	0.0
678425	4368162	0.1	0.6	0.0	0.0
678456	4368128	0.0	0.9	0.0	0.0
678490	4368092	0.1	1.2	0.0	0.0
678529	4368053	0.0	0.6	0.0	0.0
678566	4368007	0.0	0.3	0.0	0.0
678580	4368012	6.9	4.0	0.0	0.0
678581	4368010	0.3	7.4	0.0	0.0
678590	4368000	0.2	7.9	0.0	0.0
678592	4367994	1.4	2.6	0.0	0.0
678595	4367990	0.7	4.7	0.0	0.0
678598	4367987	0.2	2.9	0.0	0.0

678603	4367982	1.4	2.3	0.0	0.0
678606	4367977	1.2	3.7	0.0	0.0
678609	4367972	5.4	4.0	0.0	0.0
678612	4367968	0.4	3.9	0.0	0.0
678617	4367963	0.1	5.1	0.0	0.0
678622	4367959	0.4	5.0	0.0	0.0
678624	4367954	0.5	4.1	0.0	0.0
678627	4367949	0.1	4.9	0.0	0.0
678629	4367945	0.7	3.3	0.0	0.0
678635	4367941	1.3	4.3	0.0	0.0
678638	4367936	0.8	4.0	0.0	0.0
678642	4367931	2.1	5.3	0.0	0.0
678645	4367926	0.5	4.2	0.0	0.0
678650	4367922	0.6	5.0	0.0	0.0
678655	4367918	2.6	4.9	0.0	0.0
678660	4367913	0.6	4.7	0.0	0.0
678664	4367908	0.9	3.0	0.0	0.0
678669	4367903	1.2	2.0	0.0	0.0
678674	4367898	0.6	3.2	0.0	0.0
678678	4367890	1.4	2.0	0.0	0.0
678684	4367887	0.6	5.0	0.0	0.0
678687	4367884	0.7	5.1	0.0	0.0
678693	4367881	0.4	6.4	0.0	0.0
678698	4367878	1.1	5.0	0.0	0.0
678705	4367875	1.2	5.3	0.0	0.0
678710	4367868	0.3	3.9	0.0	0.0
678719	4367844	0.8	2.1	0.0	0.0
678722	4367841	0.8	2.1	0.0	0.0
678730	4367838	0.5	2.0	0.0	0.0
678735	4367841	0.7	3.3	0.0	0.0
678738	4367835	0.2	2.6	0.0	0.0
678742	4367830	1.4	5.4	0.0	0.0
678745	4367827	1.9	9.4	0.0	0.0
678786	4367784	0.7	2.7	0.0	0.0
678794	4367777	1.0	4.0	0.0	0.0
678802	4367770	1.8	4.8	0.0	0.0
678803	4367769	3.4	5.8	0.0	0.0
678803	4367765	2.4	5.9	0.0	0.0
678803	4367764	1.0	2.0	0.0	0.0
678816	4367756	0.9	9.0	0.0	0.0
678820	4367754	0.8	6.7	0.0	0.0
678843	4367728	0.4	6.8	0.0	0.0
678845	4367724	2.4	7.4	0.0	0.0
678847	4367717	5.8	6.0	0.0	0.0
678851	4367713	1.3	5.0	0.0	0.0
678856	4367712	1.7	5.6	0.0	0.0
678862	4367713	2.4	11.4	0.0	0.0
678865	4367704	7.0	9.0	0.0	0.0
678876	4367698	3.9	4.4	0.0	0.0
678935	4367685	0.1	1.5	0.0	0.0
678955	4367650	0.0	0.3	0.0	0.0
678975	4367629	0.7	4.5	0.0	0.0
678990	4367615	0.0	0.6	0.0	0.0
678574	4368008	0.7	4.5	0.0	0.0
678579	4368001	0.4	3.4	0.0	0.0
678805	4367761	1.2	1.7	0.0	0.0
678809	4367759	3.9	2.9	0.0	0.0
678813	4367757	0.1	1.5	0.0	0.0

678749	4367822	0.3	1.1	0.0	0.0
678754	4367818	0.3	1.9	0.0	0.0
678759	4367815	0.6	3.1	0.0	0.0
678765	4367810	0.1	3.2	0.0	0.0
678771	4367800	0.4	2.3	0.0	0.0
678778	4367794	1.2	4.0	0.0	0.0
678712	4367865	0.2	1.8	0.0	0.0
678716	4367855	0.4	2.7	0.0	0.0
678977	4367627	0.6	1.5	0.0	0.0
678973	4367631	0.7	20.7	0.0	0.0
678971	4367633	0.3	2.0	0.0	0.0
678969	4367635	0.1	3.3	0.0	0.0
678564	4368377	0.0	0.3	0.0	0.0
678602	4368342	0.0	0.3	0.0	0.0
678641	4368305	0.1	1.0	0.0	0.0
678664	4368283	0.4	5.1	0.0	0.0
678687	4368260	0.8	5.1	0.0	0.0
678690	4368263	0.5	6.3	0.0	0.0
678705	4368248	0.1	2.3	0.0	0.0
678720	4368233	0.3	4.6	0.0	0.0
678724	4368229	0.1	4.8	0.0	0.0
678728	4368225	0.2	3.2	0.0	0.0
678740	4368213	0.1	2.4	0.0	0.0
678752	4368201	0.1	4.0	0.0	0.0
678764	4368189	0.2	5.7	0.0	0.0
678776	4368177	0.2	4.2	0.0	0.0
678788	4368165	0.3	4.7	0.0	0.0
678805	4368149	0.7	7.2	0.0	0.0
678813	4368141	0.9	4.8	0.0	0.0
678816	4368137	0.9	3.0	0.0	0.0
678819	4368134	0.7	4.3	0.0	0.0
678822	4368131	0.9	4.0	0.0	0.0
678825	4368128	1.2	5.0	0.0	0.0
678828	4368125	0.8	2.8	0.0	0.0
678831	4368122	0.9	3.0	0.0	0.0
678834	4368119	0.4	3.7	0.0	0.0
678837	4368116	1.4	2.6	0.0	0.0
678840	4368113	0.4	1.7	0.0	0.0
678843	4368110	0.2	2.5	0.0	0.0
678846	4368107	0.5	3.5	0.0	0.0
678849	4368104	3.3	6.6	0.0	0.0
678852	4368101	1.1	3.0	0.0	0.0
678855	4368098	0.4	4.4	0.0	0.0
678861	4368092	0.9	6.5	0.0	0.0
678864	4368089	0.1	3.5	0.0	0.0
678867	4368086	0.5	5.9	0.0	0.0
678870	4368083	0.0	3.0	0.0	0.0
678873	4368080	0.5	4.3	0.0	0.0
678876	4368077	0.8	4.6	0.0	0.0
678879	4368074	0.3	8.4	0.0	0.0
678882	4368071	3.8	10.2	0.0	0.0
678885	4368068	0.5	11.8	0.0	0.0
678888	4368065	5.3	15.0	0.0	0.0
678891	4368062	0.5	4.2	0.0	0.0
678894	4368059	2.0	5.7	0.0	0.0
678897	4368056	1.1	4.0	0.0	0.0
678900	4368053	2.4	2.5	0.0	0.0
678905	4368046	0.7	2.2	0.0	0.0

678907	4368041	0.2	1.7	0.0	0.0
678918	4368029	0.5	2.1	0.0	0.0
678929	4368017	0.4	2.3	0.0	0.0
678940	4368005	2.9	3.8	0.0	0.0
678951	4367993	0.5	7.8	0.0	0.0
678962	4367981	0.6	5.7	0.0	0.0
678973	4367969	0.1	4.3	0.0	0.0
678984	4367957	0.2	6.6	0.0	0.0
678995	4367945	0.1	8.3	0.0	0.0
679010	4367905	0.1	5.5	0.0	0.0
679013	4367903	0.1	2.5	0.0	0.0
679018	4367896	0.1	1.8	0.0	0.0
679021	4367892	0.1	1.2	0.0	0.0
679030	4367884	0.4	3.9	0.0	0.0
679035	4367878	0.2	2.4	0.0	0.0
679041	4367873	1.8	3.0	0.0	0.0
679045	4367868	0.1	0.3	0.0	0.0
679051	4367859	1.6	2.4	0.0	0.0
679055	4367854	2.8	5.9	0.0	0.0
679064	4367845	0.5	6.3	0.0	0.0
679060	4367840	0.3	2.7	0.0	0.0
679077	4367820	0.9	3.7	0.0	0.0
679081	4367800	1.0	7.0	0.0	0.0
679085	4367813	0.5	2.8	0.0	0.0
679089	4367811	0.4	8.4	0.0	0.0
679093	4367809	0.4	5.4	0.0	0.0
679097	4367807	0.2	6.2	0.0	0.0
679105	4367803	0.2	4.7	0.0	0.0
679109	4367801	0.9	4.8	0.0	0.0
679113	4367799	1.0	6.0	0.0	0.0
679114	4367797	1.0	2.0	0.0	0.0
679116	4367795	0.4	2.7	0.0	0.0
679120	4367788	0.1	2.0	0.0	0.0
679125	4367783	0.1	5.0	0.0	0.0
679131	4367778	0.0	1.2	0.0	0.0
679137	4367771	0.0	0.3	0.0	0.0
679143	4367764	0.8	2.3	0.0	0.0
679149	4367757	0.2	2.5	0.0	0.0
679155	4367750	0.0	0.3	0.0	0.0
679161	4367743	0.1	0.3	0.0	0.0
679167	4367736	0.0	0.3	0.0	0.0
679182	4367721	0.0	0.3	0.0	0.0
679184	4367717	0.1	12.2	0.0	0.0
679200	4367699	0.0	0.3	0.0	0.0
679215	4367689	0.1	5.9	0.0	0.0
679227	4367680	0.0	0.3	0.0	0.0
679233	4367673	0.2	0.8	0.0	0.0
678695	4368257	0.2	3.0	0.0	0.0
678700	4368251	0.2	6.8	0.0	0.0
678710	4368245	0.1	3.7	0.0	0.0
678722	4368230	0.3	9.3	0.0	0.0
678744	4368209	0.1	3.0	0.0	0.0
678748	4368205	0.5	5.2	0.0	0.0
678756	4368197	0.2	3.9	0.0	0.0
678760	4368193	0.1	3.2	0.0	0.0
678768	4368185	0.2	4.5	0.0	0.0
678772	4368181	0.2	7.4	0.0	0.0
678810	4368145	0.3	3.9	0.0	0.0

679059	4367849	0.2	4.0	0.0	0.0
679073	4367840	1.3	3.3	0.0	0.0
679113	4367799	0.7	4.0	0.0	0.0
679117	4367797	0.6	5.3	0.0	0.0
678683	4368615	0.0	0.3	0.0	0.0
678719	4368578	0.0	0.3	0.0	0.0
678746	4368551	0.9	10.0	0.0	0.0
678755	4368546	0.6	6.6	0.0	0.0
678760	4368537	1.3	9.6	0.0	0.0
678766	4368531	0.6	5.0	0.0	0.0
678769	4368528	1.4	5.0	0.0	0.0
678777	4368519	0.7	7.9	0.0	0.0
678786	4368525	4.8	10.4	0.0	0.0
678786	4368513	1.3	5.5	0.0	0.0
678780	4368502	1.7	3.9	0.0	0.0
678782	4368500	1.7	1.4	0.0	0.0
678791	4368497	1.4	11.0	0.0	0.0
678795	4368495	1.4	5.6	0.0	0.0
678808	4368488	0.6	7.8	0.0	0.0
678811	4368485	0.0	0.5	0.0	0.0
678815	4368481	0.0	0.3	0.0	0.0
678831	4368485	0.8	5.3	0.0	0.0
678834	4368478	0.3	5.5	0.0	0.0
678833	4368459	0.0	0.3	0.0	0.0
678836	4368456	0.6	4.4	0.0	0.0
678837	4368457	1.1	5.0	0.0	0.0
678841	4368452	0.8	17.4	0.0	0.0
678848	4368444	0.1	1.4	0.0	0.0
678856	4368433	0.1	0.7	0.0	0.0
678863	4368426	0.0	2.1	0.0	0.0
678867	4368425	0.0	1.5	0.0	0.0
678868	4368424	0.0	0.6	0.0	0.0
678878	4368411	0.0	0.3	0.0	0.0
678912	4368391	0.0	0.3	0.0	0.0
678950	4368347	0.0	4.3	0.0	0.0
678956	4368341	0.0	1.0	0.0	0.0
678977	4368323	0.0	0.3	0.0	0.0
678997	4368305	0.0	0.3	0.0	0.0
679019	4368288	0.2	4.6	0.0	0.0
679017	4368326	0.2	4.7	0.0	0.0
679019	4368279	0.3	8.0	0.0	0.0
679026	4368276	0.1	17.6	0.0	0.0
679032	4368274	0.3	17.0	0.0	0.0
679031	4368272	0.0	1.2	0.0	0.0
679036	4368268	0.0	0.3	0.0	0.0
679052	4368254	0.0	0.6	0.0	0.0
679063	4368243	0.2	4.4	0.0	0.0
679072	4368235	0.1	1.6	0.0	0.0
679081	4368229	0.5	6.8	0.0	0.0
679086	4368226	0.1	36.5	0.0	0.0
679097	4368224	0.0	3.1	0.0	0.0
679103	4368219	0.1	4.2	0.0	0.0
679121	4368199	0.0	0.3	0.0	0.0
679127	4368192	0.0	0.7	0.0	0.0
679151	4368152	0.0	0.3	0.0	0.0
679187	4368112	0.0	0.3	0.0	0.0
679196	4368107	0.1	9.4	0.0	0.0
679224	4368078	0.0	0.3	0.0	0.0

679260	4368063	0.0	0.3	0.0	0.0
679280	4368037	0.1	4.8	0.0	0.0
679285	4368030	0.0	0.3	0.0	0.0
679288	4368026	0.0	2.4	0.0	0.0
679291	4368023	0.0	2.5	0.0	0.0
679297	4368016	0.0	2.4	0.0	0.0
679305	4368008	0.1	3.3	0.0	0.0
679313	4367998	0.1	4.6	0.0	0.0
679321	4367994	0.1	2.4	0.0	0.0
679335	4367978	0.1	1.4	0.0	0.0
679354	4367959	0.0	0.3	0.0	0.0
679379	4367936	0.0	0.3	0.0	0.0
679412	4367907	0.0	0.3	0.0	0.0
678893	4368786	0.2	2.7	0.0	0.0
678925	4368764	0.0	0.3	0.0	0.0
678932	4368757	0.0	0.3	0.0	0.0
678937	4368749	0.2	4.5	0.0	0.0
678942	4368724	1.6	7.6	0.0	0.0
678920	4368730	0.4	11.3	0.0	0.0
678943	4368709	0.1	4.4	0.0	0.0
678966	4368688	0.2	24.3	0.0	0.0
678989	4368667	0.0	0.3	0.0	0.0
679013	4368655	0.0	1.0	0.0	0.0
679031	4368635	0.2	2.6	0.0	0.0
679059	4368605	0.2	10.9	0.0	0.0
679060	4368602	0.0	0.3	0.0	0.0
679063	4368599	0.2	2.5	0.0	0.0
679072	4368597	0.1	1.8	0.0	0.0
679075	4368589	0.1	4.5	0.0	0.0
679083	4368561	0.3	3.0	0.0	0.0
679088	4368558	0.9	4.2	0.0	0.0
679093	4368555	1.0	4.0	0.0	0.0
679098	4368552	2.1	3.7	0.0	0.0
679103	4368549	0.1	1.4	0.0	0.0
679108	4368546	0.1	3.2	0.0	0.0
679116	4368545	0.6	2.3	0.0	0.0
679120	4368542	0.4	3.3	0.0	0.0
679124	4368539	0.9	2.0	0.0	0.0
679128	4368536	0.3	1.4	0.0	0.0
679132	4368533	0.6	2.5	0.0	0.0
679136	4368530	1.5	6.5	0.0	0.0
679140	4368527	0.3	2.0	0.0	0.0
679144	4368524	0.7	4.0	0.0	0.0
679170	4368498	0.2	2.3	0.0	0.0
679183	4368485	0.3	1.9	0.0	0.0
679206	4368471	2.3	2.2	0.0	0.0
679210	4368456	0.3	2.3	0.0	0.0
679221	4368445	0.3	3.3	0.0	0.0
679231	4368430	0.4	5.2	0.0	0.0
679257	4368411	0.1	1.7	0.0	0.0
679279	4368388	0.2	2.4	0.0	0.0
679294	4368370	2.8	2.3	0.0	0.0
679325	4368343	2.1	3.3	0.0	0.0
679334	4368340	4.0	3.4	0.0	0.0
679359	4368320	2.4	5.7	0.0	0.0
679362	4368313	0.9	6.0	0.0	0.0
679367	4368307	0.1	0.8	0.0	0.0
679368	4368295	0.5	6.8	0.0	0.0

679380	4368302	0.4	1.9	0.0	0.0
679383	4368300	0.7	2.9	0.0	0.0
679391	4368293	0.3	5.0	0.0	0.0
679392	4368292	2.7	10.1	0.0	0.0
679393	4368291	0.6	4.4	0.0	0.0
679404	4368280	1.7	3.4	0.0	0.0
679415	4368273	1.0	4.0	0.0	0.0
679422	4368269	3.2	3.8	0.0	0.0
679429	4368265	1.1	3.0	0.0	0.0
679436	4368259	0.3	2.5	0.0	0.0
679445	4368253	0.1	1.7	0.0	0.0
679454	4368247	0.1	1.7	0.0	0.0
679463	4368241	0.3	4.4	0.0	0.0
679472	4368235	0.2	23.2	0.0	0.0
679481	4368229	0.4	10.2	0.0	0.0
679490	4368223	0.1	13.4	0.0	0.0
679499	4368217	0.7	5.0	0.0	0.0
679492	4368198	0.2	8.8	0.0	0.0
679497	4368193	0.1	5.1	0.0	0.0
679502	4368188	0.1	5.4	0.0	0.0
679507	4368183	0.2	9.0	0.0	0.0
679512	4368178	0.2	5.1	0.0	0.0
679517	4368173	0.1	5.7	0.0	0.0
679522	4368168	0.2	15.6	0.0	0.0
679527	4368163	0.2	9.5	0.0	0.0
679532	4368158	0.1	4.0	0.0	0.0
679537	4368153	0.2	2.8	0.0	0.0
679542	4368148	0.1	4.6	0.0	0.0
679547	4368143	0.1	6.5	0.0	0.0
679560	4368131	0.1	5.8	0.0	0.0
679562	4368129	0.2	3.7	0.0	0.0
679563	4368124	0.2	3.9	0.0	0.0
679564	4368119	0.1	6.0	0.0	0.0
679565	4368114	0.1	7.0	0.0	0.0
679566	4368109	0.1	7.4	0.0	0.0
679567	4368104	0.1	19.0	0.0	0.0
679568	4368099	0.1	11.4	0.0	0.0
679569	4368094	0.1	6.9	0.0	0.0
679570	4368089	0.1	8.4	0.0	0.0
679571	4368084	0.1	22.3	0.0	0.0
679594	4368079	0.1	6.0	0.0	0.0
679611	4368066	0.1	8.4	0.0	0.0
679619	4368052	0.1	2.3	0.0	0.0
679629	4368028	0.0	0.3	0.0	0.0
679635	4368012	0.0	8.4	0.0	0.0
679362	4368667	0.0	0.3	0.0	0.0
679389	4368636	0.0	0.3	0.0	0.0
679403	4368616	0.0	0.3	0.0	0.0
679427	4368596	0.0	0.3	0.0	0.0
679443	4368576	0.0	0.3	0.0	0.0
679469	4368555	0.0	0.3	0.0	0.0
679491	4368533	0.0	0.3	0.0	0.0
679506	4368510	0.0	0.9	0.0	0.0
679520	4368499	0.4	5.1	0.0	0.0
679521	4368493	0.4	2.2	0.0	0.0
679525	4368489	0.9	29.1	0.0	0.0
679532	4368484	0.9	11.3	0.0	0.0
679536	4368480	0.0	0.3	0.0	0.0

679541	4368474	0.1	2.9	0.0	0.0
679559	4368457	0.8	8.4	0.0	0.0
679570	4368453	0.6	10.5	0.0	0.0
679575	4368446	0.8	5.5	0.0	0.0
679595	4368430	0.9	13.8	0.0	0.0
679600	4368422	0.0	0.3	0.0	0.0
679626	4368399	0.0	0.3	0.0	0.0
679642	4368382	0.0	0.3	0.0	0.0
679672	4368357	0.8	5.7	0.0	0.0
679691	4368340	0.0	0.3	0.0	0.0
679709	4368318	0.0	0.3	0.0	0.0
679732	4368298	0.0	0.3	0.0	0.0
679760	4368275	0.0	0.3	0.0	0.0
679775	4368260	0.0	0.3	0.0	0.0
679798	4368236	0.0	0.3	0.0	0.0
679833	4368203	0.0	0.3	0.0	0.0
679859	4368185	0.0	0.3	0.0	0.0
679880	4368161	0.0	0.3	0.0	0.0
679917	4368130	0.0	6.4	0.0	0.0
679941	4368106	0.0	0.3	0.0	0.0
679962	4368078	0.0	0.3	0.0	0.0
679980	4368061	0.0	0.6	0.0	0.0
680002	4368040	0.0	0.3	0.0	0.0
680022	4368023	0.0	1.4	0.0	0.0
680045	4368002	0.0	0.3	0.0	0.0
680066	4367981	0.4	1.5	0.0	0.0
680080	4367970	0.0	0.3	0.0	0.0
680091	4367965	0.0	0.3	0.0	0.0
680101	4367943	0.5	2.9	0.0	0.0
678834	4367696	1505.0	3.9	185.0	4230.0
678842	4367695	1.8	2.1	280.0	6940.0
678848	4367700	1135.0	3.6	260.0	2600.0
678853	4367697	2.5	2.9	292.0	7930.0
678850	4367693	1915.0	6.9	157.0	0.0
678844	4367690	1505.0	3.6	167.0	4710.0
678859	4367690	0.9	2.4	202.0	4800.0
678875	4367711	2.5	5.0	279.0	1875.0
678875	4367711	1145.0	3.4	204.0	7070.0
678869	4367712	1.3	3.6	276.0	0.0
678612	4368014	1.9	7.9	597.0	3560.0
678611	4368018	1225.0	2.5	3810.0	2170.0
678610	4368027	0.9	2.5	582.0	4260.0
678608	4367994	0.9	2.0	157.0	730.0
678616	4367983	0.8	9.3	118.0	1015.0
670333	4351727	0.0	0.0	20.0	51.0
670322	4351763	0.0	0.0	20.0	4.0
670320	4351763	0.0	0.6	80.0	0.0
679141	4368961	1.4	10.3	380.3	114.1
679143	4368961	1.5	5.3	379.1	198.3
679145	4368960	1.5	3.8	309.0	130.6
679139	4368961	0.2	4.9	415.0	265.4
679143	4368963	0.9	7.8	439.0	191.1
680253	4368513	0.4	0.5	117.3	57.7
680253	4368513	0.5	35.9	54.4	87.8
680253	4368513	0.2	5.4	59.5	77.0
680806	4368091	0.0	1.5	56.3	51.4
680780	4368088	0.0	0.5	95.2	15.3
680780	4368088	0.0	0.5	84.0	12.7

680750	4368083	0.3	40.6	95.1	136.9
680750	4368083	0.0	1.1	306.5	196.5
677581	4372861	0.0	0.5	37.5	15.4
678217	4373030	0.0	0.5	1.0	5.0
679321	4373589	0.0	0.5	2.3	5.0
679410	4373503	0.0	0.5	1.0	5.0
679363	4373419	0.0	0.5	5.6	5.0
679051	4373276	0.0	0.5	2.4	5.0
678834	4372890	0.5	0.5	10.4	7.0
678373	4373128	0.0	0.5	3.0	5.0
678171	4372473	0.0	0.5	1.7	5.0
678385	4373662	0.0	0.5	2.2	5.0
678475	4372103	0.0	0.5	4.6	5.0
678038	4373630	0.0	0.5	1.0	5.0
678021	4373686	0.0	0.5	1.5	5.0
677908	4373609	0.0	0.5	1.9	5.0
677285	4372741	0.0	0.5	2.4	5.0
677288	4372740	0.0	0.5	1.0	5.0
677306	4372733	0.0	4.6	1.5	5.0
677324	4372732	0.0	2.1	1.0	5.0
677525	4371740	0.0	0.5	1.0	5.0
678015	4373828	0.0	1.0	1.0	5.0
678968	4372489	0.9	4.9	7.4	8.5
678368	4367988	0.1	0.5	18.7	5.0
678835	4369657	0.0	0.5	2.9	5.0
678935	4369814	0.0	0.5	5.4	5.0
678934	4369815	0.0	0.5	1.9	5.0
678931	4369823	0.0	0.5	1.4	5.0
678939	4369820	0.0	0.8	23.0	5.0
678935	4369823	0.0	0.5	3.7	5.0
679477	4369778	0.0	0.5	1.0	5.0
679474	4369769	0.0	0.5	1.6	5.0
679463	4369770	0.0	0.5	1.0	5.0
679468	4369771	0.0	0.5	1.0	5.0
679494	4369769	0.0	0.5	1.0	5.0
679643	4370036	0.0	0.5	1.0	5.0
679956	4370144	0.6	4.7	109.4	10051.2
679962	4370121	0.1	8.7	70.6	399.0
679221	4370383	0.0	0.6	35.7	38.1
679816	4368040	0.3	13.2	427.8	171.0
679822	4368012	1.6	11.8	256.8	205.3
679838	4368001	0.5	1.5	78.9	316.8
679849	4368000	0.0	3.0	90.8	67.3
679867	4367993	0.7	13.1	162.0	611.8
679885	4367978	0.5	4.2	116.3	220.2
679901	4367972	0.9	5.6	264.5	333.3
679905	4367969	1.4	9.5	256.5	373.3
679911	4367952	0.5	4.5	437.1	533.2
679914	4367937	0.7	0.6	151.6	98.3
679914	4367937	1.4	3.3	107.3	873.3
679931	4367934	0.1	12.7	91.5	68.0
679937	4367911	0.7	8.4	181.8	261.9
679970	4367889	1.6	6.2	408.2	114.0
679980	4367888	0.4	4.3	268.5	870.1
680010	4367868	0.2	1.7	117.3	75.3
680055	4367776	0.1	7.3	147.6	30.7
679708	4367802	0.3	17.5	299.5	49.8
678972	4372556	0.2	1.7	17.4	6.1

678974	4372561	0.2	0.5	23.4	10.8
678965	4372562	1.5	8.6	2.4	17.4
678964	4372547	0.1	0.5	16.0	13.5
678979	4372526	0.2	1.2	19.8	5.0
678980	4372479	1.1	3.3	20.6	14.9
678996	4372462	1.9	8.4	11.3	7.6
678995	4372439	0.8	5.3	17.3	15.4
679005	4372405	1.2	3.9	19.6	14.6
675005	4373721	0.1	0.5	4.5	>10000.00
675007	4373722	0.0	0.5	1.0	>10000.00
677522	4371764	0.0	5.0	36.2	36.4
677443	4371915	0.0	15.9	45.7	89.5
678843	4370194	0.0	30.0	13.5	5.0
678833	4370190	0.0	41.3	17.0	5.0
679145	4370363	0.0	41.4	87.9	12.8
679146	4370360	0.0	43.9	69.2	7.4
679083	4367863	10.3	1.6	306.9	832.9
679093	4367850	0.8	3.0	114.0	164.2
679097	4367824	0.4	2.5	238.4	60.5
679141	4367696	0.0	0.5	358.0	55.0
678008	4368880	0.0	26.1	40.0	5.0
678005	4368887	0.0	17.1	109.0	5.5